



DISSERTATION

**Electronic structure and transport  
in mesoscopic devices**

ausgeführt zum Zwecke der Erlangung des akademischen Grades  
eines Doktors der technischen Wissenschaften

unter der Anleitung von  
O.Univ.-Prof. Dipl.-Phys. Dr. Joachim Burgdörfer  
und  
Univ.Ass. Dipl.-Ing. Dr. Stefan Rotter  
am Institut für Theoretische Physik  
der Technischen Universität Wien

eingereicht an der Technischen Universität Wien  
Fakultät für Physik von

Dipl.-Ing. Florian Libisch  
Matrikelnummer: 9725224  
Dannebergpl. 15/9  
1030 Wien

---

Datum

---

Unterschrift

*“Gott würfelt nicht!”*

*“God does not throw dice!”*

Albert Einstein, Solvay conference, Brussels, 1927

*“Hören Sie endlich auf, dem Herrgott Vorschriften zu machen.”*

*“Nor is it our business to prescribe to God how He should run the world.”*

Niels Bohr, *ibid.*

# Quantentransport und Eigenzustände mesoskopischer Systeme

Abstract in german - Deutsche Kurzfassung

Mesoskopische Systeme, das heißt Systeme von der Größenordnung weniger  $\mu\text{m}$ , unterliegen der durch die Quantentheorie beschriebenen Wellennatur physikalischer Phänomene. Zum Beispiel muss der Transport von Elektronen durch solche Strukturen durch eine Wellengleichung, die Schrödinger-Gleichung der Quantentheorie, beschrieben werden.

Große Fortschritte in der Fertigung kleiner und kleinster Bauelemente in der Halbleitertechnologie ermöglichen mittlerweile die Herstellung von Mikrostrukturen, deren Dynamik durch die Wellennatur der Elektronen bestimmt wird. Gleichzeitig liefert die erstmalige experimentelle Darstellung eines monoatomaren, hexagonalen Kohlenstoffgitters, genannt Graphen, neue Materialien, die zum Beispiel den Quanten-Hall-Effekt bei Raumtemperatur zeigen. Damit sind die Konsequenzen der Wellennatur der Elektronen direkt über Transportmessungen nachvollziehbar.

Die theoretische Beschreibung zweidimensionaler Leiterstrukturen ist numerisch und analytisch bereits weit fortgeschritten. Als Beispiel sei die rekursive Greensfunktionsmethode (RGM) erwähnt [1, 2, 3, 4, 5], bei der komplexe Streugeometrien in einzelne Streifen zerlegt werden, deren Greensfunktion durch direkte Inversion berechnet werden kann. Schrittweise werden diese Streifen dann aneinandergelängt. Für den Vergleich mit dem Experiment sind allerdings Effekte durch raue Umrandungen, im Material vorhandene Gitterfehler und Störstellen essentiell. Diese Effekte erfordern numerische Lösungen, die oft entweder sehr zeitaufwändig oder auf sehr spezielle Probleme zugeschnitten sind. Ziel dieser Arbeit ist daher die Entwicklung und Anwendung eines flexiblen, leistungsfähigen Verfahrens zur Beschreibung der Quantentransporteigenschaften unterschiedlichster Materialien. Zu diesem Zweck stellen wir im ersten Teil dieser Arbeit eine effiziente Methode vor, die es erlaubt, die Greensfunktion rechteckiger Module für eine große Klasse verschiedener Materialien auszurechnen sowie diese Module dann in beliebiger Anzahl und Reihenfolge zusammenzufügen. Die so erhaltene Greensche Funktion der Streugeometrie kann nun verwendet wer-

den, um die Transmission, das Schrotrauschen oder die Streuzustände der Streugeometrie auszurechnen.

Im zweiten Teil der Arbeit benutzen wir das vorgestellte Verfahren für die Beschreibung der elektronischen Struktur und der Transporteigenschaften von Graphen sowie von Normal-Supraleiter-Hybridstrukturen. Für beide Systeme existieren vereinfachte Modellbeschreibungen, die im ersten Fall auf der Dirac-Gleichung, im zweiten Fall auf der semiklassischen Quantisierung periodischer Bahnen beruhen. In beiden Fällen präsentieren wir Effekte, die im Rahmen der vereinfachten Modellbeschreibungen nicht verstanden werden können. Wir diskutieren die Gründe für dieses Versagen und bieten alternative Beschreibungen an.

Die Arbeit schließt mit einer Zusammenfassung sowie einem Ausblick auf zukünftige Projekte.

# List of acronyms

AB	Andreev billiard
arb.u.	arbitrary units
BCS	Bardeen-Cooper-Schliefer
BdG	Bogolioubov-de Gennes
BS	Bohr-Sommerfeld
DFT	density functional theory
DOS	density of states
IRAL	implicitly restarted Arnoldi-Lanczos algorithm
MRGM	modular recursive Green's function method
NN	nearest neighbor
STM	scanning tunneling microscope
SWD	Stone-Wales defect
TB	tight-binding

# Contents

<b>1</b>	<b>Introduction</b>	<b>1</b>
<b>I</b>	<b>Method and first numerical results</b>	<b>4</b>
<b>2</b>	<b>Mesoscopic devices</b>	<b>5</b>
2.1	Tight-binding approximation . . . . .	5
2.1.1	Band structure . . . . .	8
2.1.2	Parameter fit . . . . .	9
2.1.3	Continuum limit . . . . .	10
2.1.4	Large-scale devices . . . . .	12
2.1.5	Lanczos diagonalization . . . . .	14
2.1.6	Magnetic field . . . . .	15
<b>3</b>	<b>Scattering theory</b>	<b>17</b>
3.1	Infinite waveguides . . . . .	18
3.2	Modular recursive Green's function method . . . . .	20
3.2.1	The Green's function of an infinite waveguide . . . . .	22
3.2.2	The Green's function of a half-infinite waveguide . . . . .	22
3.2.3	Green's function of a rectangular module . . . . .	25
3.2.4	Assembling the modules . . . . .	26
3.2.5	Superblock structures . . . . .	28
3.2.6	Transmission coefficients . . . . .	30
3.2.7	Wave functions . . . . .	31
3.2.8	Accuracy tests . . . . .	32
<b>II</b>	<b>Applications</b>	<b>34</b>
<b>4</b>	<b>Graphene-based nanostructures</b>	<b>35</b>
4.1	Graphene . . . . .	35

4.1.1	Band structure . . . . .	36
4.1.2	Dirac equation . . . . .	39
4.2	Graphene-based quantum billiards . . . . .	41
4.2.1	Edge and bulk defects . . . . .	41
4.2.2	Density of states . . . . .	43
4.2.3	Eigenstates . . . . .	46
4.2.4	Level spacing statistics . . . . .	47
4.2.5	Magnetic fields . . . . .	51
4.3	Transport through graphene nanoribbons . . . . .	56
4.3.1	Scattering problem . . . . .	57
4.3.2	Edge roughness . . . . .	58
4.3.3	Fourier transform . . . . .	63
4.3.4	Lattice vacancies . . . . .	65
4.3.5	Stone-Wales defects . . . . .	70
4.3.6	Disordered Constrictions . . . . .	72
4.4	Bilayer graphene . . . . .	74
4.4.1	Bilayer-monolayer heterostructures . . . . .	75
<b>5</b>	<b>SN hybrid structures</b>	<b>81</b>
5.1	The physics of SN structures . . . . .	82
5.1.1	Superconductivity . . . . .	82
5.1.2	The Bogoliubov-de Gennes equation . . . . .	84
5.1.3	Andreev reflection . . . . .	85
5.2	Andreev billiards . . . . .	88
5.2.1	The periodic-orbit distribution . . . . .	89
5.2.2	Bohr-Sommerfeld approximation . . . . .	90
5.2.3	Quadratic N cavity . . . . .	93
5.2.4	Circular boundaries . . . . .	97
5.3	Beyond the BS approximation . . . . .	100
5.3.1	Derivation of the Andreev phase . . . . .	100
5.3.2	EBK quantization . . . . .	102
5.3.3	Improved BS approximation . . . . .	105
5.3.4	Eigenstate rearrangement . . . . .	107
5.4	Validity of the retracing approximation . . . . .	110
5.4.1	Stretched separable billiard . . . . .	111
5.4.2	Stretched non-separable billiard . . . . .	116
5.4.3	Diffractive effects . . . . .	118
5.4.4	Mushroom billiard . . . . .	120
5.5	Disordered Andreev billiards . . . . .	125
5.5.1	Disorder characteristics . . . . .	127
5.5.2	Wigner-Smith time delay matrix . . . . .	129

5.6	Transport through SN hybrid structures . . . . .	137
5.6.1	Scattering geometry . . . . .	139
5.6.2	The Wiedemann-Franz law . . . . .	140
<b>6</b>	<b>Outlook</b>	<b>142</b>
6.1	Fano resonances in Acoustic cavities . . . . .	142
<b>7</b>	<b>Summary</b>	<b>148</b>
<b>A</b>	<b>Supplementary calculations</b>	<b>151</b>
A.1	The Arnoldi factorization . . . . .	151
A.2	Third-nearest-neighbor tight-binding description of Graphene .	152
A.3	Thermal currents . . . . .	153
A.4	The acoustic wave equation . . . . .	154
<b>B</b>	<b>A complete reference for the MRGM</b>	<b>157</b>
B.1	Green's function of the infinite waveguide . . . . .	157
B.2	Green's function of a half-infinite waveguide . . . . .	158
B.3	Green's function of a rectangular module . . . . .	159
B.4	Assembling the modules . . . . .	159
B.5	Transmission coefficients . . . . .	160
B.6	Wave-function pictures . . . . .	161
	<b>Bibliography</b>	<b>162</b>
	<b>Acknowledgments</b>	<b>177</b>



# Chapter 1

## Introduction

Mesoscopic phase-coherent devices have become popular systems to investigate a wide variety of physical effects. The term “mesoscopic” in this context refers to the size of these systems, which exceeds microscopic dimensions but still lies below the inelastic mean free path ( $l_i$ ). In this regime, phase coherent scattering can be realized at low temperatures. As a consequence, the wave nature of the electron plays an important role: quantum confinement and interference effects result in unique material properties as well as new challenges for device engineering on the sub-micrometer scale. Applications of quantum interference effects include the realization of “qubits” based on either superconductor-normal conductor contacts [6] or carbon-based atomically thin membranes [7], high-precision interference-based metrology [8], high-mobility nanoelectronics [9], single-electron transistors [10], and tunable semiconductor lasers [11].

Recent advances in the preparation of carbon-based two-dimensional thin films [9, 12] have made available true two-dimensional systems to study experimentally. This novel material, called graphene, makes possible the observation of the integer quantum Hall effect at room temperature for the first time [13]. The reason for this is its unique bandstructure near the Fermi edge, that closely mimics the linear dispersion relation of the free Dirac equation for massless fermions. Indeed, relativistic effects such as the Klein tunnel paradox seem to be replicated in graphene, with the notable feature that the involved energy scales are easily accessible in the laboratory, without requiring the creation of particle-antiparticle pairs. Yet, the physics of graphene is governed by electrons moving through the atomic orbitals of carbon atoms at 0.003 times the speed of light, rather than at relativistic speeds. The interplay between the Dirac-like dispersion relation and the hexagonal carbon lattice generates an interesting variety of physics all by itself. We therefore investigate the eigenstates of realistic graphene-based nanodevices,

and show in which ways they differ from expectations based on the Dirac equation. We explore effects that are not included in a simple Dirac-based model, e.g. lattice defects that introduce scattering potentials with characteristic length scales of the order of the lattice constant. In open graphene-based devices, these defects break the close correspondence to the Dirac equation, and lead to enhanced backscattering. We quantitatively assess the amount of scatterers as well as the quality of the degree of correspondence to the Dirac equation. In such a way, we can understand why certain transport properties of graphene nanoribbons, e.g. the formation of size-quantization plateaus in transport experiments, remain elusive in experimental investigations.

In contrast to the perfect two-dimensional graphene lattice, semiconductor heterostructures employ differently doped materials to confine electrons to a (nearly) two-dimensional region: at the boundary between GaAs and GaAlAs it is nowadays possible to confine electrons to a two dimensional electron gas with mean free paths up to  $10\mu\text{m}$  [3, 14]. Furthermore, the fabrication of specific device geometries is readily possible, resulting in quasi-two-dimensional quantum billiard structures which ideally feature flat potential wells confined by hard wall boundaries. These quantum billiard systems serve as paradigms for simple Hamiltonian systems featuring complex dynamics [15] and have been investigated both experimentally [16][17] as well as theoretically [18][19]. Measurements show that the conduction through semiconductor heterostructure devices is, indeed, governed by interference effects due to the shape of the confining boundary rather than the inelastic mean free path [16, 20]. Depending on the geometry, a quantum billiard may thus feature either regular or chaotic dynamics. The distinction between regular and chaotic motion is an important concept in classical physics. The study of chaotic quantum billiards thus yields valuable insight into the question how these classical concepts on chaoticity translate into quantum mechanical properties such as the distribution of eigenenergies or transmission eigenvalues.

When a quantum billiard is brought into contact with a superconductor, phase-coherent scattering of electrons into holes occurs [21]. The dynamics of electrons and holes thus become connected at the superconductor. The dynamics of the resulting superconductor-normal conductor hybrid structure features an exceptionally strong quantum-classical correspondence which allows to make surprisingly accurate classical estimates for the quantum mechanical density of states. As a consequence, these systems are ideally suited to investigate questions of quantum-classical correspondence and the applicability of semiclassical approximations. We discuss the origin of discrepancies between semiclassical models and quantum mechanical calculations. Quantum diffraction and the finite Fermi wavelength result in corrections, that

eventually lead to a breakdown of semiclassical approximations.

All systems described above are described by a wave equation. They differ, however, in boundary conditions, dispersion relations, or in the type of interactions involved. Yet, the same type of wave phenomena govern the underlying physics. It is therefore desirable to have a set of numerical tools available to describe eigenstates and transport properties of these systems, without the need for a new algorithm for each different case. The aim of this thesis is to present a flexible, numerically powerful, and reliable tool set to efficiently calculate essential quantum-mechanical properties of a wide range of mesoscopic systems governed by a wave equation: We are interested in the properties of individual eigenstates, the density of states and the bandstructure, transport properties and scattering states. We show how the complex, and sometimes counterintuitive results of quantum theory can be understood within the framework of semiclassical approximations or idealized models, and in which parameter range these models remain applicable. Additionally, we point out what further physical properties of phase-coherent systems can be investigated beyond simple approximations.

This thesis is divided into two parts. In the first part, we present the numerical tool set used to describe the above systems: discretization techniques provide an efficient way to reduce the continuum problem to a matrix form that can be handled numerically. The spectrum of the system, and hence the density of states, can be calculated using matrix diagonalization routines. To describe transport through open structures, we present a modular Green's function technique suitable to describe quantum transport through different materials. For both of these problems (closed and open systems), we develop techniques to directly calculate the associated wave functions.

In the second part of this thesis, we present a detailed analysis of the physics of two types of structures: (i) graphene-based nanostructures, and their bandstructure and (ii) superconductor-normal conductor hybrid structures, their semiclassical description and its limitations. Whenever the technical details of a particular problem threaten to obscure the visibility of the underlying physics, we have moved them to the Appendix. Additionally, to create a complete reference, all formulae used in the different steps of the Green's function formulation are provided.

Finally, we give an outlook on current and future projects. As an example, we briefly discuss the time-evolution of wave packets in large-scale model systems of quantum mechanics. We conclude the thesis with a short summary.

# Part I

## Method and first numerical results

# Chapter 2

## Mesoscopic devices

The aim of this work is to investigate the physics of phase-coherent devices, that explore the wave nature of quantum mechanics. To describe quantum interference phenomena in realistic devices, one has to resort to numerical techniques. The first step in the numerical treatment of a real-world device is to capture the underlying physics in a mathematical model that can be solved on a computer. We want to describe a wide variety of different mesoscopic structures, featuring different media, bandstructures and potential landscapes. To achieve this flexibility, we introduce the tight-binding (TB) approximation, which we will use to translate the Hamiltonian of a periodic lattice structure to a matrix equation. We will discuss the advantages and limitations of the TB approach, and investigate how the material properties of a solid are represented by the TB parameters. As we will demonstrate, the TB approach can also be successfully applied to solve continuous wave equations, where an artificial TB grid accurately reproduces the continuum equation in the limit of many grid points.

### 2.1 Tight-binding approximation

To describe the physics of mesoscopic systems, we solve the Schrödinger equation (i.e. a wave-equation)

$$\mathcal{H}^{\text{mp}} |\Psi\rangle = E |\Psi\rangle \quad (2.1)$$

where  $\mathcal{H}^{\text{mp}}$  is the many-particle Hamiltonian of the periodic lattice of a solid. We consider the geometry of the lattice (i.e. the position of the nuclei) fixed, and only treat the dynamics of the electrons.  $\mathcal{H}^{\text{mp}}$  then consists of the kinetic energies of all electrons, their interactions  $V^{\text{el-el}}$ , and the potential of

the individual lattice atoms  $\mathcal{V}_i^{\text{at}}$ ,

$$\mathcal{H}^{\text{mp}} = \sum_j \frac{\mathbf{p}_j^2}{2m_e} + \sum_i V_i^{\text{at}} + \frac{1}{2} \sum_{j \neq j'} V_{jj'}^{\text{el-el}} \quad (2.2)$$

To solve the Schrödinger equation with a Hamiltonian of the form (2.2) is a challenge already for as few as two electrons. The Hartree-Fock equations (see e.g. [22], chapter 3) consist of an iterative procedure to self-consistently approximate the ground-state of a many-particle system. Density functional theory (DFT) replaces the many-particle wavefunction by an effective electron density to calculate the lowest-lying eigenstates of many-body systems (for a short introduction, see e.g. [22], chapter 6). We will not treat electron-electron interactions, but rather use the independent electron approximation [23]: the many-particle Hamiltonian  $\mathcal{H}^{\text{mp}}$  is replaced by a single-particle Hamiltonian  $\mathcal{H}$  of one electron moving through the crystal lattice. The interactions between electrons  $V^{\text{el-el}}$  are represented by an effective one-electron potential  $U(\mathbf{r})$ ,

$$\mathcal{H} = \frac{\mathbf{p}^2}{2m_e} + \sum_i V_i^{\text{at}}(\mathbf{r}) + U(\mathbf{r}). \quad (2.3)$$

Replacing all electron-electron interactions by a potential may seem, at first glance, like a crude simplification that only works for weakly interacting electrons. However, the single electron approximation is remarkably successful in spite of the presence of  $V^{\text{el-el}}$ . This can be understood based on arguments by Landau [24]: due to the Pauli exclusion principle, the available phase space for inelastic electron-electron scattering is quite small (as most states below  $E_{\text{F}}$  are already occupied). As a consequence, the scattering rate is drastically reduced. Therefore, at least for levels close to  $E_{\text{F}}$ , electron-electron interactions do not appear to invalidate the independent electron picture. The major corrections due to finite  $V^{\text{el-el}}$  rather modify the electron dispersion relation  $E(\mathbf{k})$  (which is accounted for by the potential  $U(\mathbf{r})$ ). Therefore, we do not attempt to derive  $E(\mathbf{k})$  [or  $U(\mathbf{r})$ ] for the materials we consider, but rather take ab-initio DFT calculations as a starting point of our calculations, as outlined below. In such a way, we do include corrections (to first order) to a naive single-electron picture.

To treat the Hamiltonian (2.3), we use the framework of the tight binding approximation, a widely-used formalism to translate the partial differential one-particle Schrödinger equation on a lattice to a set of matrix equations that can easily be handled numerically. The key assumption is that electronic orbitals in a solid are well-localized (or tightly bound) around each atom, and can thus be, to first order, approximated by the eigenstates of the isolated

atoms. The interactions between neighboring atoms are strong enough to require corrections to the picture of isolated atoms [introduced by  $U(\mathbf{r})$ ], but not so large as to render the atomic description completely irrelevant. Let  $|\phi_j^i\rangle$  label a bound states of an isolated atom located at  $\mathbf{r}_i$

$$\left(\frac{\mathbf{p}^2}{2m} + V_i^{\text{at}}(\mathbf{r})\right) |\phi_j^i\rangle =: \mathcal{H}_i^{\text{at}} |\phi_j^i\rangle = E_j |\phi_j^i\rangle. \quad (2.4)$$

These eigenfunctions represent a convenient base to expand the wave function  $|\Psi\rangle$ . To avoid cumbersome index notation, we combine the index  $i$  labeling the position of a specific lattice atom and the eigenstate index  $j$  into a single index  $n$ . The expansion of  $|\Psi\rangle$  can then be written as

$$|\Psi\rangle = \sum_n c_n |\phi_n\rangle, \quad (2.5)$$

where the sum runs over all atom positions and eigenenergies. Due to the presence of  $U(\mathbf{r})$  and the sum over  $V_i^{\text{at}}(\mathbf{r})$ , the solution of the one-particle Schrödinger equation (2.3) will require an infinite sum over all atomic orbitals  $|\phi_j\rangle$ . In good approximation, we can restrict the summation over atomic orbitals to a finite number of eigenstates of  $\mathcal{H}_{\text{at}}^n$  for which the eigenenergy  $E_j$  lies close to the particle energy  $E$ . In practice, it is often sufficient to include only very few orbitals per lattice site, as  $\Psi$  closely mimics an atomic orbital close to each lattice point [23].

We insert the ansatz (2.5) into the Schrödinger equation (2.3) and project on  $\langle\phi_m|$  to obtain

$$\sum_n \langle\phi_m|\mathcal{H}|\phi_n\rangle c_n = E \sum_n \langle\phi_m|\phi_n\rangle c_n. \quad (2.6)$$

The above equation lends itself to a matrix notation. We introduce the matrix representation  $H$  of the Hamiltonian  $\mathcal{H}$ ,

$$\mathcal{H} \rightarrow H_{nm} = \langle\phi_n|\mathcal{H}|\phi_m\rangle. \quad (2.7)$$

We furthermore assume that the bound levels of  $\mathcal{H}_i^{\text{at}}$  are well localized around their respective crystal atoms, i.e. the overlap with an orbital at an adjacent lattice point should be small. We then obtain an orthogonalized<sup>1</sup> basis set  $\langle\phi_n|\phi_m\rangle = \delta_{nm}$ . This allows us to write

$$H \cdot \vec{c} = E\vec{c}, \quad (2.8)$$

---

<sup>1</sup>It is also possible to formulate a non-orthogonal TB approximation, by defining  $S = \langle\phi_n|\phi_m\rangle \neq \mathbb{1}$ . This becomes, however, quite cumbersome due to the more complicated completeness relation and will not be treated in this work.

instead of the partial differential equation 2.3. A further consequence of the assumption of localized orbitals  $|\phi\rangle_n$  is that the matrix elements  $H_{mn}$  vanish if the distance  $\mathbf{r}_n - \mathbf{r}_m$  is large compared to the lattice constant, leading to a banded matrix  $H$ . The diagonal elements  $H_{nn}$  are usually called site-energies, while the off-diagonal terms represent interactions between adjacent sites. In the most simple case, one only takes into account  $H_{mn}$  for neighboring atoms (nearest-neighbor coupling). By including more distant corrections, the accuracy (and the complexity of the TB matrix) is increased.

### 2.1.1 Band structure

We now use the discretized matrix form of the Schrödinger equation (2.8) to calculate the band structure of a solid. We consider an infinite sheet of the periodic lattice. We know from Bloch's theorem that  $\Psi(\mathbf{r})$  must be, apart from a complex phase, invariant under translations by a lattice vector  $\mathbf{R}_n$

$$\langle \mathbf{r} + \mathbf{R}_n | \Psi \rangle = e^{i\mathbf{k} \cdot \mathbf{R}_n} \langle \mathbf{r} | \Psi \rangle, \quad \forall n \in \mathbb{N}. \quad (2.9)$$

$\Psi$  can thus be chosen to have the form of a plane wave times a function  $u_{n\mathbf{k}}(\mathbf{r})$  with the periodicity of the Bravais lattice

$$\langle \mathbf{r} | \Psi \rangle = e^{i\mathbf{k} \cdot \mathbf{r}} u_{\mathbf{k}}(\mathbf{r}). \quad (2.10a)$$

If we denote the number of tight binding orbitals in one unit cell by  $N_p$ ,  $u_{n\mathbf{k}}$  is determined by  $N_p$  expansion coefficients  $c_p$ ,

$$u_{\mathbf{k}}(\mathbf{r}) = \sum_{p=1}^{N_p} c_p \langle \mathbf{r} | \phi_p \rangle. \quad (2.10b)$$

If we insert the ansatz (2.10) in the Schrödinger equation (2.8), we obtain a linear system of  $N_p$  equations for the unknown coefficients  $c_p$ . Eq. (2.8) can also be viewed as an eigenvalue problem for the energy  $E$ . The eigenvalues  $E$  can thus be determined as a function of the wavevector  $\mathbf{k}$ . In such a way, the bandstructure of a periodic lattice is obtained. We emphasize that perfect periodicity is an idealization. Real solids are never absolutely pure, and in the neighborhood of impurity atoms the solid is not the same as elsewhere in the crystal [23]. One can describe a realistic solid in two steps. One first considers a perfect crystal lattice, which is genuinely periodic, and for which (2.9) is valid. In a second step, one then investigates the effects of deviations from perfect periodicity.

Following this procedure, we first consider, as a simple example, a perfect two-dimensional square crystal lattice (see Fig. 2.1). The hopping matrix



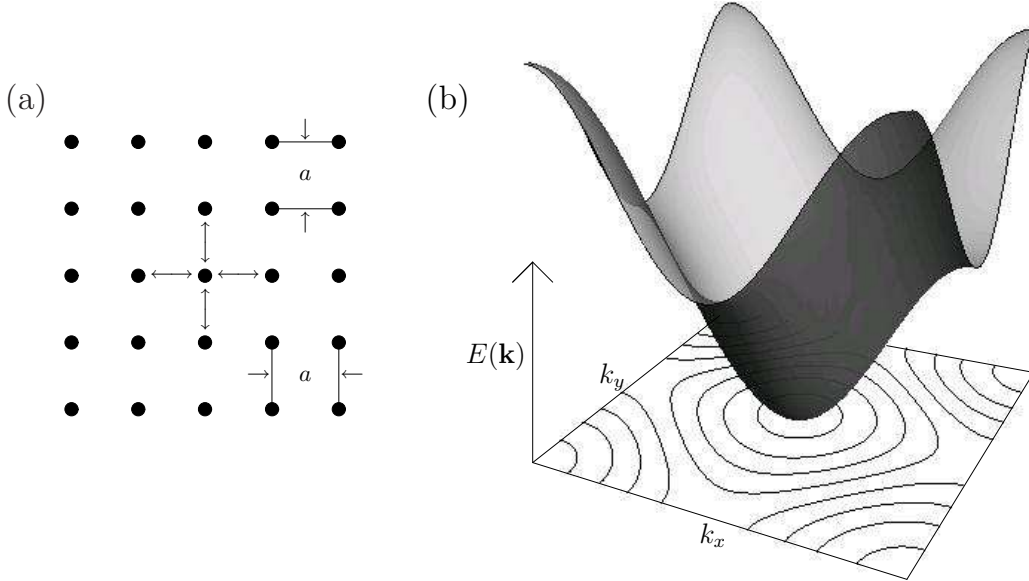


Figure 2.1: (a) Quadratic Bravais lattice. The lattice spacing is given by the lattice constant  $a$ . Each atom has four nearest neighbors (see double arrows). (b) Dispersion relation of the quadratic Bravais lattice, see Eq. 2.12.

elements  $\langle \phi_n | H | \phi_{n\pm 1} \rangle =: \gamma$  are identical for all four nearest-neighbor interactions (due to the lattice symmetry). The site energy  $\langle \phi_n | H | \phi_n \rangle =: \varepsilon_0$  is equal for all lattice atoms. The eigenvalue system (2.8) is thus reduced to

$$E \cdot \vec{c} = \varepsilon_0 \cdot \vec{c} + \gamma (e^{ik_x a} + e^{ik_y a} + e^{-ik_x a} + e^{-ik_y a}) \cdot \vec{c}. \quad (2.11)$$

The resulting dispersion relation,

$$E(\mathbf{k}) = \varepsilon_0 + 2\gamma \cos(k_x a) + 2\gamma \cos(k_y a), \quad (2.12)$$

features an approximately parabolic dispersion relation near  $E = \varepsilon_0$  [see Fig. 2.1(b)]. The slope of the parabola is determined by the interaction parameter  $\gamma$ . The proper choice of  $\gamma$  (or, more generally, of the tight binding parameters  $H_{nn'}$ ) is a subtle problem, as outlined in the following subsection.

### 2.1.2 Parameter fit

In principle, the TB parameters  $H_{nm}$  are determined by an integral over atomic orbitals [see Eq. (2.7)]. In practice, however, descriptions based on this approach perform poorly. The reason for this is the deformation of the atomic orbitals due to the presence of the solid and electron-electron interactions  $U(\mathbf{r})$ , as outlined above. This deformation is most prominent at positions in the middle between adjacent lattice atoms. Including an

increasing finite number of atomic orbitals of higher energy, i.e. higher index  $j$ , in the expansion (2.5) improves convergence quite slowly, because atomic orbitals with higher  $j$  feature strongly oscillating patterns close to the core of the atom (to be orthogonal to  $|\phi_l\rangle$   $l < j$ ) where the wave function is already well-represented. Indeed, atomic orbitals with eigenenergies  $E_j \gg E$  should not contribute to properties such as the density of states at  $E$ . Furthermore, including a large number of orbitals  $j$  greatly increases the matrix size, making the description of large structures unfeasible.

The far better approach is first to use (2.7) only as a raw estimate, and then to consider the matrix elements  $H_{nm}$  as fit parameters. One usually proceeds by comparing a band-structure  $E(\mathbf{k})$  obtained either from experiment, or from ab-initio calculations (e.g. DFT calculations) to the TB approximation  $E_{TB}(\mathbf{k})$  based on (2.8). Consequently, one avoids to give an explicit expression for  $U(\mathbf{r})$ : deviations from the atomic orbitals due to the presence of the lattice, or due to electron-electron interactions are implicitly included (as good as one can in a single-electron picture) in the (fit) values  $H_{nm}$ . By tuning the value of the matrix elements in (2.8), the mismatch

$$\delta E = \int |E(\mathbf{k}) - E_{TB}(\mathbf{k})|^2 d^2\mathbf{k} \quad (2.13)$$

can be minimized in a  $\mathbf{k}$ -region of interest. In such a way, a set of TB parameters  $\gamma_i$  is obtained for a system of infinite size. In first approximation, one can use these parameters for a finite-sized system. Especially at the boundaries, corrections can be introduced to take into account the difference between orbitals on the boundaries and in the bulk.

### 2.1.3 Continuum limit

The TB equations discussed above are well-suited to model the properties of solids featuring a periodic lattice. However, there are cases, where one does not need to take into account an underlying lattice structure. For example, macroscopic model systems for wave mechanics, such as microwave cavities or acoustic resonators, do not feature any “lattice” at all. In such cases, we need to solve a continuum wave equation (2.3). Also, the properties of several semiconductor structures, as well as metals, can be well described by a free-electron equation, by suitable definition of an effective mass that incorporates the effect of the lattice [23].

The dispersion relation of the quadratic lattice [see Fig. 2.1(b)] closely mimics the parabolic dispersion relation of a free electron for energies  $E$  close to  $\varepsilon_0$ . Indeed, in the limit of  $a \rightarrow 0$ , the dispersion relation (2.12) gives

$$E(\mathbf{k}) \approx \varepsilon_0 + 4\gamma - \gamma a^2(k_x^2 + k_y^2) + \mathcal{O}(a^4 k^4). \quad (2.14)$$

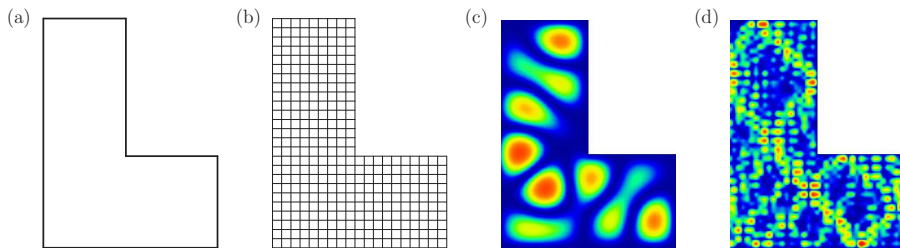


Figure 2.2: (a) Quantum billiard consisting of an L-shaped region of constant potential within hard wall boundaries. (b) TB grid used to discretize the billiard shown in (a). (c) Probability density  $|\Psi(x)|^2$  of the 16th eigenstate of the L-shaped billiard calculated using a TB grid in the continuum limit (1400 grid points used). (d) Probability density of the 164th eigenstate of the L-shaped TB grid shown in (b). As the lattice spacing  $a$  is here of the order of the wavelength [compare to (b)], the eigenstate is not a good approximation for the eigenstate of a continuum billiard.

By a suitable choice of the TB parameters,

$$\varepsilon_0 = -4\gamma, \quad \gamma = -\frac{\hbar^2}{2ma^2}, \quad (2.15)$$

the continuum equation is restored,

$$E(\mathbf{k}) \approx \frac{\hbar^2}{2m}(k_x^2 + k_y^2) + \mathcal{O}(a^2k^4). \quad (2.16)$$

As long as higher-order terms in (2.16) are small, i.e.  $a^2k_F^2 \propto (a/\lambda_F)^2 \ll 1$  (where  $\lambda_F$  is the Fermi wavelength), the dispersion relation of the tight binding grid is a good approximation for the continuum dispersion relation. This observation now allows us to employ a TB-grid also for the simulation of waves in different continuous systems.

As a simple example, consider an L-shaped quantum billiard (see Fig. 2.2). A quantum billiard consists of a region of zero potential confined by hard-wall boundaries. The dynamics of these structures is governed by the shape of the confining walls rather than scattering inside the cavity. We describe such a system by discretization on an artificial quadratic TB lattice [see Fig. 4.1(b)]: we replace the continuous wave function  $|\Psi\rangle$  by its amplitude at the lattice points  $\Psi_{ij}$ . Eigenstates of the L-shaped billiard can now be approximated [see Fig. 2.2(c)] by solving the matrix eigenvalue problem (2.8) on the tight-binding grid. Care must be taken to choose the number of grid points high enough that  $a$  represents the smallest length scale of the system,

$$a \ll \lambda_F. \quad (2.17)$$

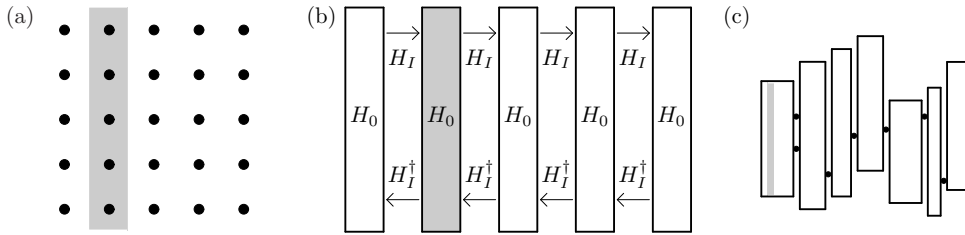


Figure 2.3: (a) A finite-sized, quadratic lattice consisting of 25 atoms. The lattice is built from five blocks (one highlighted by a grey rectangle). (b) Schematic figure of the same lattice as (a) expressed in terms of block matrices  $H_0$ ,  $H_I$  (see text). (c) A more complicated quantum dot is assembled by combining several rectangular structures of the type shown in (a,b). Black dots denote point scatterers introduced between the blocks.

Otherwise, eigenstates of the TB grid do not approximate solutions of the free Schrödinger equation [see Fig. 2.2(d)].

## 2.1.4 Large-scale devices

By solving the eigenvalue problem (2.8) for finite-sized quantum-dot structures, we can calculate their density of states, eigenenergies and eigenstates. The density of states near the Fermi energy plays an important role in transport through quantum dots. Furthermore, individual energy levels appear in transport experiments as Coulomb blockade peaks, as will be discussed in chapter 4.2.

However, the Hamiltonian matrices involved in describing quantum-dot structures quickly become large: consider the L-shaped billiard discussed in the previous subsection [see Fig. 2.2(a)]. The number of grid points  $N$  needed to correctly approximate a continuous system [i.e. to fulfill (2.17)] grows with  $\lambda_F^{-2}$ . The number of matrix elements of  $H$  is proportional to  $N^2 \propto \lambda_F^{-4}$ . At high energies (small Fermi wavelength  $\lambda_F$ ), the size of  $H$  thus quickly becomes difficult to handle. On the other hand, only a fraction of the matrix elements of  $H$  are non-zero in a nearest-neighbor TB approximation. Clearly, a systematic approach to quickly determine the non-vanishing parts of  $H$  is needed. At the same time, we need a general framework to describe the properties of different media, that does not depend on a particular structure of  $H$ . We adapt an approach Sanvito et al. have developed in the context of transport [25, 26]. The key idea is to split a rectangular, periodic structure into identical building blocks. We then exploit the periodicity of the lattice to break  $H$  down into smaller blocks of manageable size. To illustrate this,

we assemble the quadratic lattice shown in Fig. 2.3(a) by repetition of a one-dimensional chain of five atoms [see grey area in Fig. 2.3(a)]. From a more formal point of view, the Hamiltonian  $H$  of the quadratic lattice is split up into two parts: (i) an operator  $H_0$  describing the Hamiltonian of the single building block [see grey area in Fig. 2.3(b)], and (ii) an interaction operator  $H_I$  describing the connection between two adjacent blocks. The resulting Hamilton operator  $H$  is of the form [see Fig. 2.3(b)],

$$H = \begin{pmatrix} H_0 & H_I & 0 & & \\ H_I^\dagger & H_0 & H_I & 0 & \\ 0 & H_I^\dagger & H_0 & H_I & 0 \\ & 0 & H_I^\dagger & H_0 & H_I \\ & & 0 & H_I^\dagger & H_0 \end{pmatrix}. \quad (2.18)$$

Both  $H_0$  and  $H_I$  are represented by  $M \times M$  matrices, where  $M$  gives the number of TB orbitals (or lattice sites) in a single block. Note that in order to fulfill  $\mathcal{H} = \mathcal{H}^\dagger$ ,  $H_0$  must be Hermitian, which  $H_I$  in general is not. Interaction between next-to-nearest blocks are a priori not included in this approach. If, however, such an interaction is needed, two adjacent blocks may be grouped together in a single larger block which could include the next-to-nearest interactions.

As an example, the Hamilton operators  $H_0$  and  $H_I$  needed to describe the artificial TB lattice of the L-shaped quantum billiard are given by

$$H_0 = \frac{\hbar^2}{2ma^2} \begin{pmatrix} \ddots & & -1 & & \\ -1 & 4 & -1 & & \\ & -1 & 4 & -1 & \\ & & -1 & 4 & -1 \\ & & & -1 & \ddots \end{pmatrix} \quad (2.19)$$

for the dynamics of a single block, while the interaction between adjacent blocks is given by

$$H_I = -\frac{\hbar^2}{2ma^2} \mathbb{1}. \quad (2.20)$$

A rectangular piece of lattice can easily be described by a Hamilton matrix of the form (2.18). The L-shaped quantum billiard discussed above can be assembled from two rectangular modules, each consisting of several blocks  $H_0$ . More general geometries may be assembled by combining several such rectangular modules [see Fig. 2.3(c)].

While we mainly consider two-dimensional scattering structures in this thesis (we will briefly consider resonances in three-dimensional acoustic resonators), the above approach is, in principle, not limited to two dimensions,

as long as a building block structure can be defined. It is also possible to model a two-component wave function (i.e. a spinor wave) using the above formulation: we will consider SN hybrid structures that feature an electron and a hole sheet in the second part of this thesis.

Lattice defects or point impurities can most easily be implemented at the boundaries between adjacent rectangular structures [see black dots in Fig. 2.3(c)]. The TB matrix elements of  $H_0$  and  $H_I$  contain all the information needed to model the corresponding system. We will present the appropriate choice for  $H_0$  and  $H_I$  for each system discussed in this work in detail in the second part of this thesis, at the beginning of each chapter.

### 2.1.5 Lanczos diagonalization

Calculating eigenvalues and eigenvectors of a quantum dot using a direct diagonalization of  $H$  has several disadvantages. Even in the simple case of the L-shaped billiard shown in Fig. 2.2, the number of matrix elements grows with  $\lambda_F^{-4}$ , as discussed above (see Fig. 2.2). Only the lowest eigenvalues and eigenstates of this matrix are good approximations for the eigenstates of the (continuum) quantum billiard. As a consequence, only a fraction of the eigenstates of the matrix  $H$  do have a physical meaning [compare Fig. 2.2(c,d)]. An algorithm that calculates only the lowest-lying (i.e. the physical) eigenstates of a large matrix is thus desirable.

The number  $N$  of sites required to adequately model an experimentally accessible quantum dot is also large, from  $N \approx 50000$  on upwards: as an example, graphene-based quantum dots may be manufactured with diameters down to 40nm [27], corresponding to about 60000 carbon atoms. The straightforward diagonalization of the corresponding  $N \times N$  Hamiltonian matrix is numerically not feasible. In summary, we need an algorithm to efficiently determine the  $n_E \ll N$  eigenstates of a large Hamiltonian matrix  $H$  closest to the Fermi energy  $E_F$ , or, equivalently, the  $n$  smallest (in absolute value) eigenvalues of the matrix

$$A := H - E_F \cdot \mathbb{1}, \quad A |\varepsilon_i\rangle = a_i |\varepsilon_i\rangle = (\varepsilon_i - E_F) |\varepsilon_i\rangle. \quad (2.21)$$

We use the ARPACK package [28] based on the implicitly restarted Arnoldi-Lanczos algorithm (IRAL) [29, 30]. In Appendix A.1, we give a brief outline of the employed algorithm.

A key advantage of the IRAL detailed above is that only the product  $A |q_i\rangle$ , for given  $|q_i\rangle$  is needed for the iteration. Thus, the entire matrix  $A$  is never needed in memory. Furthermore, the most time-consuming part of the algorithm is the evaluation of  $A |q_i\rangle$ , which can be handled efficiently

by partitioning  $H$  in  $H_0$  and  $H_I$  as outlined above [see Eq. (2.18)]. For the results presented in this thesis,  $N$  was of the order of  $5 \cdot 10^5$ , while  $n_E \approx 10^3$ , thus determining the 1000 eigenenergies closest to the Fermi level.

### 2.1.6 Magnetic field

Under the influence of magnetic fields, one can study the formation of Landau levels, leading to the integer quantum Hall effect [31], or the Shubnikov-de Haas [23] and Aharonov-Bohm [32] oscillations in the conductance through a mesoscopic device. From an experimental point of view the magnetic-field dependence of different device properties (e.g. transmission or position of resonance peaks) can be easily investigated. To simulate the physics of a two-dimensional device in a perpendicular magnetic field  $\mathbf{B}$ , we use the Landau gauge

$$\mathbf{B} = \begin{pmatrix} 0 \\ 0 \\ B \end{pmatrix} = \nabla \times \mathbf{A}, \quad \mathbf{A} = \begin{pmatrix} -By \\ 0 \\ 0 \end{pmatrix}. \quad (2.22)$$

The above gauge retains the separability of the Schrödinger equation in  $(x, y)$  coordinates (this will be important for the efficient formulation of the scattering problem through mesoscopic devices). In contrast to an electric field, which can be included in the TB formalism by simply changing the site energies  $\varepsilon_0$ , the inclusion of a magnetic field is tricky. We use the Peierls phase factor [33]

$$H_{mn} \rightarrow H_{mn} \cdot \alpha_{mn}(\mathbf{A}), \quad \alpha_{mn}(\mathbf{A}) = \exp \left[ i \frac{e}{\hbar} \int_{\mathbf{r}_n}^{\mathbf{r}_m} \mathbf{A} \cdot d\mathbf{r} \right]. \quad (2.23)$$

Here,  $\alpha(A)$  corresponds to the phase the electron accumulates when going from  $\mathbf{r}_n$  to  $\mathbf{r}_m$ . This approach is equivalent to<sup>2</sup> the minimal substitution  $\mathbf{p} \rightarrow (\mathbf{p} - \frac{e}{c}\mathbf{A})$  [34] on a lattice. Note that, since  $\nabla \times A \neq 0$ , the integral in (2.23) is not independent of the path taken from  $\mathbf{r}_n$  to  $\mathbf{r}_m$ . For a constant, perpendicular field according to (2.22), we can evaluate the integral

$$\int_{\mathbf{r}_n}^{\mathbf{r}_m} \mathbf{A} \cdot d\mathbf{r} = -(x_m - x_n)(y_m + y_n) \frac{B}{2} \quad (2.24)$$

and thus

$$\alpha_{mn} = \exp \left[ -i \frac{e}{\hbar} (x_m - x_n)(y_m + y_n) \frac{B}{2} \right]. \quad (2.25)$$

---

<sup>2</sup>Consider the exact relation  $\alpha(p + e\mathbf{A})^2 \psi = p^2 \alpha \psi$ . (2.23) corresponds to a discretized form of this relation evaluated at the lattice points.

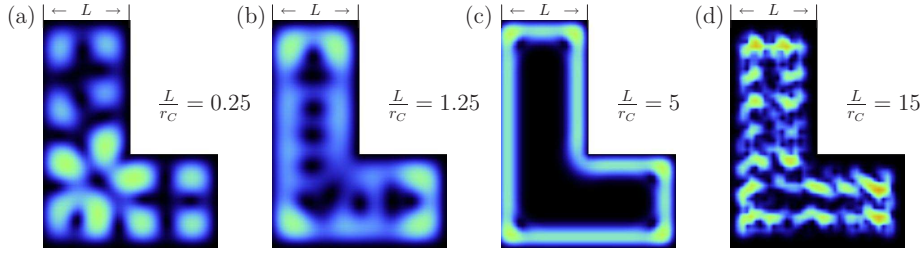


Figure 2.4: (a-c) Evolution of an eigenstate of the L-shaped quantum billiard with increasing magnetic field, as given in the inset (in units of  $L/r_C \propto B$ , where  $r_C$  is the classical cyclotron radius and  $L$  is a linear dimension of the billiard). (d) Eigenstate at very high magnetic fields: Because the flux per unit cell of the TB lattice is large [i.e. Eq. (2.26) is violated], the TB grid is no longer a good approximation for the continuum case.

The above formula allows for the inclusion of a magnetic field in our TB matrix equations. As an example, we consider the evolution of an eigenstate of the L-shaped quantum billiard with increasing magnetic field [see Fig. 2.4(a-c)]. We observe a clear transition from the low field [see Fig. 2.4(a)] to the edge state (quantum Hall) regime [see Fig. 2.4(c)].

We have so far neglected the change in atomic orbitals, and hence in the TB parameters, induced by the applied B-field. This is a good approximation for magnetic fields currently realizable in experiment, i.e. up to  $\sim 40$  T. If we use a tight-binding grid to solve the continuum case, there is another caveat: the lattice constant  $a$  of the artificial TB grid must be chosen small enough to ensure that the magnetic flux  $\Phi$  passing through an artificial lattice cell is small compared to the magnetic flux quantum  $\Phi_0 = h/e$ ,

$$\Phi = Ba^2 \ll \Phi_0 \quad \Rightarrow \quad a \ll \sqrt{\frac{\Phi_0}{B}}. \quad (2.26)$$

Otherwise, the integral for a closed loop around one cell in the grid yields a phase factor which is not small compared to  $2\pi$ , leading to unphysical effects [see Fig. 2.4(d)]. As a consequence, a fine discretization grid is necessary to describe high magnetic fields [35, 36].

We now have the tools at hand to describe the eigenstates of closed, finite-sized quantum devices, including magnetic fields. In the next chapter, we will contact these devices with two infinite waveguides, and investigate the resulting scattering problem.



# Chapter 3

## Scattering theory

In this chapter, we formulate the scattering problem for ballistic and diffusive two-dimensional structures. In line with the discussion in the previous chapter, we want to apply our method to a wide range of transport experiments involving different materials, structures, and scales. We will therefore use the general tight-binding formulation we have established in the previous section. We restrict ourselves to ballistic and diffusive transport without describing inelastic scattering or decoherence processes. The energy of the incident “particle”  $E_F$  is thus constant. We do, however, include elastic scattering at local defects, charge impurities, or rough edges, in contrast to purely ballistic descriptions.

We consider two half-infinite waveguides attached to a scattering region [see Fig.3.1(a)]. We choose a coordinate system with  $x$  in transport direction, parallel to the waveguides, and  $y$  in transverse direction, as shown in the figure. We describe transport within the Landauer-Büttiker formalism [37], i.e. the total conductance  $g$  of a mesoscopic device is expressed by its transmission  $\mathcal{T}$ ,  $g = \frac{e^2}{h}\mathcal{T}$ . A current  $I_0$  is injected from the left, and is either transmitted (with probability  $\mathcal{T}$ ) or reflected (with probability  $\mathcal{R}$ ). Since we do not include loss processes into our theory, the unitarity relation  $\mathcal{T} + \mathcal{R} = 1$  holds. The waveguides feature a potential  $V(x, y)$  which is periodic in direction of transport ( $x$ -direction), and finite only in an interval of width  $W$ , i.e.  $V(x, y) \rightarrow \infty \iff y \notin [0, W]$ , without scattering sources. Each half-infinite waveguide features a finite, discrete set of transverse eigenstates, so-called modes, which propagate either in  $+x$  (labeled  $1, \dots, N$ ) or  $-x$  (labeled by an over-lined index  $\bar{1}, \dots, \bar{N}$ ) direction. Propagation through each mode is factorized into a longitudinal, propagating part and a transverse part  $\chi(y)$  in the asymptotic region, i.e. far away from the scattering device. For a quantum waveguide of width  $W$ , featuring a constant background potential and hard wall boundaries, the transverse part is equal to

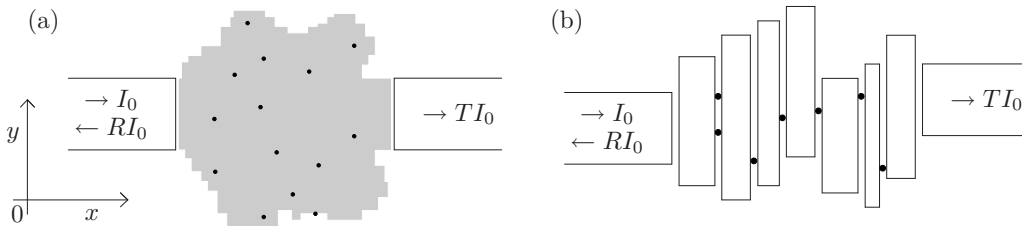


Figure 3.1: (a) Basic scattering geometry considered in this work: two half-infinite waveguides connect to a single scattering region. (b) Example of a scattering structure built up of 7 rectangular, separable modules. Point scatterers (black dots) are inserted in between the rectangles.

$\chi_j(y) = \sin(j\pi y/W)$ . For other materials, or when adding a magnetic field, more complicated transverse states will appear, and  $|\chi_j\rangle \neq |\chi_{\bar{j}}\rangle$ . The scattering wave function in a waveguide can thus be written as

$$|\psi_{in}\rangle = \sum_{j=1}^N a_j e^{ik_j x} |\chi_j(y)\rangle + \sum_{\bar{j}=1}^N b_{\bar{j}} e^{ik_{\bar{j}} x} |\chi_{\bar{j}}(y)\rangle. \quad (3.1)$$

In the left lead, the incoming current is determined by the boundary conditions at  $-\infty$ . The left-moving current is determined by the reflection in the scatterer through the reflection-coefficients  $r_{mn}$  describing the reflection from mode  $n$  into mode  $m$ . Accordingly, the right lead only contains the transmitted current, as described by  $t_{mn}$ . Note that the number of propagating modes in the left and right lead need not be identical, leading to a rectangular rather than a quadratic matrix  $t$ . The total scattering matrix of the structure

$$S = \begin{pmatrix} r & t \\ t' & r' \end{pmatrix} \quad (3.2)$$

additionally contains the reflection ( $r'$ ) and transmission ( $t' = t^\dagger$ ) from right to left lead.  $S$  is calculated via projection onto the total Green's function of the entire scattering structure,  $\mathcal{G}$ , as outlined in the following sections.

### 3.1 Infinite waveguides

In the previous chapter, we have considered rectangular block structures created by repetition of a single stripe (see Eq. 2.18), described by matrices  $H_0$  and  $H_I$ . We will now extend our considerations to infinite waveguides. By adopting the same decomposition of  $H$  as in the case of finite-sized quantum

dots, the same code to set up the geometry as well as to calculate the Hamiltonian matrices can be used both for eigenenergy and transport calculations. Instead of a finite number of blocks  $H_0$ , a waveguide is made up of infinitely many of them. As a generalization of (2.18),  $H$  may then be written as

$$H = \begin{pmatrix} \ddots & & & & & & & \\ & H_0 & H_I & 0 & & & & \\ & H_I^\dagger & H_0 & H_I & 0 & & & \\ & 0 & H_I^\dagger & H_0 & H_I & 0 & & \\ & & 0 & H_I^\dagger & H_0 & H_I & & \\ & & & 0 & H_I^\dagger & H_0 & & \\ & & & & & & \ddots & \end{pmatrix}. \quad (3.3)$$

To compute the eigenfunctions of such a Hamiltonian, at a given energy  $E$ , the Schrödinger equation may be solved analytically using a Bloch wave ansatz

$$\mathcal{H} |\Psi\rangle = E |\Psi\rangle, \quad |\Psi\rangle = \begin{pmatrix} \vdots \\ |\psi_{j-1}\rangle \\ |\psi_j\rangle \\ |\psi_{j+1}\rangle \\ \vdots \end{pmatrix}, \quad |\psi_j\rangle = e^{ik\Delta j} |\chi\rangle. \quad (3.4)$$

After inserting this ansatz into Eq. 3.3, one can obtain a non-linear eigenvalue problem for  $|\chi\rangle$ :

$$\left( H_0 + e^{ik\Delta x} H_I + e^{-ik\Delta x} H_I^\dagger \right) |\chi\rangle = E |\chi\rangle. \quad (3.5)$$

The above equation has to be solved for unknown  $k$  and given  $E$ . We multiply by  $(H_I^\dagger)^{-1} \equiv H_{-I}$  and<sup>1</sup> introduce the shorthand notation  $\beta = e^{-ik\Delta x}$ , to obtain

$$\beta H_{-I} (E - H_0) |\chi\rangle - H_{-I} H_I |\chi\rangle = \beta^2 |\chi\rangle. \quad (3.6)$$

This generalized eigenvalue problem may be solved by doubling the dimension of the system: One introduces  $|\eta\rangle := \beta |\chi\rangle$  to obtain the system of equations

$$|\eta\rangle = \beta |\chi\rangle \quad (3.7a)$$

$$H_{-I} (E - H_0) |\eta\rangle - H_{-I} H_I |\chi\rangle = \beta |\eta\rangle, \quad (3.7b)$$

---

<sup>1</sup>If  $H_I$  is degenerate (i.e.  $\det H_I = 0$ ), this inversion fails. In such a case, the block structure contains more points than possible transport channels. It is possible to remove lattice points from the tight binding grid until  $\det H_I \neq 0$  [25]

which may be written as the eigenvalue problem

$$\underbrace{\begin{pmatrix} H_{-I}(E - H_0) & -H_{-I}H_I \\ \mathbb{1} & 0 \end{pmatrix}}_A \begin{pmatrix} |\eta\rangle \\ |\chi\rangle \end{pmatrix} = \beta \begin{pmatrix} |\eta\rangle \\ |\chi\rangle \end{pmatrix}. \quad (3.8)$$

This yields  $2N$  eigenvectors as well as corresponding eigenvalues  $k_j$  ( $k_{\bar{j}}$ ). While the matrix  $A$  is non-Hermitian (this is a direct result of the eigenvalue  $\beta = e^{ik\Delta x} \in \mathbb{C}$ ) the eigenvectors of  $A$  form [see Eq. (3.4)] eigenvectors of  $H$ , which is Hermitian. As a consequence, an orthogonality relation for  $\chi_j$  exists. For real eigenvalues  $k_j \in \mathbb{R}$ , the modes are propagating with a group velocity

$$\begin{aligned} v_j &= \frac{\partial}{\partial k} \langle \psi_j | H | \psi_j \rangle = \langle \chi_j | \frac{\partial}{\partial k} [H_I e^{ik\Delta x} + H_I^\dagger e^{-ik\Delta x}] | \chi_j \rangle \\ &= i\Delta x \langle \chi_j | [H_I e^{ik_j\Delta x} + H_I^\dagger e^{-ik_j\Delta x}] | \chi_j \rangle. \end{aligned} \quad (3.9)$$

By considering the sign of  $v_j$ , one can partition the eigenstates into  $N$  right-moving  $|\chi_j\rangle$ , and  $N$  left-moving  $|\chi_{\bar{j}}\rangle$  of the form

$$|\psi_j\rangle = \frac{e^{ik_j x}}{\sqrt{v_j}} |\chi_j\rangle, \quad |\psi_{\bar{j}}\rangle = \frac{e^{ik_{\bar{j}} x}}{\sqrt{-v_{\bar{j}}}} |\chi_{\bar{j}}\rangle \quad (3.10)$$

where the factor  $1/\sqrt{v_j}$  ensures that the state is normalized to carry unit flux. As the over-lined index  $\bar{j}$  denotes left-moving states,  $v_{\bar{j}}$  is always negative, and  $\sqrt{-v_{\bar{j}}}$  is thus well-defined. The transverse eigenstates  $|\chi_j\rangle$  can now be used as basis to assemble the Green's function of the structure, as will be shown in the next section.

## 3.2 Modular recursive Green's function method

We now present a formulation of the modular recursive Green's function method (MRGM) to calculate the scattering matrix  $S(\varepsilon)$  and the scattering wave function for a large-scale scattering structure. The key idea is to break down a large device into separable, rectangular modules, each of which can be computed very efficiently [see e.g. Fig. 3.1(b)]. For purely ballistic devices consisting of a few, separable parts this approach has been implemented by Rotter et al. [35, 36]. In contrast, the standard recursive Green's function method [1, 2, 3] assembles a structure by directly inverting the Green's function of a single block, which is then added via a Dyson equation. We combine these two approaches by recursively combining not single stripes, but rectangular modules, thereby reducing needed computing resources dramatically,

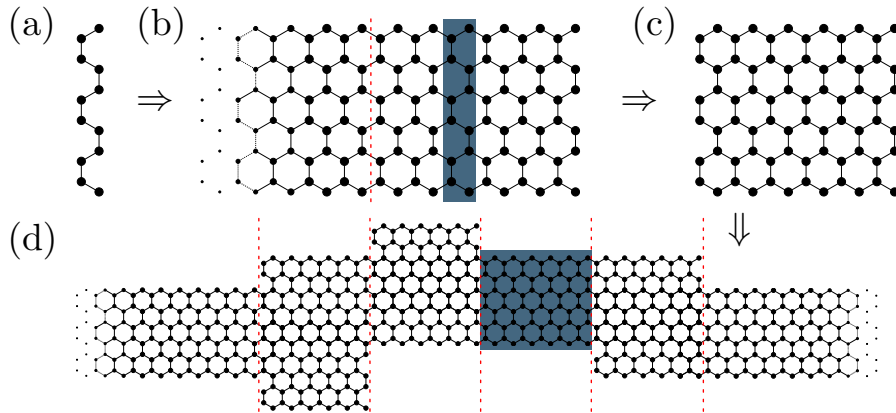


Figure 3.2: (a) Single graphene block described by the matrix  $H_0$ . (b) A half-infinite waveguide is assembled by periodic repetition of (a) (see shaded area). By cutting off a finite-length module from a half-infinite waveguide (b), a rectangular module is calculated (c), which is then used to assemble a large-scale scattering structure (d).

while still retaining the flexibility to model complicated boundary structures or scattering potentials [see e.g. point scatterers (black dots) in Fig. 3.1(b)].

The calculation of each rectangular module of width  $W$  and length  $L$  proceeds in three steps: (i) the Bloch eigenfunctions  $e^{ikx} |\chi_n\rangle$  of an infinitely long ribbon of width  $W$  are calculated, (ii) the Green's function of a half-infinite waveguide of width  $W$  is expressed as an expansion in  $|\chi_n\rangle$ , and (iii) using a Dyson equations, a rectangle of appropriate length  $L$  is carved out off the half-infinite ribbon. To better illustrate this procedure, consider a graphene-based nanoribbon. In step (i), the eigenvalue problem (3.6) is solved on a one-dimensional chain of carbon atoms [see Fig. 3.2(a)]. Periodic repetition of this chain creates a half-infinite ribbon of graphene [see Fig. 3.2(b)], from which a rectangular module is separated off by a Dyson equation [see Fig. 3.2(c)]. By combining several rectangular modules, a complex scattering geometry can now be realized [see Fig. 3.2(d)]. While this procedure seems at first glance overly complicated, it is numerically very efficient. Its key advantages are that (a) the computing time is independent of  $L$ , scaling only with the width of the ribbon, and (b) the step (i) has to be performed only once for each value of  $W$ .

### 3.2.1 The Green's function of an infinite waveguide

The Green's function  $g(x, x')$  of an infinite waveguide on a TB grid must fulfill [25]

$$(H - E)g(x, x') = \begin{cases} 0 & x \neq x' \\ \mathbb{1} & x = x' \end{cases}, \quad (3.11)$$

where  $H$  is given in Eq. (3.3). Eq. (3.11) is the discretized form of the continuous equation  $(\mathcal{H} - E)\mathcal{G} = \delta(x - x')$ . For  $x \neq x'$ ,  $g(x, x')$  must be a solution of the time-independent Schrödinger equation  $Hg(x, x') = Eg(x, x')$ . The Bloch states  $e^{ikx} |\chi_n\rangle$  calculated in the previous section are thus ideally suited as a basis to expand  $g(x, x')$ . The Green's function describes the resulting scattering state when a source is introduced to the waveguide at position  $x'$  [i.e. the term  $\mathbb{1}$  in (3.11)]. As a consequence,  $g(x, x')$  is, apart from normalization, given by a basis set  $D$  ( $\overline{D}$ ) of left (right) moving Bloch states for  $x < x'$  ( $x > x'$ ), where

$$D(x) := \sum_{j=1}^N |\chi_j\rangle e^{ik_j x} \langle \chi_j|, \quad (3.12a)$$

$$\overline{D}(x) := \sum_{j=1}^N |\chi_{\overline{j}}\rangle e^{ik_{\overline{j}} x} \langle \chi_{\overline{j}}|. \quad (3.12b)$$

In Appendix (B.1), we show that normalization can be incorporated by multiplication with a properly defined matrix  $V^{-1}$  [see Eq. (B.4)]. The total Green's function of an infinite waveguide can then be written according to [25]

$$g(x, x') = \begin{cases} D(x - x')V^{-1}, & x \geq x' \\ \overline{D}(x - x')V^{-1}, & x < x' \end{cases}. \quad (3.13)$$

Equation (3.13) is especially useful as the  $x$ -dependence enters in an analytical way [see Eq. (3.12b)], making the calculation of large-scale structures readily possible.

### 3.2.2 The Green's function of a half-infinite waveguide

As a next step to establish the Green's function of a rectangular module, we want to find an expression for the Green's function  $g^L(x, x')$  [ $g^R(x, x')$ ] of the half-infinite waveguide extending to  $-\infty$  ( $+\infty$ ). We denote the  $x$  coordinate of the rightmost (leftmost) stripe of the ribbon by  $x_1$ .  $g^R(x, x')$  [ $g^L(x, x')$ ] fulfills Dirichlet boundary conditions at  $x_0 = x_1 - \Delta x$  [ $x_1 + \Delta x$ ],

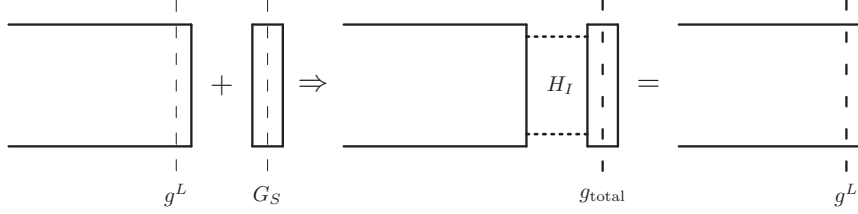


Figure 3.3: Connecting a half-infinite waveguide (with interface Green's function  $g_L$ ) to a single stripe (described by  $G_S$ ). The resulting total Green's function  $g_{\text{total}}$  must be equivalent to  $g_L$ .

i.e.  $g^R(x, x_0) = g^R(x_0, x') = 0$ . One way to proceed would be to adapt the solution  $g(x, x')$  of the infinite problem to these boundary conditions by adding a solution  $g^0$  of the homogeneous Schrödinger equation  $(E - \mathcal{H})g^0 = 0$  [25]. We derive a more efficient expression through application of a matrix Dyson equation on the Green's function of the infinite waveguide.

In its general form, a Dyson equation represents the change in a Green's function  $G_0$  due to a perturbation  $V$ ,

$$G = G_0 + G_0 V G, \quad (3.14)$$

where  $G$  ( $G_0$ ) represents the Green's function of the perturbed (unperturbed) system. In the context of lattice Green's functions,  $V$  is given by the hopping matrix  $H_I$  that connects adjacent blocks (or modules). Using (3.14), we can thus connect two disjoint modules to assemble a larger one. Conversely, we can also solve (3.14) in reversed mode, i.e. for  $G_0$  rather than  $G$ . This amounts to dissecting a larger module.

We first consider the case of  $g^L(x_1, x_1) \equiv g^L$ , i.e. the Green's function at the interface of an half-infinite waveguide extending to  $-\infty$ . We add a single block, described by  $G_S = (H_0 - E)^{-1}$ , to  $g^L$  by using a Dyson equation (see Fig. 3.3),

$$g_{\text{total}} = G_S + G_S H_I^\dagger g^L H_I g_{\text{total}}. \quad (3.15)$$

Note that the combined Green's function  $g_{\text{total}}$  is identical to  $g^L$  (see Fig. 3.3),

$$g_{\text{total}} = g^L, \quad (3.16)$$

as extending a half-infinite ribbon by one block again yields a half-infinite ribbon (see Fig. 3.3). Multiplying from the left with  $G_S^{-1} \equiv (H_0 - E)$  then yields

$$(H_0 - E)g^L = \mathbb{1} + H_I^\dagger g^L H_I g^L. \quad (3.17)$$

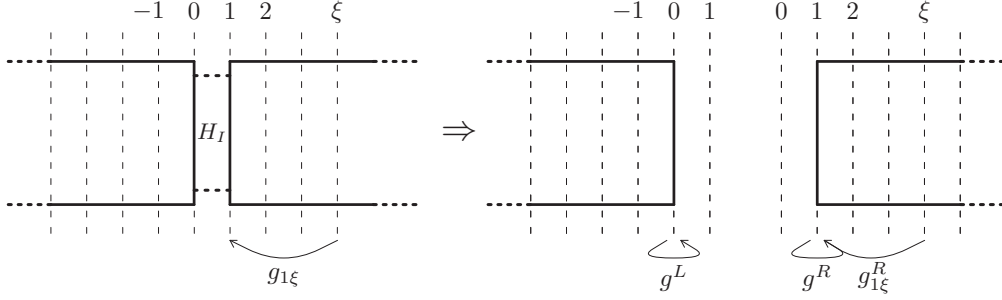


Figure 3.4: *Splitting an infinite waveguide into two half-infinite waveguides by application of a matrix Dyson equation. Dashed lines denote the  $x$ -values of the building blocks  $H_0$ . The Green's functions appearing in Eq. (3.21) are marked.*

To solve this matrix equation (quadratic in  $g^L$ ) we express  $g^L H_I =: Z$  in terms of an eigenvalue expansion,  $Z = \sum |\zeta\rangle \beta \langle \zeta|$ :

$$(H_0 - E)Z = H_I + H_I^\dagger Z^2 \Rightarrow \quad (3.18)$$

$$H_{-I}(H_0 - E)\beta |\zeta\rangle = H_{-I}H_I |\zeta\rangle + \beta^2 |\zeta\rangle, \quad (3.19)$$

with  $H_{-I} = (H_I^\dagger)^{-1}$ . The above equation is equivalent to 3.6. As a consequence,  $|\zeta\rangle \equiv |\chi\rangle$ . A detailed calculation shows, indeed, that the term  $V^{-1}$  in (3.13) exactly cancels out due to the Dirichlet boundary conditions at  $x = x_0$ . As a consequence, the expression for the interface Green's function is reduced to

$$g^L H_I = Z = \sum_{j=1}^N |\chi_j\rangle e^{ik_j \Delta x} \langle \chi_j| = \overline{D}(\Delta x). \quad (3.20a)$$

Analogously we have

$$g^R H_I^\dagger = D(\Delta x). \quad (3.20b)$$

The above formulae (3.20) to determine  $g^L H_I^\dagger$  are numerically very efficient, as a small number of matrix multiplications is needed. The interface Green's function  $g^R$  can quickly be calculated from (3.20) by multiplying with  $H_I^{-1}$ .

Note that (3.20) only gives an expression for the interface Green's function  $g^R \equiv g_{11}^R$  of the half-infinite lead (and likewise for  $g^L$ ). Let us now derive an expression for the Green's function  $g^R(x_1, x_\xi) \equiv g_{1\xi}^R$  from a point  $x_\xi \neq x_1$  inside the half-infinite waveguide to the interface at  $x_1$ . For an infinite waveguide, we have already derived the Green's function  $g_{1\xi}$  from  $x_\xi$  to  $x_1$



(see Eq. 3.13). To obtain an expression for  $g_{1\xi}^R$ , we split the infinite waveguide into two half-infinite ones by a matrix Dyson equation (see Fig. 3.4) of the form

$$g_{1\xi} = g_{1\xi}^R + g^R H_I^\dagger g^L H_I g_{1\xi}, \quad (3.21)$$

which can be solved for  $g_{1\xi}^R$ . We can directly use the expressions for  $g^R H_I$  and  $g^L H_I^\dagger$  given in Eq. (3.20) to simplify (3.21) to

$$g_{1\xi}^R = [\mathbb{1} - D(\Delta x) \overline{D}(\Delta x)] g_{1\xi} \quad (3.22)$$

resulting in a surprisingly compact expression. Expressions for  $g_{1\xi}^L$  and  $g_{\eta\xi}^R$  can be obtained by similar applications of a Dyson equation, as outlined in Appendix (B.2). We will use the Green's functions of the half-infinite waveguide to obtain an expression for the Green's function of a rectangle, as outlined below.

### 3.2.3 Green's function of a rectangular module

We now turn our attention to a rectangular module, of finite length  $L$ , containing  $n = L/\Delta x$  blocks of  $H_0$ . We denote the Green's function of the module by a capital letter  $G$ , to distinguish it from the Green's function of a (half-)infinite waveguide. To calculate both transmission amplitudes as well as scattering states, we need the Green's function of the entire scattering geometry, which we denote by  $\mathcal{G}$ . To determine  $\mathcal{G}$  involves calculating  $G(x_\xi, L) =: G_{\xi n}$  and  $G_{\xi 1}$  from both the left (1) and right ( $n$ ) side of the rectangle to an arbitrary position  $\xi$  inside. To this end, we will use a Dyson equation to decompose a half-infinite waveguide into a rectangular module and a "shorter" half-infinite waveguide.

To obtain  $G_{\xi n}$ , we consider a waveguide extending to  $+\infty$  (see Fig. 3.5). This way, we avoid evaluating the (yet unknown) Green's function  $G_{\xi 1}$  in this step, which would create a system of matrix equations. The Dyson equation for  $G_{\xi n}$  then reads (see Fig. 3.5):

$$g_{\xi n}^R = G_{\xi n} + G_{\xi n} H_I g^R H_I^\dagger g_{nn}^R \Rightarrow G_{\xi n} = g_{\xi n}^R \frac{1}{\mathbb{1} + H_I g^R H_I^\dagger g_{nn}^R}. \quad (3.23)$$

In a similar way,  $G_{\xi 1}$  may be expressed using a waveguide extending to  $-\infty$ , as outlined in Appendix B.3.

Note that in (3.23) [and likewise for  $G_{\xi 1}$ , see Appendix B.3, (B.10)], the denominator is independent of  $\xi$ , making an evaluation for many  $\xi$ , e.g. for wave-function plots, efficient. Additionally, the  $\xi$ -dependence of  $g_{\xi n}$  is given

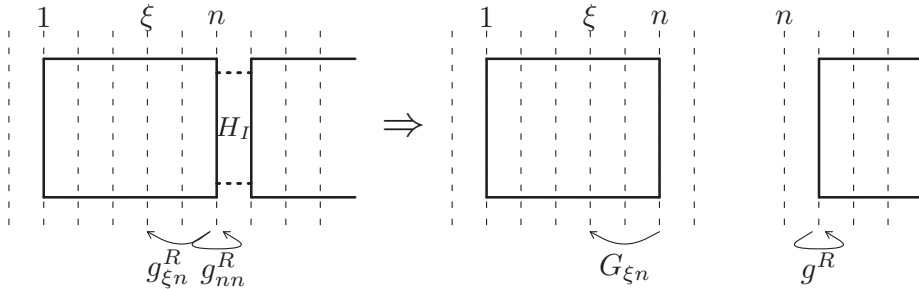


Figure 3.5: Cutting a rectangular module off a half-infinite waveguide extending to  $+\infty$  by use of a matrix Dyson equation. The  $x$  coordinates in reference to the rectangle are given. The Green's functions appearing in Eq. (3.23) are marked.

analytically [see Eq. (3.13)]. As a consequence, the time needed to compute  $G_{\xi n}$  is independent of  $L$ .

Another possibility to compute the Green's function of a rectangular region would be to use a solution  $G_0$  of the homogeneous Schrödinger equation  $(H - E)G_0 = 0$ , as mentioned above for the Green's function of the half-infinite waveguide. However, both  $D(-L)$  and  $\overline{D}(L)$  appear in the resulting matrix equations. These quantities grow exponentially as a function of  $L$  for large  $L$  due to evanescent modes with  $k_n \in \mathbb{C}$  (unlike  $D(L)$  and  $\overline{D}(-L)$ , which are exponentially suppressed). As a consequence, the equations become numerically unstable for large  $L$ , as our calculations have shown. This is not the case for (3.23), which does not contain exponentially increasing terms. We have tested the numerical stability of (3.23) for values of  $n$  up to  $10^5$ , and found no divergence.

### 3.2.4 Assembling the modules

The Green's function of the entire scattering structure  $\mathcal{G}$  can now be computed by assembling the individual rectangular modules [see Fig. 3.6]. We label quantities connected to module number  $l$  by an index  $(l)$  in round brackets. The module  $l$  is completely characterized (in terms of transmission) by the four Green's functions describing all possible connections between the leftmost and rightmost blocks, i.e.  $G_{11}^{(l)}$ ,  $G_{1n}^{(l)}$ ,  $G_{n1}^{(l)}$ ,  $G_{nn}^{(l)}$ . For a rectangle, these matrices are determined by Eq. (3.23). For a single stripe, they are all identical, and given by Eq. (3.26).

Let  $\mathcal{G}_{ij}^{(k)}$  denote the combined Green's function of the left lead and  $k$  attached rectangles. The indices  $i, j$  enumerate the first and last stripes of all the modules (see Fig. 3.6): the leftmost stripe of module  $k$  is labeled  $1^{(k)}$ , the

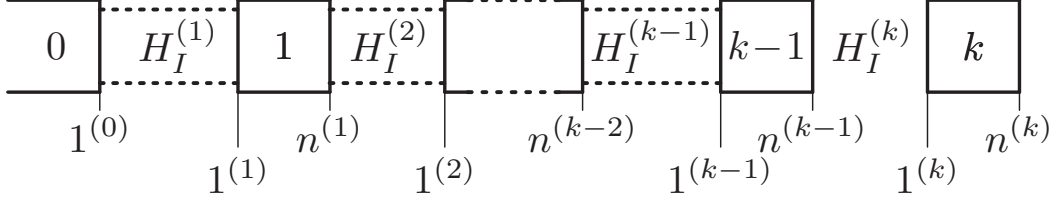


Figure 3.6: *Assembling the total scattering structure by combining modules: The left lead (labeled 0) is already connected to  $k - 1$  rectangular modules. The numbers inside the squares denote the module index. For module  $l$ , the last (first) block is labeled  $1^{(l)}$  [ $n^{(l)}$ ],  $l = 0, \dots, k$ . In the  $k$ -th step, module number  $k$  is attached via  $H_I^{(k)}$ .*

rightmost one  $n^{(k)}$ .  $\mathcal{G}_{1^{(0)}1^{(0)}}^{(0)}$  is identical to the lead Green's function  $g^L$ . Step by step, we now attach all rectangular modules to  $\mathcal{G}^{(0)}$ . In step number  $k$ , we compute  $\mathcal{G}_{ij}^{(k)}$ ,  $i, j \in \{1^{(0)}, n^{(k)}\}$  by connecting the Green's function of the  $k$ -th module,  $G^{(k)}$ , to the Green's function of the partly assembled structure,  $\mathcal{G}_{ij}^{(k-1)}$ , via the coupling matrix  $H_I^{(k)}$  (see Fig. 3.7). Simple point defects may be included by setting a matrix element of  $H_I^{(k)}$  to zero. Furthermore, adjacent rectangles may be shifted transversely relative to each other, to introduce rough edges. We include all these effects into the expressions for  $H_I^{(k)}$ .

To illustrate the above procedure, we derive an expression for the Green's function  $\mathcal{G}_{1^{(0)}n^{(k)}}^{(k)}$  from the right side of rectangle  $k$  to the left lead of the scattering structure. We first calculate the change introduced in the intermediate Green's function  $\mathcal{G}_{1^{(0)}n^{(k-1)}}^{(k-1)}$  by attaching the rectangle  $k$  (see Fig. 3.7)

$$\mathcal{G}_{1^{(0)}n^{(k-1)}}^{(k)} = \mathcal{G}_{1^{(0)}n^{(k-1)}}^{(k-1)} \frac{1}{\mathbb{1} - H_I^{(k)} G_{11}^{(k)} H_I^{\dagger(k)} \mathcal{G}_{n^{(k-1)}n^{(k-1)}}^{(k-1)}} \quad (3.24)$$

The denominator contains the contributions of rectangle  $k$  to  $\mathcal{G}_{1^{(0)}n^{(k-1)}}^{(k)}$  in all orders of  $H_I^{(k)}$ . The updated  $\mathcal{G}_{1^{(0)}n^{(k)}}^{(k)}$  can now be written as (see Fig. 3.7)

$$\mathcal{G}_{1^{(0)}n^{(k)}}^{(k)} = \mathcal{G}_{1^{(0)}n^{(k-1)}}^{(k-1)} H_I^{(k)} G_{1n}^{(k)} \quad (3.25)$$

Derivations for the other three Green's functions  $\mathcal{G}_{n^{(k-1)}1^{(0)}}^{(k)}$ ,  $\mathcal{G}_{1^{(0)}1^{(0)}}^{(k)}$ , and  $\mathcal{G}_{n^{(k-1)}n^{(k-1)}}^{(k)}$  follow similar lines. The respective formulas are given in App. B.4. After recursively attaching all rectangles making up the scattering geometry, the total Green's function  $\mathcal{G}$  of the entire scattering structure is created by attaching the right lead as the final module.

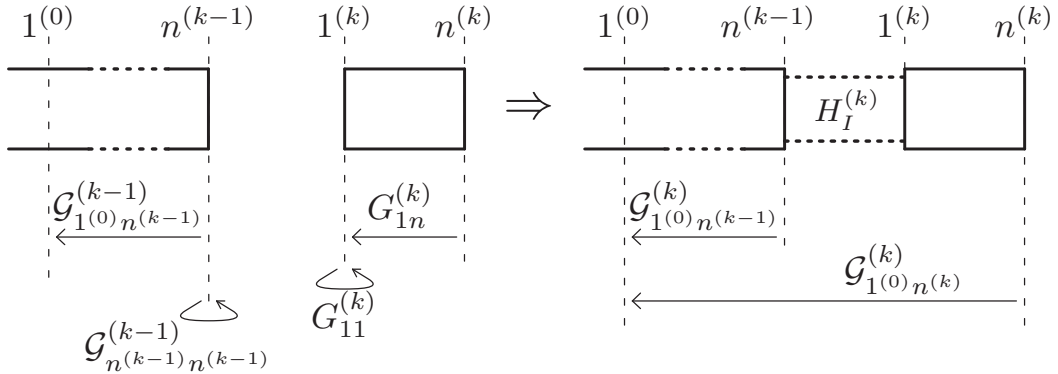


Figure 3.7: Dyson equation to attach module  $k$  [described by the Green's functions  $G_{ij}^{(k)}$ ] to the Green's function  $\mathcal{G}_{1^{(0)}n^{(k-1)}}^{(k-1)}$  already containing the left lead and  $k - 1$  rectangles. The resulting Green's function  $\mathcal{G}_{1^{(0)}n^{(k)}}^{(k)}$  is given in Eq. (3.25).

### 3.2.5 Superblock structures

The above method to derive the Green's function of a scattering geometry is ideally suited to describe the transport through large, ballistic devices, that can be described by a few distinct modules. Disorder, however, breaks the separability in transverse ( $y$ ) and longitudinal ( $x$ ) direction required by the analytic expansion of the Green's function in lead modes, leading to a prohibitively large number of individual rectangles. To efficiently model the conductance of large-scale disordered devices, a method to include arbitrary, non-separable potentials is thus needed. We start from a small device: a combination of rectangular blocks and individual, non-separable stripes is employed to include disorder. As an example, consider the inclusion of a short-range scatterer in a nanoribbon, as shown schematically in Fig. 3.8(a). A single stripe, containing a short-range scatterer, is embedded between two extended, ballistic rectangular modules. The Green's function of the disordered stripe can be calculated by direct inversion of the Hamiltonian  $H^S$  of the single stripe according to

$$G_S = \frac{1}{H^S - E - i\eta}, \quad (3.26)$$

which is easily feasible for stripe sizes up to 1000 points. Note that the stripe may well have a non-vanishing extension in  $x$ -direction, as long as it does not contain more than roughly  $10^4$  sites. The additional numerical effort to perform the matrix inversion (3.26) in order to include one such defect is negligible.

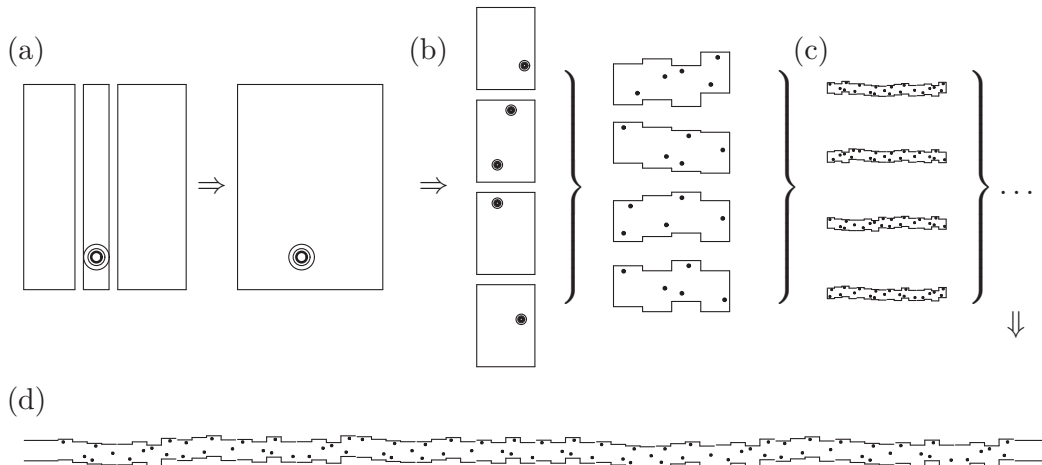


Figure 3.8: *Schematic picture of the inclusion of many point scatterers into a scattering geometry: (a) by combining two separable rectangular modules with a single stripe containing a defect, a larger, non-separable module containing a single defect is obtained. (b) Different realizations of the rectangle shown in (a) are then combined into superblocks. The order of the building blocks is changed randomly. (c) By iteratively performing step (b), increasingly complex supermodules are obtained. The size of the calculated scattering structure increases exponentially (with a linear increase of computing time).*

However, to build up large scale devices using this method gets unfeasible, as the computing time increases linearly with the number of defects (for each defect, a stripe has to be directly inverted). To avoid this, one can employ a supermodule approach, as suggested by Feist et al. [38]: We calculate the Green’s function of a few, e.g. four, different realizations of a short-range scatterer (e.g. an edge defect, a lattice vacancy, etc.) using the methods outlined above. Then, in a second step, these modules are randomly combined into different “supermodules” [see Fig. 3.8(b)]. Each supermodule thus features several point scatterers at random positions. This recombination step uses exactly the same algorithm as outlined above to assemble the scattering structure. The resulting Green’s functions describing all possible paths of transport between the leftmost stripe of the supermodule and the rightmost one can then be used to include the supermodule into the scattering geometry itself, or to create another, larger supermodule: By repeatedly recombining the modules, we exponentiate the size of the structure by the number of modules contained in one supermodule, while only adding the (constant) computing time to combine the modules [see Fig. 3.8(c)]. As

a consequence, the size of the structure increases exponentially, while the computing time increases only linearly.

### 3.2.6 Transmission coefficients

Once the Green's function  $\mathcal{G}$  of the scattering structure is known, the total transmission and reflection of the device can be determined using projection onto the lead eigenstates<sup>2</sup>  $|\chi_n\rangle$ . To calculate the corresponding expressions, we note that the Green's function of the infinite waveguide is reduced to a normalized, propagating Bloch state [see Eq. (3.10)] using the projection operator [25]

$$P_n(x) := V |\chi_n\rangle \frac{e^{ik_n x}}{\sqrt{v_n}}, \quad g_{xx'} P_n(x') = \frac{e^{ik_n x}}{\sqrt{v_n}} |\chi\rangle. \quad (3.27)$$

As shown by Sanvito [26],  $P_n$  also gives the scattering wave function  $\psi$  of an incoming mode  $m$  if applied to the total Green's function  $\mathcal{G}$ . An expression for the reflected wave function in the left ( $|\psi_n^L\rangle$ ) and the transmitted wave function in the right ( $|\psi_n^R\rangle$ ) lead can thus be derived by applying  $P_n(x)$  onto the Green's function of the scattering region,

$$|\psi_n^L\rangle = \mathcal{G}_{LL} P_n, \quad |\psi_n^R\rangle = \mathcal{G}_{RL} P_n, \quad (3.28)$$

where we have labeled the first blocks  $1^{(0)}$  and  $1^{(N_k+1)}$  of the left and right leads  $L$  and  $R$  respectively. The same wave functions are, on the other hand, also given by the transmission and reflection coefficients as

$$|\psi_n^L\rangle = \left[ \frac{1}{\sqrt{v_n}} |\chi_n\rangle + \sum_{m=1}^N \frac{r_{mn}}{\sqrt{-v_m}} |\chi_{\bar{m}}\rangle \right], \quad |\psi_n^R\rangle = \sum_{m=1}^N \frac{t_{mn}}{\sqrt{v_m}} |\chi_m\rangle. \quad (3.29)$$

Both expressions for  $|\psi_n^L\rangle$  can now be set equal to derive an expression for the transmission and reflection coefficients

$$t_{mn} = \sqrt{\frac{v_m}{v_n}} \langle \chi_m | \mathcal{G}_{RL} V | \chi_n \rangle, \quad T = \sum_{m,n=1}^N |t_{mn}|^2, \quad (3.30)$$

$$r_{mn} = \sqrt{\frac{-\bar{v}_m}{v_n}} \langle \chi_{\bar{m}} | \mathcal{G}_{LL} V - \mathbb{1} | \chi_n \rangle, \quad R = \sum_{m,n=1}^N |r_{mn}|^2. \quad (3.31)$$

---

<sup>2</sup>We assume here that both leads are described by the same matrices  $H_0, H_I$ . The more general case of different leads is treated in App. B.5.

According to the Landauer-Büttiker formalism [37] the total conductance  $G$  (that should not be confused with a Green's function!) through the quantum dot with  $N$  propagating modes is given by

$$G = \frac{2e^2}{h} \sum_{m,n=1}^N |t_{mn}|^2, \quad (3.32)$$

where the factor 2 counts the spin degree of freedom. The unitarity condition  $T + R = N$  provides a convenient way to check the consistency of the numerical calculations. We find unitarity to be fulfilled with deviations less than  $10^{-8}$  even for large-scale structures.

### 3.2.7 Wave functions

The above formalism to calculate the transmission coefficient can easily be extended to determine the entire scattering wave function. For an incoming wave consisting of a superposition of several modes, we extend the definition of  $P_j$  [see (3.27)] according to

$$P(x) = \sum_{j=1}^N c_j P_j(x), \quad (3.33)$$

where the coefficients  $c_j$  are the expansion coefficients of the incoming plane wave in transverse modes. The resulting wave function  $\psi$  at a given coordinate  $x$  in the scattering structure is then given by

$$\psi(\mathbf{r}) = \mathcal{G}_{x1(0)} P(1), \quad (3.34)$$

where  $\mathbf{r}$  is any point in the entire scattering structure.

Using the MRGM,  $\psi$  can be determined in a feasible amount of time in the following way. Consider a point  $\mathbf{r}$  located inside module  $k$  at block  $\xi^{(k)}$ . The total Green's function  $\mathcal{G}_{\xi^{(k)}1(0)}$  from the left exit to  $\xi^{(k)}$  consists of two contributions, containing the paths entering the module either on the right or on the left side (see Fig. 3.9):

$$\mathcal{G}_{\xi^{(k)}1(0)} = G_{\xi_1}^{(k)} H_I^{\dagger(k)} \mathcal{G}_{n^{(k-1)}1(0)} + G_{\xi_n}^{(k)} H_I^{(k)} \mathcal{G}_{1^{(k+1)}1(0)}. \quad (3.35)$$

Note that  $\mathcal{G}$  contains all the information about the remaining scattering geometry, while  $G_{\xi_1}^{(k)}$  and  $G_{\xi_n}^{(k)}$  only depend on the module considered.

$\mathcal{G}$  is costly to determine. On the other hand, only the leftmost term in  $G_{\xi_1}^{(k)}$  and  $G_{\xi_n}^{(k)}$  includes a dependence on  $\xi$ , namely in the Green's function of

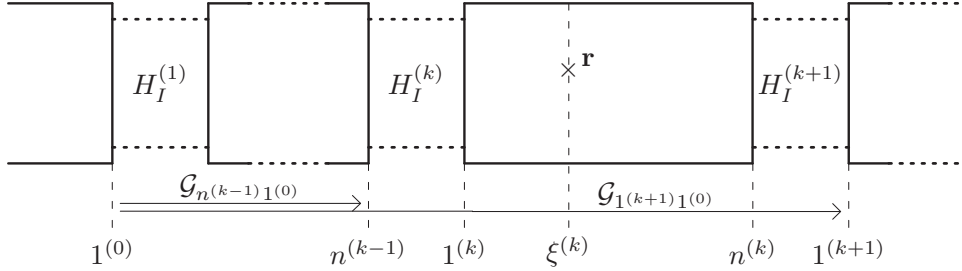


Figure 3.9: *Two path contributions connect the left lead with point  $\mathbf{r}$  in module  $k$ : either (i) from  $1^{(0)}$  to  $n^{(k-1)}$  (described by  $G_{n^{(k-1)}1^{(0)}}$ ) and then entering module  $k$  via  $H_I^{(k)}$  from the left or (ii) from  $1^{(0)}$  to  $n^{(k-1)}$  (described by  $G_{1^{(k+1)}1^{(0)}}$ ) and subsequently entering module  $k$  via  $H_I^{(k+1)}$  from the right [see Eq. (3.35)].*

the infinite lead [see Eq. (3.23)]. By defining a suitable projection operators (for details, see Appendix B.6) we can reduce the  $\xi$ -independent contribution to one-dimensional vectors  $|p^{(k)}\rangle$  and  $|q^{(k)}\rangle$  that are independent of  $\mathbf{r}$ , and have to be evaluated only once for each rectangular module. To determine  $\psi$  in the module  $k$ , one only needs to evaluate

$$\psi^{(k)}(\mathbf{r}) = \overline{D}(1-x)|p^{(k)}\rangle + D(x-l)|q^{(k)}\rangle. \quad (3.36)$$

This greatly reduces the amount of computing time needed to determine the wave functions in each rectangular module.

The wave functions in the leads are constructed using the transmission and reflection coefficients,

$$\psi^L(\mathbf{r}) = \sum_{j=1}^N c_j \left[ \frac{e^{ik_j x}}{\sqrt{v_j}} |\chi_j\rangle + \sum_{m=1}^N r_{mj} \frac{e^{ik_m x}}{\sqrt{v_j}} |\chi_m\rangle \right], \quad (3.37)$$

$$\psi^R(\mathbf{r}) = \sum_{j,m=1}^N c_j \frac{t_{mj}}{\sqrt{v_m}} e^{ik_m x} |\chi_m\rangle. \quad (3.38)$$

These can be evaluated even for complicated structures, where calculating the Green's function at every point is too time-consuming.

### 3.2.8 Accuracy tests

To ensure the validity of our numerical calculations, we checked both the unitarity of our  $S$ -matrix as well as the Onsager relations [3], which were both fulfilled to an accuracy level of at least  $10^{-8}$ . Furthermore, we compared



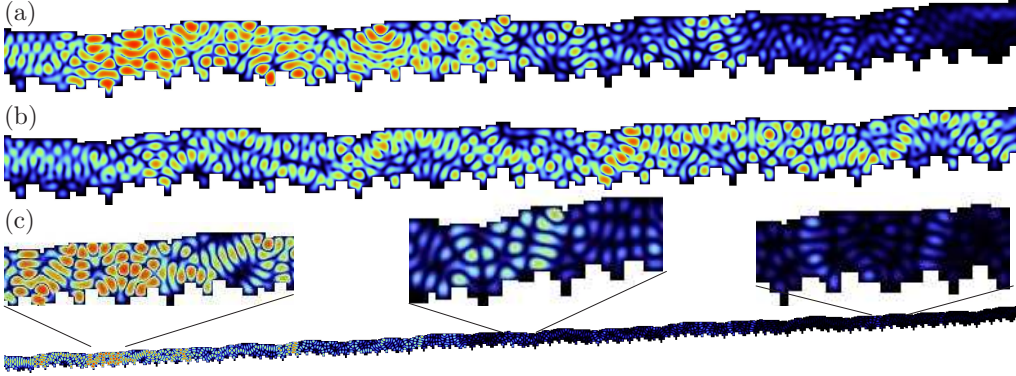


Figure 3.10: (a) Scattering state of a rough-edged quantum nanowire (constant potential  $V = 0$  confined in  $y$ -direction by hard wall boundaries) of length  $L \approx 100\lambda$  (where  $\lambda$  is the wavelength of the incoming wave). The edge of the ribbon features roughness on a length scale  $\delta W \approx \lambda$ . We use 94 rectangular modules (and a total number of 667 blocks) in the calculations. The onset of Anderson localization exponentially suppresses transport, leading to low scattering state amplitudes on the right side of the picture. (b) Same as (a), but at a different resonance energy. The wave function does not decay as fast as in (a). (c) A longer nanowire,  $L \approx 500\lambda$ , consisting of 382 rectangles (2641 blocks). Transport is strongly suppressed for  $\lambda \approx \delta W$ .

the MRGM results with both analytical calculations (for those geometries where formulas are available) as well as with existing implementations of the MRGM available for ballistic quantum dot devices [35]. We find perfect agreement for both transmission values and scattering wave functions. The key advantage of the modular technique presented here as compared to older implementations is the flexibility both in the Hamiltonian matrix as well as in the device geometry.

Calculation of the scattering wave function  $\psi$  is another way to check the validity of our approach: Even small errors in the solution of a Dyson equation lead to non-continuous jumps or singularities in  $\psi$ . Furthermore, the result was carefully checked to ensure that  $\psi$  fulfills both boundary conditions and the Schrödinger equation itself. An example for the wave function of a long quantum wire is given in Fig. 3.10: the MRGM technique allows us to treat a structure size several orders of magnitude larger than the wavelength. We can thus visualize e.g. the onset of Anderson localization in rough-edged quantum wires. We are not aware of any other numerical method capable of calculating the scattering states for such large structures accurately and in a feasible amount of time.

# Part II

## Applications

# Chapter 4

## Graphene-based nanostructures

### 4.1 Graphene

Graphene [39, 40], the first true two-dimensional (2D) solid, is attracting considerable attention, mostly due to unique dynamics of electrons near the Fermi energy which closely mimics that of a massless Dirac Hamiltonian [see Fig.4.1(b)]. Moreover, the double cone structure near the  $K$  and  $K'$  points of the sub-lattices in reciprocal space gives rise to a near “pseudo-spin” degeneracy, suggesting an analog of Dirac four spinors. Envisioned applications range from high-mobility nanoelectronics [9], spin-qubits in graphene quantum dots [7] and the creation of “neutrino” billiards [41, 27]. Spin coherence times in graphene are expected to be very long due to potentially weak spin-orbit and hyperfine couplings [42, 43] making graphene quantum dots promising candidates for future spin based quantum computation [7]. However, confining electrons in graphene is a challenge, mainly due to the gapless electronic structure and the Klein tunneling paradox [44, 45, 46]. This difficulty has recently been overcome by structuring 2D graphene and quantum mechanical confinement effects have been observed in nanoribbons [47, 48, 49], interference devices [50], single electron transistors [10, 51] and graphene quantum billiards [27].

While the consequences of the hexagonal symmetry of the perfect honeycomb lattice are well understood theoretically, realistic samples of graphene feature finite-size effects, symmetry-breaking due to point scatterers and charged impurities. The question remains to what extent these defects will influence the properties of graphene. Interest in this area is rapidly growing. However, conventional analytical techniques fail for large-scale devices with random impurities or lattice defects. One has to resort to more complicated analytical approaches (e.g. random magnetic fields to describe

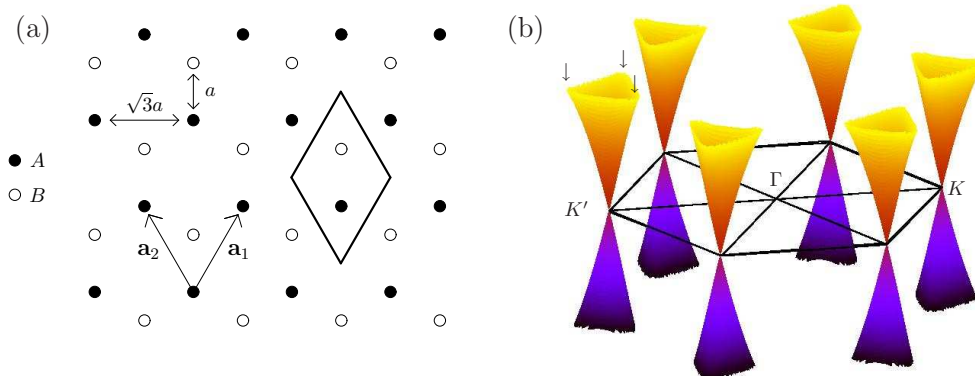


Figure 4.1: (a) Two-dimensional hexagonal Bravais lattice formed by two lattice vectors  $\mathbf{a}_1 = (\frac{3}{2}a, \frac{\sqrt{3}}{2}a)$ ,  $\mathbf{a}_2 = (\frac{3}{2}a, -\frac{\sqrt{3}}{2}a)$ , where  $a$  is the lattice constant. Each unit cell (one highlighted by a box) contains two atoms [labeled by solid ( $A$ ) and open ( $B$ ) circles]. Vectors  $\mathbf{b}$  label the position of the individual atoms in the unit cell. In the present case,  $\mathbf{b}_A = (\mathbf{a}_1 + \mathbf{a}_2)/3$  (solid circles), and  $\mathbf{b}_B = 2(\mathbf{a}_1 + \mathbf{a}_2)/3$  (open circles). (b) The conical dispersion relation of an infinite graphene plane, as obtained by the third-nearest neighbor tight-binding approach. Arrows mark the triangular deformation of one double-cone (see text).

the crumpling of graphene flakes [52]), or numerical techniques. After determining the matrices  $H_0$ ,  $H_I$  needed to model graphene in our numerical framework, we will investigate the eigenstates of graphene-based devices, and elucidate the influence of the graphene lattice. We then proceed to the transport case, and investigate the consequences of lattice defects and disorder on the resistance of graphene nanoribbons.

#### 4.1.1 Band structure

Graphene consists of a periodic two-dimensional hexagonal lattice of carbon atoms [see Fig. 4.1(a)]. The periodicity of the hexagonal lattice is described by a Bravais lattice formed by two base vectors  $\mathbf{a}_1$ ,  $\mathbf{a}_2$ . One unit cell contains two carbon atoms, labeled  $A$  and  $B$ . The electronic structure of graphene near the Fermi edge is dominated by the  $p_z$  orbitals of the carbon atoms. Therefore, only the  $p_z$ -orbital contributes to transport (while the other three orbitals of the outer shell form three  $sp^2$  hybrid orbitals that build up the lattice), reducing the number of tight-binding (TB) orbitals to one per carbon atom.

We now derive a TB formulation for the bandstructure of graphene. Each atom of type  $A$  [solid circles in Fig. 4.2(a)] is surrounded by three neighbors

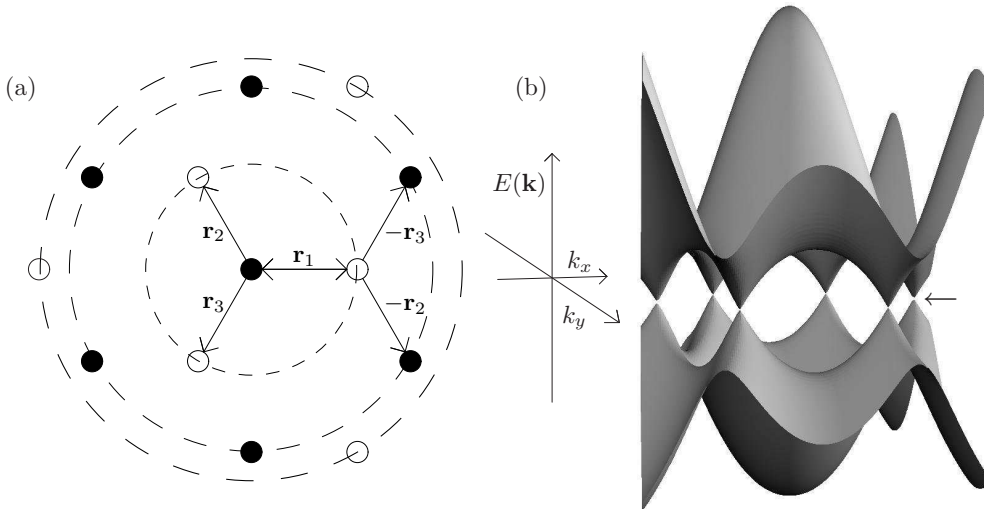


Figure 4.2: (a) Enlarged view of a part of the hexagonal Bravais lattice shown in Fig. 4.1. The nearest-neighbors of an A-atom are three B atoms (see smallest dashed circle). Second and third nearest neighbors are six A atoms and 3 B atoms, respectively (see larger dashed circles). (b) Three-dimensional representation of the dispersion relation  $E(\mathbf{k})$  of a hexagonal Bravais lattice in third nearest-neighbor TB approximation. An arrow marks one of the six touching points of the two bands.

of type B, at relative positions  $r_1 = (\mathbf{a}_1 - 2\mathbf{a}_2)/3$ ,  $r_2 = (\mathbf{a}_1 + \mathbf{a}_2)/3$  and  $r_3 = (\mathbf{a}_2 - 2\mathbf{a}_1)/3$ . Conversely, the three nearest neighbors of B are all of type A, at relative positions  $-\mathbf{r}_3, -\mathbf{r}_2$  and  $-\mathbf{r}_1$ . The hopping matrix element  $\langle \phi_A | H | \phi_B \rangle =: \gamma_1$  has to be identical for all nearest-neighbor (NN) interactions (due to the lattice symmetry). The site energy  $\langle \phi_n | H | \phi_n \rangle =: \varepsilon_0$  is equal for both sites A, B. In first NN coupling, the eigenvalue system is thus

$$\begin{pmatrix} \varepsilon_0 & \gamma_1 f_1(\mathbf{k}) \\ \gamma_1 f_1(-\mathbf{k}) & \varepsilon_0 \end{pmatrix} \cdot \begin{pmatrix} c_A \\ c_B \end{pmatrix} = E \begin{pmatrix} c_A \\ c_B \end{pmatrix}, \quad (4.1)$$

where we have introduced the shorthand notation

$$f_1(\mathbf{k}) = e^{i\mathbf{k}\mathbf{r}_1} + e^{i\mathbf{k}\mathbf{r}_2} + e^{i\mathbf{k}\mathbf{r}_3}. \quad (4.2)$$

To more accurately reproduce the features of a realistic graphene flake, we include third NN coupling [see Fig. 4.2(a)] [53]. This allows for four free parameters, namely the site-energy  $\varepsilon_0$  and the overlap integrals  $\gamma_{1,2,3}$ , representing the interaction with the first, second and third nearest neighbor [see Fig. 4.2(a)]. The resulting dispersion relation [see App. A.2 for details] features a double-cone structure with a linear dispersion relation near  $E = 0$  [see Fig. 4.2(b)]. We determine the  $\gamma_i$  by minimizing the mismatch to ab-initio

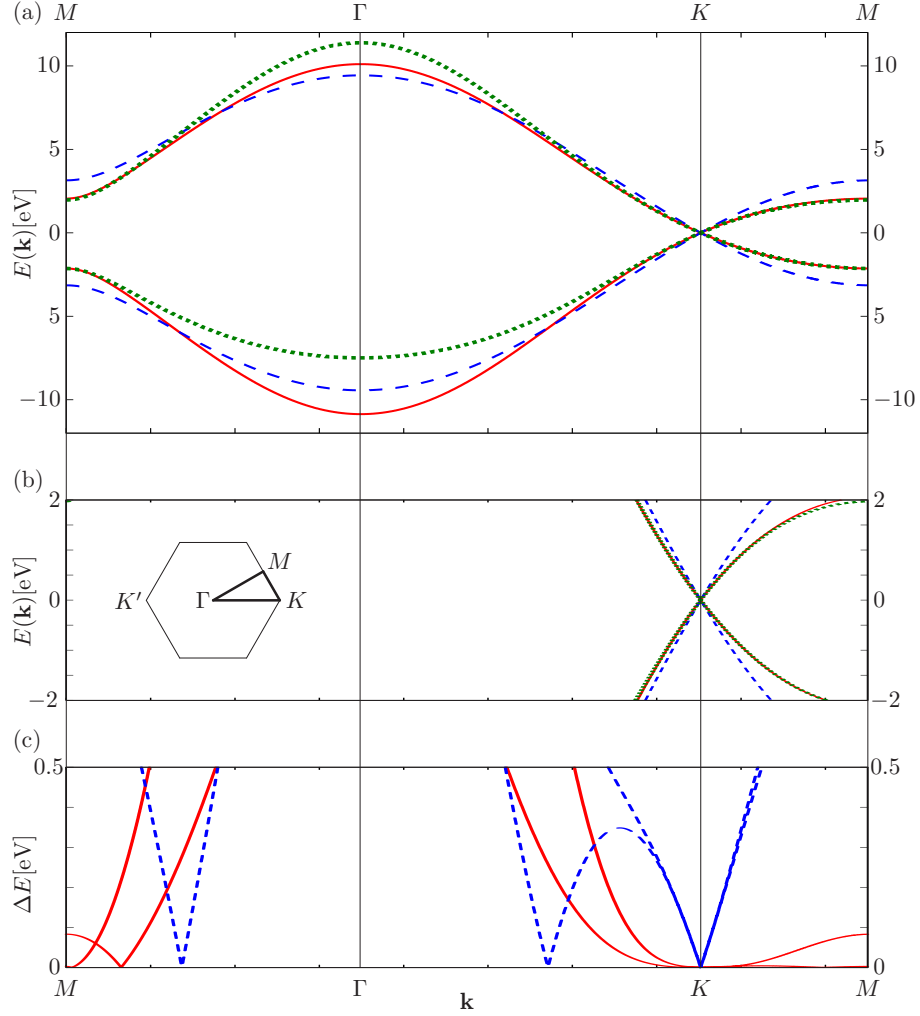


Figure 4.3: (a) Bandstructure of an infinite graphene sheet, calculated with NN tight-binding ( $E^{(1)}$ , dashed blue line), third NN TB ( $E^{(3)}$ , solid red line) and ab-initio calculations ( $E^{(\infty)}$ , dotted green line [53]), calculated on a path connecting  $M$ ,  $K$  and  $\Gamma$  points, as shown in the inset. (b) Enlarged view of the energy region  $\pm 2$  eV around the Dirac point. (c) The difference  $\Delta E = |E^{(\infty)} - E^{(i)}|$  [see Eq. (4.4)] of first (solid red line) and third (dashed blue line) NN coupling to the ab-initio result.

calculations of the bandstructure, taken from Reich et al. [53], as explained in section 2.1.2. As the transport properties of graphene are determined by the bandstructure near the Dirac point, we perform the fit in an energy interval of  $\pm 2\text{eV}$  around the Fermi energy. We find the set of parameters

$$\varepsilon_0 = -0.026, \quad \gamma_1 = -3.145, \quad \gamma_2 = -0.42, \quad \gamma_3 = -0.35. \quad (4.3)$$

We compared these fits to results from ab-initio calculations as well as from a first-nearest neighbor tight-binding description [see Fig. 4.3(a)]. We find that the additional freedom of choosing  $\gamma_2$  and  $\gamma_3$  greatly increases the accuracy of the tight-binding description, in particular in energy regions close to the Dirac point. Due to the hexagonal lattice, the double-cone structure of the dispersion relation near the Fermi energy becomes deformed [see arrows in Fig. 4.1(b)]. This effect is commonly referred to as triangular warping [54]. Near the  $K$ -point, triangular warping results in a pronounced asymmetry in the Dirac-cone [see Fig. 4.3(b)], which is not correctly accounted for by the first NN TB calculations. For a more quantitative comparison, we calculated the error

$$\delta E = |E_{TB} - E_{a.i.}| \quad (4.4)$$

of both third and first NN TB compared to ab-initio results [see Fig. 4.3(c)]. We find that the deviations of the first NN TB approximations are non-zero even for  $\mathbf{k}$  values close to the Dirac point. In particular, the triangular warping effect is underestimated. Reich et al. also provide tight-binding parameters for third NN coupling [53]. However, they use a non-orthogonal TB description. The comparison in Fig. 4.3(c) shows that the inclusion of three TB parameters is already sufficient to capture all essential features of the graphene bandstructure.

### 4.1.2 Dirac equation

The linear dispersion relation of the graphene band structure near the Dirac point closely resembles the dispersion relation of a free massless Dirac equation,

$$\begin{pmatrix} 0 & \partial_x + i\partial_y \\ \partial_x - i\partial_y & 0 \end{pmatrix} \begin{pmatrix} \phi_A \\ \phi_B \end{pmatrix} = E \begin{pmatrix} \phi_A \\ \phi_B \end{pmatrix}. \quad (4.5)$$

It is, indeed, possible to arrive at (4.5) by a linearization of the equation for the bandstructure of graphene [see (4.1)] as shown by Semenoff [55]. The two-component vector  $(\phi_A, \phi_B)$  which appeared due to the two atoms in a unit cell here takes the form of a two-component spinor. This allows for the definition of the so-called pseudo-spin  $s_p$ , which is determined by the

distribution of the wave function on the  $A$  and  $B$  sub-lattices. The plane wave solution for the free massless Dirac equation is

$$\langle \mathbf{r} | \phi_\varphi \rangle = \begin{pmatrix} e^{i\frac{\varphi}{2}} \\ e^{-i\frac{\varphi}{2}} \end{pmatrix} e^{i\mathbf{k}\cdot\mathbf{r}}, \quad \mathbf{k} = k \begin{pmatrix} \cos \varphi \\ \sin \varphi \end{pmatrix}, \quad (4.6)$$

where  $\varphi$  is the angle between  $\mathbf{k}$  and the  $x$ -axis [41]. The factor  $\varphi/2$  in the exponent of the spinor components has profound consequences on the properties of  $|\phi_\varphi\rangle$ . For scattering potentials that act equally on both sub-lattices (i.e. with a characteristic length scale much larger than the lattice constant  $a = 1.42\text{\AA}$ ) pseudo-spin is conserved. The interference of two spinors (4.6) moving at different angles  $\varphi, \varphi'$  is proportional to

$$\langle \phi_{\varphi'} | \phi_\varphi \rangle = 2 \cos \frac{\varphi - \varphi'}{2}. \quad (4.7)$$

For a backscattered wave,  $\varphi' = \pi - \varphi$ , and the matrix element (4.7) vanishes. As a consequence, backscattering is strongly suppressed in a perfect, infinite graphene layer due to destructive interference. On the other hand, the pseudo-spin becomes ill-defined at the edges or at short-range impurities in a realistic, finite size graphene nanostructure. We will discuss the consequences of realistic impurities and edges on the eigenstates of graphene quantum dots in the following sections.



## 4.2 Graphene-based quantum billiards

Classical and quantum (Schrödinger) billiards have taken central stage in studies elucidating the quantum-to-classical crossover in both regular and chaotic devices. Theoretical and experimental studies mostly for electron billiards have revealed surprising new physical phenomena with far-reaching applications. Dirac (including neutrino [41]) billiards, which have been difficult to realize experimentally, are now gaining increasing attention due to recent advances in the manufacture of graphene nanodevices [9, 48]. Graphene-based quantum dots allow for the experimental realization of billiards with a Dirac-like dispersion relation for the first time. In the following section we will show that a graphene billiard features clear signatures for physics beyond the model of a confined massless Dirac spinor. Using the numerical methods presented in the first part of this thesis, we are able to simulate realistic graphene quantum dots with linear dimensions of up to 45 nm, a size that nowadays can be reached experimentally. This work was mainly motivated by recent advances in fabricating dots with linear dimension  $d$  ranging from a few hundred nm down to about 40 nm, and determining their nearest neighbor energy level spacing distribution [27, 51]. We analyze the influence of rough edges and disorder on dot wave functions, the density of states (DOS) and the nearest neighbor spacing distribution (NNSD). We find clear signatures for physics well beyond the simple model of a confined massless Dirac spinor pointing to the importance of the graphene band structure beyond the Dirac cones. We address the question to what extent the electron spectra now experimentally accessible via measurements of Coulomb blockade peaks reveal information on the roughness and size of the graphene quantum dot. To put it provocatively: Can one “hear” the rugged shape of a drum if it is made of a graphene flake?

### 4.2.1 Edge and bulk defects

We investigate graphene dots with linear dimensions  $d = \sqrt{4WL/\pi}$  between 10 and 40 nm containing between 6000 and 75000 carbon atoms. This size agrees with currently fabricated devices [27]. The shape of the dots is chosen such that in absence of edge roughness the dot becomes rectangular. One motivation of this choice was the remarkable result [41] that a Dirac neutrino billiard of rectangular shape, in sharp contrast to a rectangular Schrödinger billiard, would feature chaotic dynamics with broken time-reversal symmetry. The reason for this lies in the chirality of the spin of Dirac neutrinos: The spin dependence on  $\varphi$  (see Sec. 4.1.2) keeps track of the orientation of the neutrino. At a scattering event, the pseudo-spin is rotated either clockwise or counter-

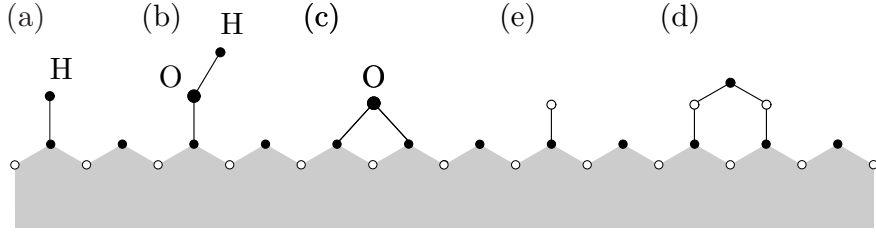


Figure 4.4: *Different types of local edge defects on a zigzag edge: absorption of impurity atoms such as (a) hydrogen, (b) OH-groups or (c) oxygen, or (d,e) a additional carbon atoms instead of a well-defined edge termination.*

clockwise (depending on chirality). If time is reversed, the rotation direction of the pseudo-spin is reversed. This results in a Berry phase contribution of  $-1$ , that breaks time reversal invariance.

The edges of finite-sized graphene devices have been the focus of many investigations [56, 57, 58]. Due to the gapless bandstructure of graphene, experimental structures usually are etched, e.g. by oxygen plasma etching [27]. In contrast, in conventional semiconductor heterostructures (e.g. quantum dots made of GaAs-GaInAs), confinement is achieved by gate voltages resulting in smooth boundary conditions. The etching process employed in graphene results in an edge roughness of the order of several unit cells [59], leading to an irregular edge structure. As a consequence, the symmetries of the honeycomb lattice are broken at the edges [see Fig. 4.4(d-e)]. Another source of edge disorder are impurity atoms (mainly hydrogen and oxygen) which are absorbed at the edge [see Fig. 4.4(a-c)], and thus locally change the DOS. We can include such absorption in our simulations by changing the site energies of tight-binding orbitals at individual carbon atoms located at the edges. Because a carbon atom at the edge only has two nearest neighbors, the C-C bond length decreases. We incorporate this feature by increasing the nearest-neighbor coupling parameter  $\gamma_1$  to the outmost carbon atoms by 12% in accordance with recent ab-initio density functional calculations [60] of finite-width graphene nanoribbons. Edge roughness is simulated by modulating the horizontal or vertical boundary of the dot by steps of height  $\pm\delta w$  and length  $\pm\delta l$  randomly chosen from the interval  $[0, \Delta W]$ ,  $\Delta W \ll d$  [see Fig. 4.5(a)]. We refer to  $\Delta W$  as the amplitude of edge roughness which varies between 0.3 nm (weak disorder) and 2 nm (strong disorder). The resulting piece-wise straight edge features alternating zig-zag and armchair sections [see Figs. 4.5(b)].

Bulk scattering in graphene occurs due to lattice defects (i.e. lattice va-

cancies or impurity atoms) and charged coulomb impurities. The latter results in finite-range scattering, while the former corresponds to short-range scatterers that locally break  $AB$  symmetry. We model short-range scatterers by introducing an additional on-site energy  $\varepsilon_0 = 0.1\text{eV}$  on randomly chosen lattice sites. For finite-range disorder, we include a potential

$$V(\mathbf{r}) = V_0 e^{-\frac{1}{\alpha}|\mathbf{r}-\mathbf{r}_0|} \quad (4.8)$$

centered at a randomly selected lattice site  $\mathbf{r}_0$  [see Fig. 4.5(c)]. The screening length  $\alpha$  was chosen at 5nm, i.e. larger than the lattice constant. We use an impurity density  $n_i < 1.8 \cdot 10^{-3}$  impurities/carbon, as estimated by recent work [61], resulting in about 10 to 100 defects per flake.

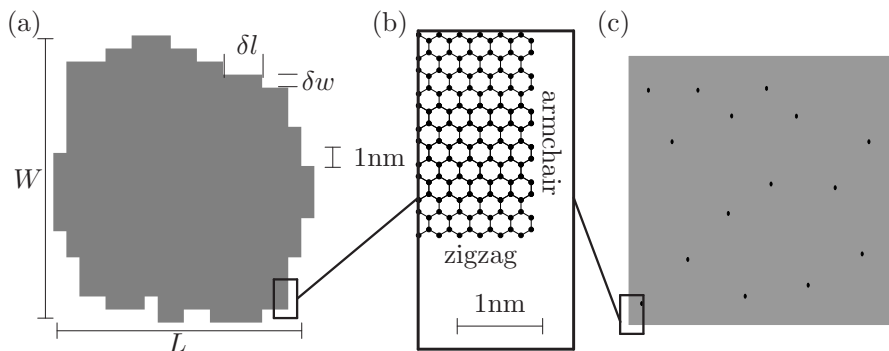


Figure 4.5: *Schematic diagrams of graphene quantum billiards: (a) (Approximately) rectangular quantum dot with rough edges. (b) Rectangular segment of a graphene flake, vertical edge armchair, horizontal edge zig-zag terminated. (c) Rectangular graphene quantum dot with randomly placed point scatterers.*

The spectrum of the graphene quantum dots is determined by the IRAL algorithm (see section 2.1.5). We obtain the 500 eigenstates closest to the Fermi edge. Our ensemble averages for the DOS  $\langle \rho \rangle_\xi = \langle \sum_i \delta(E - E_i) \rangle_\xi$  encompass typically 5000 disorder realizations  $\xi$ .

## 4.2.2 Density of states

If graphene-based quantum dots were to be described by a Dirac equation, the DOS close to the Fermi energy would feature the linear dispersion relation of a massless Dirac particle  $\varepsilon$ ,

$$\rho(\varepsilon) = \frac{1}{2(\hbar v_F)^2} d^2 |\varepsilon|, \quad (4.9)$$

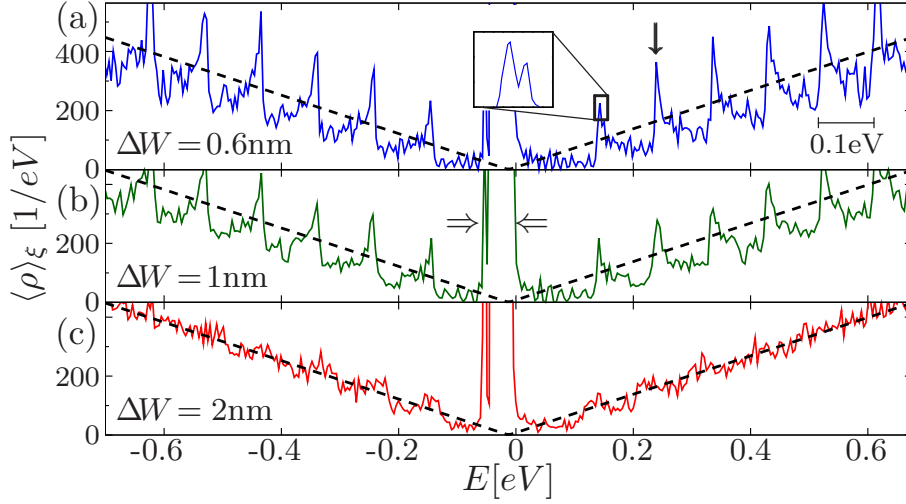


Figure 4.6: *Ensemble-averaged density of states  $\langle \rho(E) \rangle_\xi$  of graphene quantum dots with increasing edge roughness. The size of all devices is equal,  $d = 20\text{nm}$  (20,000 atoms). The edge roughness increases, see different values for  $\Delta W$  in the sub-figures. The width  $W$  of the flakes is  $16\text{nm}$ . Dashed lines indicate the averaged linear DOS for Dirac billiards according to Eq. (4.9). The inset shows a magnification of the  $K - K'$  splitting of  $12\text{meV}$ . The single peak just below  $E = 0$  is due to localized states at the zigzag edges, see text.*

where  $d = \sqrt{4WL/\pi}$  is the effective diameter of a dot with area  $WL$  and  $\varepsilon$  is measured relative to the conical intersection [Fig. 4.5(a)] assumed to coincide with the Fermi edge. However, the simulated DOS for graphene quantum dots [see Fig. 4.6] displays marked deviations from Eq. (4.9). For weak disorder pronounced size quantization peaks appear [see e.g. vertical arrow in Fig. 4.6(a)]. Their positions are determined by the smallest linear dimension of the flake [57, 62, 63]. We have investigated both cases  $W < L$  ( $W > L$ ), and find the same qualitative behavior. In the following, we assume  $W < L$ . Note that width ( $W$ ) and length ( $L$ ) of the rectangular flake are not strictly equivalent as the vertical boundary features an arm-chair border while the horizontal forms a zig-zag border. The distance between the quantization peaks is  $\Delta E = \hbar v_F \pi / W \approx 1.5/W[\text{eV}]$ , width  $W$  given in nm. This yields an analytic prediction for the energy separation of  $0.1\text{eV}$  for the peaks in Fig. 4.6. Weak disorder, i.e. small edge roughness can induce coupling between the cones at  $K$  and  $K'$  [Fig. 4.5(a)]. This manifests itself by a fine structure of size quantization by lifting the degeneracy [inset in Fig. 4.6(a)]. The quantum confinement peaks in the graphene dot are enhanced compared to a corresponding Schrödinger billiard of the same geometry in part because

of both the altered dispersion relation and the additional degeneracy. Strong disorder smears out size quantization patterns and the DOS begins to resemble that of a zero-mass Dirac fermion in free space (Eq. 4.9). Only when the edge roughness can be limited to the sub-nanometer scale, quantized conductance in graphene nanoribbons persists [49].

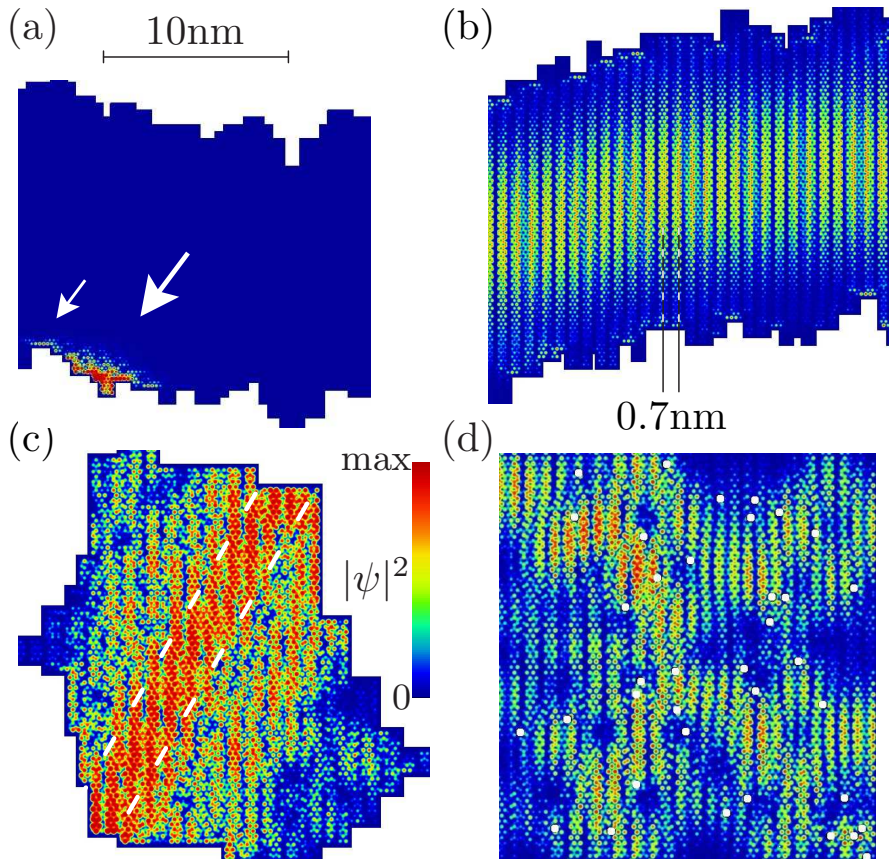


Figure 4.7: *Eigenstates of graphene-based quantum dots. The dot area is about  $225\text{nm}^2$  (13.000 carbon atoms) Eigenenergies are (a) 65 meV (b) 220 meV (c) 650 meV (d) 1020 meV respectively. The edge roughness parameter  $\Delta W = 1\text{nm}$  in (a-c) while  $n_i = 0.005$  in (d). White arrows in (a) mark the localized wavefunction near the zigzag edge (see text). White dots in (d) mark the center of long-range impurities.*

Even in the limit of strong disorder, the prominent peak in the DOS near the Fermi edge remains unchanged. A direct look at the wave function [Fig. 4.7(a)] reveals its origin. The peak in the DOS is due to a large number of strongly (Anderson-)localized states at the edges of the graphene flake. Each eigenstate features a non-vanishing amplitude only at a few,

not always spatially connected carbon atoms, with a decay length into the bulk of typically 0.5 nm [see left arrow in Fig. 4.7(a)]. We find that the eigenenergies of these states are extremely sensitive to the site energies at the corresponding lattice sites. This agrees well with the experimental observations of strong fluctuations of Coulomb resonance positions as a function of an applied side gate voltage in the electron transport through graphene constrictions [10]. We expect that the different functional groups (e.g. H- or OH-, see Fig.4.4) attached to the outermost carbon atoms may strongly influence the local DOS and the distribution of localized eigenstates of this localization peak relative to the Fermi edge. In particular, the on-site energies of the carbon atoms situated at the outmost zigzag edge will vary strongly with position (as different functional groups, on-site potentials due to the substrate, etc. influence the local electrostatic potential). The detailed description of the resulting site energies is beyond the scope of this work.

### 4.2.3 Eigenstates

Delocalized states contributing to the size quantization peaks show pronounced features well beyond the simple picture of a confined zero-mass Dirac particle. While the transverse quantization resembles that of a conventional conductor, the interference pattern in the electron probability density [Fig. 4.7(b)] results from the simultaneous presence of multiple wavelength scales for the cone near the  $K$  point (unlike wave functions near the  $\Gamma$  point), in  $\mathbf{k} = (k_F + v_F\pi/L, v_F\pi/W)$ : Parallel to armchair edges (i.e. in vertical direction in Fig. 4.7), the wavelength is of the order of twice the width of the ribbon-like dot  $\approx 32$  nm. Parallel to zigzag edges, (i.e. in horizontal direction in Fig. 4.7) the wave oscillations are much shorter with a typical wavelength of 0.7 nm [see Fig. 4.7(b)] resulting from beating (frequency ratio 3:2) between lattice periodicity  $a = 0.24$  nm and the Fermi wavelength  $\lambda_F \approx 0.37$  nm. We find beating patterns with this characteristic length scale to be universally present in all delocalized states, even in the presence of finite-range disorder. Only because of the sub-nanometer length scale of  $\lambda_F$  at the  $K$  point is the graphene dot sensitive to edge roughness and disorder on a length scale of a few nanometers. This would not be the case if the Dirac cone were situated at the  $\Gamma$  point. The reason for the  $K$ -point  $(k_F, 0)$  [as opposed to the points at 60 and 120 degrees,  $(k_F/2, \pm\sqrt{3}k_F/2)$ ], to appear in the eigenstate shown in Fig. 4.7(b) is the orientation of the zigzag (armchair) edges in the flake parallel (orthogonal) to the  $(k_F, 0)$  direction. Note, however, that all three directions appear for higher transverse quantum numbers, resulting in enhancements along the three zigzag-directions of the lattice [i.e. horizontal, 60 and 120 degrees, see dashed lines in Fig. 4.7(c)]. As a consequence,

eigenstates feature a 2D hole (“swiss-cheese”) pattern emerging from the interference of plane waves rotated by 60 degrees relative to each other [see Fig. 4.7(d)].

#### 4.2.4 Level spacing statistics

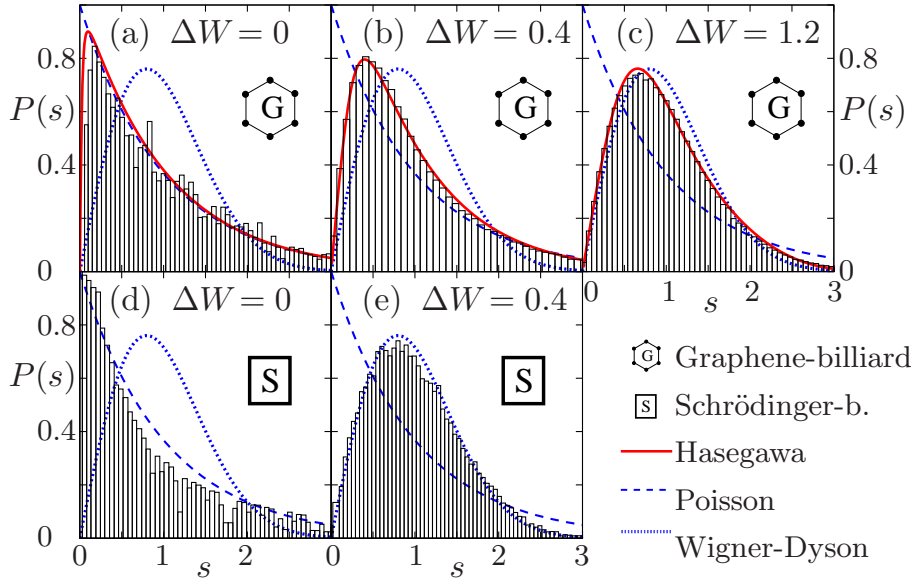


Figure 4.8: *Distribution  $P(s)$  of the mean level spacing for different billiards. (a) Rectangular graphene flake with smooth edges ( $\beta = 0.07$ ). (b) Graphene flake with finite edge roughness  $\Delta W = 0.5$  nm ( $\beta = 0.4$ ), (c) with  $\Delta W = 1$  nm ( $\beta = 2.5$ ). (d,e) Schrödinger billiards with same edge roughness as (a,b), see text. The solid red curve shows fits to the Hasegawa distribution. Dashed (dotted) lines show a Wigner-Dyson (Poisson) statistic as guide to the eye.*

In order to delineate the influence of disorder and edge roughness on the energy level statistics, we have determined the NNSD,  $P(\Delta E)$ , i.e. the probability that the energy difference between two adjacent energy levels is  $\Delta E$ , for different amplitudes  $\Delta W$  of edge roughness as well as different scatterer concentrations  $n_i$ . Within the framework of quantum dynamics of Schrödinger billiards,  $P(\Delta E)$  follows a Poisson distribution for separable (classically regular) shapes while it should display a Wigner-Dyson (or GOE) distribution for irregularly shaped (classically chaotic) billiards. In contrast, even rectangular shaped Dirac neutrino billiards have been shown to feature a GUE distribution because of the broken time reversal symmetry due to

chirality [41]. After spectral unfolding [ $s = \bar{\rho}(\varepsilon_i)$ , with  $\langle P(s) \rangle = 1$  and  $\langle sP(s) \rangle = 1$ ] we find for the ideal rectangular graphene dot ( $\Delta W = 0$ ) a near-perfect Poisson distribution [see Fig. 4.8(a)]. We do not expect a perfect fit to the Poisson limit, because the rectangular shape of the flake is only approximated by the hexagonal lattice, i.e. on the length scale of the lattice spacing separability is broken. By gradually increasing either the edge roughness or the defect concentration  $n_i$ , the distribution smoothly evolves into a Wigner-Dyson like statistics [see Fig. 4.8(b,c)]. Clearly, such a behavior reflects the conservation of time-reversal symmetry in graphene quantum dots. Among the distribution functions suggested for the transition regime for classically mixed phase space [64, 65, 66, 67, 68], the best fit for the disorder parameters and geometries investigated was achieved for the two-parameter Hasegawa distribution [69]

$$P_H(s; \alpha, \beta) = N \frac{\rho s e^{-\rho s - (\alpha \rho s)^2 / 2}}{\sqrt{\rho^2 s^2 e^{-\alpha^2 \rho^2 s^2} + \beta^2 e^{-2\rho s}}}, \quad (4.10)$$

where  $\rho$  and  $N$  are determined by the normalization conditions  $\langle P_H \rangle = \langle sP_H \rangle = 1$  [69]. While the control parameter  $\beta$  describes the transition from Poissonian ( $\beta = 0$ ) to Wigner-Dyson statistics ( $\beta \rightarrow \infty$ ),  $\alpha$  is a system-specific constant. Indeed, we find  $\alpha = 0.75$  to correctly reproduce our numerically obtained NNSD for different values of both edge roughness as well as for different concentrations of scatterers [see Fig. 4.8(a-c)]. A strong edge roughness of 2nm (or impurity concentration  $n_i = 5 \cdot 10^{-3}$ ) is required to reach the completely chaotic limit, i.e. a Wigner-Dyson NNSD statistics. Remarkably, for moderate values of the edge roughness amplitude ( $\Delta W = 0.6$  nm) a Schrödinger billiard and a graphene billiard of the same geometry display a markedly different NNSD (Fig. 4.8): While for moderate disorder values the Schrödinger billiard has already reached the Wigner-Dyson limit ( $\beta \rightarrow \infty$ ), for the graphene the NNSD still is closer to the Poisson limit, pointing to the unique spectral properties of graphene. The quasi-regular dynamics in graphene is more stable against disorder than in corresponding Schrödinger billiards.

To further elucidate the evolution from regular to chaotic dynamics in graphene-based nanostructures we investigated the density distribution of eigenstates, i.e. the distribution of values  $\eta := |\psi(\mathbf{r})|$  and  $\eta^2$ . In the chaotic GOE limit, the former follows a Gaussian distribution

$$P(\eta) = \frac{2}{\pi} e^{-\frac{\eta^2}{\pi}}, \quad I(\eta) = \int_0^\eta P(\eta) d\eta = \text{erf} \frac{\eta}{\sqrt{\pi}}, \quad (4.11)$$



while the latter is described by the Porter-Thomas distribution [70]

$$P(\eta^2) = \frac{1}{\sqrt{2\pi\eta}} e^{-\frac{\eta}{2}}, \quad I(\eta^2) = \operatorname{erf} \sqrt{\frac{\eta}{2}}, \quad (4.12)$$

which has originally been suggested to describe the distribution of resonance widths (i.e. transition probabilities) in nuclear reactions. For graphene billiards, we find a (slow) convergence to the RMT predictions for both distributions (see Fig. 4.9), in line with the slow convergence of the NNSD to the GOE limit.

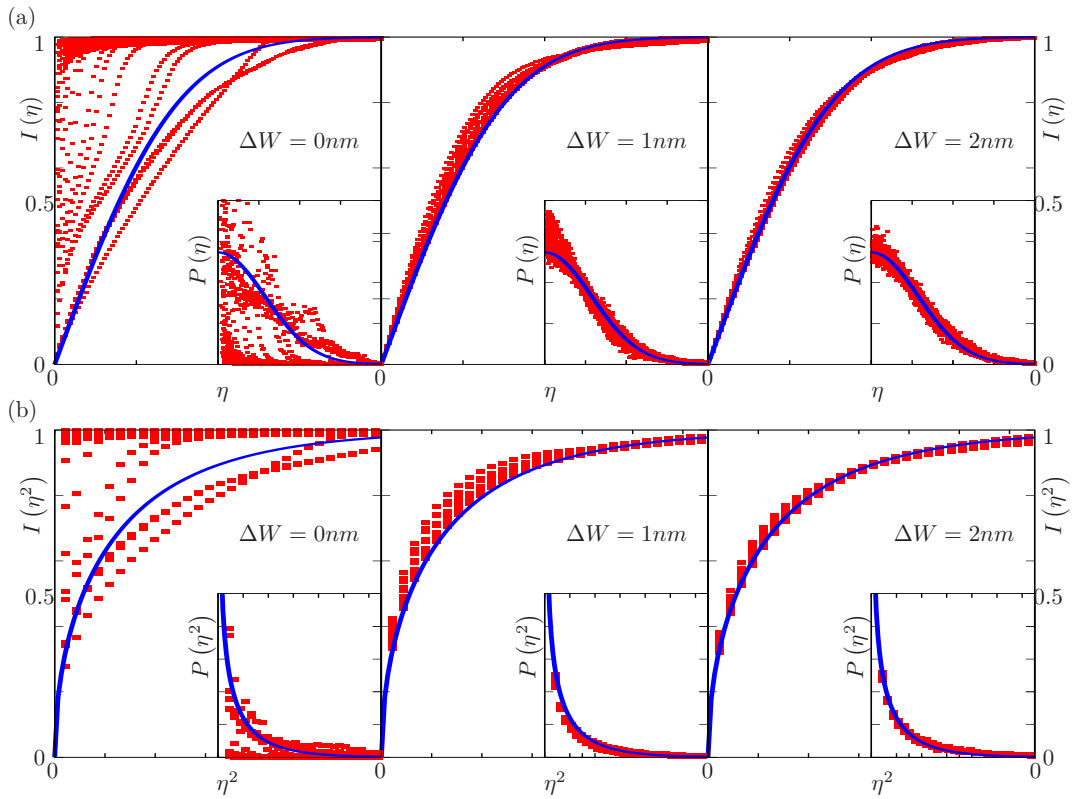


Figure 4.9: *Integrated distributions functions  $I(\eta) = \int_0^\eta P(\eta)d\eta$  of values  $\eta := |\psi(\mathbf{r})|$  (a) and  $\eta^2$  (b), for increasing values of edge disorder as given in the figures. An ensemble of function for 20 eigenstates is shown. The inset shows the corresponding non-integrated distributions. The blue solid line shows the RMT predictions for the GOE case (see text).*

The reason for the increased stability of graphene-based devices against chaotic dynamics is closely related to the electronic structure of graphene

at the  $K$  point [Fig. 4.1(b)]. In a classical rectangular ballistic billiard with only rectangular edges along the armchair or zig-zag direction an additional constant of motion, the magnitude of the linear momentum  $|\mathbf{k}|$ , exists. Such billiards are therefore classically regular irrespective of the number or size of the edges. By contrast Schrödinger billiards with wavenumbers near the  $\Gamma$  point cannot resolve the exactly rectangularly shaped edges due to the larger de Broglie wavelength and thus mimic chaotic dynamics. For the same size of the edges  $\Delta W$ , the graphene eigenstate features a much shorter wavelength due to the position of the Dirac cone near the  $K$  point in the Brillouin zone. The quantum dynamics of the graphene billiard is therefore closer to the classical limit and its level statistics closer to the Poisson limit of regular dynamics.

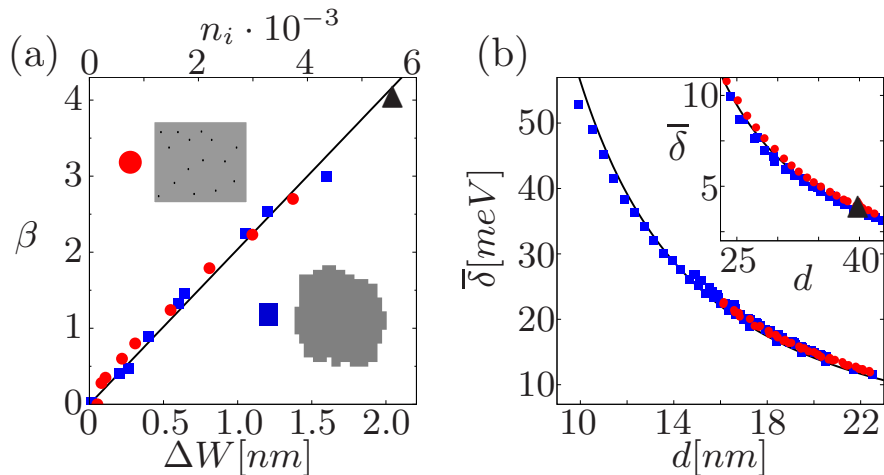


Figure 4.10: *Dependence of level statistics on the roughness and size of graphene quantum dots. (a) Dependence of the control parameter  $\beta$  for the transition from a Poisson to a Wigner-Dyson distribution (Eq. 4.10) on the edge roughness amplitude  $\Delta W$  or the defect density  $n_i$ . (b) Dependence of rescaled mean-level spacing  $\bar{\delta} = \langle \Delta E \cdot E/E_0 \rangle \text{meV}$ , where  $E_0$  was taken at  $100 \text{meV}$ , on the size of the quantum dot. Triangles represent experimental data, rescaled by  $E/E_0 = 25/100$  to take into account the energy dependence of the DOS [27].*

Of potential technological significance is the dependence of the nearest-neighbor spacing distribution on the disorder of a graphene billiard which might be used as a quantitative indicator. For all three classes of disorder we consider (edge roughness, short and long range disorder) we find a linear relation between the NNSD parameter  $\beta$  and the edge roughness amplitude,  $\beta \approx 2\Delta W$ , and between  $\beta$  and the defect density,  $\beta \approx 0.7n_i$  [Fig. 4.10(a)].

As  $\beta$  can be obtained with high precision from a fit to  $P(s)$ , the edge roughness or defect density can be deduced from the NNSD. We suggest that this dependence could be used to estimate the disorder in experimentally realized regularly shaped graphene quantum dots. Numerically, we find  $\beta \approx 4$  in a fit to data for recent experimental investigations of a 40nm graphene billiard [27], corresponding to an effective roughness  $\Delta W_e \approx 2$  nm, or an effective defect rate of  $n_i \approx 5.5 \cdot 10^{-3}$  (see black triangles in Fig. 4.10). As the second moment  $\sigma = \langle s^2 P(s) \rangle_\xi$  of the NNSD decreases with increasing disorder, one could alternatively obtain an estimate for the roughness of a flake from  $\sigma$ . We find however, that the dependence on  $\beta$  is numerically more reliable, as the entire distribution is used for a fit to  $P_H$ .

While the shape of the unfolded NNSD,  $P(s)$ , is sensitively dependent on disorder, it is to a good degree of approximation independent of the size of a graphene flake. By contrast, the absolute level spacing  $\langle \Delta E \rangle$  contains direct information on the size of quantum confinement. By rescaling each level spacing by the local energy, relative to a fixed energy  $E_0 = 100meV$ , one obtains the energy independent expectation value

$$\bar{\delta} = \left\langle \Delta E \cdot \frac{E}{E_0} \right\rangle = (\hbar v_F)^2 \frac{2}{d^2 E_0} = \frac{5500 \text{ nm}^2}{d^2} meV. \quad (4.13)$$

This rescaled mean level spacing is, indeed, independent of edge roughness and disorder [see Fig. 4.10(b)]. Note that in spite of the large contribution of Anderson localized states near the Fermi edge the mean level spacing accurately follows Eq. (4.13). To achieve agreement with Eq.(4.13) we have included in the ensemble the states up to 1eV away from the Fermi edge. The increased spacing of the more distant levels offsets the clustering of the localized levels near the Fermi edge. Agreement with the experimental data point [27] near  $d = 40$  nm is remarkably good. While one still “cannot hear the imperfect shape of a drum”, the size and roughness of graphene quantum dots can be, indeed, inferred from the spectral properties.

## 4.2.5 Magnetic fields

Using the Peierls substitution presented in section 2.1.6 we now include a magnetic field into our graphene flake eigenenergy calculations. The solution of the Dirac equation in a magnetic field  $B$  yields Landau levels at energies  $E_n^D$  which, in contrast to materials with parabolic dispersion relation, feature a square-root dependence on  $B$  [71], according to

$$E_n^D = \text{sgn}(n) \sqrt{2e\hbar v_F^2 |n| B}, \quad n \in \mathbb{Z}. \quad (4.14)$$

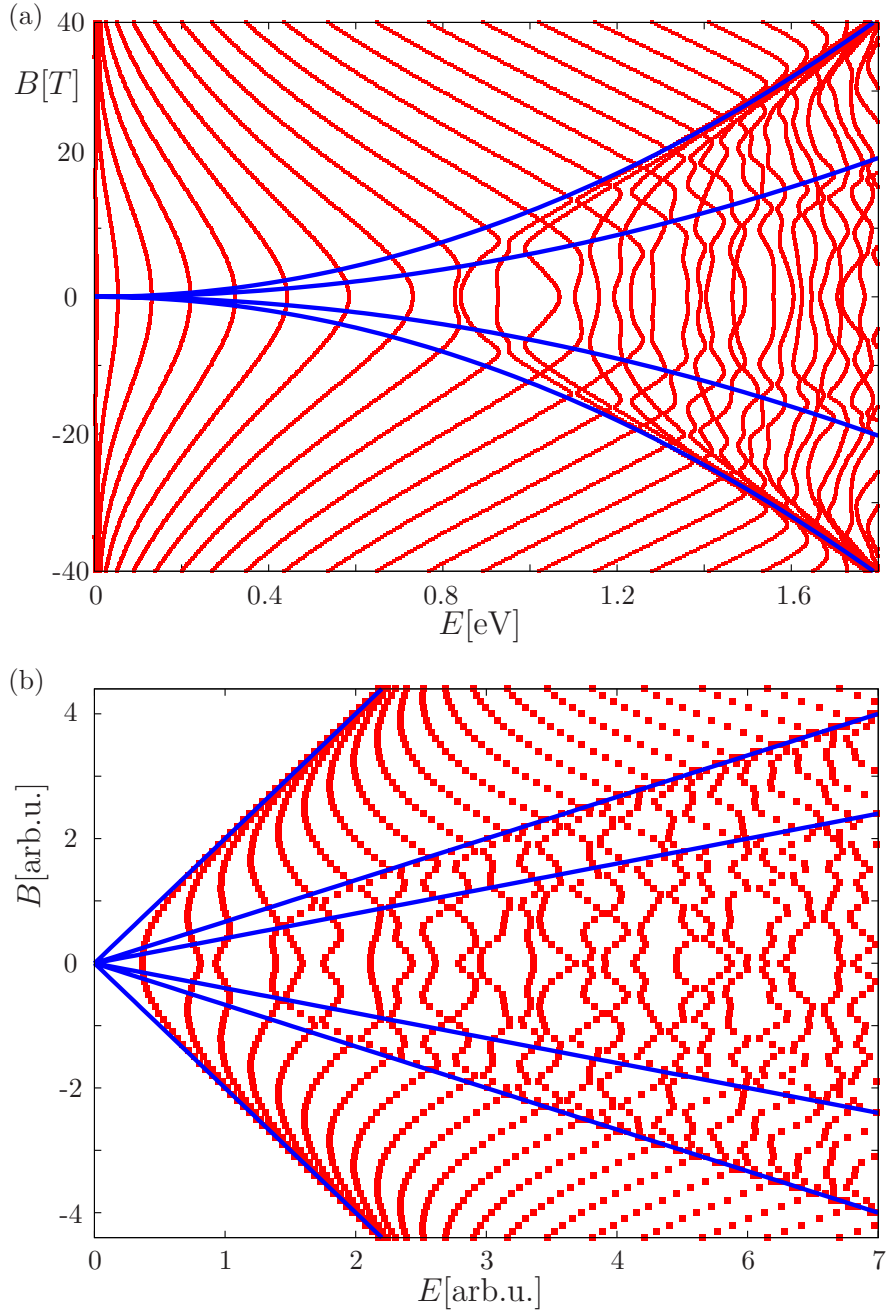


Figure 4.11: (a) Energy levels of a graphene-based quantum dot (diameter  $d = 40\text{nm}$ ) as a function of a perpendicular magnetic field. Blue lines mark the first and second Landau levels [see Eq. (4.14)]. (b) Energy levels of a Schrödinger quantum billiard of the same size as (a). Blue lines mark the first three Landau levels [see Eq. (4.21)].

In graphene-based quantum dots, we expect (4.14) to be a good approximation for states at the center of the dot. Close to the edge, edge roughness will lead to deviations from the Landau levels of a perfect Dirac equation. We have investigated the eigenstates of a graphene-based quantum dot with a diameter  $d = 45\text{nm}$  in a perpendicular magnetic field. We observe the formation of Landau levels with the expected square root dependency (4.14) [see Fig. 4.11(a)]. The first Landau level  $E_1^D$  separates regions of qualitatively different behavior: eigenenergies above  $E_1^D$  feature a complicated  $B$ -dependence as a result of many avoided crossings. In contrast, eigenenergies below  $E_1^D$  slowly converge (for increasing  $B$ ) towards  $E_0^D$  in parallel, well separated lines. We give an estimate for the number of states  $N$  in a Landau level: on average, the density of states in a graphene-based quantum dot features a linear dependence on  $E$ , according to (4.9). The number of states  $N$  in an energy interval symmetric around the Dirac point is thus

$$N(E) = \int_{-E}^{+E} \rho(\varepsilon) d\varepsilon = \frac{1}{2(\hbar v_F)^2} d^2 E^2. \quad (4.15)$$

By combining (4.14) and (4.15) we obtain the number of states  $N(E_1^D)$  in the energy interval  $[-E_1^D, E_1^D]$  around the Landau level at  $E_0^D$ ,

$$N_1(E_1^D) = \frac{2e}{h} (\pi d^2) B = 4 \frac{\Phi}{\Phi_0}, \quad (4.16)$$

where  $\Phi$  is the magnetic flux through the dot and  $\Phi_0$  is the magnetic flux quantum  $h/(2e)$ . For a dot diameter of  $d = 45\text{nm}$  we find  $N_1 \approx 3B$ . When counting the number of lines in Fig. 4.11(a) in the interval  $[-E_1^D, E_1^D]$  at different magnetic field strengths, we do not find that (4.16) is well-represented. The reason for this is the number of localized states near  $E_F = 0$  (as discussed in Sec. 4.2.3) that locally decreases the density of states. Nevertheless, (4.16) will enable us to give an estimate for the number of states in-between Landau levels, as outlined in the following paragraph.

For an infinite sheet of graphene, energy levels are described by (4.14) even for an arbitrary weak magnetic field. The question thus arises at which magnetic field strength an experimental formation of Landau levels will be observed in a quantum dot. To give an estimate, we consider the length scale of an individual Landau orbit, which is given by the magnetic length

$$l_c = \sqrt{\frac{\hbar c}{eB}} = 25.7\text{nm} \frac{1}{\sqrt{B}}, \quad (4.17)$$

where  $B$  is given in Tesla. We expect Landau level formation as soon as  $l_c$  is small compared to the dot radius: only states located at a distance of

at least  $l_c$  away from the edge of the flake can be expected to follow bulk Landau level statistics, uninfluenced by edge effects. We define an effective dot diameter

$$d_{\text{eff}} \approx d - l_c \quad (4.18)$$

which reflects the reduced dot area  $A_{\text{eff}}$  for which eigenenergies should be well described by bulk Landau levels.<sup>1</sup> We can then argue that only a fraction

$$\nu := A_{\text{eff}}/A, \quad A_{\text{eff}} = \frac{\pi}{4}(d_{\text{eff}})^2 \quad (4.19)$$

of eigenenergies should, at a given magnetic field strength, follow the  $B$ -field dependence of Landau levels (4.14). The remaining

$$N_\nu = N(1 - \nu) \quad (4.20)$$

states still “feel” the influence of the finite dot size, and feature eigenenergies  $\varepsilon$  in-between Landau levels. For a magnetic field strength of  $B = 10\text{T}$ , we obtain (for the  $d = 45\text{nm}$  dot we consider)  $\nu = 0.42$ , and thus  $N_\nu = 17.4$  states that have not yet reached the Landau level at  $E_0^D = 0$ . Half of these states should be located in the electron side of the spectrum. From the data shown in Fig. 4.11, we can simply count the number of states between 0 and  $E_1^D$  for a fixed magnetic field to check the validity of Eq. (4.20). Results are given in Tab. 4.1 for four different field strengths. In view of the simplicity of our argument, the agreement with numerical data is surprisingly good. Conversely, the number of energy levels in between Landau levels should give an estimate for the effective diameter  $d_{\text{eff}}$  of the dot. While (4.19) does not take into account bulk scattering (i.e. eigenenergies are assumed to follow Landau level quantization in the bulk of the flake), it still serves as an estimate for the amount of impurities and edge scattering in an experimental graphene flake. Moreover, (4.20) may be evaluated at different magnetic field strengths to obtain statistics. We note, however, that field strength of above about 7 Tesla will be needed to observe a sufficient convergence of eigenenergies towards Landau levels in experiment.

Note that our argument relies on comparison to the DOS at finite and zero magnetic field. For conventional Schrödinger based quantum dots, this is not readily possible, as forbidden energy regions (i.e. energy regions where the DOS = 0) are introduced by high magnetic fields. For illustration, we plot the energy levels of a conventional Schrödinger quantum dot featuring

---

<sup>1</sup>As we consider an approximately circular dot, we can use the simple relation (4.18). For more general dot shapes, the relation between  $d_{\text{eff}}$  and  $l_c$  becomes more complicated. Note that  $d_{\text{eff}}$  is bounded from below by the edge roughness of the dot.

$B[\text{T}]$	$\frac{1}{2}N_\nu$ [Eq. (4.20)]	$\frac{1}{2}N_\nu$ [Fig. 4.11]
10	8.6	9
20	13	13
30	16.4	15
40	19.2	19

Table 4.1: *Number of eigenstates in between Landau levels for four distinct magnetic field values based on either Eq. (4.20), or counting of states in Fig. 4.11.*

parabolic dispersion [see Fig. 4.11(b)]. The corresponding Landau levels  $E_n^S$  feature a linear dependence on energy,

$$E_n^S = \hbar \frac{eB}{m} \left( n + \frac{1}{2} \right), \quad n \in \mathbb{N}. \quad (4.21)$$

As a consequence, there are no allowed states for energies below  $E_1^S$ , while there is no such forbidden energy region in graphene (due to the existence of  $E_0^D$ ). For low field strength, however, the patterns created by avoided crossings look remarkably similar for Schrödinger and Dirac based systems.

### 4.3 Transport through graphene nanoribbons

Following the discussion of eigenstates in finite-sized graphene-based quantum dots, we now proceed to the scattering problem through graphene-based devices. The powerful numerical method presented in the first part of this thesis allows for an investigation of realistically-sized graphene-based scattering structures. In particular, we are interested in the influence of the hexagonal graphene lattice on the conductance through graphene nanoribbons. We introduce different lattice distortions that act differently on  $A$  and  $B$  lattice sites and thus break pseudo-spin conservation. As a consequence, backscattering occurs (as pseudo-spin-based arguments why backscattering is suppressed in graphene no longer apply, see section 4.1.2). To obtain a quantitative estimate of the backscattering caused by different lattice defects, we investigate the Fourier transform of the scattering states. We find pronounced peaks near the  $K$  and  $K'$  points of the reciprocal lattice, that give quantitative evidence of the amount of  $K - K'$  scattering.

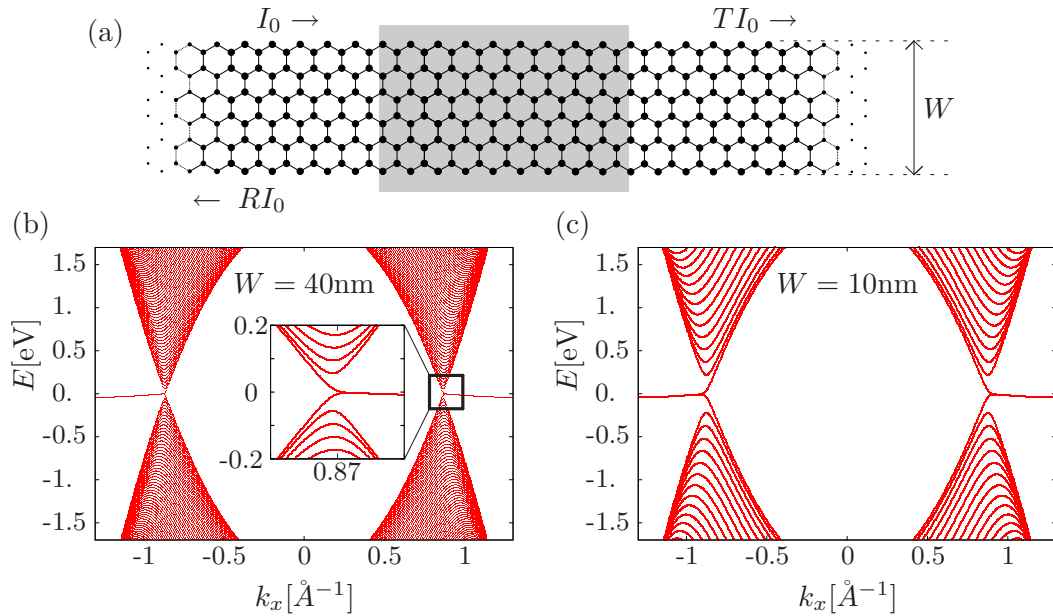


Figure 4.12: (a) Schematic drawing of a zigzag graphene nanoribbon with finite width  $W$ . We introduce lattice defects or edge roughness inside the grey scattering area. Dispersion relations are shown for  $W = 40$  (b) and  $W = 10$  (c).



### 4.3.1 Scattering problem

Since the first experimental discovery of graphene nanodevices four years ago [12] transport measurements on graphene nanodevices have been performed in many groups (see e.g. [10, 12, 46, 59] to name a few). The energy of current-carrying electrons in graphene is controlled experimentally by applying a back-gate voltage  $V_{BG}$ , that changes the number of charge carriers in the graphene flake by

$$N = \eta V_{BG}, \quad (4.22)$$

where  $\eta \approx 7.2 \cdot 10^{14} V^{-1} m^2$  is an approximation for the capacity of the graphene flake [72]. Unfortunately, this estimate depends not only on device characteristics, but also on the applied back gate voltage. Experimentally,  $\eta$  can be determined with high accuracy for a given device from the lever-arm of Coulomb diamonds [10, 51]. The number of states  $N$  in (4.22) can also be related to the density of states: the Fermi sphere will be filled, at thermal equilibrium, to the energy necessary to accommodate all  $N$  states. Due to the linear dispersion of graphene, the number of states  $N$  is proportional to  $E^2$ ,

$$N = \frac{1}{\pi(\hbar v_F)^2} E^2 \quad (4.23)$$

from which follows a square-root relation between the back gate voltage, and the energy at the Fermi edge

$$E = \hbar v_F \sqrt{\eta V_{BG} \pi}. \quad (4.24)$$

In the following, we will use (4.24) to present the transmission as a function of back-gate voltage instead of the particle energy.

We consider scattering through an infinitely long nanoribbon of width  $W$  (i.e. we do not model the contact region). The edge of the ribbon is cut along a zigzag line of the hexagonal lattice [see Fig. 4.12(a)]. In a finite region of length  $L$ , we introduce edge roughness or defects into the ribbon [see shaded area Fig. 4.12(a)] and calculate the resulting transmission  $T$  and reflection  $R$ .

Due to the finite width of the nanoribbon, the transverse component of the wavevector becomes quantized. As a consequence, the cone-like dispersion relation of graphene is reduced to a discrete set of curves [see Fig. 4.12(b)]. The distance in energy between adjacent curves is proportional to  $W^{-1}$ , i.e. discrete modes (and thus quantization steps) are more widely spaced for narrow ribbons [compare (b) and (c) in Fig. 4.12]. As a result, the conductance  $G$  of an ideal graphene nanowire features quantization steps with the height of two conductance quanta,  $2e^2/h$  (neglecting spin), due to the two contributions of the  $K$  and  $K'$  cone. As will be shown, the quantization plateaus in

the conductance of graphene nanoribbons are very sensitive to disorder. As a consequence, the experimental demonstration of size quantization peaks in graphene remains elusive, although recent publications claim to have found equally-spaced plateau signatures in transport measurements they attribute to quantization steps [49].

### 4.3.2 Edge roughness

In section (4.1.2), we have discussed one of the consequences of the graphene pseudo-spin  $s_p$  on scattering processes in graphene: due to destructive interference between an incoming and a retro-reflected wave, backscattering is strongly suppressed. This argument, however, heavily relies on the conservation of  $s_p$ , which is a good quantum number only for an infinite, perfect sheet of graphene. Once the symmetry between  $A$  and  $B$  sub-lattices is broken,  $s_p$  is no longer conserved, and arguments based on pseudo-spin conservation may fail.

As outlined in section 4.2.1, edge effects play an important role in graphene nanodevices. To investigate the influence of edge scattering on the transport properties of graphene, we use the model for edge-roughness we developed in the context of graphene quantum billiards. We consider sample ribbons of about 40nm width, corresponding to roughly 400 carbon atoms in transverse direction. Five different ribbon widths in the range  $40 \pm 0.5$ nm are employed to simulate rough edges [see Fig. 4.13(a)]. A graphene nanoribbon is then assembled out of a random sequence of 35 rectangular modules [see Fig. 4.13(b)]. The length of each rectangular module is chosen at random in the range of 0.24 to 10nm. Finally, all modules are connected to two ideal half-infinite graphene waveguides. We average over 100 realizations  $\xi$  of nanoribbons to eliminate non-generic features of particular ribbon configurations.

In such rough-edged ribbons we find conductance to be much lower at energies away from the Dirac point compared to a smooth-edged ribbon of equal width [see Fig. 4.13(c)]. Conductance drops symmetrically around  $E = 0$ , i.e. electron-hole symmetry is conserved. The quantization steps due to the transverse confinement are strongly suppressed. Indeed, there seems to be a pronounced dip in transmission instead of a step (see arrows in Fig. 4.13). This counterintuitive *reduction* of transmission with *increasing* energy has also been found by other numerical descriptions of transport through graphene nanoribbons [5]. Considering the dynamics of the free Dirac equation, the pronounced effect of the edges seems, at first glance, surprising. However, due to the abrupt termination of the lattice at the edge the pseudo-spin becomes ill-defined upon reflection at the edges. As a consequence, we ex-

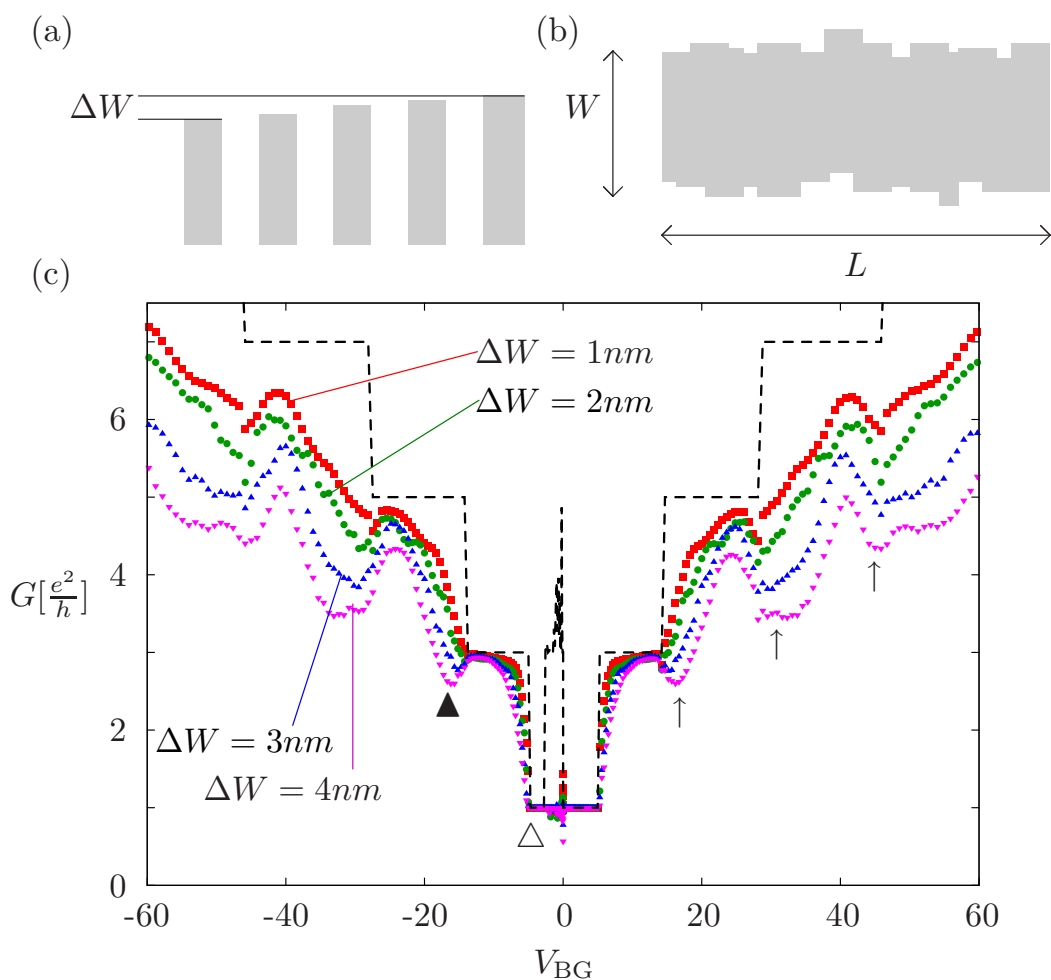


Figure 4.13: (a) Five building blocks of different height in a range  $W \pm \Delta W$  were used to (b) assemble a rough-edged graphene nanoribbon. (c) Ensemble-averaged conductance of 40nm wide graphene ribbons with different degree of edge roughness  $\Delta W$ , as shown in the inset. Conductance of a smooth ribbon is shown as dashed black line. Arrows ( $\uparrow$ ) mark dips in the conductance (see text). A Solid [open] triangle marks the energy of the scattering state shown in Fig. 4.14 (a) [(b)].

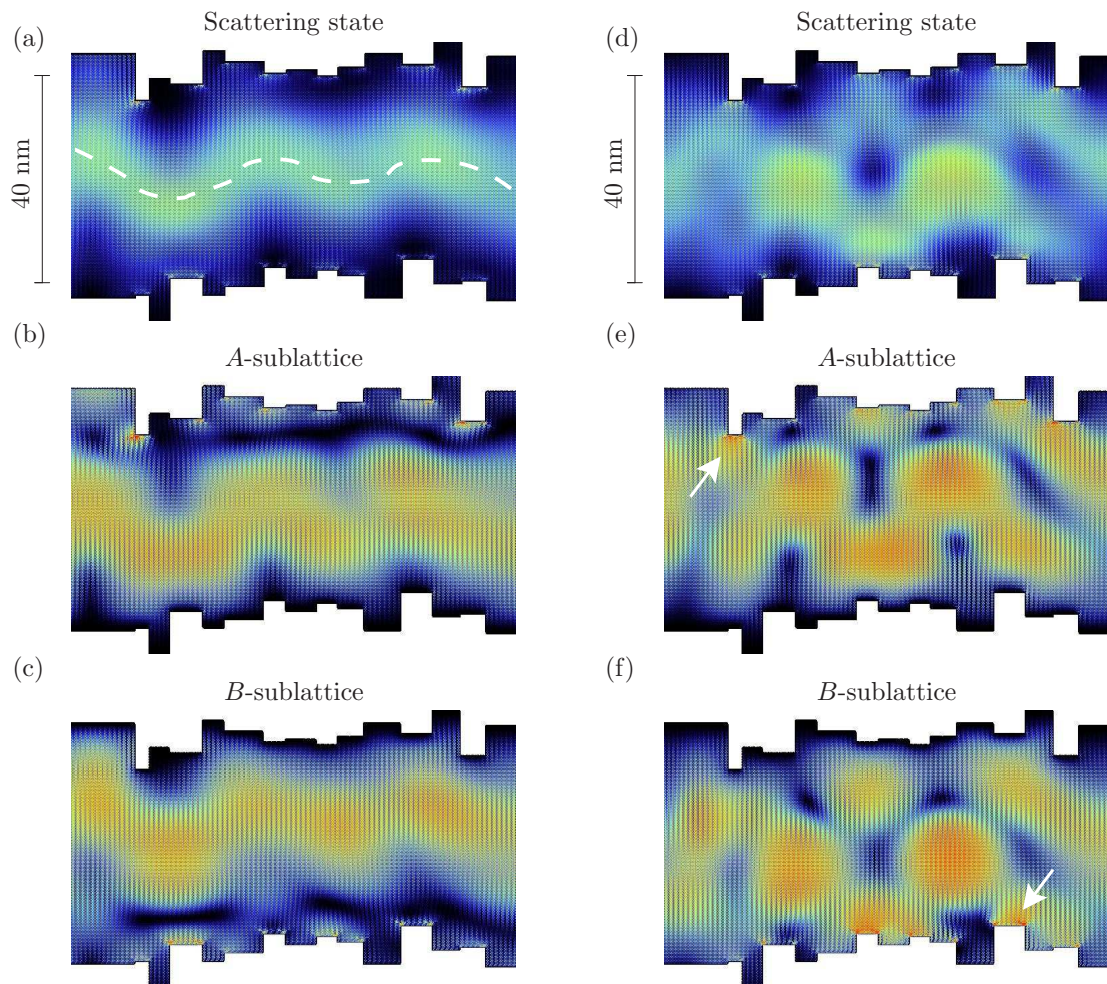


Figure 4.14: (a) “Snake-like” scattering state of a rough-edged graphene nanoribbon [see open triangle in Fig. 4.13(c)]. A dashed white line has been inserted as guide to the eye (see text). (b) A sublattice [(c) B sublattice] of the scattering state shown in (a). (d,e,f) Same as (a,b,c) at different energy [see solid triangle in Fig. 4.13(c)]. White arrows mark deviations between the A and B sublattices (see text).

pect pseudo-spin conservation to break down as soon as edge roughness is introduced.

To further elucidate the role of the pseudo-spin in realistic, edge-disordered graphene nanoribbons, we consider individual scattering states of the disordered nanoribbon. States with energy close to the Dirac point [an energy region where conductance is only weakly affected by edge disorder, see open triangle in Fig. 4.13(c)] feature comparatively low amplitude at the edges [see Fig. 4.14(a)]. However, if we plot the wave functions on the  $A$  and  $B$  sub-lattice separately, we find unexpected differences between the scattering wave functions on the  $A$  and  $B$  sub-lattice, clearly marking the breakdown of the pseudo-spin solutions presented in Eq. (4.6) [see Fig. 4.14(b,c)]. We find an enhancement of the  $A$  ( $B$ ) sub-lattice scattering wave function at the upper (lower) edges of the ribbon, i.e. at those edges where the outmost carbon atom is of type  $A$  ( $B$ ) [see Fig. 4.14(b,c)]. Near the center of the ribbon, the scattering state features a uniform “snake-like” pattern that seems unaffected by edge disorder [see white dashed line in Fig. 4.14(a)]. These states correspond to the perfectly conducting channel described by Wakabayashi et al. [73]. For scattering states at energies where the transmission is reduced by edge disorder [see solid triangle in Fig. 4.13] interaction with the rough edge structure is more pronounced [compare Fig. 4.14(a,d)], resulting in strong differences between the  $A$  and  $B$  sub-lattices. We find strong localization of the wave function near corners of the edges that are only visible in one sub-lattice [see white arrows in Fig. 4.14(e,f)]. We therefore attribute the dramatic drop in conductance to pronounced backscattering at the corners, where the AB symmetry is broken: simple arguments for the reduction of backscattering in graphene based on the conservation of pseudo-spin fail at the edges of the lattice.

To better understand the interference pattern visible in the scattering states [see e.g. Fig.4.14(d)], we integrate out the  $y$  component of the scattering wave function,

$$|\bar{\psi}(x)|^2 = \frac{1}{W} \int_0^W |\psi(\mathbf{x})|^2 dy. \quad (4.25)$$

We find oscillating patterns with two distinct length scales [see Fig. 4.15(a)]: (i) the short beating period of  $\lambda = 0.7nm$ , as discussed in section 4.2.3 [responsible for the “fuzziness” of the oscillation pattern in Fig. 4.15] corresponding to the distance (in  $k$  space) between the  $\Gamma$  and  $K$  points and (ii) a much slower variation with a length scale  $\Lambda \approx 30nm$  [see  $\Lambda$  in Fig. 4.15], which corresponds to the wavelength associated with the linear dispersion relation  $E = v_F \hbar k$ , i.e. from the  $K$  point to a particular point on the Dirac cone associated with the scattering state. These two length scales differ by

two orders of magnitude.

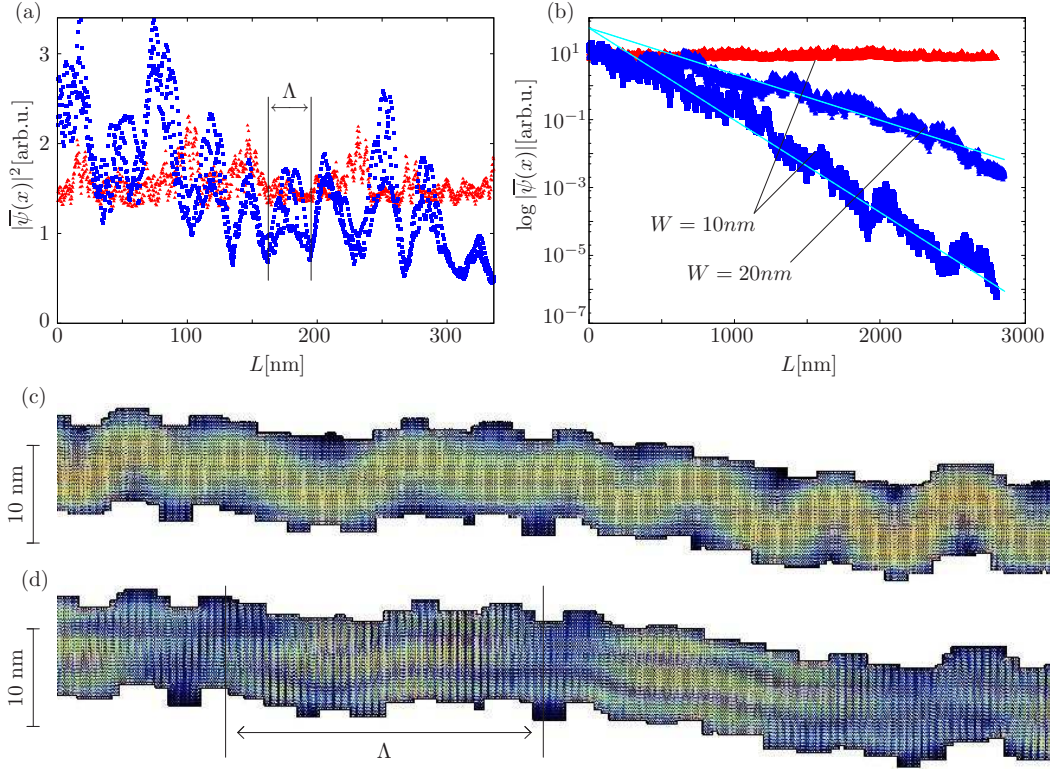


Figure 4.15: (a) Probability distribution  $|\overline{\psi}(x)|^2$  of two scattering states in a 10nm wide nanoribbon with edge roughness  $\Delta W = 0.8\text{nm}$ . (b) Logarithmic plot for the two states shown in (a) and a scattering state of a 20nm wide ribbon (see inset) for ribbon length  $L$  up to  $3\mu\text{m}$ . (c) Part of the non-localized [(d): localized] eigenstate shown in (a). The oscillation period  $\Lambda$  is marked in (d).

As shown by Anderson in 1958, random disorder leads to exponential localization of scattering states [74]. In the case of the graphene nanoribbons discussed above, edge roughness, in particular sharp corners where the A-B lattice symmetry is broken, plays the role of disorder, thus leading to Anderson localization in edge-disordered graphene nanoribbons [56]. For ribbon lengths  $L = 3\mu\text{m}$ , we find a near-perfect exponential decay of the scattering wave function over 8 orders of magnitude [see Fig. 4.15(b)]. We fit a localization length

$$|\overline{\psi}(x)|^2 \approx e^{-l/l_A}, \quad l_A \approx 160\text{nm}. \quad (4.26)$$

For broader ribbons [see, e.g.,  $W = 20\text{nm}$  in Fig. 4.15(b)], we find longer localization lengths scaling with  $\delta W/W$ , i.e.,  $l_A \approx 320\text{nm}$  for  $W = 20\text{nm}$  [see lines in Fig. 4.15(b)]. Superimposed on the exponential decay (4.26) are oscillations on the scale of  $\Lambda$  that result in large-scale fluctuating patterns in the scattering wave function [see Fig. 4.15(d)]. In contrast, the snake-like perfect-conducting channel features no localization effect even on a length scale of  $3\mu\text{m}$ . The wave function patterns look uniform over the entire extension of the nanoribbon [see Fig. 4.15(c)].

### 4.3.3 Fourier transform

In contrast to  $AB$  scattering (that changes pseudo-spin)  $K$ - $K'$  scattering does not depend on the pseudo-spin. To disentangle these two types of scattering present in graphene, we consider the Fourier transform of a Bloch state

$$\psi_n(x, y) = e^{ik_{xn}x} \chi_n(y) \quad (4.27)$$

in the left half-infinite waveguide incident on the disordered part of the nanoribbon [i.e. the shaded region in Fig. 4.12(a)].  $\chi_n(y)$  represents the transverse eigenfunctions of mode  $n$  propagating in  $x$ -direction with wavenumber  $k_{xn}$  (see discussion in section 3.1). The Fourier transform of (4.27) is given by

$$\tilde{\psi}_n(\mathbf{k}) = \mathcal{F}[\psi_n(\mathbf{r})] = \frac{1}{\sqrt{2\pi}} \int_A d\mathbf{r} \psi_n(\mathbf{r}) e^{-i\mathbf{k}\cdot\mathbf{r}}, \quad (4.28)$$

[see Fig. 4.16(a)], where the integral goes over a finite area  $A$  in the asymptotic region of the waveguide, i.e. far away from the scattering device. For a hexagonal lattice, the real and the reciprocal lattice are rotated by 90 degrees with respect to each other [23]. The first Brillouin zone for the zigzag ribbons we consider is thus given by a hexagon resting on a side rather than a tip [see white hexagon in Fig. 4.16(a)]. Due to the finite size of  $A$ , the Fourier transform features a grid of horizontal and vertical lines. In contrast, the Fourier transform of a plane wave in an infinite sheet of graphene would feature non-vanishing amplitudes only near the  $K$  and  $K'$  points of the reciprocal lattice. For the Bloch state (4.27), we find vertical lines only through the  $K'$  points [see Fig. 4.16(a)]. There is no discernible fine structure near the  $K'$  point [see inset in Fig. 4.16(a)], since the incoming state (4.27) only consists of a single mode. To better visualize the amount of  $K$  and  $K'$  contributions to  $\tilde{\psi}(\mathbf{k})$ , we integrate over the  $k_y$  coordinate

$$|\overline{\tilde{\psi}(k_x)}|^2 = \frac{1}{N} \int dk_y |\tilde{\psi}(\mathbf{k})|^2. \quad (4.29)$$

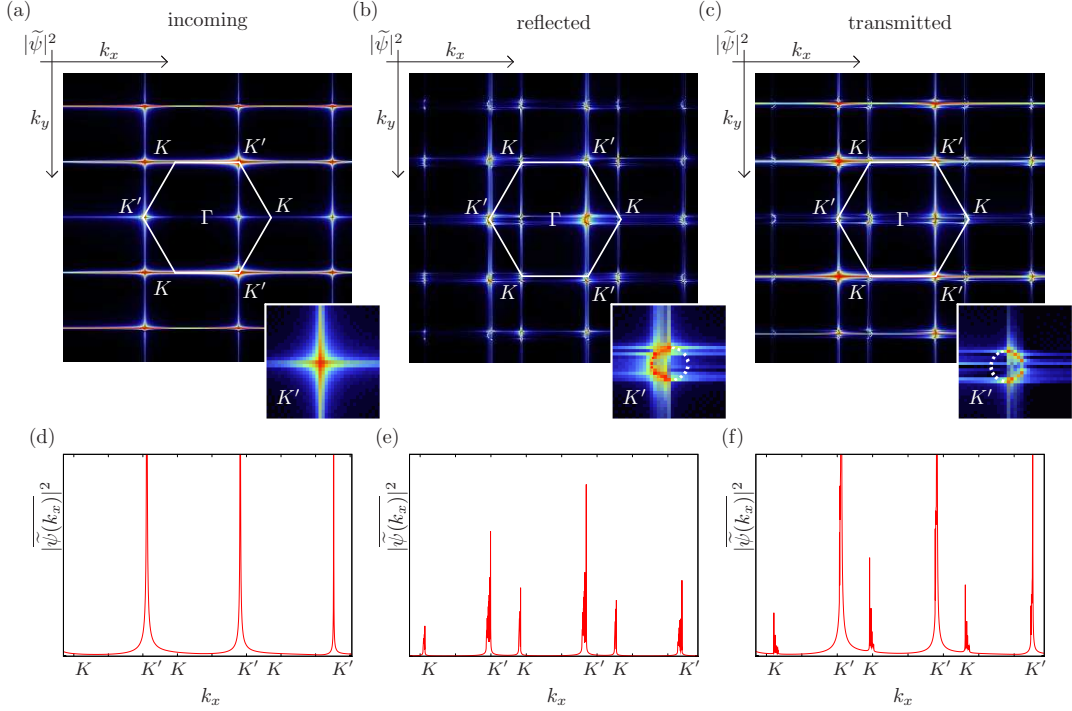


Figure 4.16: *Two-dimensional Fourier transform  $|\tilde{\psi}(\mathbf{k})|^2$ , and projection  $|\tilde{\psi}(k_x)|^2$  (see Eq. 4.29) of the incoming (a,d), reflected (b,e) and transmitted (c,f) part of the scattering state in the waveguides. The inset shows an enlarged view of the  $K'$  point [a white dotted half-circle is inserted as guide to the eye in (b), (c), see text]. The first Brillouin zone of the reciprocal lattice is shown as white hexagon.*

For the Bloch state (4.27) the projected Fourier transform (4.29) features peaks at the  $k_x$  values corresponding to  $K'$  [see Fig. 4.16(d)]. If we choose different mode numbers  $n$  in (4.27), we find modes featuring non-vanishing amplitude only at either  $K$  or  $K'$  lines. This shows that the individual modes in a graphene nanoribbon correspond, indeed, to either  $K$  and  $K'$  contributions, i.e. no  $K$ - $K'$  mixing is introduced in the mode basis.

Let us now consider the scattering of the incoming Bloch state (4.27) in the disordered part of the graphene nanoribbon. The scattering off the disordered edges is described by reflection ( $r_{mn}$ ) and transmission ( $t_{mn}$ ) matrices of the nanoribbon. The Fourier transform of the reflected and transmitted part of (4.27) is thus given by

$$\tilde{\psi}_n^T(\mathbf{k}) = \sum_m \mathcal{F}[t_{mn} \cdot \psi_m(\mathbf{r})], \quad \tilde{\psi}_n^R(\mathbf{k}) = \sum_m \mathcal{F}[r_{mn} \cdot \psi_m(\mathbf{r})] \quad (4.30)$$

far away from the scattering device [see Fig. 4.16(b,c)]. Depending on the



amount of  $K$ - $K'$  scattering inside the cavity, both reflected and transmitted Fourier transforms feature non-vanishing amplitudes at both  $K$  and  $K'$  lines [see Fig. 4.16(e,f)]. The relative strength of the  $K$  and  $K'$  lines is directly correlated to the amount of  $K$ - $K'$  scattering. Furthermore, there is an additional fine structure near the  $K'$  and  $K$  points: a half-circle forms around the Dirac points [see inset in Fig. 4.16(b,c)]. The surface of section of the double-cone bandstructure with a plane of constant energy is a circle, the diameter of which is given by the energy. In the reflected (transmitted) part of the wave function, we only see the left half (right half) part of this circle, corresponding to negative (positive) group velocities [the other half-circle corresponds to opposite momentum, compare dashed white circles in the inset of Fig. 4.16(b) and (c)]. The reason why the circular fine-structure does not appear in the Fourier transform of the incoming Bloch state lies in the number of modes available to build up the Fourier transform: for the incoming wave, only a single mode  $n$  contributes. As a consequence, there is only a single  $k_{xn}$  component in the Fourier transform. In contrast, the scattered wave consists of many mode contributions  $\sum_m t_{mn}\psi_m$ . The reason for the spreading of the reflected and transmitted wave function onto the complete half-circle lies in the pronounced  $AB$  scattering at the rough edges, that breaks pseudo-spin conservation, and thus distributes the reflected wave along the entire accessible half-circle of the bandstructure. The Fourier transform thus allows us to assess the amount of both  $K$ - $K'$  scattering (by the relative amplitude around the  $K$  and  $K'$  points in the reciprocal lattice) and  $AB$  scattering (by the spreading around one distinct  $K$  point).

#### 4.3.4 Lattice vacancies

Up to now, we have only considered edge disorder in the transport properties of graphene. As discussed in the previous subsection, scattering at rough edges breaks the  $AB$  symmetry and leads to pronounced  $K$ - $K'$  scattering at the edges. At energies close to the Dirac point, we have identified snake-like states that are completely unaffected by edge disorder. Comparison with experimental data on the transmission through graphene nanostructures (see e.g. [27]) shows, however, a much lower conductance than our model, in particular near the Dirac point. This discrepancy can only partly be attributed to the neglected electron-electron interaction: While we do not expect agreement in the Coulomb-blockade regime, we do expect qualitative agreement away from the Dirac point. The obvious culprit lies in the assumption of a perfect graphene lattice in the bulk of the structure. Before combining both edge and bulk disorder in the same device, we will now investigate different types of lattice defects. To disentangle the effect of edge and bulk disorder

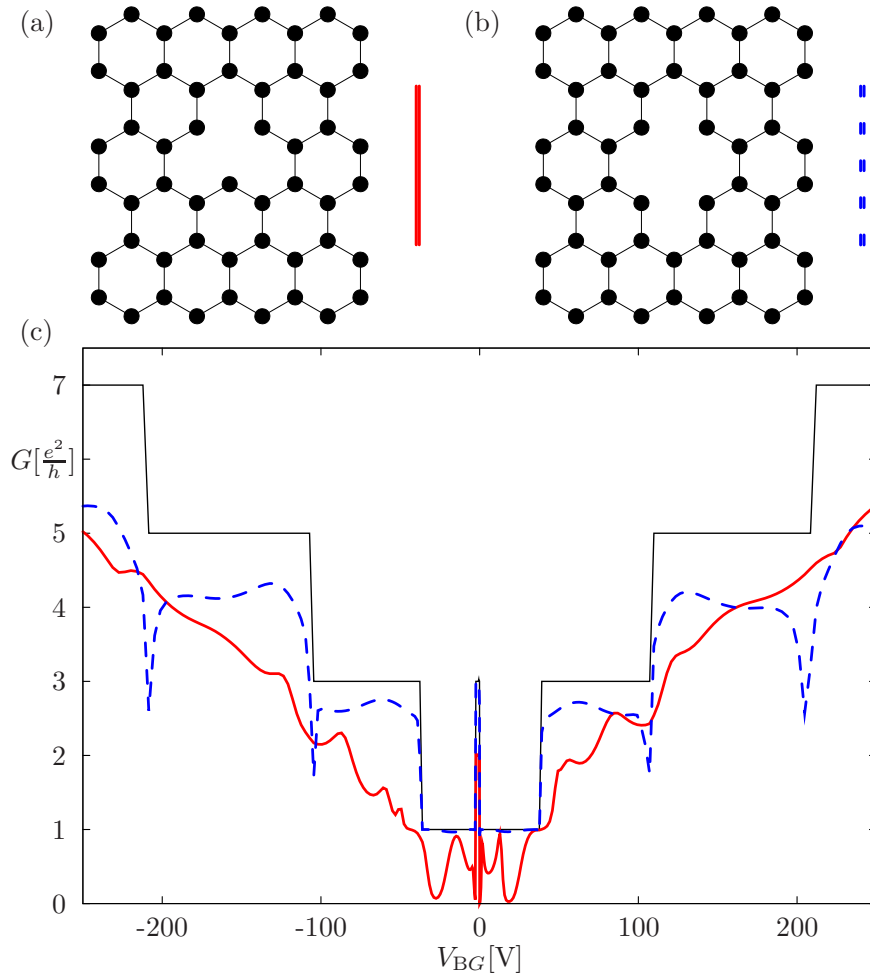


Figure 4.17: *Lattice vacancy defects in graphene: (a) A single-atom vacancy breaks AB-symmetry in graphene. (b) In the case of a two-atom vacancy AB-symmetry is restored by removing both atoms of a unit cell. (c) Conductance of a 20nm wide graphene nanoribbon with ten single-atom vacancies [solid red line, see (a)] or ten two-atom vacancies [dashed blue line, see (b)] in an area of 200 nm<sup>2</sup>.*

we will assume perfect zigzag edges for the time being.

As a simple model for lattice defects, we consider a single lattice vacancy, i.e. one carbon atom is removed from the graphene lattice [see Fig. 4.17(a)]. We consider an ensemble average over many configurations of randomly removed carbon atoms parameterized by an defect density of  $n_i = 10^{-3}$  defects per carbon (see discussion in section 4.2.1). We find that conductance is strongly suppressed even by a low concentration of impurity scatterers [see solid red line in Fig. 4.17(c)]. In particular, transmission around the Dirac point is strongly reduced by bulk disorder, in contrast to edge disorder [compare Fig. 4.13]. Furthermore, we note that size quantization steps are completely washed out by impurity scattering, i.e. the transmission becomes almost linear as function of back gate  $V_{BG}$  [see solid red line in Fig. 4.17(c)]. To elucidate the role of  $AB$  scattering for bulk disorder, we consider a double vacancy, i.e. we remove both atoms of a unit cell [see Fig. 4.17(b)]. In contrast to a single vacancy, this defect does not break  $AB$  symmetry. We now compare the impact of a set of configurations of single vacancies to the exact same configurations of double vacancies. We find the surprising result that double vacancies reduce the transmission far less than the single vacancy defects, even though the number of missing carbon atoms is actually doubled for the double-vacancy defect [see dashed blue line in Fig. 4.17(c)]. Furthermore, size quantization steps appear prominently for the double vacancy defect. We thus attribute the strong suppression of size quantization plateaus in graphene to the breaking of  $AB$ -symmetry. This becomes clear if one connects the pseudo-spin  $s_p$  with the transverse quantum number  $n$ : In the solution for the free Dirac equation (4.5),  $s_p$  is connected to the angle of wave propagation. Accordingly, the ratio between  $k_x$  and  $k_y$  is determined by the pseudo-spin. Through the introduction of defects that break pseudo-spin conservation, the transverse quantum number  $n$  becomes ill defined, resulting in the strong suppression of transverse quantization steps. Conversely, the absence of size-quantization plateaus in experiment hints at broken  $AB$ -symmetry for experimental structures. As rough edges break pseudo-spin conservation as well, the experimental demonstration of size quantization steps in graphene seems challenging as long as no novel techniques to reduce edge scattering are found.

Further evidence for the connection of transverse quantum number and pseudo-spin can be gathered by comparing the scattering states of graphene nanoribbons with either single or double vacancies. For single vacancies, the transmitted wave function does not feature a discernible  $x$ -dependence [see Fig. 4.18(a)], meaning that the transmitted wave function features a superposition of many transverse modes. In contrast, the transmitted scattering state in a nanoribbon with double-vacancies features clear oscillating

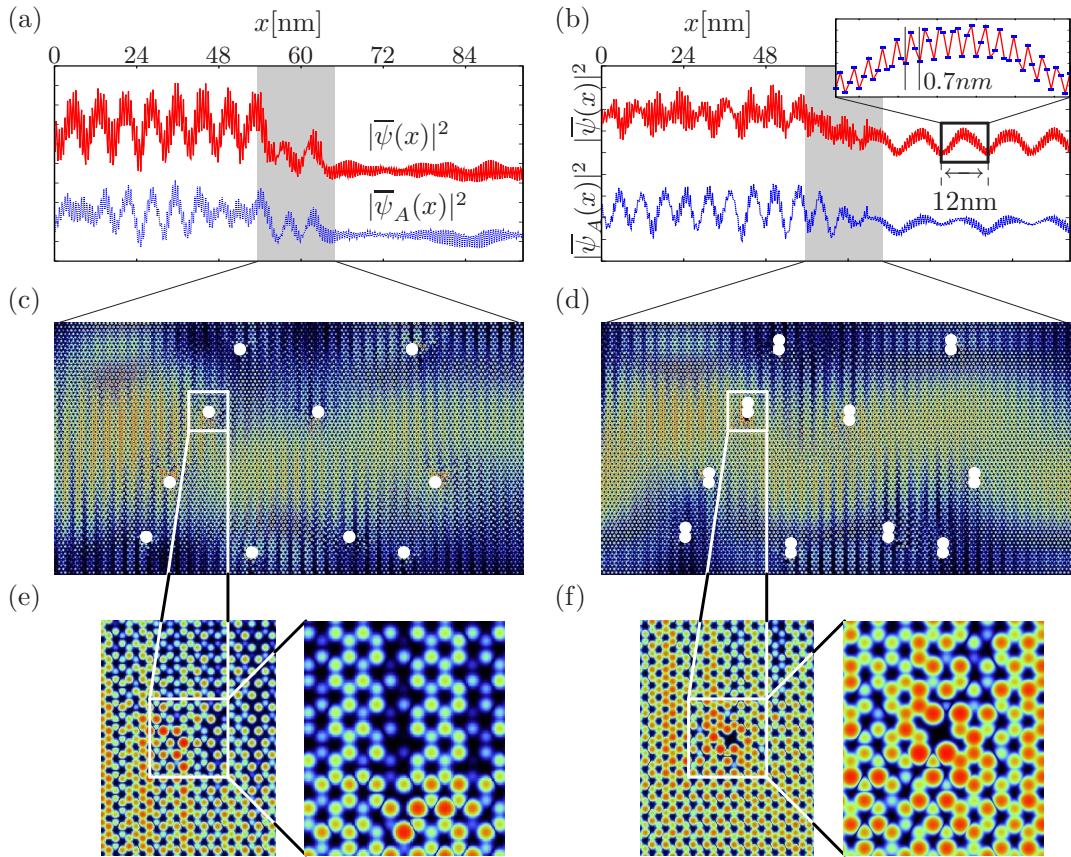


Figure 4.18: Projected total wave function density  $|\overline{\psi}(x)|^2$  [see Eq. (4.25)] and density  $|\overline{\psi}_A(x)|^2$  of sub-lattice A for the scattering through a 10nm wide graphene nanoribbon featuring ten (a) single vacancy [(b) double vacancy] impurities. The scattering wave function in the disordered region is given in (c,d). Defect positions are marked by white circles (not to scale). A white rectangle marks the area shown enlarged in (e) for a single and (f) for a double vacancy.

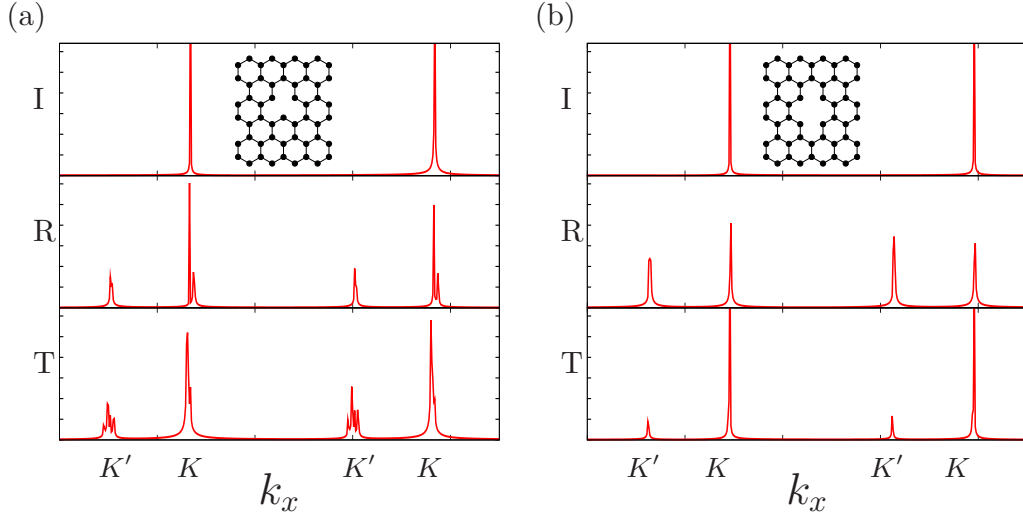


Figure 4.19: *The Fourier transform of the Incoming (labeled I), reflected (labeled R) and transmitted (labeled T) part of the scattering wave function shown in Fig. 4.18 for (a) single vacancies and (b) double vacancies.*

patterns with a wavelength  $\Lambda \approx 12nm$  [see Fig. 4.18(b)], and the familiar beating pattern on the much smaller length scale  $\lambda = 0.7nm$  (see Sec. 4.2.3). The wave-function pattern looks, at first glance, much “smoother” in the case of double vacancies [compare Fig. 4.18(c,d)]. This is even more apparent in a close-up of the wave function around a single defect: For single vacancies, defects “disrupt” the wave function patterns, leading to qualitatively different interference patterns on different sides of a defect [see Fig. 4.18(e)], while for double vacancies, the wave functions seem to “float” around the defect, without being much disturbed [see Fig. 4.18(f)].

To investigate the amount of scattering introduced by the different type of lattice vacancies on a quantitative level, we again calculate the Fourier transform for incoming, reflected and transmitted asymptotic scattering states [see Eq. 4.28]. As expected, we find pronounced  $AB$  scattering (i.e. broad peaks in the transmitted and reflected Fourier transform) in the case of single vacancies [see Fig. 4.19(a)]. In contrast, the Fourier transform for the double-vacancy nanoribbon features narrow peaks (conserved pseudo-spin), but pronounced amplitudes at  $K$  and  $K'$  lines (strong  $K$ - $K'$  scattering) [see Fig. 4.19(b)].

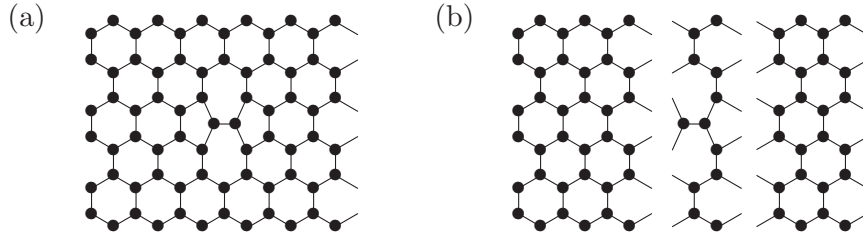


Figure 4.20: (a) *Stone-Wales defect: four Hexagons are replaced by two pentagons and two heptagons, thus breaking the  $AB$  symmetry of the graphene lattice.* (b) *Inclusion of a Stone-Wales defect into a graphene nanoribbon by adding one deformed block into an otherwise perfect nanoribbon.*

### 4.3.5 Stone-Wales defects

To ensure that our results do not depend on a particular choice of defect type, we treat the Stone-Wales deformation (SWD): Four hexagons are replaced by two heptagon-pentagon pairs [see Fig.4.20(a)]. As a consequence, the symmetry of the lattice is broken, and  $AB$ -scattering occurs. To model a SWD in our tight-binding approach, we introduce a single stripe of rearranged carbon atoms, that can be sandwiched between two ideal rectangular modules [see Fig.4.20(b)]. In first order approximation, we adapt the tight-binding parameters of the graphene ribbon to model the coupling parameters at the SWD. We neglect the (local) curvature of the graphene sheet induced by the presence of heptagon and pentagon rings [75].

Qualitatively we find the same effect as for the single-vacancy defect: The size quantization plateaus are washed out by as few as 5 SWD in  $10^6$  atoms [see Fig. 4.21(a)]. We furthermore find strong enhancement of the wave function at the point of the defect [see Fig. 4.21(b)], resulting in pronounced backscattering. Note that rough edges, lattice vacancies and the Stone-Wales defect all lead to the same qualitative results: strong  $AB$  scattering at short-range impurities that break the sublattice symmetry, leading to pronounced backscattering and a suppression of size quantization steps. We therefore conclude that these results do not depend on our particular choice of defects, but represent a more general result for short-range scattering in graphene nanostructures.

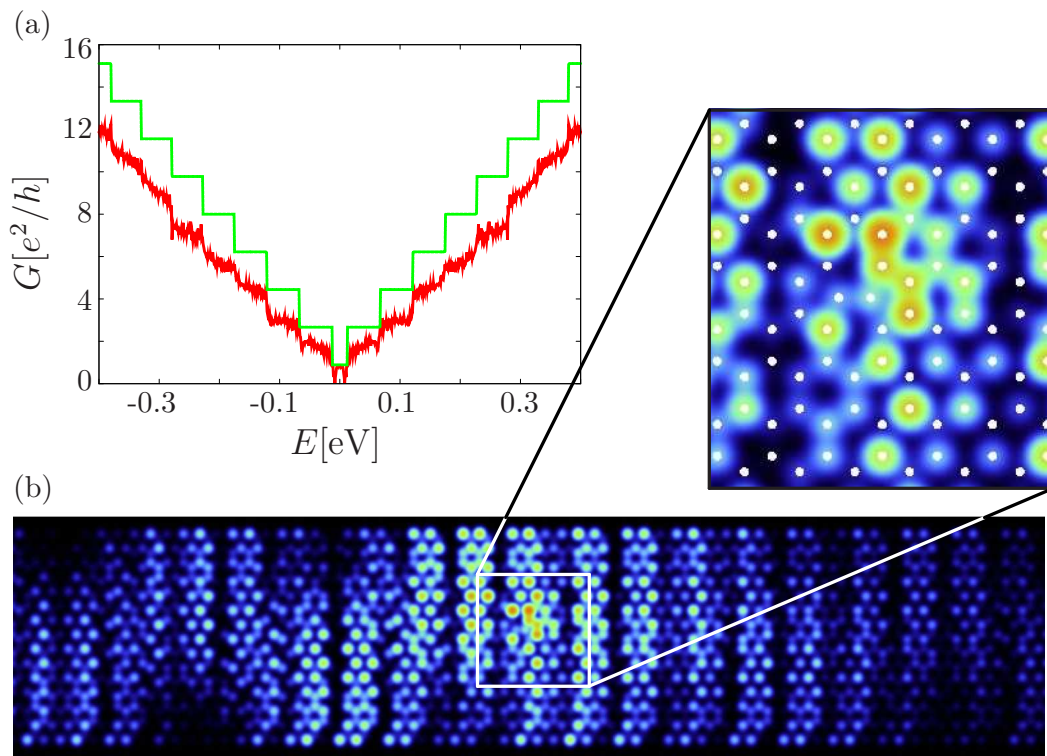


Figure 4.21: (a) Transmission through a nanoribbon featuring five Stone-Wales defects in an area containing  $10^6$  carbon atoms. The conductance of a perfect nanoribbon is shown as staircase (green). (b) Localization of a scattering state of a graphene nanoribbon (width 22nm) in the presence of a Stone-Wales defect.

### 4.3.6 Disordered Constrictions

Using the models for edge and bulk disorder developed above, we will now attempt to describe quantum transport through a realistic disordered graphene nanoconstriction. We include a roughness  $\Delta W = 2.2\text{nm}$ , and vary the impurity concentration  $n_i$  in the range of  $2 \cdot 10^{-3}$  to  $10^{-4}$  [see Fig. 4.22(a)]. We compare our results with experimental data for a single 20 nm wide constriction of graphene at 4 Kelvin [see dashed black line in Fig. 4.22(a)] [27]. Close to the Dirac point, we find quantitative agreement for a disorder concentration of  $n_i \approx 1 \cdot 10^{-3}$ , in line with recent investigations [61]. In this regime, disorder is strong enough to cause localization: close to the Dirac point (i.e. for a low number of transverse modes) the potential landscape of the constriction results in a series of disorder-induced wave-function maxima with a typical diameter of 20nm [see horizontal lines in Fig. 4.22(b)]. Resonances inside these dots result in transmission minima [see solid triangles in Fig. 4.22(c)]. In a multi-electron picture, such resonances should result in Coulomb blockade peaks. While our scattering model is unable to reproduce transmission data in the Coulomb blockade regime, we can qualitatively understand in which energy region Coulomb blockade occurs. The evolution of Coulomb blockade peaks can then be discussed in the framework of quantum dot eigenstates (see section 4.2).



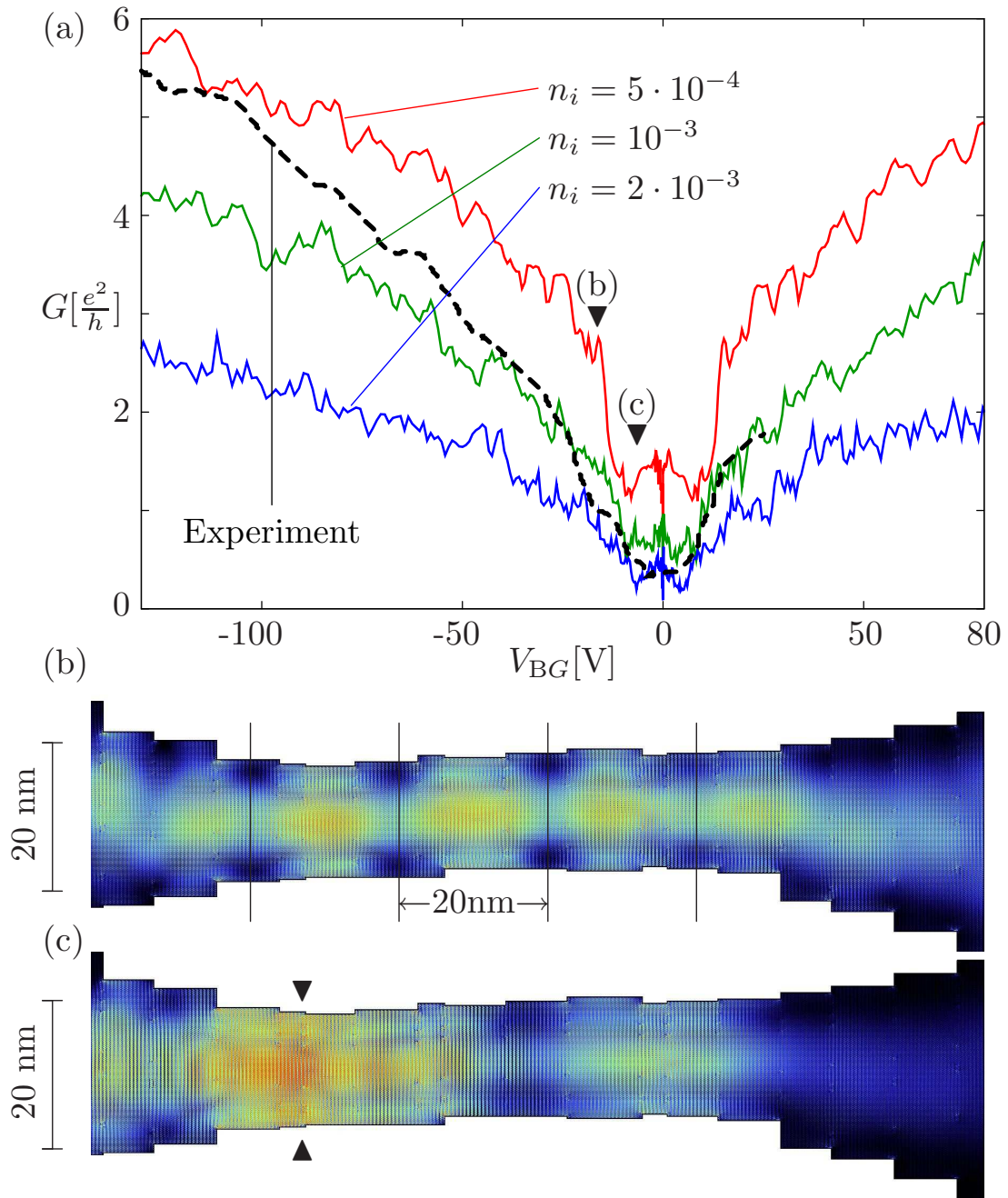


Figure 4.22: (a) Transmission of a 20 nm wide disordered graphene nanoconstriction as a function of back gate voltage  $V_{BG}$  for three different impurity concentrations  $n_i$  as given in the inset. Experimental data (dashed curve) was taken from [27]. Solid triangles denote eigenenergies for which the scattering states are plotted in (b,c). Horizontal lines in (b) mark the oscillation period of the scattering state (see text). Solid triangles in (c) mark the x-position of a resonance.

## 4.4 Bilayer graphene

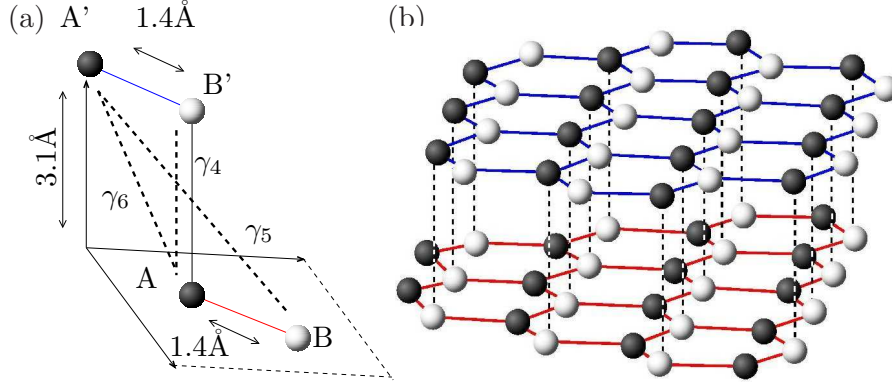


Figure 4.23: (a) Unit cell of bilayer graphene containing four carbon atoms. Dashed lines represent the tight-binding interactions we consider:  $\gamma_4$  describes  $AB'$  interaction,  $\gamma_5$   $A'B$  and  $\gamma_6$   $AA'$  as well as  $BB'$ . (b) Bilayer graphene with  $AB$ -stacking: the atoms labeled  $A'$  in the upper plane are positioned directly above those labeled  $B$  in the lower plane (see dashed lines).

As a final point in our treatment of graphene-based nanostructures, we will briefly discuss the physics of two sheets of graphene stacked on top of each other. The resulting material is commonly called bilayer graphene (see Fig. 4.23). The introduction of a second layer changes the dispersion relation dramatically. As there are now four C-atoms in a unit cell [see Fig. 4.23(a)] the bandstructure of bilayer graphene features four bands that contribute to transport. To calculate the resulting band structure, we include three additional intra-layer coupling parameters  $\gamma_4$ ,  $\gamma_5$  and  $\gamma_6$  [see Fig. 4.23], while keeping the inter-layer parameters (4.3) fixed. By comparison to recent *ab-initio* bandstructures [76] we find the parameter set [77]

$$\gamma_4 = -0.31, \quad \gamma_5 = -0.23, \quad \gamma_6 = -0.13. \quad (4.31)$$

Instead of a linear crossing at a double-cone, one finds a parabolic dispersion relation (see Fig. 4.24). While the special properties of a linear bandstructure are lost, bilayer graphene is most interesting from the experimental point of view due to the possibility to create a band gap: If top and bottom layer are perfectly identical, the parity of the wave function with respect to the  $z$  direction is a “good” quantum number, and the bands touch at the Fermi level. If this degeneracy is lifted by an applied voltage, the Wigner-von Neumann non-crossing rule [34] predicts avoided crossings at  $E_F$ , i.e. a gap opens because the two parabolas no longer touch [see Fig. 4.24(c)]. This

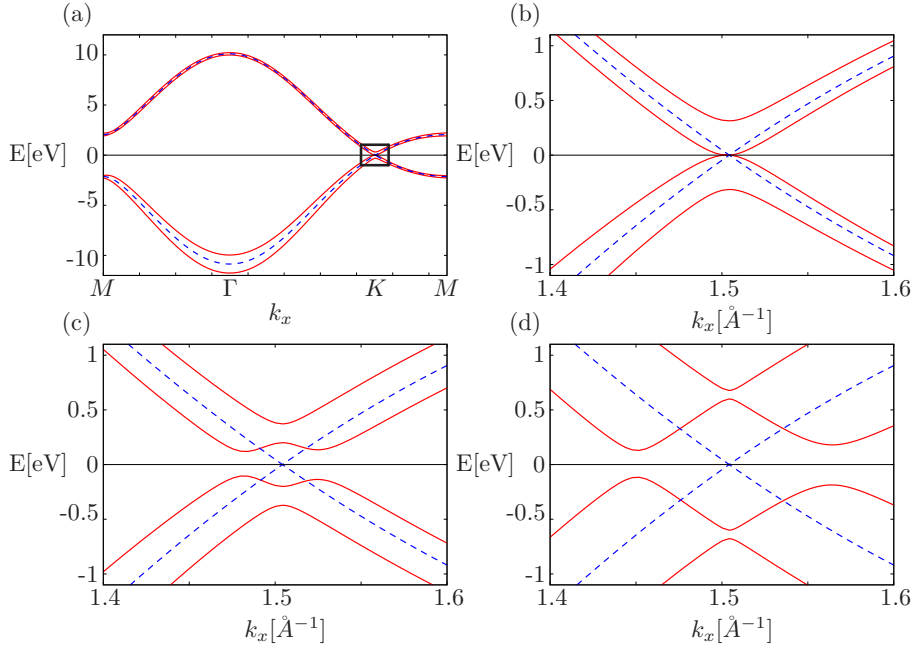


Figure 4.24: (a) Tight-binding calculation of the dispersion relation of monolayer (red solid line) and bilayer graphene (blue dashed line). The area around the  $K$ -point marked by a black rectangle is shown in (b). (c) Formation of a gap in bilayer graphene due to an applied potential difference of 0.2 eV between top and bottom layer. (d) Same as (c) for a potential difference of 0.6 eV between top and bottom layer.

has recently been observed experimentally [78], making the confinement of particles by the application of electrostatic potentials possible in bilayer graphene. The size of the excitation gap is limited, however, to approximately 200meV. At higher potential differences we observe that only the position of the band minima in  $k$ -space changes while the gap size remains constant [see Fig. 4.24(d)].

#### 4.4.1 Bilayer-monolayer heterostructures

When graphene nanostructures are created by mechanical exfoliation and then deposited on  $S_iO_2$  wafers, flakes of different size and thickness emerge. Even single flakes often feature regions of different thickness, i.e. a different number of layers. Monolayer graphene can reliably be tested using spatially resolved Raman spectroscopy [79] to ensure that graphene devices feature only a single atomic layer. However, in the complicated process of creating a

graphene nanodevices, small patches of bilayer graphene could remain. We are thus interested in the influence of a small portion of bilayer graphene deposited onto an otherwise perfect monolayer structure (see inset in Fig. 4.25).

We investigate a monolayer-bilayer-monolayer (MBM) sandwich structure, where the monolayer connects perfectly to the lower bilayer sheet [see inset in Fig. 4.25(b)]. We find a non-monotonic behavior of the transmission as a function of the length  $L$  of the bilayer region: for a single (1-D) chain of carbon atoms ( $L = 0.24\text{nm}$ ) atop a 30nm wide graphene nanoribbon, the transmission features pronounced quantization steps, and lies very close to the ideal values of  $(2n + 1)e^2/h$ ,  $n \in \mathbb{N}$  [see dashed blue line in Fig. 4.25(a)]. For a broader region ( $L = 0.96\text{nm}$ , corresponding to four unit cells) the transmission, and in particular the quantization steps, are strongly suppressed [see solid red line in Fig. 4.25(a)]. By adding one additional chain of carbon atoms ( $L = 1.2\text{nm}$ ), the transmission increases again to about 95% of the value at  $L = 0.24\text{nm}$ , and quantization steps re-emerge [see dotted green line in Fig. 4.25(a)]. To obtain a more systematic description, we calculated the mean Transmission  $\langle T \rangle$  in an energy window of  $2\varepsilon$  around the Dirac point

$$\langle T \rangle = \int_{-\varepsilon}^{\varepsilon} T(E) dE \quad (4.32)$$

as a function of  $L$  [see Fig. 4.25]. We find a pronounced decrease in conductance to about one third of the value for a perfect monolayer nanoribbon [see dashed line in Fig. 4.25(b)].

To understand the behavior of the average conductance discussed above, we consider the interface between a bilayer and a monolayer [see Fig. 4.26(a)]. As a rough estimate on the transmission of such an interface, we use a simple counting argument: As there are twice as many available orbitals in bilayer than in monolayer, the transmission probability from bilayer to monolayer  $T_{BM}$  should be  $T_{BM} \approx 50\%$  [see Fig. 4.26(a)]. Onsager's relation [3] then tells us that the transmission from monolayer to bilayer  $T_{MB}$  should also be  $T_{MB} \approx 50\%$ . From these estimates we can calculate the transmission of an MBM hybrid structure [see Fig. 4.26(b)] by summing up individual contributions to the total transmission: The most simple direct transmission "path" corresponds to transmission at both the MB interface and the BM interface, with a total weight of  $T_{MB} \cdot T_{BM} = 1/4$  [see Fig. 4.26(b)]. Further contributions involve multiple internal reflections at the  $BM$  interface. All contributions to  $T_{MBM}$  can be summed up in a geometric series [see Fig. 4.26(b)]

$$T_{MBM} = T_{MB} \underbrace{(1 + R_{BM}^2 + R_{BM}^4 + \dots)}_{\frac{1}{1-R_{BM}^2}} T_{BM} \approx \frac{1}{2} \cdot \frac{1}{1-\frac{1}{4}} \cdot \frac{1}{2} = \frac{1}{3} \quad (4.33)$$

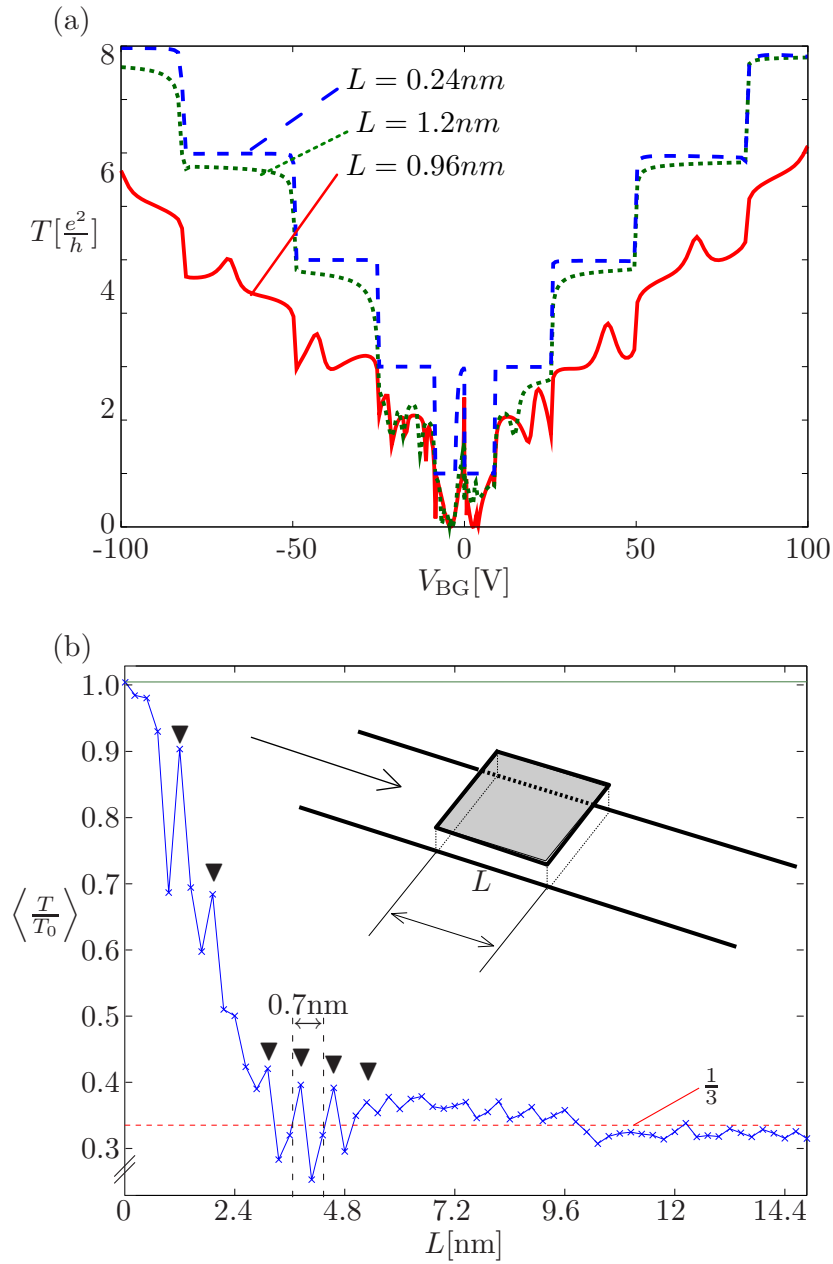


Figure 4.25: (a) Transmission through three MBM heterostructures (for device geometry see inset (b)) with different length  $L$  of the bilayer region as given in the inset. (b) Mean Transmission  $\langle T/T_0 \rangle$  ( $T_0$  is the mean transmission of a perfect monolayer) of a MBM heterostructure (see inset, the top layer of the bilayer region is shaded) as a function of the length of the bilayer  $L$ . For large  $L$ , the curve oscillates around  $1/3$  (dashed red line). Solid triangles mark local maxima of the mean transmission due to interference effects.

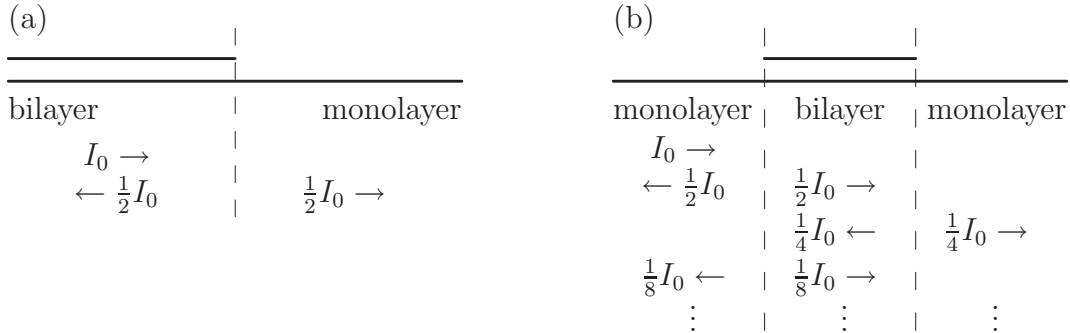


Figure 4.26: (a) *Transmission through the interface between monolayer and bilayer.* Approximately one half of an incoming current  $I_0$  is transmitted from mono- to bilayer graphene. (b) *Transmission of a monolayer-bilayer-monolayer (MBM) structure.* Multiple reflections at the MB and BM boundaries result in a total transmission of  $T_{\text{MBM}} = 1/3$  [see Eq. 4.33].

which is precisely the value found in our calculations [see dashed line in Fig. 4.25]. The above argument is only valid if the distance between the BM and MB interfaces (i.e. the width  $L$  of the bilayer region) is large enough so that the reflections to the left and to the right can be considered independently. This is the reason for values of  $T$  larger than  $1/3$  we find at small  $L$ .

Superimposed on the rapid decay to a transmission value  $1/3$ ,  $\langle T \rangle$  features an oscillating structure with a characteristic wavelength of  $\lambda \approx 0.7\text{nm}$  [marked in Fig. 4.25], that can be understood based on the beating pattern discussed in section (4.2.3). Due to the parabolic dispersion relation of bilayer graphene the wavelength of the beating patterns is slightly larger in bilayer ( $\lambda \approx 0.75\text{nm}$ ) than in monolayer graphene ( $\lambda \approx 0.72\text{nm}$ ). Resonant states form in the top layer if the length  $L$  of the bilayer region is an integer multiple of the wavelength  $L = n\lambda$ ,  $n \in \mathbb{N}$ . Indeed, we find maxima of the mean conductance for  $L/\lambda = 1.6, 2.6, 4.1, 5$ , and  $6.$ , and  $7$ . [see solid triangles in Fig. 4.25(b)], which fits well to the expected relation. The non-integer values for small  $L$  are most probably due to the nontrivial phase for the reflection at the BM interface, which gives a small correction. Because the lattice spacing and  $\lambda$  are incommensurable, we can identify regions where the oscillating pattern is stronger because  $L/\lambda$  is close to an integer [see region with solid triangles in Fig. 4.25(b)] and regions where  $L/\lambda$  falls “in-between” integer numbers, and no distinct oscillation pattern emerges.

If we consider the energy-dependent transmission for a length  $L$  where the averaged transmission  $\langle T \rangle$  has a minimum, we can obtain destructive interference by suitably tuning the energy of the incoming particle, i.e. the transmission vanishes [see Fig. 4.27(a)]. In such a way, even small frag-

ments of bilayer graphene can lead to a dramatic reduction of transmission. While the rectangular structures simulated in this section represent a strong simplification, our main results (namely that a sizeable fraction of current is retro-reflected at an MB boundary) remains valid for more complicated geometries. We are currently investigating the quantitative influence of different MBM hybrid structures on transport properties.

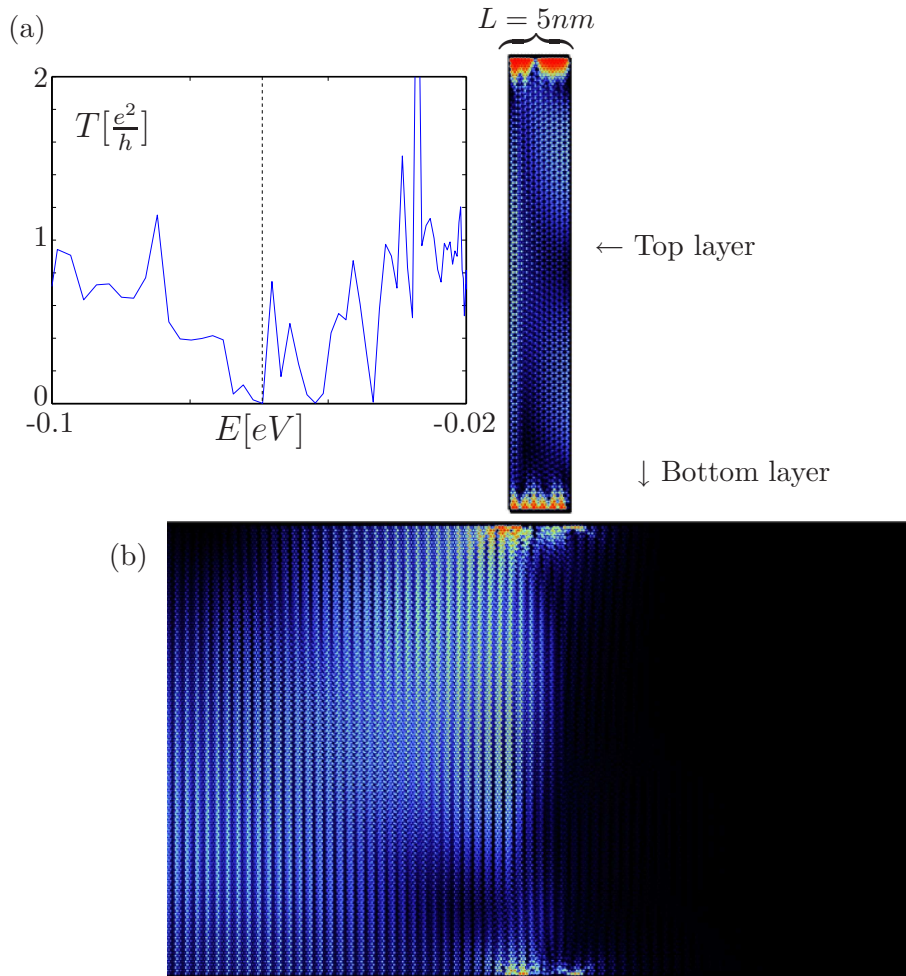


Figure 4.27: (a) Transmission through a short ( $L = 5nm$ ) region of bilayer graphene sandwiched between two monolayer regions (ribbon width  $W = 30nm$ ). (b) Scattering state at the energy marked with a dashed line in (a) where transmission  $T \approx 0$ . The wave function inside the top layer is shown separately [77].





# Chapter 5

## SN hybrid structures

The second class of systems we investigate in this thesis are superconductor-normal conductor (SN) hybrid structures [21]. These devices feature a number of physical phenomena due to the unusual and sometimes counterintuitive properties of the interface between the normal- and superconducting regions. Due to the superconducting proximity effect, signs of weak superconductivity are introduced into the normal conductor [80, 81, 82]. An electron incident on the SN interface from the N region will be reflected as a hole by the process of Andreev reflection [83]. This process phase-coherently couples electron and hole excitations, which are otherwise decoupled in a normal conducting ballistic metal. Mesoscopic, phase-coherent SN interfaces feature macroscopic quantum interference effects [84] that play a crucial role in Josephson junctions, i.e. two superconductors connected by a thin, normal conducting barrier [85], single-electron transistors [86], as well as superconducting qubits in quantum computation [87, 6]. Squids, superconducting rings with a normal conducting point contact, can be used to measure magnetic fields with an accuracy of a single flux quantum, which is sensitive enough to measure the displacement of bar resonators at the quantum limit [8] or the weak magnetic fields of a human brain [88].

In this chapter, we will demonstrate how the tools given in the first part of this thesis can be used to simulate SN hybrid structures (see section 5.1). We will give an introduction into the physics of a normal conducting quantum dot brought into contact with a superconductor, a so-called Andreev billiard. We demonstrate that these billiards feature a close correspondence between the quantum mechanical density of states, the classical phase space structure, and wave-function patterns in Andreev eigenstates. We introduce the Bohr-Sommerfeld approximation, that allows us to intuitively explain the structures of the state counting function, i.e. the integrated DOS, in Andreev billiards (see section 5.2). We consider the reasons for observed discrepancies

between semiclassical and quantum mechanics, how to improve the BS approximation (see section 5.3), and under which conditions it fails (see section 5.4). To be able to describe those systems, for which semiclassical results are unavailable (e.g. disordered Andreev billiards), we present a theory beyond classical orbits to describe and explain the evolution of the DOS (see section 5.5). Finally, we treat transport through open SN hybrid structures and discuss the effects of a finite phase difference between two superconductors (see section 5.6).

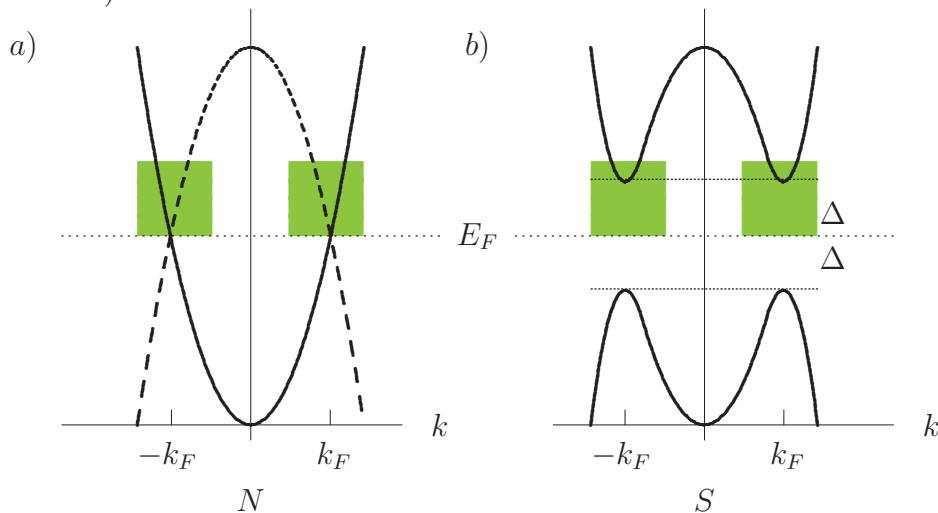


Figure 5.1: Schematic plot of excitation energies  $E$  vs wavenumber  $k$  along an axis passing through the center of the Fermi sphere for normal conducting metal ( $N$ , a) and superconductor ( $S$ , b) [89][90]. In the normal conductor, the hole excitation is shown as dashed line.

## 5.1 The physics of SN structures

We will now present a short overview of the physics of the SN hybrid structures studied in this thesis. For a more complete coverage, see e.g. the book by deGennes [21].

### 5.1.1 Superconductivity

Superconductivity was discovered by Kamerlingh Onnes in 1911. Performing experiments on mercury, he found that its resistance abruptly dropped to zero below 4.2K. A satisfactory explanation for this phenomenon was not found before 1957, when Bardeen, Cooper and Schrieffer (BCS) developed a theory [91], which states that for sufficiently low temperatures, electrons

form bound pairs, so called Cooper pairs. These pairs are formed by introducing electron-electron coupling via a constant weakly attractive force  $-V_{\text{BCS}}$  for electrons near the Fermi edge. This attractive force between the two equally charged electrons is due to electron-phonon coupling (Fröhlich coupling [92]). The exact treatment of the electron-phonon interaction is quite complicated. However, the crude approximation used by BCS theory is sufficient to successfully describe many aspects of superconductivity, such as vanishing resistance and the Meissner-Ochsenfeld effect. The effect of  $V_{\text{BCS}}$  is to create an energy gap around the Fermi energy in the dispersion relation, as shown in Figure 5.1(b). The size of this gap is  $2\Delta$ .  $\Delta = |\Delta|e^{i\phi}$  is called the pair potential or gap parameter of the superconductor. It is the binding energy of two electrons forming a Cooper pair.

The dispersion relation of conduction electrons in a metal may be approximated by the parabolic dispersion relation of a free electron gas [see Figure 5.1(a)] with a properly defined effective mass [23]. In contrast, there is no available state in the gap  $[E_F - \Delta, E_F + \Delta]$  due to Cooper pair formation in a superconductor [see Figure 5.1(b)]. Thus, inelastic scattering is not possible as long as the excitation energy lies below  $2\Delta$ . As a consequence, the resistance drops to zero as long as thermal excitations lie below the gap, i.e.  $k_B T < \Delta$ . The solid becomes superconducting. The spatial dependence of  $\Delta$  is determined by [93]:

$$\Delta(\mathbf{r}) := -V_{\text{BCS}}(\mathbf{r}) \sum_{\varepsilon > 0} v^*(\mathbf{r})u(\mathbf{r})(1 - 2f(\varepsilon)) \quad (5.1)$$

where the sum includes all states with positive  $\varepsilon$ .  $f(\varepsilon)$  is the Fermi function,  $u$  and  $v$  denote the electron and hole wave functions inside the superconductor.

Inside a superconductor, at some distance from the surface,  $V_{\text{BCS}}$  is constant and  $\Delta$  assumes its bulk value  $|\Delta_0|e^{i\phi}$ . At the surface of the superconductor  $V_{\text{BCS}}(x)$  drops abruptly to zero. Equation (5.1) is a self-consistency relation: the exact value of  $\Delta$  depends on the wave functions  $u$  and  $v$  inside the superconductor. These wave functions, in turn, depend on  $\Delta$ . To avoid the complications of solving (5.1), we assume that the length scale at which  $\Delta$  drops from its bulk value to zero is much smaller than the Fermi wavelength. Under these assumption, a step function model for  $\Delta$ ,

$$\Delta = |\Delta_0|e^{i\phi}\theta(x - x_{SN}), \quad (5.2)$$

is plausible [93]. Here,  $x_{SN}$  is the position of the superconductor-normal conductor (SN) interface. The SN hybrid structures we consider in the following sections contain one single superconductor. As a consequence, the phase of  $\Delta$  only produces a phase factor between electron and hole sheet, that has no

physical relevance. Therefore, we will set  $\phi \rightarrow 0$  for the time being. In the last section of this chapter, we will discuss the physics of a scattering device, where the phase difference between two superconductors  $\Delta\phi = \phi_1 - \phi_2$  will play an important role.

### 5.1.2 The Bogoliubov-de Gennes equation

An elegant way to describe a superconductor system is the Bogoliubov-de Gennes (BdG) equation. It consists of a linear expansion of the exact equations of motions of electron and hole excitations (i.e. a linearization of the Ginzburg-Landau equation [21]). The single-particle dynamics of electron and holes are modeled by the effective mass approximation [94] in the framework of the free Schrödinger equation, without taking into account the crystal lattice. The single particle Hamiltonian for the electron,  $\mathcal{H}^S$ , is then given by

$$\mathcal{H}^S = -\frac{\hbar^2}{2m_{\text{eff}}} \left( \frac{\partial^2}{\partial x^2} + \frac{\partial^2}{\partial y^2} \right) + V(\mathbf{r}) - E_F \quad (5.3)$$

The potential landscape of the SN structure is given by  $V(\mathbf{r})$ . We subtract the Fermi energy  $E_F$  from the Hamiltonian to obtain a symmetric excitation energy  $\varepsilon$  with respect to  $E_F$ . In such a way, an electron excitation above and a hole excitation below  $E_F$  both share the same energy  $\varepsilon$ . As a consequence, the single-particle Hamiltonian of a hole is given by  $-(\mathcal{H}^S)^*$  (the asterisk denotes complex conjugation), which reproduces the inverted dispersion relation of the hole [see dashed line in Fig. 5.1(a)].

To implement the coupling between electron and hole introduced by BCS theory, we write the Schrödinger equations for electron and hole excitation as one matrix equation, obtaining the BdG equation [21]

$$\mathcal{H} \begin{pmatrix} |u\rangle \\ |v\rangle \end{pmatrix} = \begin{pmatrix} \mathcal{H}^S & \Delta \\ \Delta^* & -(\mathcal{H}^S)^* \end{pmatrix} \begin{pmatrix} |u\rangle \\ |v\rangle \end{pmatrix} = \varepsilon \begin{pmatrix} |u\rangle \\ |v\rangle \end{pmatrix}. \quad (5.4)$$

The resulting dispersion relation is shown in Figure 5.1(b). The off-diagonal term in the matrix Hamiltonian in Eq. (5.4) represents the coupling between electron and hole. The electron and hole wave functions  $u$  and  $v$  are coupled to each other by the pair potential  $\Delta$  in the superconductor and decoupled in the normal conductor because of the step function model (5.2). The superconductor thus connects electron and hole dynamics of the normal conducting quantum dot.

To apply the numerical techniques developed in the first part of this thesis, we need to define each of the block matrices  $H_0$  and  $H_I$  for both the

normal and superconducting regions. As the BdG equation (5.4) is a continuum equation, we introduce a tight-binding grid in the continuum limit, as outlined in section 2.1.3. The resulting matrix representation of the continuum operator  $\mathcal{H}^S$  is thus of the form

$$H_0^S(E_F) = \frac{\hbar^2}{2m_{\text{eff}}a^2} \begin{pmatrix} \ddots & -1 & & & \\ -1 & 4 & -1 & & \\ & -1 & 4 & -1 & \\ & & -1 & 4 & -1 \\ & & & -1 & \ddots \end{pmatrix} - \mathbb{1} \cdot E_F, \quad (5.5)$$

for the interaction of a single block, while the interaction of adjacent blocks is given by

$$H_I^S = -\frac{\hbar^2}{2m_{\text{eff}}a^2} \mathbb{1}. \quad (5.6)$$

In the superconducting region, the discretized formulation of the BdG equation to electron and hole sheets is straightforward. We use the block matrices

$$H_0 = \begin{pmatrix} H_0^S & \Delta \mathbb{1} \\ \Delta^\dagger \mathbb{1} & -(H_0^S)^* \end{pmatrix}, \quad H_I = \begin{pmatrix} H_I^S & 0 \\ 0 & -(H_I^S)^* \end{pmatrix}. \quad (5.7)$$

Due to the step function model (5.2) electron and hole sheet do not interact in the normal-conducting region. Thus, we may calculate each sheet separately, using  $H_0^S$  and  $H_I^S$  for the electron, as well as  $-(H_0^S)^*$  and  $-(H_I^S)^*$  for the hole sheet. For technical reasons, it is convenient to combine the Green's function of electron ( $G_e$ ) and hole ( $G_h$ ) modules (after evaluating them separately) to a combined Green's function of a rectangular N-region of the form

$$G = \begin{pmatrix} G_e & 0 \\ 0 & G_h \end{pmatrix}. \quad (5.8)$$

We minimize the numerical effort in calculating the Green's function of the N-region while still retaining the advantage of the rectangular block structures:  $G$  can easily be combined with the Green's function of a superconducting module by the  $H_I$  defined in (5.7) to form a SN hybrid structure. We thus have obtained a complete set of matrices to describe eigenstates of and transport through SN hybrid structures. We will now proceed with an overview of the effects introduced by the SN interface.

### 5.1.3 Andreev reflection

So-called Andreev reflections were explained by Andreev in 1964 [83]. They occur when an electron moving inside the normal conducting quantum dot

with a small excitation energy  $\varepsilon$  above the Fermi energy  $E_F$  hits a superconductor - normal conductor (SN) boundary. Small in this context means  $\varepsilon < \Delta$  [see Fig. 5.1(b)]. We assume an ideal SN-interface, meaning that there is no tunnel barrier and no mismatch between Fermi energies and effective masses in the N- and S-region. By exciting another electron, the electron forms a Cooper pair which continues into the superconductor [83, 95]. This second electron leaves a hole excitation with energy  $\varepsilon$  below the Fermi energy. The probability of this process is close to unity in the considered energy region, as shown below. In contrast to specular reflection at a metal-insulator interface [see Fig. 5.2(a)], the Andreev-reflected hole is retro-reflected into the normal conductor, due to momentum conservation [see Fig. 5.2(b)]. If both the pair potential  $\Delta$  of the superconductor and the excitation energy  $\varepsilon < \Delta$  are small compared to the Fermi energy,  $\Delta \ll E_F$ , the dispersion relation can be linearized close to the Fermi level. Then, the reflected hole has the opposite velocity of the electron, and the Andreev reflection is perfect.

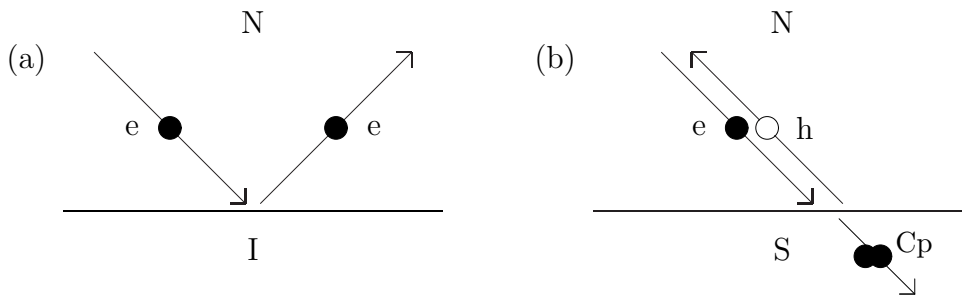


Figure 5.2: (a) Normal reflection by an insulator (I) versus (b) Andreev reflection by a superconductor (S) of an electron with a small excitation energy  $\varepsilon$  above the Fermi energy  $E_F$ . Andreev reflection conserves momentum, as the hole has negative effective mass. The missing charge of  $2e$  continues into the superconductor as a Cooper pair [93].

We will now derive the properties of Andreev reflection in the limit of  $\varepsilon \ll \Delta \ll E_F$  from the Bogoliubov-deGennes equation (5.4) [89, 96]. Consider a SN system, where the SN interface is situated at  $x_{\text{SN}} = 0$ . The superconductor (normal conductor) extends to  $-\infty$  ( $\infty$ ) in negative (positive)  $x$  direction. Using the same approach as in [89], we make an ansatz of a plane electron wave incident on the SN interface

$$\begin{aligned} \psi_N &= (e^{-ik_e x} + ae^{ik_e x}) \begin{pmatrix} 1 \\ 0 \end{pmatrix} + be^{-ik_h x} \begin{pmatrix} 0 \\ 1 \end{pmatrix} \\ \psi_S &= ce^{-iq^- x} \begin{pmatrix} \gamma \\ 1 \end{pmatrix} + de^{iq^+ x} \begin{pmatrix} \gamma^* \\ 1 \end{pmatrix}. \end{aligned} \tag{5.9}$$

where  $\gamma = \Delta/(\varepsilon + i\sqrt{\Delta^2 - \varepsilon^2})$ ,  $|\gamma|^2 = 1$ . The approximation  $\varepsilon \ll \Delta \ll E_F$  results in  $k_{e,h} \approx q^\pm \approx k_F$ . We will discuss this approximation, and possible improvements, in section 5.3. The coefficient  $|a|^2$  gives the probability for normal reflection,  $|b|^2$  the one for Andreev reflection. At the SN interface, the wave function and its derivative have to be continuous,

$$\psi_N(0) = \psi_S(0), \quad \partial_x \psi_N|_{x=0} = \partial_x \psi_S|_{x=0} \quad (5.10)$$

Following Cserti et al., [97], we insert the ansatz (5.9) into the wave function matching conditions (5.10). The solution of the system of equations is  $a = d = 0$ ,  $b = c = 1/\gamma$ . An incident electron is thus, in the simplified picture we now discuss, retro-reflected as a hole with probability  $|b| = 1$ . The phase difference between incoming electron and Andreev reflected hole is equal to the phase of  $b$ ,

$$\arg(b) = -\arg(\gamma) = -\arccos\left(\frac{\text{Re}(\gamma)}{|\gamma|^2}\right) = -\arccos(\varepsilon/\Delta). \quad (5.11)$$

A similar calculation based on a hole wave incident on the SN interface shows an equal phase factor for an Andreev reflected electron. We will need these phase contributions for a semiclassical description of SN-hybrid structures.

## 5.2 Andreev billiards

Andreev billiards have recently raised much experimental [98, 99, 100] and theoretical [101, 102, 103, 93, 104, 105, 106, 96, 107] interest (for a review see [108]). They are formed by bringing a ballistic, normal-conducting quantum dot in contact with a superconductor [see Fig. 5.3]. A characteristic quantity in an Andreev billiard is the state counting function (i.e. the integrated density of states), which has been studied by many authors [109, 110, 111, 112, 113, 114]. It features many special properties, such as a minigap close to the Fermi energy in the case of chaotic N regions [109, 115, 93], large gaps in the case of certain regular N-regions [116], or a distinct cusp structure [97].

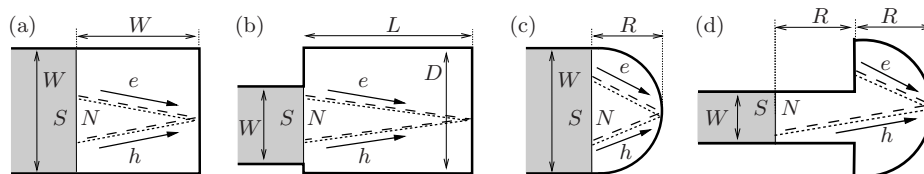


Figure 5.3: (a) Quadratic, separable Andreev billiard with left side replaced by a superconductor. (b) Non-separable rectangular Andreev billiard, only a fraction  $W/D$  of the left side is superconducting. (c) Half-circle Andreev billiard. (d) Mushroom Andreev billiard with the SN interface in the stem of the mushroom. The superconducting areas (S) are shaded. The dashed lines show periodic orbits created by two Andreev reflections at the contact between normal and superconductor.

One interesting feature of Andreev billiards is that already an elementary semiclassical description based on the Bohr-Sommerfeld (BS) quantization rule for periodic orbits leads to very accurate predictions for the state counting function [117]. Quite in contrast, great effort must be taken to find a reasonably accurate semiclassical description of normal conducting systems when no superconducting walls are present (e.g. by including the introduction of diffractive effects [118][119]). The standard approximation made to describe Andreev billiards semiclassically is the exact retracing of electron and hole trajectories [see orbits in Fig. 5.3] [120, 93]. The consequences of this assumption are profound: all trajectories emanating from the SN-interface are strictly periodic. The classical dynamics of the combined SN-system become entirely regular, even and in particular when the normal conducting cavity would feature chaotic dynamics [see Fig. 5.3(d)] [121]. Unlike in chaotic or integrable systems, periodic orbits are no longer isolated in Andreev billiards but form continuous manifolds that dominate the classical phase space and,



in turn, the density of states [21, 122, 123]. This continuum of periodic orbits is a unique property of Andreev billiards.

We will investigate Andreev billiards of different shape (see Fig. 5.3) in order to compare the semiclassical predictions for the state-counting function to quantum mechanical calculations. All of these structures feature a flat potential landscape inside the normal-conducting region, i.e.  $V(\mathbf{r}) \rightarrow \infty$  ( $V(\mathbf{r}) = 0$ ) for  $\mathbf{r}$  outside (inside) the dot area. Thus, scattering only occurs at the boundary of the quantum dot. As a consequence, the dynamics is determined by the dot shape. We begin our discussion with the most simple case of a rectangular dot with separable boundary conditions [Fig. 5.3(a)]. By reducing the width of the superconducting interface, the boundary conditions become non-separable [see Fig. 5.3(b)]. In rectangular cavities, the absolute value of the cartesian components of the electron momentum  $\hbar k_x$  ( $\hbar k_y$ ) are conserved. We therefore consider Andreev billiards with curved boundaries, to test whether the quality of the BS approximation depends on a conserved  $|\hbar k_x|$  [see Fig. 5.3(c)]. We finally treat a mushroom billiard to test the BS approximation for the case of non-integrable dynamics [see Fig. 5.3(d)]. The semiclassical properties of all of these structures we will now investigate are determined by the distribution of periodic orbits.

### 5.2.1 The periodic-orbit distribution

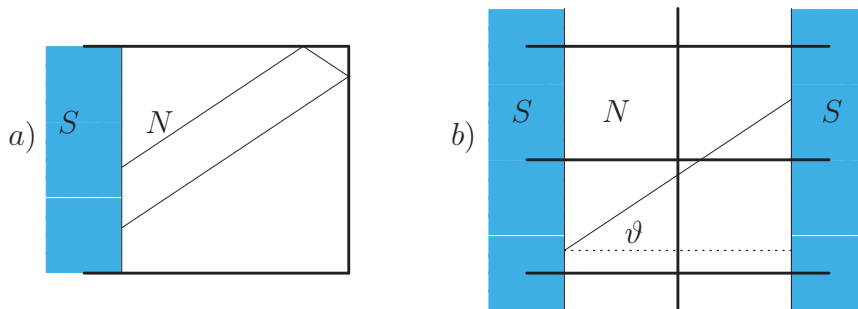


Figure 5.4: (a) Quadratic ( $D = L$ ) quantum dot with one side replaced by a superconductor ( $W = D$ ). The trajectory shown forms a closed Andreev loop containing two Andreev reflections. (b) shows the same trajectory in the extended zone scheme (scaled down by a factor of two). By arranging multiple billiards next to each other, any trajectory can be drawn as straight line. The angle  $\vartheta$  can be used to express the length  $s$  of the trajectory:  $s = 2L / \cos(\vartheta)$ .

As mentioned above, periodic orbits form continuous manifolds in Andreev billiards: Due to the creation of periodic orbits by Andreev reflection,

any path connecting the SN interface with itself becomes a periodic (see orbits in Fig. 5.3). The length distribution  $P(s)$  of these periodic orbits is thus equal to the classical pathlength distribution of the normal conducting cavity, i.e. the probability that a classical particle entering the cavity with an angular distribution of  $\cos(\theta)$  exits after a pathlength of  $s$ . It is normalized to one:  $\int P(s)ds = 1$ .

The distribution of periodic orbits plays a central role in the semiclassical description of Andreev billiards. We will therefore derive an analytical expression for  $P(s)$  for the simplest geometry we consider, a rectangular cavity with one entire side replaced by a superconductor, the separable box geometry (see Fig. 5.4). As the superconducting boundary covers one side completely, the separability of the system is conserved. Consider the extended zone scheme as shown in Figure (5.4,b). Every path leaving the entrance with an angle  $\vartheta$  has a length  $s = 2L/\cos\vartheta$ . As a simple approximation, we assume that the angular distribution of the different paths is described classically by a cosine. This is a good approximation for more than 10 open modes in the lead<sup>1</sup>.

$$P(\vartheta)d\vartheta = \cos(\vartheta)d\vartheta = \cos(\vartheta)\frac{\cos(\vartheta)^2}{2d\sin(\vartheta)}ds = \frac{4d^2}{s^3\sqrt{1 - \left(\frac{2d}{s}\right)^2}}ds$$

For a more general shape of the cavity, numerical Monte Carlo calculations using Eq. (5.20) were used to determine  $P(s)$ . Typically 1.500.000 trajectories with an angular distribution of  $\cos(\theta)$  were employed. As a prototype system, consider a quadratic cavity of dimensions  $L \times L$  where only a fraction  $W/L$  of the left side is superconducting [see insets in 5.5(b-d)]. If  $W$  is only slightly smaller than  $L$ , a few additional peaks corresponding to reflections at the non-superconducting part of the left wall of the cavity appear [see Fig. 5.5(b)]. For  $W \ll L$ , the resulting path length distribution features a quite complicated fine structure [see Fig. 5.5(c,d)].

## 5.2.2 Bohr-Sommerfeld approximation

The BS quantization rule is an elementary quantization scheme used to describe *periodic motion* in the early days of quantum mechanics [34]. Periodic orbits formed by the hole retracing the path of the electron play the essential role in the dynamics of Andreev billiards. As a consequence, we can apply the Bohr-Sommerfeld approximation.

---

<sup>1</sup>More complicated calculations using Fraunhofer diffraction lead to different angular distributions for the different transverse modes [124]. A sum over all open modes approximately reproduces the cosine distribution.

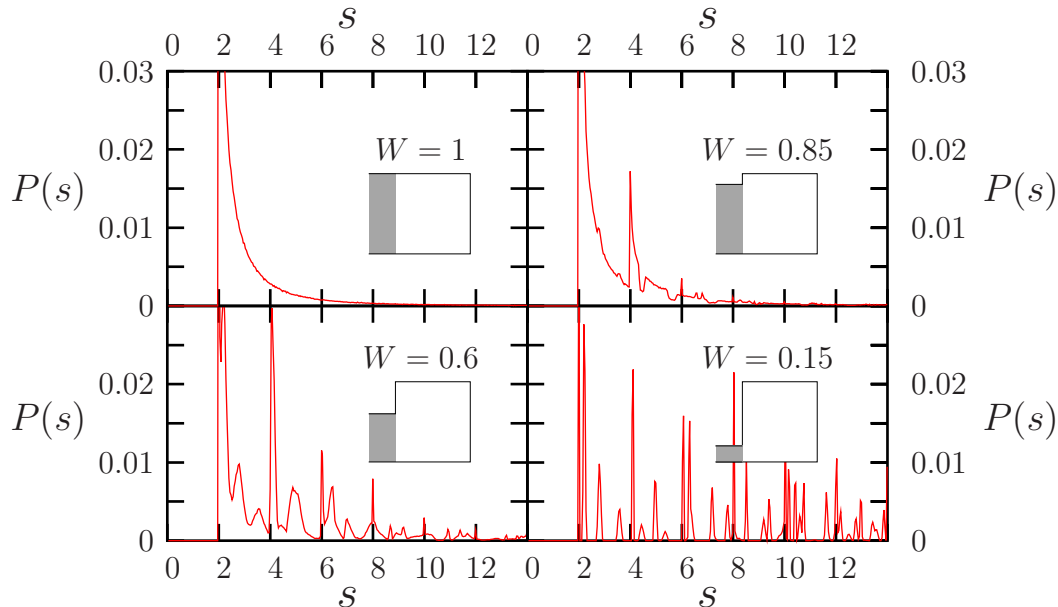


Figure 5.5: Numerically calculated  $P(s)$  for different lead widths as shown in the insets in a  $1 \times 1$  rectangle. The peak at  $s = 2$  represents paths exiting the cavity after being reflected at the right wall once. The smaller the lead, the more complicated the structure of  $P(s)$ .

We want to derive a semiclassical prediction for the state counting function. To this end, we start out from the semiclassical density of states [117]

$$\rho_{\text{BS}}(\varepsilon) = N \int_0^\infty ds P(s) \sum_{n=0}^\infty \delta(\varepsilon - \varepsilon_n(s)). \quad (5.12)$$

$\varepsilon_n(s)$  is chosen such that the energy level fulfills the Bohr-Sommerfeld quantization condition for the action  $S$ :

$$S = S_e - S_h = \int \mathbf{p}_e d\mathbf{q}_e - \int \mathbf{p}_h d\mathbf{q}_h = 2\hbar\pi(n + \frac{\mu}{4}) \quad (5.13)$$

where  $\mu$  is the Maslov index [125], which describes phase contributions due to classical turning points, e.g. reflections at the SN interface or the hard wall boundary.

For hard walls and zero potential inside, the line integral (5.13) gives the action, i.e. the length of the trajectory  $s$  times the wavenumber  $k$ . The action of the hole excitation contributes with a negative sign. We consider a periodic orbit, a trajectory of length  $s$  connecting the superconducting lead with itself.

$$S = \hbar s(k_e - k_h) = s\hbar k_F \left( \sqrt{1 + \frac{\varepsilon}{E_F}} - \sqrt{1 - \frac{\varepsilon}{E_F}} \right) \approx s \frac{2\varepsilon}{v_F}. \quad (5.14)$$

In the last step, we used a Taylor expansion of first order. The difference in energies between electron and hole is  $2\varepsilon$ . The main part of the phase the electron accumulates while transversing the billiard is compensated by the hole retracing it. Thus, the action of a periodic orbit varies much slower with the length of  $s$  than for a normal conducting system.

Additionally, we have to take into account the phase shift of  $-2 \cdot \arccos(\frac{\varepsilon}{\Delta})$  due to the two Andreev reflections (see Eq. 5.11). We do not need to consider other reflections at the normal conducting hard wall boundary each contributing a phase jump of  $\pi$ , because the sum of both the electron and the hole reflection add up to a total contribution of  $2n\pi$ , where the integer  $n$  denotes the number of reflections. A phase shift of integer multiples of  $2\pi$  is irrelevant as the phase is only defined modulo  $2\pi$ . The complete phase accumulated in one closed trajectory is thus

$$\phi = \frac{2\varepsilon s}{\hbar v_F} - 2 \cdot \arccos\left(\frac{\varepsilon}{\Delta}\right). \quad (5.15)$$

According to Bohr-Sommerfeld, the semiclassical quantization condition for the energies  $\varepsilon$  of a periodic Andreev orbit of length  $s_n$  requires the above phase to be equal to  $2n\pi$ ,

$$s_n(\varepsilon) - \left[ n\pi + \arccos\left(\frac{\varepsilon}{\Delta}\right) \right] \frac{\hbar v_F}{\varepsilon} = 0. \quad (5.16)$$

Inserting this expression into Equation (5.12) we obtain

$$\rho_{BS}(\varepsilon) = N \int_0^\infty ds P(s) \sum_{n=0}^\infty \delta[s - s_n(\varepsilon)] |\partial_\varepsilon s_n(\varepsilon)|. \quad (5.17)$$

The derivative of  $s_n(\varepsilon)$  appears because of the familiar formula  $\delta(f(x)) = \sum_i \delta(x - x_i) / |f'(x_i)|$ . The sum over  $i$  can be left out because  $s_n(\varepsilon)$  is strictly monotonic in  $\varepsilon$  and thus only has one root. To compare the results of the semiclassical approximation with quantum mechanical calculations, it is useful to consider the semiclassical state counting function

$$N_{BS}(\varepsilon) = \int_0^\varepsilon d\varepsilon' \rho_{BS}(\varepsilon') \quad (5.18)$$

$$= N \int_0^\infty ds P(s) \sum_{n=0}^\infty \int_0^\varepsilon d\varepsilon' \underbrace{\delta(s - s_n(\varepsilon')) |\partial_{\varepsilon'} s_n(\varepsilon')|}_{\delta(\varepsilon' - \varepsilon_n)}. \quad (5.19)$$

Using Equation (5.16) one can perform the integral over  $\varepsilon'$  using the delta function to obtain

$$N_{BS} = M \sum_{n=0}^\infty \int_{s_n(\varepsilon)}^\infty P(s) ds. \quad (5.20)$$

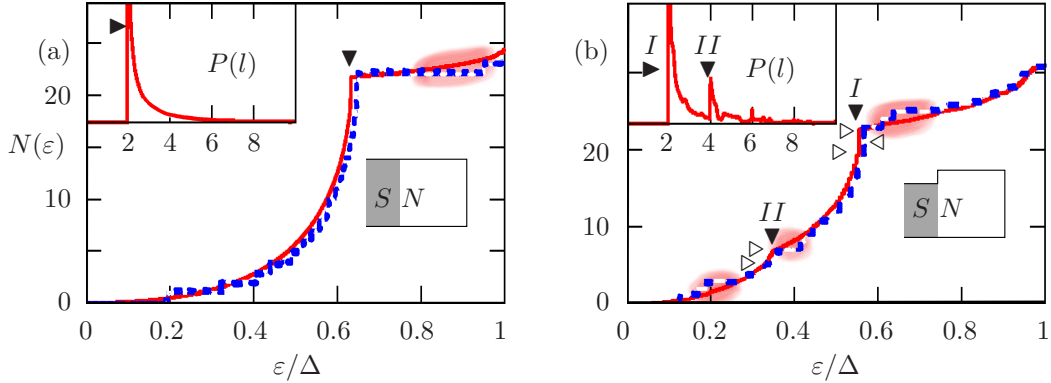


Figure 5.6: The quantum mechanical state counting function  $N_{\text{QM}}(\varepsilon)$  (solid red staircase) and its semiclassical BS estimate  $N_{\text{BS}}(\varepsilon)$  (dashed blue line) for two quadratic cavities with different lead widths as shown in the insets [ $k_{\text{F}} = 20.5\pi/W$ ,  $W = L(a)$ ,  $0.8L(b)$ ]. The top left insets show the classical path length distribution in units of the cavity length  $L$ . Solid triangles mark pronounced cusps in  $N(\varepsilon)$  and their classical origin. The quantum number  $n$  (Eq. 5.16) increases from 0 to 1 at  $I$ . Open triangles mark the energy positions of states whose wave functions are displayed in Fig. 5.7. Shading marks the regions where the BS approximation deviates from quantum results.

The above equation gives the semiclassical estimate for the state counting function of Andreev billiards. In comparison to similar equations for normal-conducting structures (e.g. the Gutzwiller trace formula, see [125]), it is exceedingly simple, due to the presence of a continuum of periodic orbits present in Andreev billiards. The exact shape of the paths connecting the superconductor with itself does not enter anywhere in (5.20). The number of reflections at the normal conducting walls are irrelevant. The entire information of the specific geometry enters via  $P(s)$ .

### 5.2.3 Quadratic N cavity

We are now ready to investigate the correspondence between the BS prediction for the state counting function  $N_{\text{BS}}$  derived above and exact quantum mechanical results for the state counting function,

$$N_{\text{QM}}(\varepsilon) = \sum_i \theta(\varepsilon - \varepsilon_i), \quad (5.21)$$

where the  $\varepsilon_i$  are eigenenergies of the BdG equation. The classical path length distribution shows apart from one peak no additional fine structure [see inset

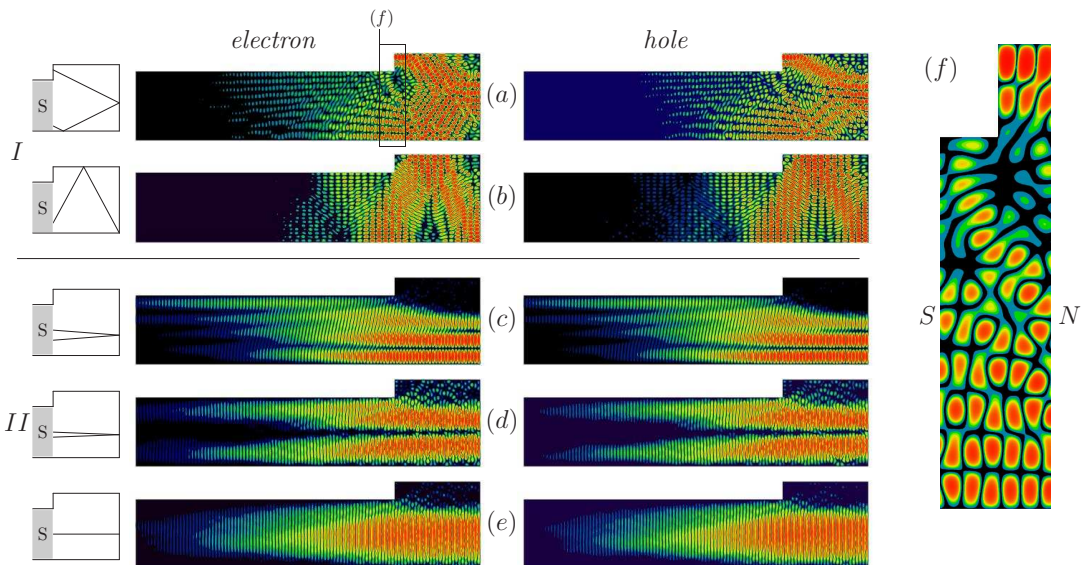


Figure 5.7: (a)-(d) shows the electron and hole wave functions  $|u(\mathbf{x})|^2$  and  $|v(\mathbf{x})|^2$  at values of  $\varepsilon$  indicated by open triangles in Fig. 5.6(b):  $\varepsilon/\Delta$  is (a) 0.565, (b) 0.566, (c) 0.33, (d) 0.355. The corresponding classical orbits are indicated on the left. (f) shows an enlarged view of the S-N interface for the eigenstate in (a).

in Fig. 5.6(a)]. Accordingly, the semiclassical prediction for the state counting function,  $N_{BS}$ , features a single cusp [marked by a solid triangle in Fig. 5.6(a)] due to the  $n = 0$  series of states, i.e. the first term in the sum of (5.20). There are fine-scale fluctuations in the distribution of quantum-mechanical eigenenergies on a scale below the mean level spacing, which are not resolved by the BS approximation. We will improve the semiclassical description of this system by an EBK quantization that remedies these shortcomings in the next section.

By reducing the width of the SN interface [see inset in Fig. 5.6(b)], additional features in the classical path length distribution, and hence the state counting function, appear. A second cusp starts to form, corresponding to the second peak in  $P(s)$  [see Fig. 5.6(b)]. Overall, the BS approximation performs quite well. In particular, it reproduces and intuitively explains the position of both cusps. The position of the cusps is predicted very accurately by the BS approximation with an error well below the mean level spacing of  $0.09\Delta$ .

Assuming the validity of the retracing approximation, the semiclassical quantization condition [Eq. (5.16)] allows to map every excitation energy  $\varepsilon$

onto a path length  $s_n$  of a periodic Andreev orbit. Consider, e.g., the energy at the cusp marked  $I$  in Fig. 5.6(b) that corresponds to a path length  $s_0 = 2L$ , which is the length of the shortest classical Andreev-reflected orbit of the system [see  $P(s)$  in the inset of Fig. 5.6(b)]: the electron leaves perpendicular to the SN-interface, is reflected at the opposing wall and returns to the SN-interface. Quantum mechanical wave functions evaluated at the cusp energy indeed feature pronounced, scar-like enhancement along the orbit “bundle” [126] with length  $s = 2L$  [see in Fig. 5.7(b)]. Wave functions with neighboring energy values below the cusp feature additional nodes in transverse direction [see Fig. 5.7(a)]. Note that also eigenstates near the cusp marked  $II$  in Fig. 5.7(c, d) correspond very nicely to the path-bundles of the expected length. Consistent with the good agreement of the BS quantization with the quantum calculations, the electron and hole wave function densities agree very well with each other. To the extent that bundles of classical trajectories cause the density enhancement in the wave function, and bundles of hole- and particle-orbits agree with each other, this is to be expected. Conversely, a hallmark of the breakdown of retracing are dissimilar density distributions in the particle ( $u$ ) and hole ( $v$ ) wave functions, as we recently observed [127, 114]. Looking more closely, we find discrepancies between the exact quantum mechanical calculations for  $N_{\text{QM}}(\varepsilon)$  and its semiclassical counterpart  $N_{\text{BS}}(\varepsilon)$ , which are indicated by the shaded areas in Fig. 5.6(a) and (b). For the two systems considered in Fig. 5.6 we note that the mismatch between the quantum and the semiclassical results is located at rather well-defined values of the excitation energy  $\varepsilon$ . Note that the mismatch tends to occur at values of  $\varepsilon$  which lie just *above* the energy values of a cusp. Since pathlength and energy at fixed quantum number  $n$  are inversely proportional to each other [see Eq. (5.16)] the energies *above* the cusp which is associated with quantum number  $n$  [e.g. the one marked  $I$  in Fig. 5.6(b)] correspond to the longest orbits associated with quantum number  $n + 1$ . The deficiencies of the BS approximation are evidently caused by contributions from long orbits.

To further elucidate the correspondence between the classical phase space structure and the eigenstates of Andreev billiards, we consider a Poincaré surface of section at the SN-interface. The conjugate variables  $y$  and  $p_y$  denote the position along the SN-interface, and the momentum parallel to it. Each point  $(y, p_y)$  corresponds to a starting point of a trajectory with length  $s(y, p_y)$  [e.g. the point  $(W/2, 0)$  would correspond to the orbit in Fig. 5.7(e), which the length  $s(W/2, 0) = 2L$ ]. The BS approximation yields, in turn, a connection between orbit length and eigenenergy. If there is, indeed, a strong correlation between the classical phase space structure and Andreev eigenstates, a quantum mechanical phase space distribution should feature

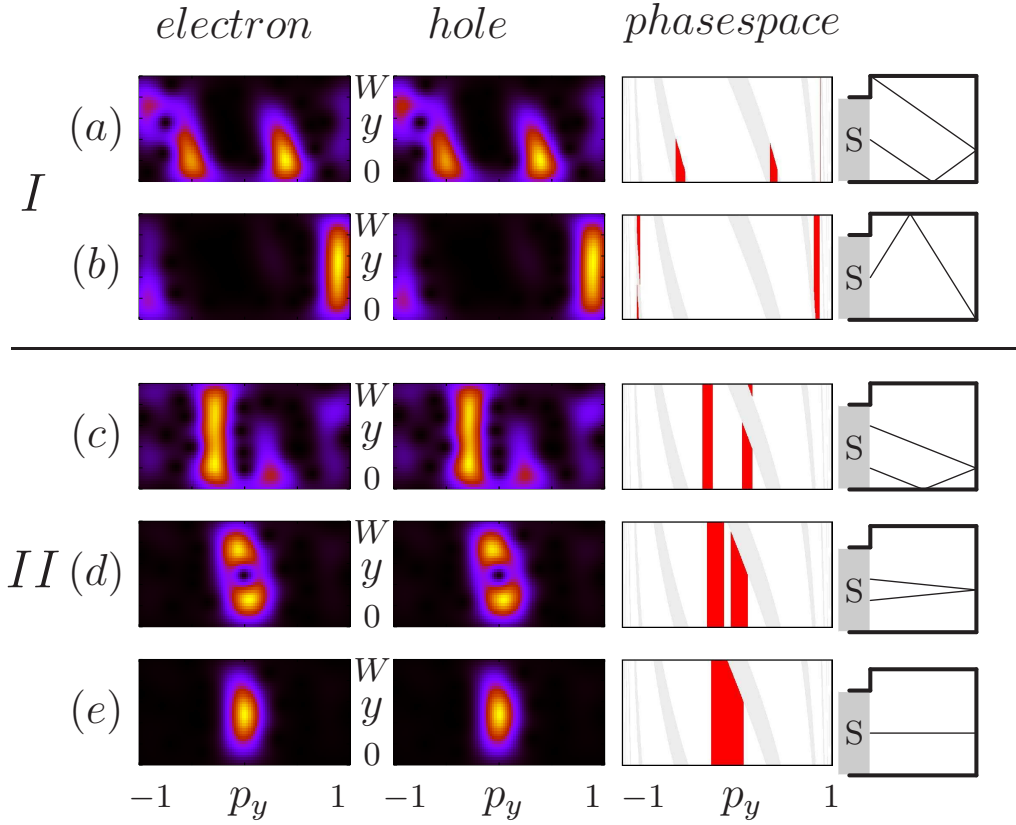


Figure 5.8: (a)-(e) show the Husimi distribution, classical phase space, and classical orbits for electron and hole wave functions  $|u(\mathbf{x})|^2$  and  $|v(\mathbf{x})|^2$  for the states shown in Fig. 5.7. The Husimi projection is evaluated at the SN interface,  $p_y$  corresponds to the transverse impulse,  $y$  to the transverse position on the SN interface. An orbit of appropriate length  $s_0$  (according to the BS-quantization 5.16) is shown to the right. Dark red (light grey) areas in classical phase space mark those points, for which the orbit length  $s(y, p_y) \in [s_0 - \frac{\lambda_F}{4}, s_0 + \frac{\lambda_F}{4}]$  ( $s \geq 4L$ ).



strong enhancements around those points  $(y, p_y)$  for which  $s(y, p_y)$  is close to the value predicted by the BS approximation. To check this statement, we calculate a Husimi projection [128] at the SN interface,

$$f_H(p_y, y) = |\langle y_0 p_y | \eta \rangle|^2, \quad \langle y | y_0 p_y \rangle := \frac{1}{\sqrt{2\sigma\sqrt{\pi}}} e^{\frac{i}{\hbar} p_y y} e^{-\left(\frac{y-y_0}{2\sigma}\right)^2}. \quad (5.22)$$

The state  $|y_0 p_y\rangle$  is a coherent state localized on the SN interface at  $y_0$  ( $p_y$ ) in position (momentum) space, with an uncertainty  $\Delta y = \sigma$  ( $\Delta p_y = \frac{\hbar}{2}\sigma^{-1}$ ).  $|\eta\rangle$  corresponds to electron ( $u$ ) and hole ( $v$ ) sheet, respectively. We choose  $\sigma \approx \lambda_F$ , where  $\lambda_F$  is the Fermi wavelength.

We find that the structures of classical phase space are accurately reproduced by the Husimi distribution (see Fig. 5.8). As expected, the electron and hole Husimi distributions closely mimic each other, even more so than the eigenstates themselves (compare electron and hole sheet of the state labeled (a) in 5.7 and 5.8. We observe, however, that only those eigenstate very close to a cusp (the ones labeled (b), (d) and (e) in Fig. 5.7 and 5.8) feature a strongly localized Husimi distribution that vanishes in areas where  $s_n(\varepsilon) \neq s(y, p_y)$ . The reason for this is that the phase-space structure of the smaller bundles, i.e. their area in phasespace is too small ( $< \hbar$ ) to be entirely resolved by the quantum eigenstate, resulting in contributions to the Husimi distribution that do not fit to a simple BS quantization.

## 5.2.4 Circular boundaries

The quadratic cavities discussed in the previous subsection separate in cartesian coordinates, i.e. they preserve the absolute values of the  $k_y$  and  $k_x$  components of the electron (and hole) wavenumber. The close correspondence between quantum mechanical eigenstates and the classical phase space structure we have shown above might be connected to this non-generic feature of the system we consider. To ensure that this is not the case and the above results apply, indeed, to Andreev billiards with more general boundaries, we consider a circular billiard shape: A half-circle of radius  $R$  connected to a superconducting lead [see inset in Fig. 5.10(a)]. In this geometry, the invariance of the momentum components is broken due to reflections at the circular boundary. Likewise, angular momentum is not conserved due to reflections at the straight section. We implement the curved boundary by discretizing the specific module in a polar (instead of a cartesian) grid [36].

Another contrast to the rectangular structures discussed above is apparent in the semiclassical pathlength distribution  $P(s)$  [see Fig. 5.10(a)]: Instead of an exponential tail, the path length distribution strictly vanishes for trajectories longer than  $R\pi$ , the circumference of the half-circle.

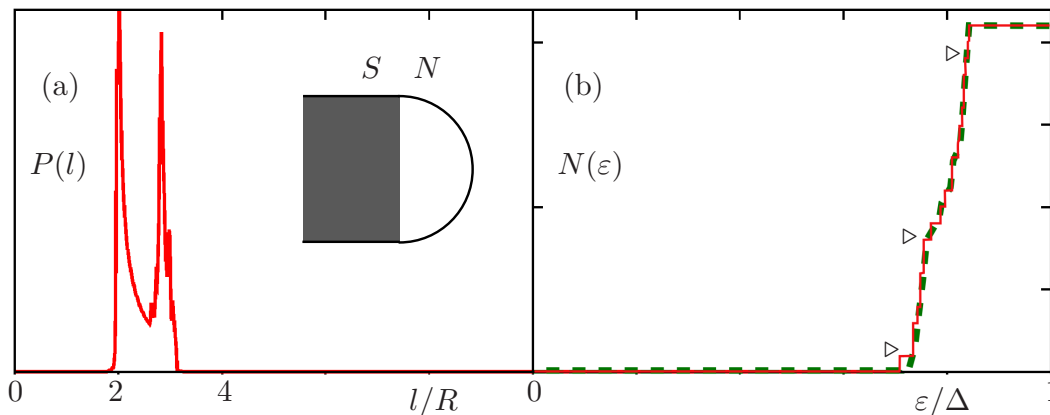


Figure 5.9: (a) Path length distribution  $P(s)$  and (b) quantum mechanical (red staircase) and semiclassical (green dashed line) state counting function of the half-circle Andreev billiard. The Fermi energy  $E_F = (21.5\pi)^2/2$ ,  $\Delta = 0.02E_F$ . Eigenstates are shown in Fig. 5.10 for energies marked by open triangles.

The eigenenergies thus fall within a very narrow energy window, the lower bound of which is determined by the longest, and the upper bound by the shortest classical path possible [see Fig. 5.9(b)].  $N_{BS}$  agrees with the quantum mechanical calculations of the state counting function for the regular half-circle billiard remarkably well. As expected, the eigenstate corresponding to the lowest energy (i.e. the longest orbit) shows strong enhancements along the corresponding classical skipping orbit along the circular boundary [see Fig. 5.10(a)]. Even eigenstates in the intermediate energy regions feature wave function patterns strongly reminiscent of classical orbits [see Fig. 5.10(b)]. Similar patterns found in the wave functions of pseudointegrable normal billiards have been referred to as “superscars” [129]. From this we learn that the conservation of longitudinal momentum is not a requirement for the strong correlation between classical phase space structures and eigenstates in Andreev billiards.

There is one unexpected peculiarity, though. The eigenstate corresponding to the shortest classical orbit [see Fig. 5.10(c)] is not situated at the top of the cusp [see open triangles in Fig. 5.9(b)]. Obviously, the structure of the eigenstate is in line with the predictions of the BS approximation. A cut through the wave function density along the orbit even reveals how the phase difference between electron and hole is build up in the normal-conducting region [see Fig. 5.10(d)]. The culprit thus must be the Andreev phase term

(5.11), which is not sufficiently accurate to explain the observed small energy shift. We will give an improved expression for the Andreev phase that explains the above effect in detail, in the next section.

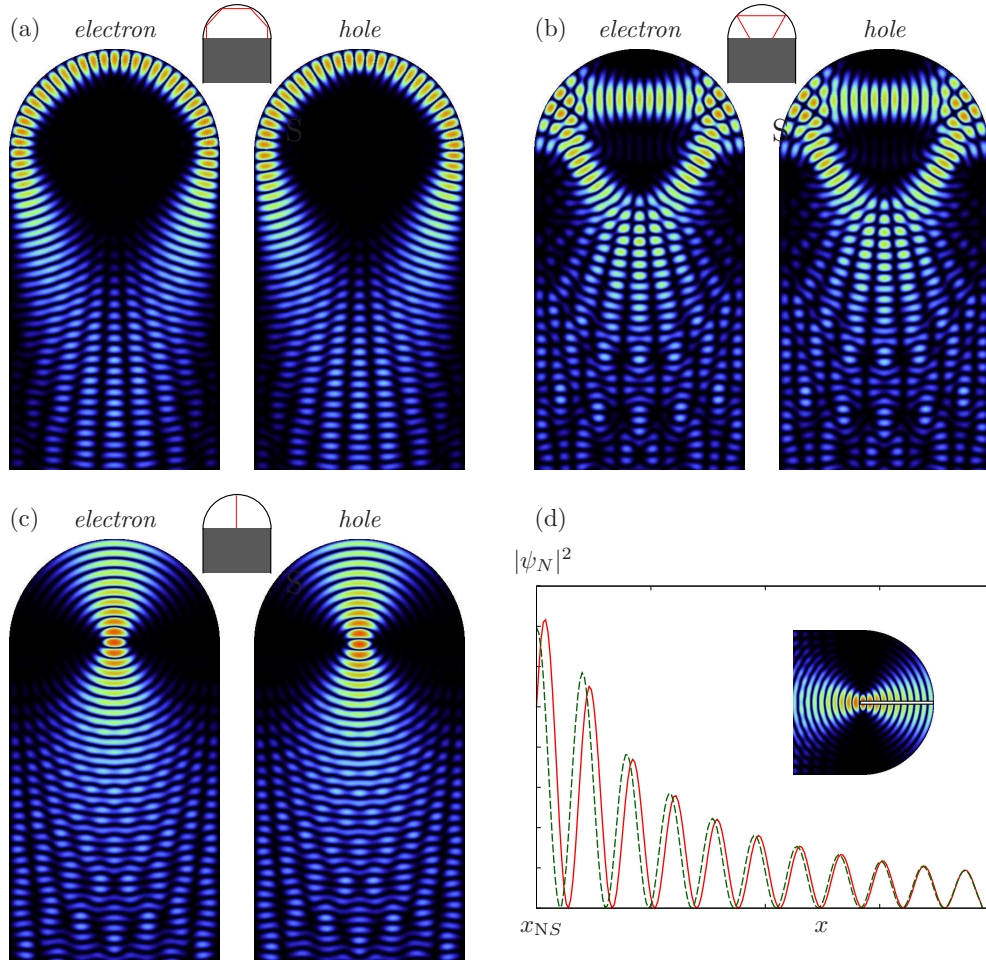


Figure 5.10: (a)-(c) Density of electron and hole eigenfunctions  $|\psi|^2$  of the half-circular Andreev billiard for three different excitation energies  $\varepsilon = 0.736\Delta$ (a),  $0.747\Delta$ (b), and  $0.836\Delta$ (c). The Fermi energy  $E_F = (21.5\pi)^2/2$ ,  $\Delta = 0.02E_F$ . Both the similarity between electron and hole wave function and the enhancement along bundles of semiclassical orbits can be seen. (d) shows a cut through the electron (green, solid line) and hole (blue, dashed line) probability density depicted in (c) along the classical orbit shown in the inset.

## 5.3 Beyond the BS approximation

In this section, we will closely investigate the phase correction term needed to semiclassically describe the Andreev retroreflection process. We want to explain the small but significant discrepancies between semiclassical BS approximation and quantum mechanical results observed in the previous section. We derive a series expansion for the phase shift between electron and Andreev reflected hole in powers of the excitation energy. To lowest order, we find a contribution to the phase shift caused by the mismatch in wavenumbers between normal- and superconducting region, which is present even in the case of identical Fermi energies. To our knowledge, this contribution was previously neglected in other theoretical works. This term is not negligible for geometries featuring a comparatively large portion of superconducting boundary. In the special case of a rectangular quantum dot in contact with a superconductor, we find sinusoidal oscillations in the density of states, which can be perfectly accounted for by our expression. To demonstrate that our results are not restricted to special geometries, we show that also eigenstates in an Andreev billiard confined by a circular boundary can be explained by our theory.

We start out with a derivation of a general expression for the phase shift at an SN boundary due to Andreev reflection in section 5.3.1. We then return to the distinct Andreev billiard systems discussed in the previous section: (i) the separable box geometry, where our results can be applied to an Einstein - Brillouin - Keller quantization (subsection 5.3.2) (ii) the non-separable rectangular geometry, where we will add our results to the BS quantization of periodic orbits (subsection 5.3.3) and (iii) the half-circle geometry, which not only is non-separable, but additionally breaks the invariance of longitudinal momentum due to reflections at the circular boundary (subsection 5.3.4).

### 5.3.1 Derivation of the Andreev phase

We start out our discussion by looking more closely at the quantum mechanical solution at a SN interface. We will consider an interface of finite width  $W$ , in a waveguide which is superconducting for  $x < x_{\text{SN}}$ . Instead of a single plane wave, we thus obtain transverse eigenfunctions  $\chi_n(y) = \langle y | \chi_n \rangle = \sqrt{2/W} \sin(n\pi y/W)$ . We make an ansatz for the wave function in the normal

( $\psi_N$ ) and superconducting ( $\psi_S$ ) part of the waveguide:

$$\begin{aligned}\psi_N(\mathbf{x}) &= \sum_{n=1}^N \chi_n(y) \begin{pmatrix} c_n^e \sin(k_n^e x + \beta_n^e) \\ c_n^h \sin(k_n^h x + \beta_n^h) \end{pmatrix} \\ \psi_S(\mathbf{x}) &= \sum_{n=1}^N b_n \chi_n(y) e^{-\Im q_n x} \begin{pmatrix} \sin(\Re q_n x + \phi_n^e) \\ \sin(\Re q_n x + \phi_n^h) \end{pmatrix},\end{aligned}\quad (5.23)$$

where  $k_{yn} = n\pi/W$  is the transverse wavenumber,  $\chi_n(y) = \sqrt{2/W} \sin(k_{yn}y)$  are the transverse eigenfunctions of the infinite waveguide. In contrast to the ‘‘handwaving’’ derivation of the Andreev phase (5.11), we now correctly distinguish between

$$k_n^{e,h} = \sqrt{\frac{2m_{\text{eff}}}{\hbar^2} (E_F \pm \varepsilon) - k_{yn}^2}, \quad (5.24)$$

the longitudinal wavenumber in the normal conducting region of the waveguide, and

$$q_n = \sqrt{\frac{2m_{\text{eff}}}{\hbar^2} (E_F - i\sqrt{\Delta^2 - \varepsilon^2}) - k_{yn}^2}, \quad (5.25)$$

in the S-region.  $\Re q$  and  $\Im q$  denote the real and imaginary part of  $q$  respectively. We have made use of the fact that, in the absence of a magnetic field, time reversal symmetry allows us to choose the wave function to be real. In the following, we take  $x_{\text{SN}} = 0$  to simplify our notation.

We insert the ansatz (5.23) into the wave function matching conditions (5.10) at the SN-interface. The transverse eigenfunctions are orthogonal to each other, and identical in the  $N$  and  $S$  region. As a consequence, the matching conditions (5.10) separate into  $4N$  linearly independent equations. It is important to note that the procedure is exact up to this point as it does neither rely on  $\Delta \ll E_F$  nor on approximately perpendicular angles of incidence on the SN interface. Thus, the Andreev retroreflection process is described in full detail within the framework of the BdG equation.

After eliminating the unknown coefficients  $c_n^{e,h}$  and  $b_n$  by division, one arrives at:

$$\frac{\Re q_n - \Im q_n \tan(\phi_n^e)}{k_n^e} \tan k_n^e L = \tan \phi_n^e, \quad (5.26a)$$

$$\frac{\Re q_n - \Im q_n \tan(\phi_n^h)}{k_n^h} \tan k_n^h L = \tan \phi_n^h. \quad (5.26b)$$

with  $E_F^n = (\hbar k_n)^2/2m_{\text{eff}}$  and  $k_n = k_n^{e,h}(\varepsilon = 0)$ . To obtain an analytical

expression of the Andreev phase, we rewrite the tangents according to

$$f(x) \tan \alpha = \tan \left[ \alpha + \sum_{k=0}^{\infty} f_k x^k \right], \quad (5.27)$$

where  $f(x)$  is a smooth function. As the  $\tan(x) \in [-\infty, \infty]$ , it is always possible to determine coefficients  $f_k$  in such a way that the above identity holds for a given  $x$ . To determine the  $f_k$ 's that are independent of  $x$ , consider a Taylor expansion of both the right and left hand side of Eq. (5.27) around  $x = 0$ . By comparing coefficients of the different powers of  $x$ , the  $f_k$  are uniquely determined. This is, of course, only possible if  $f(x)$  has a Taylor-expansion around  $x = 0$ . In the present case, we use  $x = \varepsilon/E_F^n \ll 1$  as expansion parameter for  $f^{e,h}(x) = [\Re q_n^{e,h} - \Im q_n^{e,h} \tan(\phi_n^{e,h})]/k_n^{e,h}$ . We insert the identity (5.27) into Eq. (5.26), using , with  $E_F^n = (\hbar k_n)^2/2m_{\text{eff}}$ . By applying some trivial algebra, we arrive at the expansion

$$\beta_n^h - \beta_n^e + \sum_{k=1}^{\infty} (f_k^e - f_k^h) \left[ \frac{\varepsilon}{E_F^n} \right]^k = m\pi + \phi_n^e - \phi_n^h. \quad (5.28)$$

The term  $m\pi$  appears because the tangent is periodic in  $\pi$ . The zeroth order expansion coefficient  $f_0$  must be the same for the electron and the hole, as we expand around  $\varepsilon = 0$ , and thus cancels. The first non-vanishing contribution is thus given by  $f_1^{e,h} = \sin(2\beta_n^{e,h})/4$ . Note that Eq. (5.28) gives a, within the framework of the BdG equation, exact account of the phase shift in our model system. We will now proceed by applying Eq.(5.28) to different model systems.

### 5.3.2 EBK quantization

The expressions we derived in the Bohr-Sommerfeld treatment of Andreev billiards [see Eq. (5.16)] contained terms up to order  $\varepsilon/E_F$ . Including the first-order term in the series Eq. (5.28) amounts to

$$(k_n^e - k_n^h)L = m\pi + \phi_{eh} - \underbrace{\frac{\varepsilon}{4E_F^n} (\sin 2\beta_n^e + \sin 2\beta_n^h)}_{\phi_{\text{SN}}^e + \phi_{\text{SN}}^h}, \quad (5.29)$$

where we inserted  $\phi_n^e - \phi_n^h = \arccos(\varepsilon/\Delta) = \phi_{eh}$ . The different terms in (5.29) correspond closely to those in the semiclassical BS quantization condition (5.16). The term on the left hand side mimics the linearized difference in action between electron and hole. We stress here that (5.29) is the result

of an analytic ansatz to solve the BdG equation while (5.16) is the result of a semiclassical quantization of periodic orbits. Note that the semiclassical quantization relies on the two large quantities  $S_e$  and  $S_h$  nearly canceling each other and thereby giving a contribution of the order  $\varepsilon/E_F$ , which cannot be considered large compared to  $\hbar$ . However, a semiclassical approximation consists of neglecting terms of order  $\hbar$ . From this point of view, it is surprising that a semiclassical description of Andreev billiards relying on periodic orbits works as well as it does.

The term  $\phi_{eh}$  in (5.29) describes the phase difference between electron and hole wave function in the superconductor [see Eq. (5.11)]. The last term on the right hand side corresponds to the two phase jumps  $\phi_{SN}$  caused by the different wavelengths in the N- and S-region. It resembles the phase shift accumulated by a beam of light when it transverses a thin layer of e.g. glass, which has a refraction index  $\mathbf{n} \neq 1$ . To see this, consider a standing plane wave  $\sin(k_1x + \phi_1)$  with wavenumber  $k_1$ , in contact with a transparent medium at, e.g. a layer of glass, at  $x = 0$ . The light enters the glass with a wavenumber  $k_2 = k_1 + \delta k$  and a phase  $\phi_2$ . The standing wave has to fulfill the matching conditions at the boundary

$$A \sin(\phi_1) = B \sin(\phi_2) \quad (5.30a)$$

$$k_1 A \cos(\phi_1) = k_2 B \cos(\phi_2) \quad (5.30b)$$

at  $x = 0$ . Using again the relation (5.27), this results, to first order in  $\delta k$ , in

$$\phi_1 - \phi_2 \approx \frac{\delta k}{2k_1} \sin(2\phi_1) + m\pi. \quad (5.31)$$

This has the same form as the correction term  $\phi_{SN}$  in Eq. (5.29). Thus, the complete phase correction due to one Andreev reflection consists of: (i) one phase shift of  $\phi_{SN}^e$  upon entering the superconductor as electron; (ii) the phase shift of  $\arccos(\varepsilon/\Delta)$  due to the transition from electron to hole and (iii) a second contribution of  $\phi_{SN}^h$  upon leaving the superconductor again as a hole.

In order to test the above results, we will apply them to the different geometries we considered in the previous section. We again begin with the simple case of the quadratic box geometry. Due to the separability of this structure, the phases  $\beta^{e,h}$  can be determined analytically using the boundary conditions at the right wall,  $\phi_N(L, y) = 0$ . The total phase shift  $\phi_A$  due to Andreev reflection amounts to

$$\phi_A = \phi_{SN}^e + \phi_{SN}^h + \phi_{eh} = \arccos\left(\frac{\varepsilon}{\Delta}\right) - \frac{\varepsilon}{4E_F^n} [\sin(2k_n^e L) + \sin(2k_n^h L)]. \quad (5.32)$$

This expression can now be used in a semiclassical description of the density of states. Due to the separability of the structure, the two dimensional problem can be decomposed into two one-dimensional ones. This allows us to use the Einstein-Brillouin-Keller (EBK) quantization [125] to quantize the action along the two topologically distinct orbits present in the billiard. One is the motion in  $x$  direction, involving the superconductor:

$$\frac{S_x}{\hbar} \oint_{\mathcal{C}_x} k_x^{e,h} dx = 2L(k_x^e - k_x^h) = 2[n\pi + \phi_A]. \quad (5.33)$$

The action of the hole contributes with a negative sign. The periodic Andreev orbit  $\mathcal{C}_x$  corresponds to an electron and hole with zero momentum in  $y$ -direction. The quantization condition in  $y$  direction is a simple box quantization

$$\oint_{\mathcal{C}_y} k_y dy = 2k_y D = 2m\pi. \quad (5.34)$$

We insert this quantization in  $y$ -direction into (5.33), and introduce the short hand notation  $k_x^m(\pm\varepsilon) = k_m^\pm$ , with

$$k_m^\pm = \sqrt{\frac{2m_{\text{eff}}}{\hbar^2}(E_F \pm \varepsilon) + \left(\frac{m\pi}{W}\right)^2}, \quad (5.35)$$

The quantization condition for  $x$  [Eq. (5.33)] then reads

$$[n\pi + \phi_A] = L [k_m^+ - k_m^-]. \quad (5.36)$$

This is a transcendental equation in  $\varepsilon(n, m)$ , which allows us to calculate individual energy levels in a cavity with  $W = D$  semiclassically. EBK quantization of Andreev billiards can be viewed as the analogue to the adiabatic quantization of smooth soft-wall chaotic billiards, for completely integrable systems [130, 131]. Note that the BS approach yields only an approximation to the smoothed state counting function  $N(\varepsilon)$ . In contrast, the EBK formulation allows us to calculate semiclassically the individual energy levels of the separable box cavity.

To check the merits of the additional phase term, we compare the semiclassical EBK results with and without phase contribution  $\phi_{\text{SN}}^{e,h}$  to the exact quantum mechanical eigenenergies calculated by solving the BdG equation (see Fig. 5.11). We observe previously unreported sinusoidal oscillations in the integrated DOS, which are perfectly accounted for by the inclusion of  $\phi_{\text{SN}}$ . Due to the high number of transverse modes (50), two full periods are discernable. We will derive an expression for the oscillation period below, when we consider non-separable structures.



For separable structures, as the box discussed here, the phase index  $\phi_{\text{SN}}$  may be calculated to arbitrary accuracy by including higher orders in the expansion (5.27). Note that while semiclassical expansions are usually performed in powers of  $\hbar$ , the special properties of Andreev billiards suggest  $\varepsilon/E_{\text{F}}^n$  as appropriate order parameter: For  $\varepsilon = 0$ , Andreev reflection is ideal and exactly described by a Maslov index of 1 (i.e. a phase of  $\pi/2$ ). For finite  $\varepsilon$ , corrections due to the different properties of normal- and superconductor start to appear.

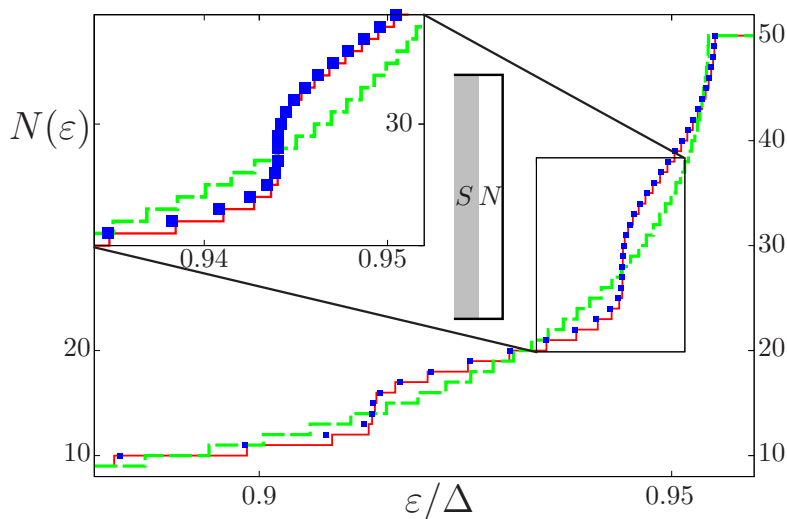


Figure 5.11: Quantum mechanical state counting function (red staircase) and semiclassical BS approximation with (blue squares) and without (green dashed line) the term (5.38) describing the wavelength mismatch between normal and superconductor (see text). We consider a broad SN interface ( $W = D = 10L$ ), 50 open modes and a Fermi wavenumber of  $k_{\text{F}} = 50.51\pi$ . The inset shows a close up view of one oscillation.

### 5.3.3 Improved BS approximation

We now proceed to the non-separable box geometry, i.e.  $W < L$  (see the inset of Fig. 5.12). This system cannot be described by a simple EBK approach. To correct the Maslov index using  $\phi_{\text{SN}}$ , we have to find an expression for the phase  $\beta^{e,h}$  of the wave function at the SN interface. A semiclassical interpretation is the phase difference accumulated between incoming and outgoing particle by the movement in  $x$  direction, i.e. the one perpendicular to the SN interface. Because  $\theta$ , the angle of incidence on the SN interface, is (up to a sign) a constant of motion in rectangular billiards, this phase

difference is given by  $\beta^{e,h} = k_F l \cos^2 \theta$ . Expanding the semiclassical EBK quantization [Eq. (5.33)] to first order in  $\varepsilon$  then results in

$$\frac{m_{\text{eff}}}{\hbar^2} \frac{\varepsilon}{k_F} s = m\pi + \phi_{eh} + \varepsilon \frac{\sin(k_F s \cos^2 \theta)}{2E_F \cos^2 \theta}, \quad (5.37)$$

where we used the semiclassical approximation [125]  $k_F^n \approx k_F \cos \theta$ .

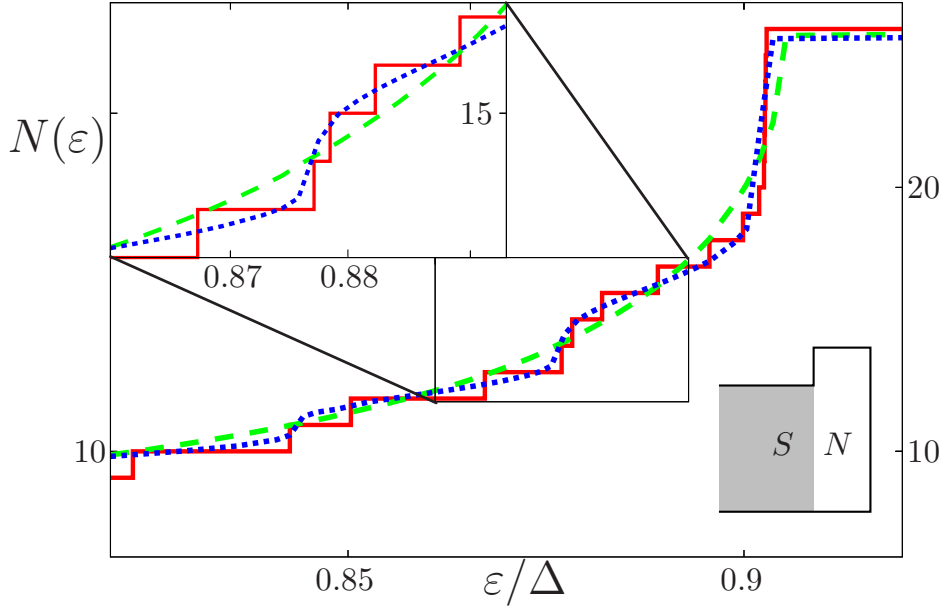


Figure 5.12: Comparison between quantum mechanical state counting function  $N_{\text{QM}}(\varepsilon)$  (red solid staircase), and semiclassical BS approximation with (blue dotted line) and without (green dashed line) a phase contribution  $\phi_{\text{SN}}$ . The left inset shows a magnification. The non-separable geometry is shown in the bottom right inset:  $D/W = 1.3$ ,  $L/W = 0.3$ , and  $k_F = 25.51\pi$ .

Unlike the phase  $\arccos(\varepsilon/\Delta)$ , the term  $\phi_{\text{SN}}$  in Eq. (5.29) depends on the angle of incidence  $\theta$ , and thus cannot be directly inserted into Eq. (5.20). In order to solve this problem, we introduce a modified path length  $\tilde{s}$  according to

$$\tilde{s} = s - \frac{\sin(k_F s \cos^2 \theta)}{k_F \cos^2 \theta}, \quad (5.38)$$

which takes into account the phase jump due to the transition from normal to superconductor. This definition enables us to rewrite Eq. (5.37) as

$$\tilde{s} = (m\pi + \phi_{eh}) \frac{\hbar^2}{m_{\text{eff}}} \frac{k_F}{\varepsilon}. \quad (5.39)$$

When calculating the different individual trajectories needed to determine the path length distribution  $P(s)$ , the length of each trajectory is modified according to (5.38). The resulting modified distribution  $\tilde{P}(\tilde{s})$  can then be used in Eq. (5.20). A similar trick was used in Ref. [114] to include the influence of soft potential walls.

When compared to quantum mechanical calculations, our additional phase contribution reproduces the oscillations due to  $\phi_{\text{SN}}$  in the quantum mechanical state counting function very accurately (Fig. 5.12). We determine the oscillation period  $\Lambda$  from Eq. (5.38) by dividing  $2\pi\varepsilon$  by the argument of the sine

$$\Lambda = \frac{2\pi\varepsilon}{2k_{\text{F}}^n L} \approx \frac{\pi\varepsilon s}{k_{\text{F}} L^2} \approx \frac{\hbar^2}{m_{\text{eff}}} \frac{\pi^2}{2L^2}, \quad (5.40)$$

where we used the BS expression for  $\tilde{s}$  (5.39), with  $m = 0$  (for the first cusp),  $\phi_{eh} \approx \pi/2$  in the last step. When compared to the mean level spacing  $\delta E = \pi\hbar^2/(W L m_{\text{eff}})$ , [97] this gives a ratio  $\Lambda/\delta E \approx \pi W/(2L)$ . The amplitude of the oscillations depends on the relative weight of the phase correction compared to the geometric trajectory length  $s$  in Eq. (5.38). As a consequence, we expect the contribution  $\phi_{\text{SN}}$  to be important in an arbitrarily shaped Andreev billiard if (i) the width of the superconducting region is large compared to the average length of periodic Andreev orbits in order for the oscillations amplitude to be of the order of the mean level spacing and (ii) the average trajectory length  $s$  is at least of the order of the linear dimension of the billiard. We speculate that these requirements for the appearance of the oscillations not met in many systems might be the reason why the contribution of  $\phi_{\text{SN}}$  has not been considered previously.

### 5.3.4 Eigenstate rearrangement

We now return to the peculiar shift in eigenenergies we observed at the end of the previous section for the half-circle geometry (see subsection 5.2.4). The application of our extension is more challenging for this system: Due to the curved boundary, the angle of incidence on the SN interface,  $\theta$ , is not conserved between subsequent reflections at the interface. As a consequence, trajectories with equal length have a wide range of possible angles of incidence (i.e. unlike the rectangular case, where  $s = 2nL/\cos(\theta)$ ). Consequently, the contribution of  $\phi_{\text{SN}}$  to the smoothed density of states  $N(\varepsilon)$  goes to zero. This explains why the general agreement between  $N_{\text{BS}}$  and  $N_{\text{QM}}$  already was very satisfactory without taking into account an additional phase correction. However, the above considerations can still be applied to individual energy levels. To extend the definition of  $\phi_{\text{SN}}$  to a given Andreev state, consider a one-dimensional wave of the form  $\phi(x) = \sin(kx + \alpha)$ . The phase  $\alpha$  can

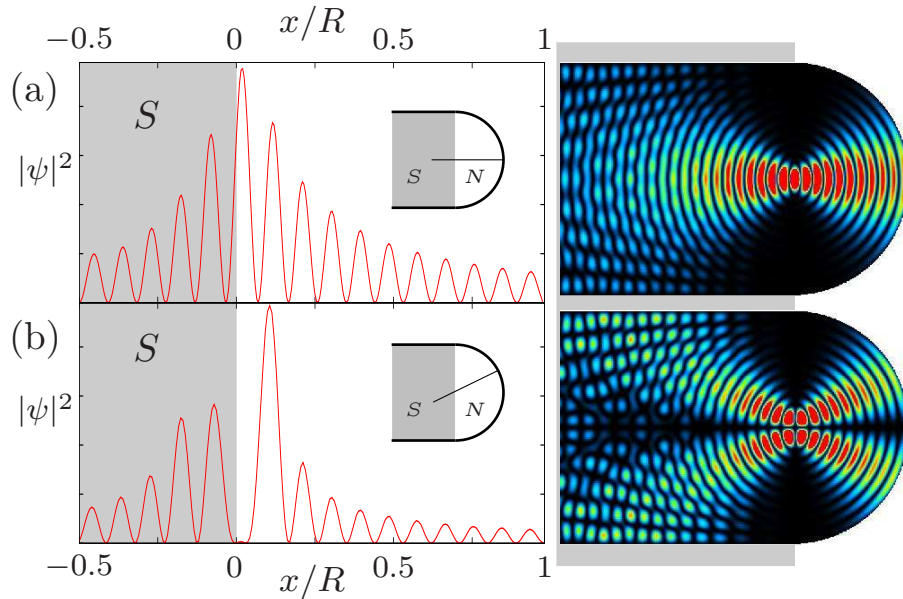


Figure 5.13: Two eigenstates of a half-circular Andreev billiard connected to a superconducting lead. The graphs to the left show a cut through the two-dimensional wave function along the semiclassical orbit marked in the inset. While the derivative of the wave function at the SN interface is maximal in (a), it vanishes in (b). As a consequence, the contributions of  $\phi_{\text{SN}}$  to the two different eigenstates are different (see text).

be connected to the logarithmic derivative  $\mathcal{F}_0 = \partial_x \ln \phi^{e,h}|_{x=0}$  of  $\phi$  by  $\alpha = \arctan \mathcal{F}_0/k$ . This allows us to express  $\phi_{\text{SN}}$  by the value of the quantum mechanical wave function at the SN-interface according to

$$\phi_{\text{SN}}^{e,h} = \alpha_S - \alpha_N = \frac{\varepsilon \mathcal{F}_0^{e,h}/k_F}{1 + (k_F \mathcal{F}_0)^2}. \quad (5.41)$$

We will now apply this expression to two eigenstates of the half-circle billiard to explain an observed energy shift between states of different parity: The half-circle geometry is symmetric upon inversion of the  $y$  direction. A quantum mechanical treatment yields a noticeable energy shift of  $0.01\varepsilon/\Delta$  between eigenstates of even and odd parity. A semiclassical BS approximation for the state with the shortest  $s = 2R$ , where  $R$  is the radius of the half-circle, predicts an energy of  $\varepsilon = 0.842\Delta$ . This coincides with the quantum mechanical calculations for the bound state with the highest energy. [which semiclassically corresponds to the smallest  $s$ , see Eq. (5.39)]. The mean level spacing in the normal dot amounts to  $\delta E = 0.15\Delta$ , making the above semiclassical result exceedingly accurate. Apparently, no correction due to  $\phi_{\text{SN}}$  is

required. The corresponding eigenstate is shown in Fig. 5.13(b). Note that it is a state of odd parity with respect to the  $y$  axis. It shows a distinct enhancement along two bundles [124] of semiclassical trajectories of length  $s = 2R$ . When considering the value of the wave function at the SN interface [Figure 5.13(a) shows the electron density along the semiclassical orbit], we find that it has a pronounced minimum precisely at the SN interface  $x_{\text{SN}} = 0$ . As a consequence, the above expression for  $\phi_{\text{SN}}$  [see Eq. (5.41)] vanishes, as expected from the accurate result of the semiclassical BS approximation. The eigenstate shown in Fig. 5.13(b) is even. It shows a similar enhancement along a semiclassical orbit of length  $2R$ , which, however, leaves the center of the half-circle perpendicular to the SN interface. Its quantum mechanical eigenenergy of  $\varepsilon = 0.836\Delta$  is, however, lower than for the state shown in (b), even though the corresponding semiclassical orbit is by no means longer. In contrast to the odd state, the wave function does not vanish at the SN interface, as can well be seen in Fig. 5.13(a). There is a maximum of the logarithmic derivative at  $x \approx x_{\text{SN}}$ , which upon insertion into Eq. (5.41) yields a phase correction of  $2\phi_{\text{SN}} = 0.006$ . This correction shifts the semiclassical prediction down to  $\varepsilon = 0.837\Delta$  (from 0.842). The expression for  $\phi_{\text{SN}}$  is not only able to qualitatively explain the energy shift between the two states, but gives an accurate quantitative prediction. We apply Eq. (5.41) to the other eigenstates of the half-circle Andreev billiard with equally good agreement. The reason for a systematic shift between even and odd states is that the Bessel function  $J_0$ , which is only included in the solution for even states, is the only one which gives a contribution at the center of the half-circle, the starting point of most semiclassical trajectories at energies close to the cusp. As a consequence, only those eigenstates give a non-vanishing  $\mathcal{F}_0$ .

## 5.4 Validity of the retracing approximation

After discussing the Andreev reflection process as well as its influence on the state counting function, we now turn our attention to the limitations of the semiclassical description. The BS approach to the DOS of an Andreev billiard relies on three assumptions: exact retracing of electron-hole trajectories (referred to as assumption A1 in the following, [130]), the absence of any quasi-periodic orbits other than the ones caused by Andreev reflection (assumption A2, [132]), and the applicability of semiclassical approximations (assumption A3, [133, 130, 134, 135, 136]), i.e.  $\lambda_D \ll \sqrt{A}$ , where  $\lambda_D$  is the de Broglie wavelength and  $A$  is the area of the  $N$  billiard. Our aim is to assess the validity of the retracing approximation and to provide quantitative criteria for its applicability for a given structure. Non-retracing electron-hole orbits leave their mark on the Andreev wave functions as well. We find that Andreev states which correspond to non-retracing orbits (i.e. those that are not well-described by a BS-approximation) break the close correspondence between the electron and hole wave function patterns. The analysis of the eigenstates thus allows us to check on the merits and limitations of the BS approximation against the exact quantum mechanical results.

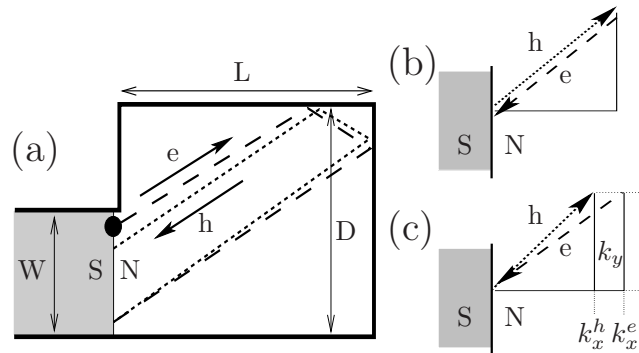


Figure 5.14: (a) Andreev billiard with a rectangular normal-conducting ( $N$ ) region. The superconducting ( $S$ ) lead is assumed to be half-infinite (shaded area). The dashed and dotted lines depict an “almost retracing” electron-hole orbit created by Andreev reflection at the  $SN$ -interface. For better visibility the starting point of the orbit is marked by a dot. (b) perfect Andreev reflection, i.e.  $\theta_e = \theta_h$ . (c) imperfect Andreev reflection,  $\theta_e \neq \theta_h$ ,  $k_y^e = k_y^h$ .

We will explore the validity and breakdown of the retracing approximation and the resulting BS quantization by returning to the rectangular cavities discussed in the previous section. In the following subsections, we consider different ratios  $D/W$  and  $D/L$  (see Fig. 5.15). With this parameter

space at our disposal we can probe and disentangle the validity of assumptions A1 to A3. Since within the framework of perfect Andreev reflections combined SN-Andreev systems become regular and, in fact, periodic irrespective of the underlying regular or chaotic dynamics of the  $N$ -cavity, we expect many of our results to be valid for arbitrary  $N$ -cavities. To explicitly test this assumption, we will investigate a cavity featuring chaotic dynamics in subsection 5.4.4.

### 5.4.1 Stretched separable billiard

The intuitive picture of ideal Andreev reflections [Fig. 5.14(b)] lends itself to a semiclassical description and, more specifically, to a periodic-orbit quantization, as discussed in the previous sections. However, the retroreflection process is not perfect. The electron approaches the SN-interface with wave number

$$k_e = \sqrt{\frac{2m_{\text{eff}}}{\hbar^2}(E_F + \varepsilon)} \quad (5.42)$$

and angle  $\theta_e$  relative to the interface normal. The hole leaves the interface with wavenumber

$$k_h = \sqrt{\frac{2m_{\text{eff}}}{\hbar^2}(E_F - \varepsilon)}. \quad (5.43)$$

and a corresponding angle  $\theta_h$ . Since the component along the interface is exactly conserved because of translational invariance,  $k_{e,y} = k_{h,y}$  (or  $v_{e,y} = -v_{h,y}$ ) the components normal to the interface will be, in general, different  $k_{e,x} \neq k_{h,x}$ , leading to imperfect retracing [Fig. 5.14(c)]. Only in the limit  $\varepsilon \rightarrow 0$  (or  $\varepsilon/E_F \rightarrow 0$ ) perfect Andreev reflection  $k_{e,x} = k_{h,x}$  (or  $v_{e,x} = -v_{h,x}$ ) ensues. The retracing approximation consists now of the assumption A1 of perfect reflection,  $v_{e,x} = -v_{h,x}$ , for all  $\varepsilon$  in the interval  $0 \leq \varepsilon \leq \Delta$ . The validity and breakdown of this assumption will be explored in the following.

Under assumption A1 all trajectories emanating from the SN-interface are strictly periodic. For  $N$ -cavities featuring hard chaos, every trajectory will eventually hit the SN-interface, thus yielding a globally periodic system. For  $N$ -cavities with mixed or regular dynamics, certain regions of the phase space may remain decoupled from the interface and thus may feature both continuous manifolds of strictly periodic orbits and islands with quasi-periodic motion. Neglecting the latter contribution to the DOS implies assumption A2.

We now stretch the billiard to  $D/L \ll 1$  [see Fig. 5.15(a)] without, however, changing the Fermi energy  $E_F$  of the system. The distance  $s$  traveled between two encounters with the SN-interface is, for the shortest orbits, at

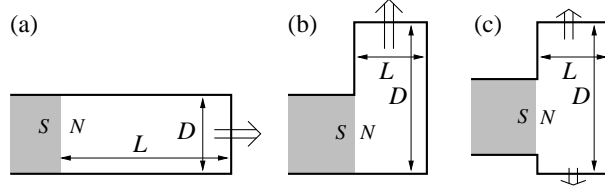


Figure 5.15: *Geometries with tunable boundaries: (a) stretched N-cavities with  $L \gg D$  but with  $D$  equal to the width of the SN-interface  $W = D$ . (b) stretched N-cavities with  $D \gg L$  but constant length  $L$  (lower boundary of  $S$  and  $N$  aligned). (c) as (b) but SN-interface at arbitrary position on the entrance side.*

least  $2L$ . The effect of imperfect retracing, originating from the difference in angles between  $\theta_e$  and  $\theta_h$ , is a divergence between electron and hole trajectories ( $\propto s$ ), which is amplified by large  $L$ . We introduce as a measure for the imperfect retracing the lateral displacement  $\delta y$  on the interface between the hole and the particle trajectory after one loop (see Fig. 5.16),

$$\begin{aligned} \delta y &= s |\sin(\theta_e) - \sin(\theta_h)| \\ &= s \frac{\varepsilon \sin \theta}{E_F} + O(\varepsilon^2), \end{aligned} \quad (5.44)$$

where  $\theta = \theta_{e,h}|_{\varepsilon=0}$ . For the particular geometry considered [Fig. 5.15(a)],  $\delta y$  increases linearly with both the trajectory length  $s$  and the excitation energy  $\varepsilon$ . Note that the ratio  $\varepsilon/E_F$  is, in general, much smaller than one, i.e.  $\varepsilon \leq \Delta \ll E_F$ .

This classical scale for the mismatch between the particle and hole orbits should be related to the quantum scale, i.e. the linear dimension of the wave packet estimated by the de Broglie wavelength  $\lambda_F$ . We thus introduce  $r = |\delta y|/\lambda_F$  as order parameter for the error of retracing. For  $r \ll 1$  the wave packet cannot resolve the mismatch and the BS approximation should work well. Conversely, as  $r$  reaches the order of unity, quantization based on the existence of a continuum of periodic orbits should fail.

To probe the breakdown of the retracing approximation quantitatively, we compare the semiclassical with the quantum density of states (DOS), which are obtained from the state counting function  $N(\varepsilon)$  as

$$\rho_{\text{BS,QM}}(\varepsilon) = \frac{\partial N_{\text{BS,QM}}(\varepsilon)}{\partial \varepsilon} \quad (5.45)$$

since the DOS is more sensitive to errors than the (smoothed) spectral staircase. Results for two cavities with different values of  $L$  are shown in



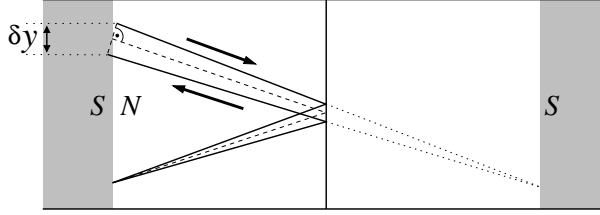


Figure 5.16: *Imperfect Andreev reflection in the fundamental and extended zone scheme. The returning hole hits the SN-interface a distance  $\delta y$  apart from the starting point of the particle.*

Fig. 5.17(a) and (b). This example illustrates that the degree of agreement between  $\rho_{\text{QM}}$  and  $\rho_{\text{BS}}$  is indeed controlled by  $r$ . The following trends can be observed: (i) due to the comparatively shorter length  $s$  of orbits in (a), the overall agreement there is better in (a) than in (b). (ii) The agreement in (b) deteriorates for larger values of  $\varepsilon/\Delta$ , since the mismatch in retracing increases with  $\varepsilon$ .

As a measure for the average mismatch between  $\rho_{\text{QM}}$  and  $\rho_{\text{BS}}$  in an Andreev billiard of given geometry we use the quantity  $\overline{\delta y}$ ,

$$\overline{\delta y} = \frac{1}{\pi\Delta} \int_{-\pi/2}^{\pi/2} d\theta \cos\theta \int_0^\Delta d\varepsilon \delta y = \frac{2L\Delta}{\pi E_F}, \quad (5.46)$$

i.e.  $\delta y$  averaged over all  $\varepsilon$  and all angles. For this particular geometry  $s = 2L/\cos\theta$ . The error in the DOS is quantified in terms of the root mean square (RMS) deviation  $\delta\rho$  between  $\rho_{\text{BS}}$  and  $\rho_{\text{QM}}$ ,

$$\delta\rho = \sqrt{\frac{1}{\Delta} \int_0^\Delta d\varepsilon |\rho_{\text{QM}} - \rho_{\text{BS}}|^2}. \quad (5.47)$$

As expected, as long as  $\bar{r} = \overline{\delta y}/\lambda_F \ll 1$ , the retracing approximation is sufficiently accurate to reproduce the DOS on the scale of the mean level spacing [see Fig. 5.17(c)]. Note that resolution of individual levels is beyond the scope of the BS approximation. As discussed in the previous section, an EBK quantization is needed for an accurate quantization of individual levels. As  $\bar{r}$  approaches unity the oscillations in the quantum DOS cannot be resolved any longer. The error  $\delta\rho(\overline{\delta y})$  appears to saturate, in agreement with the observation that in this regime the main peaks in Fig. 5.17(b) [corresponding to the main cusps in  $N(\varepsilon)$ ] remain well described by the retracing approximation. Identifying the latter with the shortest Andreev-reflected orbits of length  $\sim 2L$  allows a simple explanation as to why even a drastic elongation of the

cavity leaves the cusps well described by the retracing approximation: orbits of length  $\sim 2L$  correspond to strictly horizontally injected trajectories (with  $\theta = 0$ ). They do not accumulate any lateral displacement  $\delta y$  irrespective of the length of the orbit and  $\varepsilon$ . While the average value  $\overline{\delta y}$  is increasing with growing cavity elongation (due to orbits with  $\theta \neq 0$ ), the horizontal orbits limit the increase  $\delta\rho(\overline{\delta y})$ , leading to the observed saturation in Fig. 5.17(c) for  $\overline{\delta y} > \lambda_F$ .

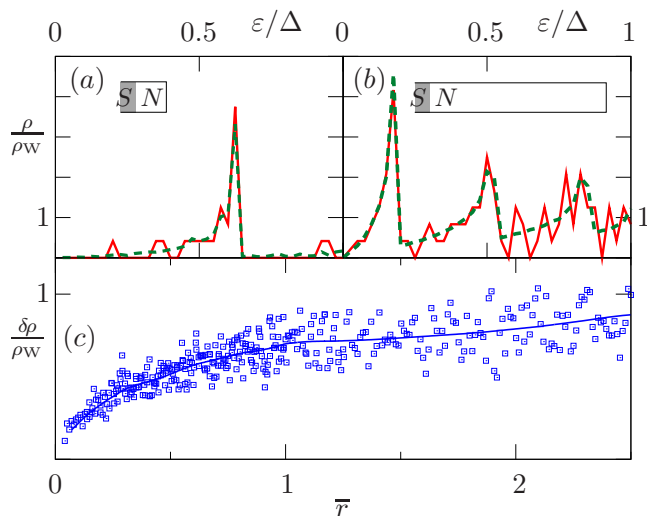


Figure 5.17: The DOS calculated quantum mechanically (red solid curve) and by the BS approximation (green dashed curve) for two different geometries with ratios of (a)  $L/D = 1$  and (b)  $L/D = 6$  (see insets) in units of the Weyl approximation of the DOS per unit area,  $\rho_W = m_{\text{eff}}/(\hbar^2\pi)$ . (c) error of the semiclassical prediction  $\delta\rho$  [Eq. (5.47)] as a function of an energy-averaged  $\bar{r}$  [Eq. (5.46)] for 300 different ratios of  $L/D \in [1, 20]$ . The solid blue line shows a smoothed average (30 adjacent points) of the recorded data.

Additional evidence that the discrepancy between the quantum DOS and the BS spectrum is due to the retracing assumption (A1) and not due to the failure of semiclassics itself (A3) can be gained from an EBK quantization presented in the previous section. This alternative is of particular interest as it only relies on assumption A3, but does not involve the additional assumptions A1 and A2, thus allowing to disentangle the validity of the semiclassical approximation from that of the retracing approximation. As the EBK quantization invokes quasi-periodic rather than periodic motion no assumption of retracing is involved. Moreover, regions in phase space that will not make contact with the SN-interface are in this geometry of measure zero, i.e. assumption A2 is valid. We therefore transform the EBK results (5.36) for

$\varepsilon(n, m)$  into a state counting function

$$N_{EBK} = \int_0^\varepsilon d\varepsilon' \sum_{m,n} \delta[\varepsilon' - \varepsilon(n, m)] \quad (5.48)$$

and compare both semiclassical approximations with the quantum results.

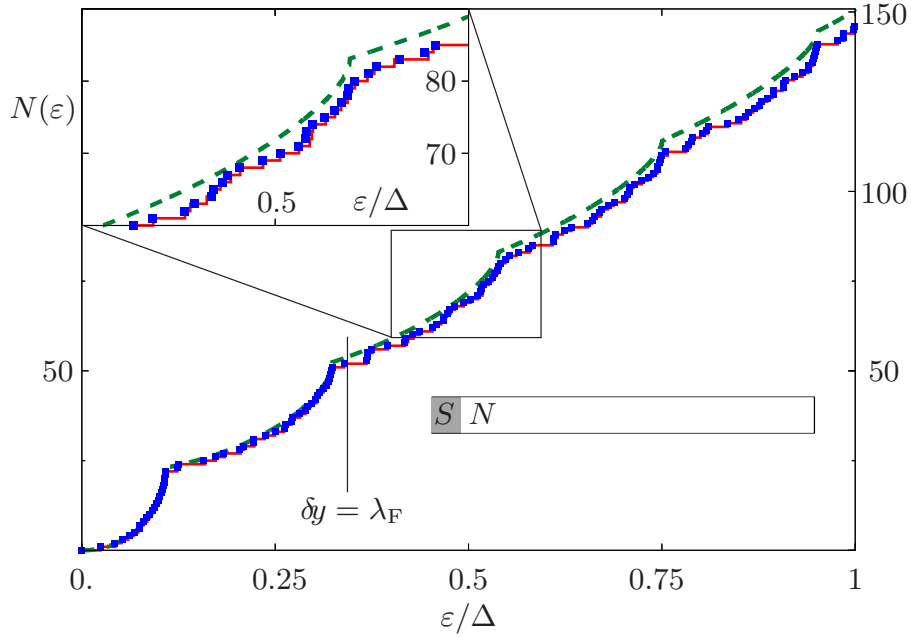


Figure 5.18: Comparison of the exact quantum mechanical state counting function  $N_{QM}$  (red staircase) with the semiclassical BS (green dashed line) and EBK (blue squares) approximations for a highly elongated cavity ( $L/D = 10$ ), as shown in the lower inset. Quantum mechanical and EBK solutions are nearly indistinguishable. The upper inset shows a magnification. The energy for which  $\delta y = \lambda_F$  is marked.

In sharp contrast to the discrepancy between  $N_{QM}$  and  $N_{BS}$ , we observe that  $N_{QM}$  and  $N_{EBK}$  agree almost perfectly in the whole energy interval  $0 \leq \varepsilon \leq \Delta$  (see Fig. 5.18) even for very elongated cavities where most orbits are non-retracing ( $\delta y > \lambda_F$ ). The criterion  $\delta y \approx \lambda_F$  is found to be a good estimate for the transition point where the BS quantization deviates from both the EBK quantization and the exact quantum spectrum. The case of the elongated  $N$ -billiard clearly demonstrates that the failure of the BS quantization in this case is due to the retracing assumption (A1), but not due to the failure of semiclassics (A3) itself.

### 5.4.2 Stretched non-separable billiard

We focus now on billiards stretched in the direction of the SN-interface with  $D/W \gg 1$  and  $D/L \gg 1$  [Fig. 5.15(b,c)]. For  $D/W > 1$  the Andreev billiard becomes non-separable and an EBK quantization is no longer rigorously justified. As the wave functions (Fig. 5.19) clearly indicate, the retracing approximation breaks down with large discrepancies between the particle ( $|u|^2$ ) and hole ( $|v|^2$ ) densities occurring. For this system, one obvious culprit for differences to quantum results is assumption A2. An extended region of classical phase space (Fig. 5.20) remains decoupled from the SN-interface. Consequently, the quantum DOS is associated, in part, with decoupled regions which are not represented at all by the BS approximation. It has previously been pointed out for other geometries (whispering gallery trajectories in circular billiards) that Andreev billiards indeed feature quantum states that are not associated with periodic orbits [97].

A more detailed inspection reveals that a certain class of wave functions has the following features: (1) The probability density at the SN-interface is typically low – corresponding to decoupling from the superconductor. This suggests that the SN-interface effectively acts like a hard-wall boundary. (2) Integrating the probability density in the electron- and hole-part of the N-region typically shows a strong asymmetry. For the case depicted in Fig. 5.19(c) we calculate a probability of 98.3% for the hole component and only 1.3% for the particle component. The coupling with the superconductor is very weak, resulting in a probability of 0.4% of finding the particle in the superconducting lead. These observations suggest that the particles in such non-retracing states are quasi-bound in either the electron- or the hole-space with only infrequent and short excursions to their mirror-space. As a consequence we may employ again an EBK quantization scheme to estimate the corresponding energy level of the Andreev state, however now separately in either the space of the quasi-bound particle or hole. Exploiting the assumption of weak coupling to the SN-interface, we replace the SN-interface by a hard-wall (box) boundary. Applying this approach e.g. to the state depicted in Fig. 5.19(a), the EBK quantization

$$E_{n,m} = \frac{\hbar^2}{2m_{\text{eff}}} \left[ \left( \frac{n\pi}{L} \right)^2 + \left( \frac{m\pi}{D} \right)^2 \right] \quad (5.49)$$

implies for the density of the “isolated” electron state  $n = 6$  maxima in  $x$ -direction and  $m = 205$  maxima in  $y$ -direction. Inserting these quantum numbers yields an excitation energy of  $\varepsilon_{\text{box}} = 0.753\Delta$ , which is very close to the exact eigenenergy of the Andreev eigenstate of  $\varepsilon_{\text{QM}} = 0.760\Delta$ . Analogously, the state depicted in Fig. 5.19(c) has quantum numbers  $n = 1$ ,  $m = 41$ ,

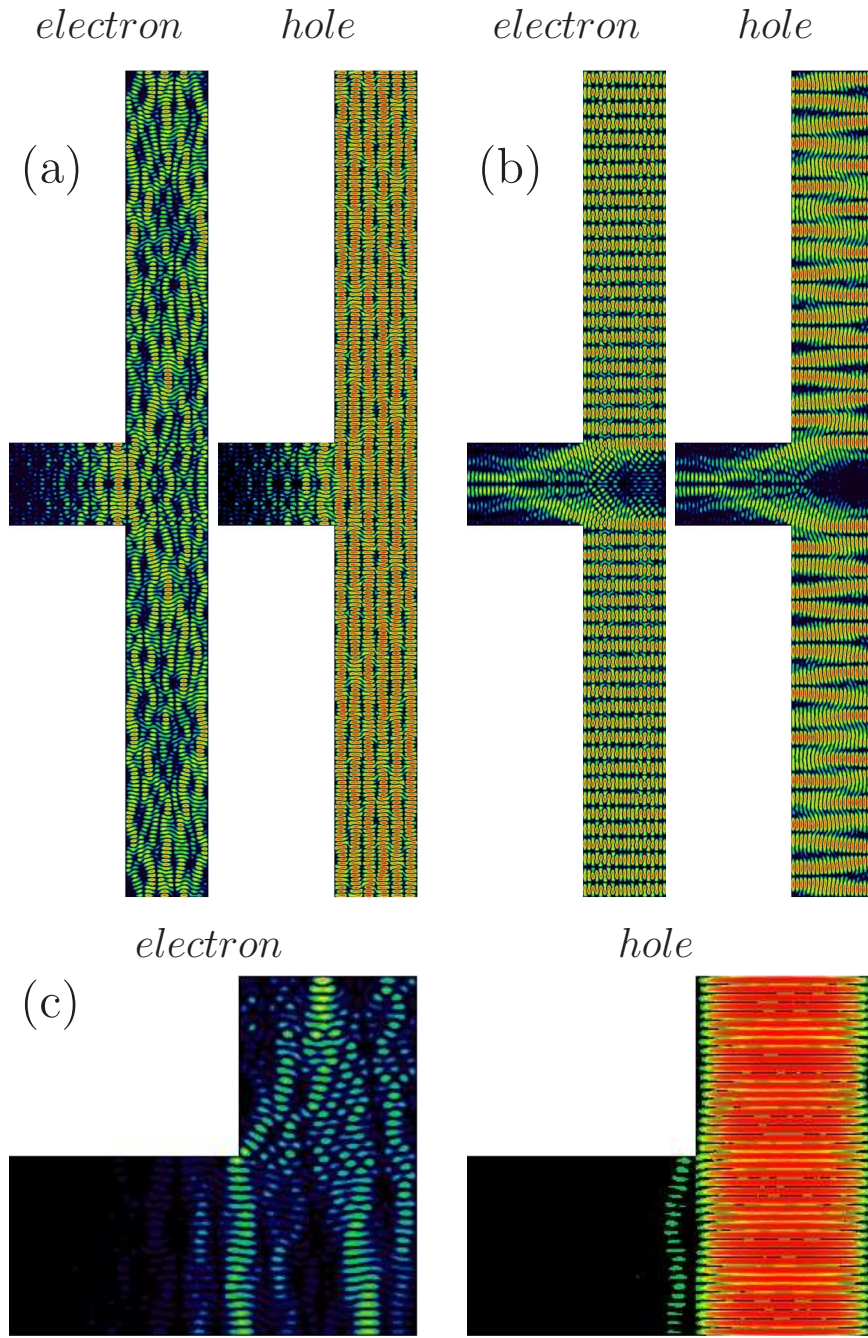


Figure 5.19: Selected Andreev eigenstates of non-separable Andreev billiards stretched parallel to the SN-interface displaying a large discrepancy between electron and hole wave function patterns. (a)  $L/D = 10, \varepsilon = 0.760\Delta$ ; (b)  $L/D = 10, \varepsilon = 0.766\Delta, k_F = 21.5\pi/W$ ; (c)  $L/D = 2, \varepsilon = 0.040\Delta, k_F = 20.5\pi/W$ ;

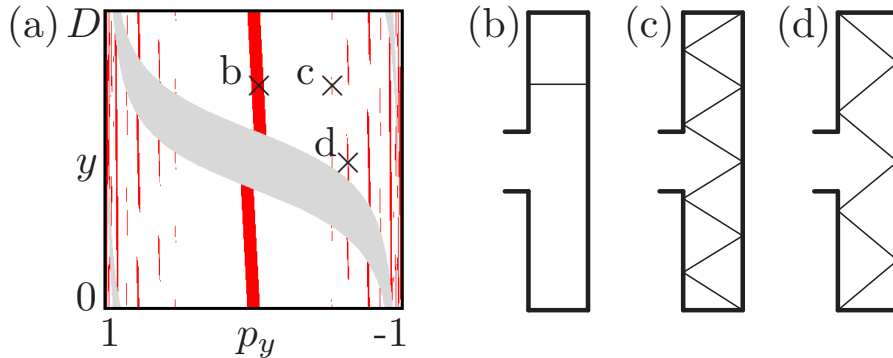


Figure 5.20: (a) Poincaré surface of section of a stretched non-separable Andreev billiard, taken at the right vertical side, opposing the SN-interface:  $W/D = 5$ ,  $W = L$ . The light gray area marks regions of classical phase space coupled directly to the entrance lead, with one single reflection at the right wall. Dark red areas show regions of classical phase space decoupled from the superconducting lead. Classical trajectories corresponding to selected areas of phase space are shown in (b)-(d).

corresponding to a hole excitation of  $\varepsilon_{\text{box}} = 0.038\Delta$ , which compares well to the eigenenergy of the Andreev eigenstate of  $\varepsilon_{\text{QM}} = 0.040\Delta$ . While the position of these Andreev states can thus be explained fairly accurately by a box (or EBK) quantization, they are obviously not included in a standard BS approximation which considers only retracing electron-hole orbits. This illustrates the failure of assumption A2 while semiclassics (assumption A3) still remains applicable.

### 5.4.3 Diffractive effects

For the present hard-wall  $N$ -cavities, introducing non-separability implies simultaneously the introduction of diffractive edges and corners [137] (see Fig. 5.15). In the preceding example, diffractive effects were present but for the special group of states considered of minor importance. The latter was confirmed not only by the density distributions in the Andreev states (Fig. 5.19) but also by the accuracy of the EBK prediction. We can now enhance diffractive effects by considering only moderately stretched cavities  $D/W > 1$  with arbitrary position of the SN-interface. As shown in Fig. 5.21, we can thus realize Andreev billiards with zero corners ( $D/W = 1$ ), one corner ( $D/W > 1$ , lower boundary of S and N aligned), and two corners ( $D/W > 1$ , arbitrary position of the SN-interface). Diffractive effects originate from potential variations on a length scale smaller than the de Broglie

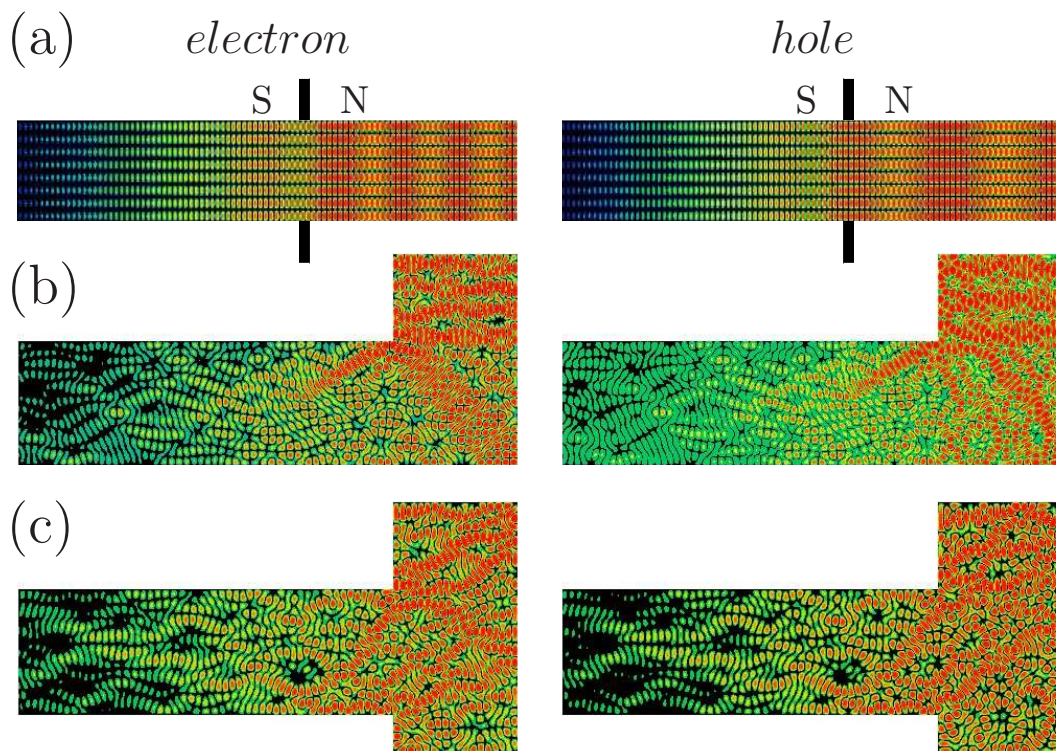


Figure 5.21: Selected Andreev eigenstates of systems with (a) no diffractive corners ( $L/D = 1.6$ ,  $W = D$ ,  $k_F = 20.5\pi/W$ ,  $\varepsilon/\Delta = 0.48$ ); (b) one diffractive corner ( $D/L = 1.7$ ,  $W = L$ ,  $k_F = 21.5\pi/W$ ,  $\varepsilon/\Delta = 0.72$ ); (c) two diffractive corners ( $D/L = 1.7$ ,  $W = L$ ,  $k_F = 20.5\pi/W$ ,  $\varepsilon/\Delta = 0.82$ ).

wavelength. In a semiclassical picture, diffractive scattering gives rise to a non-deterministic, stochastic angular distribution. It certainly prevents the deterministic perfect retracing of orbits.

Traces of diffractive scattering can be directly seen in the wave function [see Fig. 5.21(b,c)]. The density enhancement representing a scar of a classical trajectory hits the corner of the SN-interface. As a result the trajectory “splits” into a bouncing-ball orbit and a broad angular distribution. Significant differences between the particle ( $|u|^2$ ) and hole ( $|v|^2$ ) density in the retracing orbit are clearly visible.

For a more quantitative assessment we compare again the quantum and the BS-results for the DOS [see Fig. 5.22(a,b)] and find, similarly to the case of the separable geometry, that for larger  $D$  the mismatch  $\delta\rho$  in the DOS increases. If we compare, however, how the error  $\delta\rho$  scales with the geometric retracing mismatch  $\delta y$  [Fig. 5.22(c)], we find that in the Andreev billiard with a diffractive corner the average mismatch is considerably larger than for the geometry without a sharp corner. The difference in  $\delta\rho$  at fixed  $\overline{\delta y}$  can be thus attributed to diffraction. Note that diffractive scattering is an additional mechanism for the failure of the retracing approximation, which is independent of the failure induced by long electron-hole orbits.

Additional evidence along these lines is presented in Fig. 5.23 where the mismatch  $\delta\rho$  between the BS approximation and the quantum results as a function of the geometrical aspect ratio of the normal-conducting region is compared for three geometries with either (a) zero, (b) one, or (c) two diffractive corners at the SN-interface. As expected, the mismatch increases (1) for larger aspect ratios and (2) at fixed aspect ratio for an increasing number of diffractive corners. Further support comes from the observation that the mismatch  $\delta\rho$  for the cavity with two diffractive corners is, to a large degree, independent of the position of the lead, as shown in Fig. 5.23.

Unlike other sources for the failure of the retracing approximation discussed above, diffraction limits the validity of standard semiclassical approximations itself, i.e. of assumption A3. Methods for describing diffractive effects semiclassically by including pseudo-paths [119, 138] and non-deterministic scattering [139] have been explored for scattering at open  $N$  cavities. They play a crucial role in determining the  $S$ -matrix for such devices. The present results demonstrate that diffractive corrections come into play also for Andreev systems.

#### 5.4.4 Mushroom billiard

The different cavities discussed above all feature regular dynamics in the normal-conducting case (i.e. with the superconductor replaced by a hard



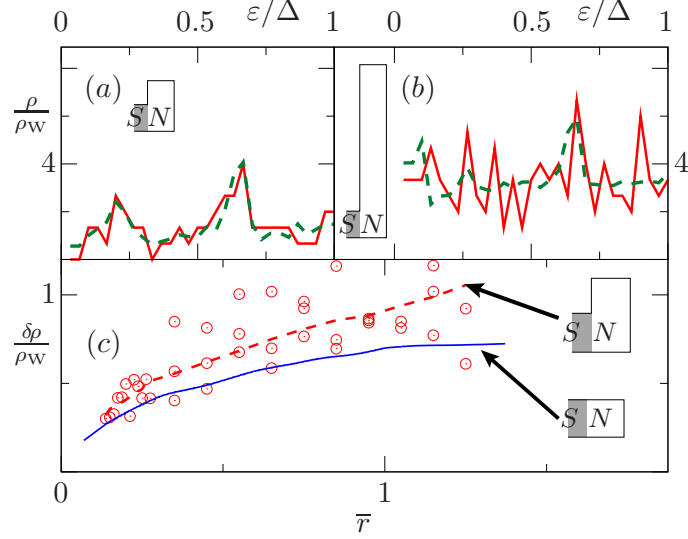


Figure 5.22: The DOS calculated quantum mechanically (red solid curve) and by the BS approximation (green dashed curve) for two different geometries with ratios of (a)  $L/D = 1$  and (b)  $1/8$  (see insets), in units of the Weyl estimate of the DOS per unit area,  $\rho_W = m_{\text{eff}}/(\hbar^2\pi)$ . (c) Error of the retracing approximation  $\delta\rho$  [Eq. (5.47)] for transversely elongated cavities (red circles) as a function of  $\bar{r}$ . The solid blue (dashed red) line shows the average error for longitudinally (transversely) elongated cavities (see also Fig. 5.17).

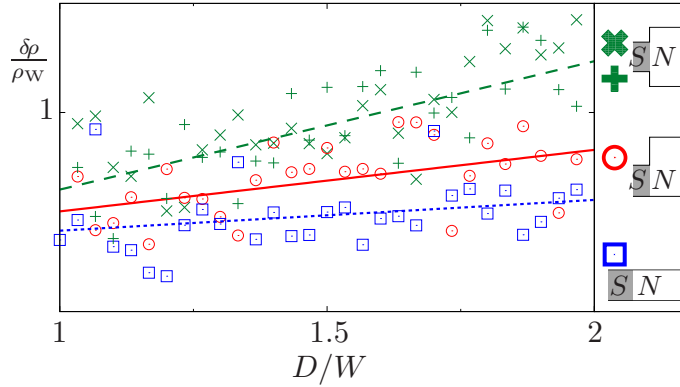


Figure 5.23: Error of the retracing approximation  $\delta\rho$  as a function of  $D/W$  for geometries with no (blue square, dashed line), one (red circle, solid line) and two (green cross, dashed line) diffractive corners. Different orientations of the cross refer to different positions of the superconducting lead. The lines show a linear root mean square fit of the data.

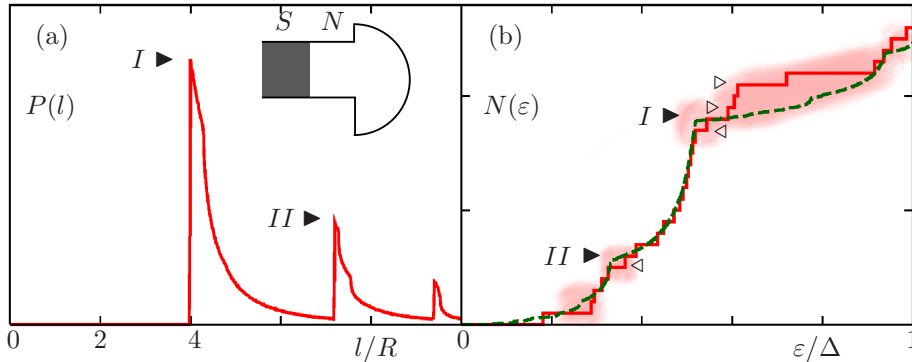


Figure 5.24: (a) Path length distribution  $P(s)$  and (b) state counting function  $N(\varepsilon)$  of the mushroom Andreev billiard. The Fermi energy  $E_F = (17.5\pi)^2/2$ ,  $\Delta = 0.02E_F$ . Two peaks in the path length distribution [marked I and II in (a)] result in corresponding cusps in the state counting function [marked accordingly in (d)]. Open triangles denote energies for which eigenstates are shown in Fig. 5.25.

wall boundary.) To show that our results also apply to a more general set of geometries, we now proceed to a cavity featuring both regular and chaotic dynamics. We again consider a half-circle connected to a lead. If the diameter of the half-circle is chosen larger than the lead width, the billiard takes on the shape of a mushroom. To obtain chaotic dynamics in the normal-conducting case, we move the SN interface a distance  $R$  away from the straight side of the half-circle [see inset in Fig.5.24(a)]. The classical phase space of the resulting structures features a chaotic sea coupled to the stem of the mushroom (where the superconductor is located) and a single regular island of skipping orbits along the boundary of the half-circle [140]. As shown below, these properties lead to explicit violation of all three assumptions A1-A3.

We first check whether the connection between the classical phase space topology, the DOS and superscar patterns in the eigenstates survive for chaotic dynamics. Due to the phase space structure in mushroom billiards, a wide variety of path topologies exists. As a consequence, the classical path length distribution shows pronounced structures [see Fig. 5.24(a)], which translate to several distinct cusps in the state counting function, as discussed in the previous section. We expect eigenstates associated with these different peaks to show different topological structures in their wave function patterns. Indeed, the eigenstates just below a cusp, i.e. the ones best described by the semiclassical approximation, can be distinguished by characteristically different superscar patterns: The first and most prominent peak in the pathlength spectrum  $P(s)$  [marked I in Fig. 5.24(a)] denotes states with length  $s \approx 4R$

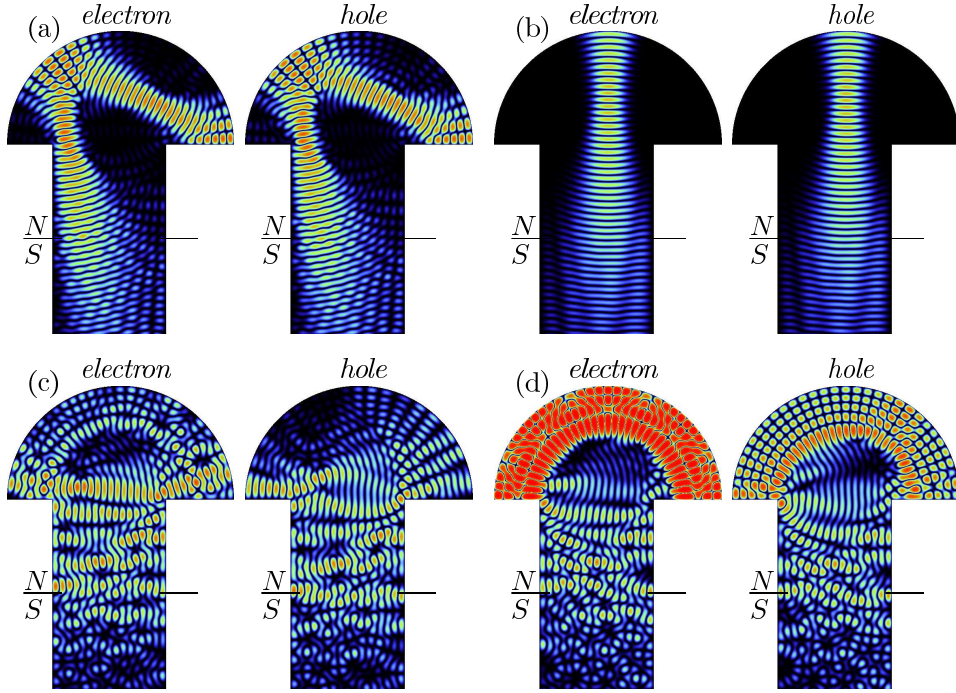


Figure 5.25: (a)-(d) Density of electron and hole eigenfunctions  $|\psi|^2$  of the mushroom Andreev billiard for four different excitation energies  $\varepsilon = 0.33\Delta$ (a),  $0.52\Delta$ (b),  $0.59\Delta$ (c), and  $0.61\Delta$ (d). The Fermi energy was chosen at  $E_F = (17.5\pi)^2/2$ ,  $\Delta = 0.02E_F$ . The corresponding state counting function is shown in Fig. 5.24.

featuring the expected superscar pattern similar to the half-circle billiard [see Fig. 5.25(b)]. The state counting function shows a corresponding cusp (marked I in Fig. 5.24), which is predicted quite accurately by the semi-classical theory. A second cusp (marked II in Fig. 5.24) features eigenstates reflecting once at the straight side of the mushroom hat [see Fig. 5.25(a)]. For both classes of states, patterns in the electron and hole wave functions agree very well.

Overall, however, the correspondence between  $N_{BS}$  and  $N_{QM}$  is, as expected, worse than for regular structures [as indicated by the shaded areas in Fig. 5.25(b)]. The reason for this is the violation of all three assumptions A1-A3: Since we consider a chaotic cavity, nearby trajectories diverge exponentially from each other. Thus, even a small difference in angle between electron and Andreev reflected hole eventually leads to a failure of the semi-classical orbits to close (violation of A1). This observation is in line with the well-known failure of the BS approximation to yield the energy gap for

chaotic  $N$  billiards, [135, 123, 109] also caused by long orbits.

Especially pronounced discrepancies between  $N_{\text{BS}}$  and  $N_{\text{QM}}$  appear in the relatively flat region of the state counting function just above the cusp marked  $I$  in Fig. 5.25(b). The reason for the failure of the semiclassical retracing approximation can be readily seen in the wave functions: electron and hole eigenstate do not mirror each other, most notably for the whispering gallery states, i.e. states trapped in the regular island of the mushroom [140, 97], corresponding to a violation of A2. As expected, these states feature a strong asymmetry in the overall probability density between electron and hole [see Fig.5.25(d)].

Finally, diffractive scattering at the entrance corners to the mushroom lead to a general failure of semiclassical theories (violation of A3). The wave function densities show “fuzzy” patterns without discernable enhancement near a single periodic orbit. However, they do show high amplitudes at the diffractive corner. Furthermore, the patterns found for electron and hole do not agree with each other [see Fig. 5.25(c)].

## 5.5 Disordered Andreev billiards

In the previous sections, we have studied the dynamics of clean Andreev structures, i.e. scattering only happens at the boundary. We will now introduce disorder to the Andreev billiards. We will consider correlation lengths of the disorder below the Fermi wavelength. As a consequence, scattering off the disorder is essentially non-classical S-wave scattering. Corrections in the semiclassical description due to short-range scattering off disorder have to be introduced [135, 141, 142, 143]. Each scattering event introduces random changes in the orbits of electron and hole leading to an immediate breakdown of retracing. The resulting corrections may turn out to be so large as to render a prediction for the structures of the DOS based on the BS approach unreliable. Accordingly, most structures present in the density of states are averaged out by random scattering events.

Yet there remain interesting features in the density of states even for strongly disordered Andreev systems [109, 117, 144, 145, 81, 131, 146, 147]. In particular, the DOS near the Fermi edge ( $E_F$ ) is reduced and may exhibit an “excitation gap” ( $E_1$ ). This is a direct consequence of the coupling between electron and hole sheet in the normal metal mediated by Andreev reflection. The resulting coupled electron-hole excitations mimic those found in superconductors. Details of this reduced DOS are determined by the dynamics in the Andreev billiard which, in turn, depends on the boundary geometry, the position of the SN interface and on the potential surface in the AB. The distance  $E_1$  of the first excited state in the grain (“billiard”) from the Fermi level (set equal to zero in the following) marks the size of the excitation gap in the energy spectrum. While being much smaller than the bulk gap  $\Delta$  of the superconductor,  $E_1 \ll \Delta$ ,  $E_1$  may considerably exceed the mean level spacing  $\delta$ , i.e. the average energy distance between adjacent eigenstates, thus signaling the appearance of a gap.

In a realistic metal sample brought into contact with a superconductor, deviations from the ballistic limit by disorder scattering play an important role. If the elastic mean free scattering path  $\ell$  is smaller than the linear dimension of the metal grain, the trajectory between two successive Andreev reflections at the SN-interface is dominated by disorder scattering in the interior of the grain rather than by ballistic scattering off the grain boundaries. It has been suggested that the shortening of electron-hole orbits or, equivalently, of the average dwell time  $\tau_d$  between successive Andreev reflections by disorder scattering would lead to an increase of the excitation gap as compared to that of a clean SN junction [80, 143]. Such a trend would qualitatively be in line with recent investigations [135] which have found that the gap in the ensemble averaged density of states of an AB increases as the

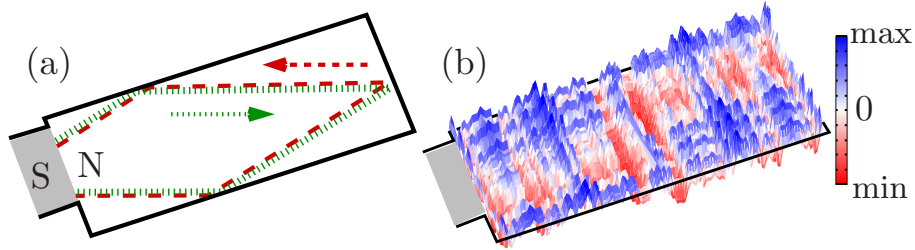


Figure 5.26: (a) Geometry of an Andreev billiard (AB) consisting of a rectangular normal (N) conductor of dimension  $(1.5W, 3W)$ , where  $W$  is the width of the junction with the superconductor (S). The dotted (dashed) line depicts the electron (hole) part of a periodic electron-hole orbit created by Andreev reflection at the SN-interface. (b) A sample realization of the landscape of the disorder potential inside N.

mean free path decreases with respect to the clean, ballistic limit (under the assumption of constant average dwell times  $\tau_d$ ).

Our discussion of the BS approximation in the previous sections suggests that the eigenstates closest to the Fermi energy are not well described by a semiclassical quantization of periodic Andreev orbits even in the case of clean systems: this energy region corresponds either to very long orbits or to orbits disconnected from the SN interface. Indeed, the formation of a sizeable excitation gap in chaotic Andreev billiards as predicted by Random Matrix Theory (RMT) and verified numerically [109], is not reproduced by the BS approximation [148]. To understand the behavior of the excitation gap in disordered Andreev billiards, we will thus need a new approach based on quantum mechanics: the Wigner-Smith time-delay matrix [149, 150].

In this section, we present numerical *ab initio* simulations for a two-dimensional disordered AB. We investigate the distribution of the lowest-lying energy states in a disordered Andreev billiard by solving the Bogoliubov-de Gennes equation numerically. Contrary to conventional predictions we find a *decrease* rather than an *increase* of the excitation gap relative to its clean ballistic limit. We relate this finding to the eigenvalue spectrum of the Wigner-Smith time delay matrix between successive Andreev reflections. We show that the *longest* rather than the *mean* time delay determines the size of the excitation gap. With increasing disorder strength the values of the *longest* delay times increase, thereby, in turn, reducing the excitation gap.

### 5.5.1 Disorder characteristics

We choose a rectangular normal(N)-conducting cavity with dimensions  $(1.5W, 3W)$  where  $W$  is the width of the superconducting lead [see Fig. 5.26(a)]. We construct the disorder potential [Fig. 5.26(b)] by decomposing the N region into two quadratic modules of dimension  $(1.5W, 1.5W)$  within each of which we employ a separable random potential,  $V_\xi(x, y) = V_{\xi_x}(x) + V_{\xi_y}(y)$  [ $\xi_x, \xi_y$  denote two different statistical samples, jointly referred to as  $\xi \equiv \{\xi_x, \xi_y\}$ ]. This “trick” is employed for reasons of numerical efficiency, in particular for small  $\lambda_F$  [36]. We ensure truly random scattering by destroying any unwanted separability by rotating by  $180^\circ$  the random potentials in the two squares relative to each other [see Fig. 5.26(b)]. Disorder is represented by elastic scattering off a potential distribution with short-range disorder with a correlation length  $l_V$  small compared to the Fermi wavelength,  $l_V/\lambda_F = 0.12$ . The spatial correlation of the random potential is characterized by  $\langle V_\xi(x, y)V_\xi(x+a, y) \rangle_{x,y} = \langle V_\xi(x, y)V_\xi(x, y+a) \rangle_{x,y} = V_0^2 \times \exp(-a/l_V)$ , with  $\langle \dots \rangle_{x,y}$  indicating a spatial average over the whole disorder area and  $l_V$  the correlation length. For a given realization  $\xi$  the potential has zero spatial average,  $\langle V_\xi(x, y) \rangle_{x,y} = 0$ , and an amplitude,  $V_0 = \sqrt{\langle [V_\xi(x, y)]^2 \rangle_{x,y}}$ , which is chosen to be small compared to the Fermi energy,  $V_0/E_F \lesssim 0.2$ . For  $V_0 \rightarrow 0$  the dynamics in the normal conducting part of the AB is entirely ballistic (no disorder scattering) and regular (due to the rectangular confinement). Calculations are performed with  $N = 24$  open transverse modes fitting in the lead width  $W$  of the superconductor. The superconducting gap  $\Delta$  was chosen as  $0.2E_F$  to ensure that the energy  $E_1$  of the lowest-lying eigenstate fulfills  $E_1 \ll \Delta$ .

In the fully ballistic limit, i.e., in the absence of any disorder,  $V_0 = 0$ , we find the lowest energy  $E_1$  to be four times larger than the AB’s mean level spacing  $\delta$  [see Fig. 5.27(a) for the lowest eigenenergies]. To investigate the influence of the disorder on the energy spectrum we now gradually increase the disorder amplitude  $V_0$ . For each value of  $V_0$  we calculate the full energy spectrum (below the superconducting gap  $\Delta$ ) for 500 different disorder realizations  $\xi$ , and determine the ensemble averaged state-counting function  $N(\varepsilon)$  (i.e., the integrated DOS) in the ensemble-average. For very weak disorder strength,  $V_0/E_F = 0.007$ , we find  $\langle N(\varepsilon) \rangle_\xi$  to be still very close to the fully ballistic limit of  $V_0 = 0$  where the spectral density close to  $E_F$  is strongly suppressed relative to the Weyl estimate  $N(\varepsilon) = \rho\varepsilon$  for the DOS per unit area  $\rho = m_{\text{eff}}/(\pi\hbar^2)$  [see Fig. 5.27(a)]. Increasing the disorder amplitude  $V_0$ , however, gradually shifts  $N(\varepsilon)$  towards the Weyl distribution [see Fig. 5.27(a,b)]. In particular, we find the size of the excitation gap to be *reduced* with increasing values of  $V_0$ , rather than increased. The reduction of

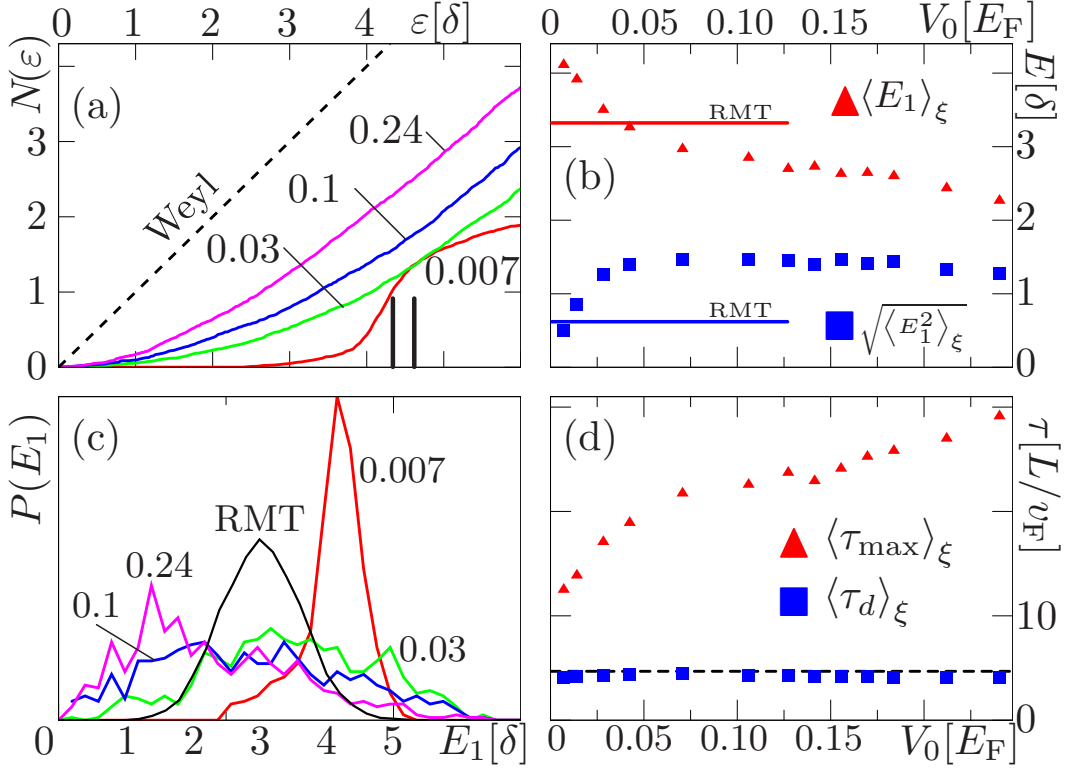


Figure 5.27: (a) Disorder-averaged state counting function,  $\langle N(\varepsilon) \rangle_\xi$ , for four different disorder strengths  $V_0/E_F = 0.007, 0.03, 0.1$  and  $0.24$  (colored solid lines) and Weyl estimate (black dashed line). The two lowest energy eigenvalues of the disorder-free system are marked by vertical bars. (b) Evolution of the mean gap  $\langle E_1 \rangle_\xi$  (red triangles) and the root mean square deviation (blue squares) as a function of disorder strength  $V_0$  (in units of  $E_F$ ). Horizontal lines mark the RMT predictions. (c) Statistical distribution of the lowest eigenvalue  $E_1$  for four disorder strengths  $V_0$  (colored lines) compared with the RMT distribution (black line). (d) Dependence of the Wigner-Smith delay times on disorder strength  $V_0$ . Both the mean delay time, i.e., the dwell time  $\langle \tau_d \rangle_\xi$  (blue squares), and the maximum delay times  $\langle \tau_{\max} \rangle_\xi$  (red triangles) are shown. The black dashed line shows the estimate  $\langle \tau_d \rangle_\xi = 2\pi/N\delta'$  from [151].



$E_1$  is a sizeable (factor 2 in the range  $0 \leq V_0/E_F \leq 0.2$ ) and robust effect. For comparison we also show the gap as predicted by RMT for chaotic systems [see Fig. 5.27(b)]. These RMT estimates are based on a numerical calculation representing the internal dynamics of the normal conductor in the AB by an ensemble of 8000 symmetric random matrices of size  $M \times M$  [82].  $M$  is assumed to scale with the ratio of cavity circumference  $C$  to the size of the SN junction  $W$ ,  $M = N \times C/W$  (for  $N = 24$  modes in the SN-interface we obtain  $M = 216$ ). While the RMT value of the gap,  $E_1 \approx 3.28\delta$ , is in reasonable agreement with our numerical data for finite disorder strength  $V_0 \neq 0$ , significant discrepancies appear for the second moment (i.e. the variance) of the distribution  $\sqrt{\langle E_1^2 \rangle_\xi}$  [see Fig. 5.27(b,c)]. The full quantum calculation shows first a steep increase in the variance with increasing disorder strength before leveling off, whereas the RMT result underestimates the width of the distribution drastically. It should be noted that, strictly speaking, the limit of RMT is only expected to hold for  $M \gg N \gg N^{1/3} \gg 1$  [109]. The latter limit is difficult to reach in any realistic simulation for a two-dimensional cavity. The fact that both the gap size and the variance stay at an almost constant value in a whole interval of the disorder strength,  $0.1 \leq V_0/E_F \leq 0.2$ , possibly points to a saturation effect due to the disorder-induced randomization of otherwise boundary-specific scattering dynamics. The reduction of gap size and variance for stronger disorder,  $V_0/E_F > 0.2$ , may be related to a transition from weakly disordered scattering to diffusive or localized dynamics.

### 5.5.2 Wigner-Smith time delay matrix

The strong *reduction* of the gap size with increasing disorder points to a mechanism qualitatively different from the behavior of the mean dwell time  $\langle \tau_d \rangle_\xi$ , which is only negligibly affected by increasing disorder [see Fig. 5.27(d)]. To uncover the underlying physics we employ a rigorous approach that allows to relate the energy spectrum of a quantum system to the dwell time distribution that does invoke neither any semiclassical approximation nor random matrix assumptions. Key to our approach is the relation between the Wigner-Smith (WS) time delay matrix  $Q$  and the scattering matrix  $S$  [150, 149],

$$Q(\varepsilon) = -i\hbar S^\dagger(\varepsilon)\partial S(\varepsilon)/\partial\varepsilon. \quad (5.50)$$

Equation (5.50), well-known for scattering systems, can be applied to the (bound) spectrum of an AB since an eigenstate of the AB occurs at an energy  $\varepsilon$  for which the determinant [152]

$$\det[1 + S(\varepsilon)S^\dagger(-\varepsilon)] = 0, \quad (5.51)$$

where  $S(\varepsilon)$  is the scattering matrix of the open, normal-conducting cavity with the superconductor replaced by a normal conducting waveguide of identical width  $W$ . Expanding  $S(\varepsilon)$  around the Fermi energy ( $\varepsilon = 0$ ) for small  $\varepsilon$  yields

$$S(\varepsilon)S^\dagger(-\varepsilon) = \mathbb{1} + 2\frac{i}{\hbar}\varepsilon Q + \dots \approx \exp\left(2\frac{i}{\hbar}\varepsilon Q\right), \quad (5.52)$$

and, in turn, the approximate quantization condition for Andreev states [153]:

$$1 + \exp\left(2\frac{i}{\hbar}\varepsilon\tau_n\right) = 0. \quad (5.53)$$

The Wigner-Smith delay times  $\tau_n$  are the eigenvalues of  $Q$ . They correspond to “sticking” times inside the normal-conducting cavity between entering and leaving the cavity through the opening. Since in an AB the opening is replaced by an SN junction,  $\tau_n$  measures the dwell-time between two successive Andreev reflections.

The values of  $\tau_n$  (with  $n \leq N$ ) provide a basis-independent measure for the sticking time of “quantum trajectories” without invoking model-specific assumptions or semiclassical approximations apart from truncation errors. The only limitation of Eq. (5.53) is the error of order  $O(\varepsilon^2)$  due to the Taylor expansion and approximate resummation to the unitary operator  $S(\varepsilon)S^\dagger(-\varepsilon)$  [Eq. (5.52)]. Equation (5.53) relates the energy spectrum at small  $\varepsilon$  to the largest delay-time eigenvalues. In particular, the size of the excitation gap  $E_1$  is determined by the maximal delay time value  $\tau_{\max}$ , such that

$$E_1 \approx \frac{\hbar\pi}{2\tau_{\max}} \equiv \tilde{E}_1. \quad (5.54)$$

The disorder-averaged maximum delay time,  $\langle\tau_{\max}\rangle_\xi$ , is, indeed, monotonically increasing with increasing disorder strength  $V_0$  [Fig. 5.27(d)]. In turn, Eq. (5.54) suggests that the disorder-averaged gap  $\langle E_1\rangle_\xi$  will be reduced.

To probe for the correlation between maximum delay time ( $\tau_{\max}$ ) and the gap size ( $E_1$ ) hinted at by Eq. (5.54), we have performed a statistical analysis of the distribution of  $(E_1, \tau_{\max})$  pairs for 500 disorder realizations (Fig. 5.28), converted to  $(E_1, \tilde{E}_1)$  pairs using Eq. (5.54). For perfect correlation we should expect the histogram to feature non-zero bins only along the diagonal ( $\tilde{E}_1 = E_1$ ). Deviations from a perfect correlation, resulting in part from the Taylor expansion Eq. (5.52), provide a measure for the accuracy of the estimate  $\tilde{E}_1$  as compared to the exact gap size  $E_1$ . For small disorder strength ( $V_0/E_F = 0.007$ ) the correlation between  $E_1$  and  $\tilde{E}_1$  is, indeed, near-perfect and non-zero bins occur only in a very limited range of values  $E_1, \tilde{E}_1$  [see Fig. 5.28(a)]. With increasing disorder strength [ $V_0/E_F = 0.03$ , see

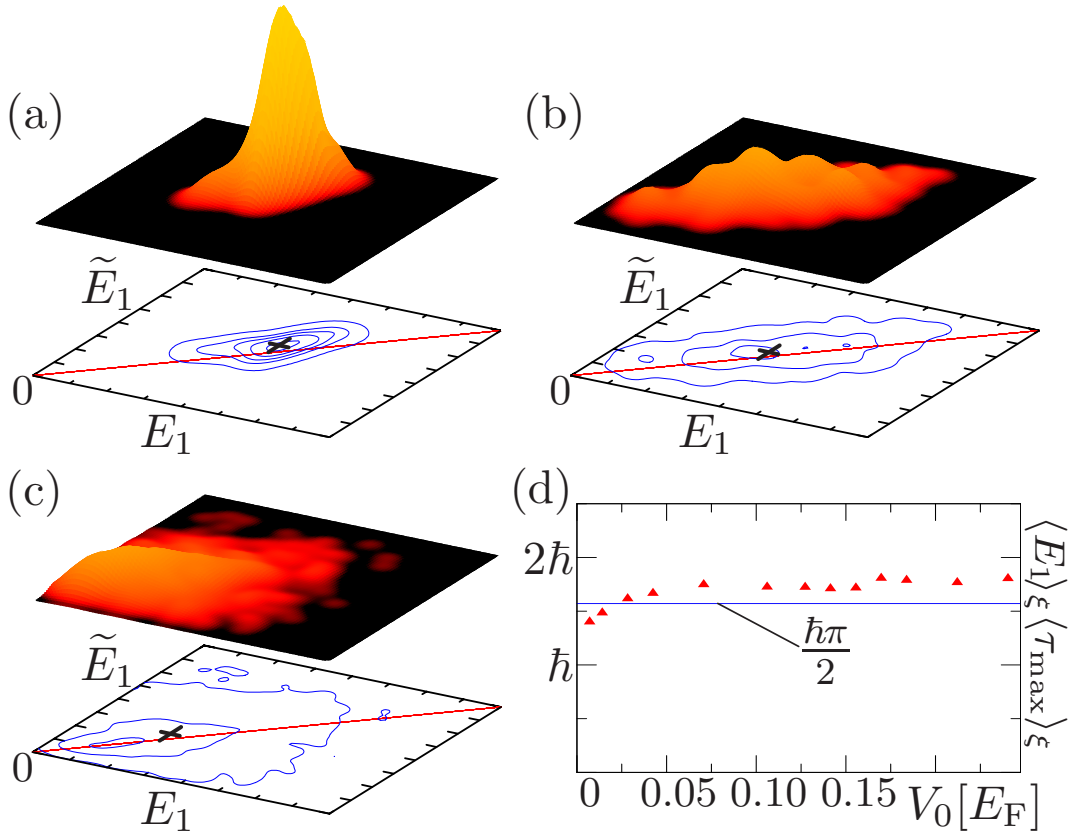


Figure 5.28: Smoothed distribution of  $(E_1, \tilde{E}_1)$  pairs for three different strengths of the disorder potential, (a)  $V_0/E_F = 0.007$ , (b)  $0.03$ , (c)  $0.24$  (500 realizations of disorder were used). Black crosses in the contour plot mark the mean value of the distribution. Perfect  $(E_1, \tilde{E}_1)$  correlation would correspond to non-vanishing density only along the diagonal (drawn in the contour plot as guide to the eye). (d) Product of the mean gap size  $\langle E_1 \rangle_\xi$  and the mean of the maximum Wigner-Smith delay time  $\langle \tau_{\max} \rangle_\xi$  as a function of disorder strength. The constant value  $\hbar\pi/2$  [predicted by Eq. (5.54)] is shown for comparison.

Fig. 5.28(b)] the maximum in the distribution shifts to smaller values of  $E_1$  and  $\tilde{E}_1$  while remaining correlated near the diagonal. Both observations underscore that increased disorder decreases the gap which is, indeed, correlated with the maximum WS time-delay eigenvalue. For much stronger disorder [ $V_0/E_F = 0.24$ , see Fig. 5.28(c)], the  $(E_1, \tilde{E}_1)$  correlation is diminished as off-diagonal bins become more significantly populated. While, on average, the connection between the disorder-induced reduction of the gap and the increase of the maximal delay time  $\langle \tau_{\max} \rangle_\xi$  still holds, see Fig. 5.28(d), for *individual* strong disorder realizations this picture breaks down and small (large) gap sizes may well occur for systems with small (large) values of  $\tau_{\max}$ .

The present simulations allow to directly inspect the effect of disorder scattering on the wave function densities in the particle and hole sectors. The latter provide a microscopic picture of the decay of correlations between gap and maximum delay time. In the ballistic limit  $V_0 = 0$ , the electron and hole wave function tend to closely mirror each other [Fig. 5.29(a)] in agreement with retracing electron and hole orbits between two Andreev reflections. With increasing disorder the similarity between wave components in the electron and hole sheet gradually disappears [see Fig. 5.29(b)]. This observation supports the picture that for strong disorder the wave function of

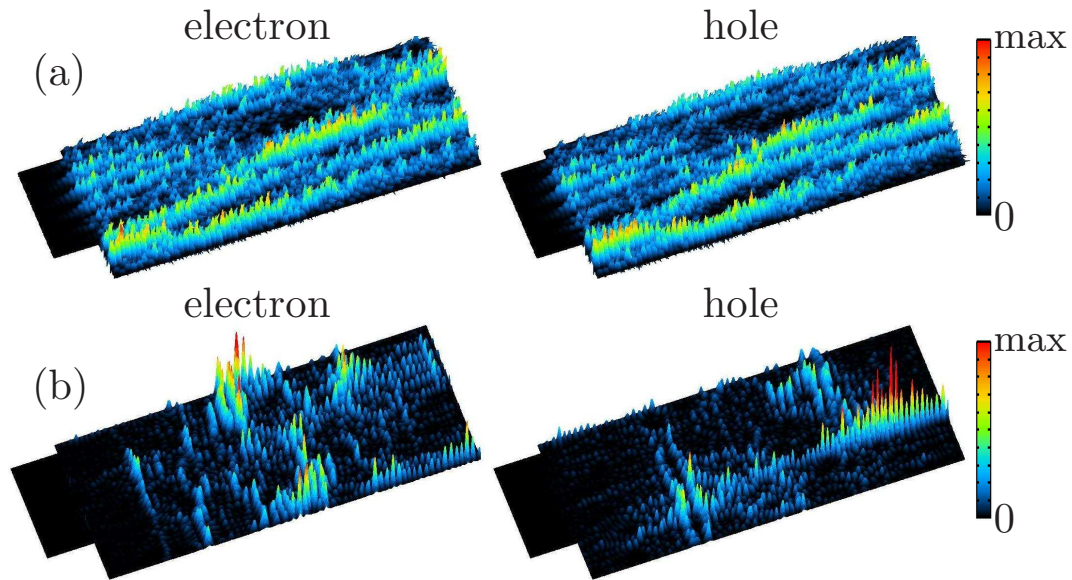


Figure 5.29: *Electron and hole probability densities of the lowest Andreev eigenstate at (a) zero disorder potential, (b) finite disorder strength  $V_0/E_F = 0.15$  (one disorder realization).*

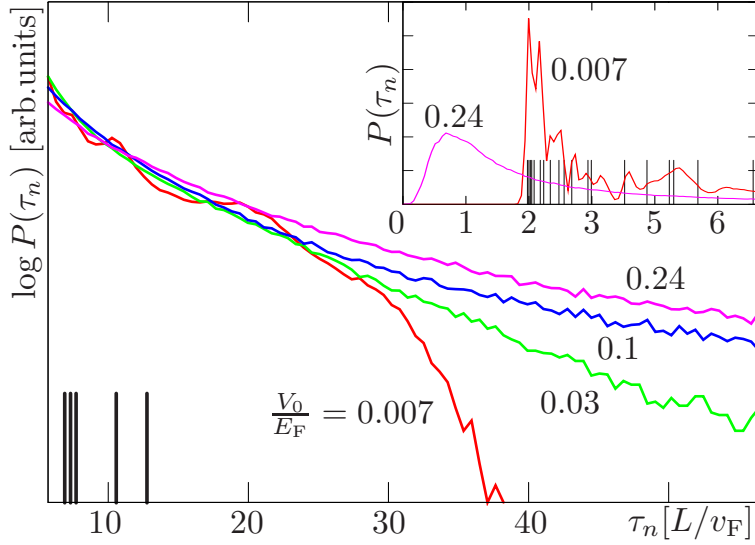


Figure 5.30: *Distribution of Wigner-Smith delay times,  $P(\tau_n)$  (colored lines) for an ensemble average over 500 disorder realizations  $\xi$  and different disorder strength ( $V_0/E_F = 0.007, 0.03, 0.1, 0.24$ ). For each  $\xi$  and  $V_0$ , the delay times are evaluated at 135 different energies in an interval  $E_F \pm 0.1\Delta$ . Increasing the disorder strength  $V_0$  amplifies the long time tail of  $P(\tau_n)$  (main plot, logarithmic scale), but concurrently produces much shorter delay times (see top right inset). The disorder-free delay times are indicated by vertical bars, with the lowest values starting at  $\tau \approx 2L/v_F$  (the time of flight across the cavity length  $L = 3W$  and back) and the largest value at  $\tau \approx 13L/v_F$ .*

the lowest AB eigenstate is largely determined by disorder scattering in the interior rather than by Andreev reflections at the SN interface. Accordingly, the dwell time between two Andreev reflections loses significance.

It is now instructive to inquire into the origin of the discrepancy to those models suggesting that the presence of disorder induces an increase rather than a decrease of the gap in comparison to its clean, ballistic limit [80, 143]. The key here is the disparate behavior of the maximum,  $\langle \tau_{\max} \rangle_\xi \equiv \langle \max_{n=1, N} \tau_n \rangle_\xi$ , and of the average dwell time,  $\langle \tau_d \rangle_\xi \equiv \langle \sum_n \tau_n / N \rangle_\xi$ , the latter of which enters the estimates for the behavior of the gap given in [80, 143]. For the system under study here, disorder scattering is obviously able to "delay" for long-lived scattering states the interval between two successive Andreev reflections. The presence of disorder not only *increases*  $\langle \tau_{\max} \rangle_\xi$ , but also *reduces* the minimal delay time  $\langle \tau_{\min} \rangle_\xi$  (see Fig. 5.30). As a consequence, the distribution of delay times  $P(\tau_n)$  becomes "stretched", while leaving the mean value  $\langle \tau_d \rangle_\xi$  almost unchanged. The fact that the average dwell time

$\langle \tau_d \rangle_\xi$  stays almost unaffected by the increasing disorder [see Fig. 5.27(d)] is in agreement with a general relation [151] between the averaged trace of the matrix  $Q$  [see Eq. (5.50)],  $\langle \text{tr} Q \rangle_\xi$ , and the mean spacing  $\delta'$  of resonant levels in a (normal-conducting) scattering system,  $\langle \text{tr} Q \rangle_\xi = 2\pi/\delta'$  or, equivalently,  $\langle \tau_d \rangle_\xi = \pi/N\delta$  (note that  $\delta' = 2 \times \delta$ , with  $\delta$  being the mean level spacing in the corresponding AB). Consequently, the mean dwell time should be entirely independent of the disorder configuration. This is, indeed, very accurately confirmed by our numerical results for  $\langle \tau_d \rangle_\xi$  [see Fig. 5.27(d)]. In turn,  $\langle \tau_d \rangle_\xi$  is not suitable for characterizing correlations between gap size and disorder strength, because of its independence of  $V_0$ . Therefore, relating the gap size to the mean dwell time  $\langle \tau_d \rangle_\xi$  also fails to account for the gap reduction observed here. Note that we have used the definition of the gap as the position of the *lowest* energy state in the AB above the Fermi energy (as in [82]). This definition should not be confused with the gap size in the average density of states for a large number of energy levels (as in [148, 135]). Also, our definition of the mean dwell time as the mean of the Wigner-smith delay times,  $\langle \tau_d \rangle_\xi = \langle \frac{1}{N} \sum_{n=1}^N \tau_n \rangle_\xi$ , should not be confused with other definitions used in the literature. Clearly, the present results do not preclude an increase of the excitation gap with increasing disorder for particular boundary shapes, e.g. for a gapless excitation spectrum in the absence of disorder. The present analysis suggests, however, that also in such systems the behavior of the longest WS time delay eigenvalue will control the behavior of the gap.

The results in Fig. 5.30 demonstrate that for a disordered cavity the strength of the disorder ( $V_0$ ) does have a crucial influence on the distribution of delay times  $P(\tau_n)$  (in particular for long times). For chaotic cavities it was found both classically [154] and quantum mechanically [109, 155, 36] that the long time tail of delay times does *not* depend on certain system-specific parameters as, e.g., the Lyapunov exponent. We therefore expect that the statistical distribution of the gap size undergoes a crossover between the present case of a disordered AB and the case of a chaotic AB. It would be interesting to study such a crossover numerically, e.g., by tuning the disorder correlation length  $l_V$  from the diffractive limit of  $l_V \ll \lambda_F$  to the ballistic (chaotic) limit of  $l_V \gg \lambda_F$ .

With the help of Fig. 5.30, we can furthermore explain the loss of correlations among pairs  $(E_1, \tilde{E}_1)$  for strong disorder [Fig. 5.28(c)]: The amplification of the maximal proper delay times  $\langle \tau_{\max} \rangle_\xi$  by the increasing disorder translates into an increase of the high frequency components in the elements of the scattering matrix  $S(\varepsilon)$ . As, however, the estimate of the gap size,  $\tilde{E}_1$ , relies in part on a Taylor expansion of  $S(\varepsilon)$  [see Eq. (5.52)] which can only capture weakly energy dependent (i.e., low-frequency) components, the accu-

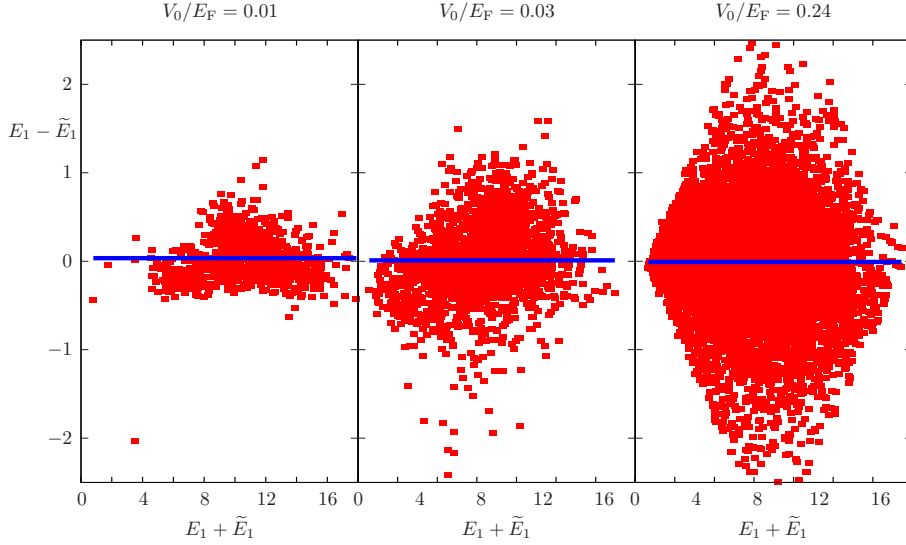


Figure 5.31:  $(E_1 + \tilde{E}_1, E_1 - \tilde{E}_1)$ -pairs for three different strengths of the disorder potential as given in the figure. A blue line indicates the mean value  $\langle E_1 - \tilde{E}_1 \rangle_\xi$ . For perfect correlation in  $(E_1, \tilde{E}_1)$ , all points would lie on the  $E_1 - \tilde{E}_1 = 0$  line.

racy of  $\tilde{E}_1$  deteriorates with increasing disorder strength, thereby gradually diminishing the correlations among pairs  $(E_1, \tilde{E}_1)$ . The behavior of the mean values  $\langle E_1 \rangle_\xi$  and  $\langle \tilde{E}_1 \rangle_\xi$  can be understood by considering the distribution of values  $d_E = (E_1 - \tilde{E}_1)/2$  (corresponding to a projection of the distributions of Fig. 5.28(a-c) on an axis perpendicular to the diagonal  $E_1 = \tilde{E}_1$ ). As we have verified numerically (see Fig. 5.31), the width of this distribution,  $\text{var}(d_E) = \sqrt{\langle d_E^2 \rangle_\xi}$ , increases with increasing  $V_0$ , while its mean value stays almost unaffected by the disorder strength at  $d_E \ll \delta$ . We speculate that the errors due to the Taylor expansion and the resummation of  $S^\dagger(\varepsilon)S(-\varepsilon)$  [see Eq. (5.52)] are randomly distributed and thus cancel out on average over many disorder realizations. This would explain why the averaged values  $\langle E_1 \rangle_\xi$  and  $\langle \tilde{E}_1 \rangle_\xi = \langle \tau_{\max}^{-1} \rangle_\xi$  remain correlated [see Fig. 5.28(d)] while the correlation between individual pairs  $(E_1, \tilde{E}_1)$  breaks down.

In summary, we have numerically calculated the energy spectrum of electron-hole states in a rectangular Andreev billiard with a tunable disorder potential. In apparent contrast to qualitative models based on the mean cavity dwell time  $\langle \tau_d \rangle_\xi$ , we find a *decrease* rather than an increase of the gap size when increasing the disorder amplitude. We show that this decrease is controlled by the disorder dependence of the *largest* Wigner-Smith delay

time  $\tau_{\max}$  between subsequent Andreev reflections at the SN-interface. The average dwell time  $\langle\tau_d\rangle_\xi$ , on the other hand, only depends on the mean level spacing, and is thus neither correlated to the evolution of the gap size nor to the disorder scattering strength. Stronger disorder, however, drastically increases the value of  $\tau_{\max}$  for long-lived scattering states. For sufficiently strong disorder the correlation between the gap size and  $\tau_{\max}$  eventually breaks down for *individual* disorder realizations, as the eigenenergies of the system are then more strongly influenced by the specific disorder potential rather than by the Andreev reflection process.



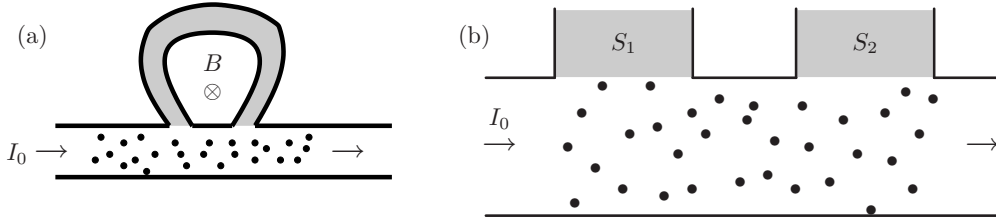


Figure 5.32: *Transport through a normal-conducting diffusive metal in contact with both ends of a horseshoe-shaped superconductor is investigated. (a) Experimental realization of two superconducting contacts with different phases: A region of finite magnetic field is enclosed by a superconducting loop (the magnetic field is non-zero only in a non-conducting region). (b) Scattering geometry containing two superconducting regions, and a diffusive metal (point scatterers represented by black dots) in between.*

## 5.6 Transport through SN hybrid structures

We have thus far ignored the complex phase of the pairing potential  $\Delta$ . This is justified as long as a structure contains only one superconducting region as only a relative phase is physically relevant. The interplay between two superconductors (or two spatially separated parts of a single superconductor) of different phase  $\phi$  leads, on the other hand, to many interesting interference phenomena [85]. In particular, there is a robust enhancement (or suppression) of current in open Andreev structures, depending on the relative phase of the superconductors, that can be understood based on the periodic orbits of closed Andreev billiards. This effect is interesting from an experimental point of view, as it allows to tune the transmission through a diffusive metal on a small energy scale by bringing it in contact with two superconductors and changing the relative phase of the superconductors by, e.g., a magnetic field. As has been shown by Vavilov et al. [156], a variation of the conductance on an energy scale small compared to  $k_B T$  leads to a mismatch between the electrical and thermal current. In contrast, the Wiedemann-Franz law predicts a proportionality relation between electrical and thermal currents for diffusive metals at low temperatures. We present a system for which this apparent contradiction could be directly investigated experimentally.

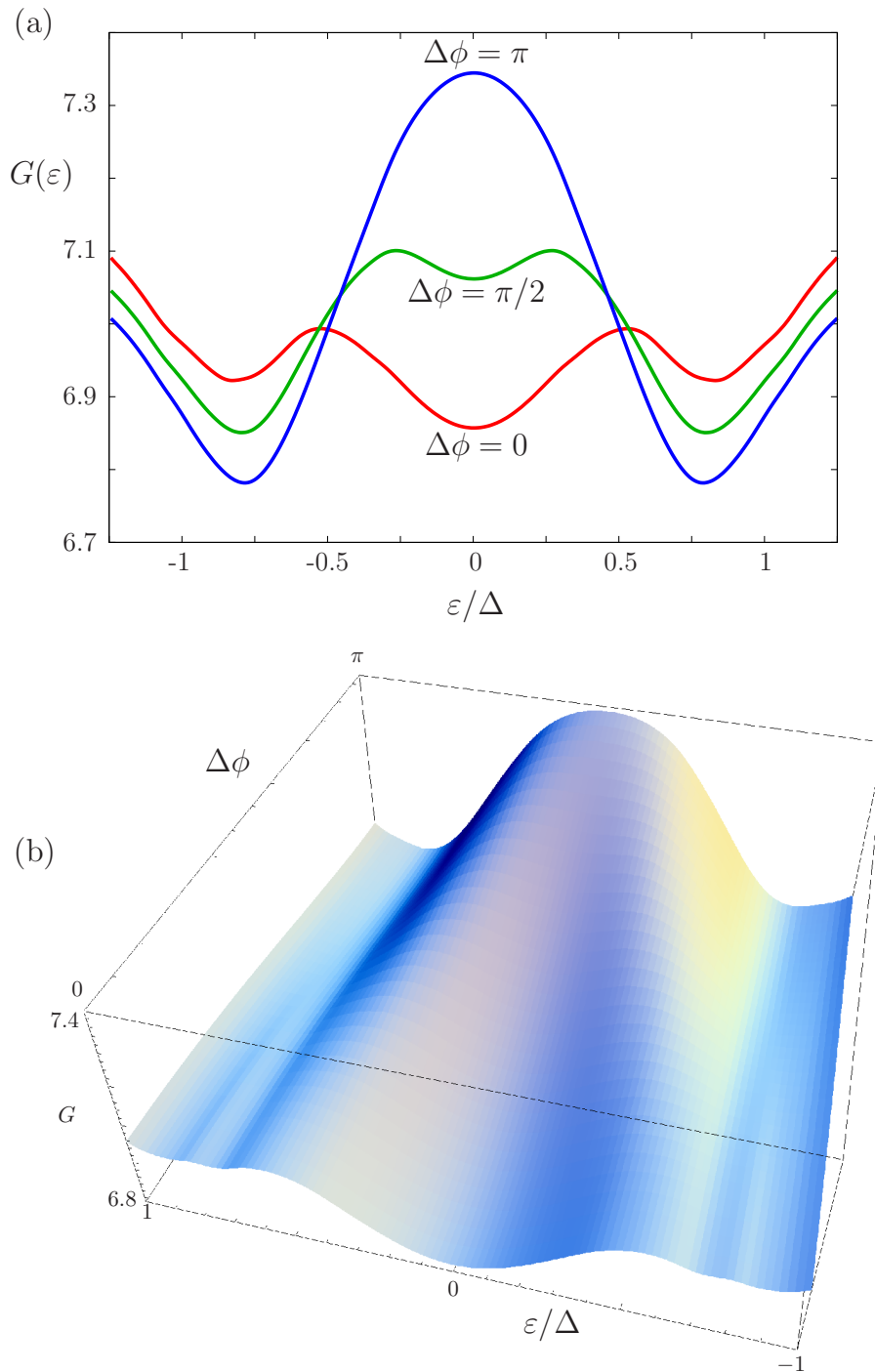


Figure 5.33: Disorder averaged conductance  $G_0$  (over 100 realizations of disorder scatterers) of a two-superconductor hybrid structure [see Fig. 5.32(b)] as a function of energy  $\epsilon$  (counted from the Fermi level) (a) for three values of the relative phase  $\Delta\phi$  between the superconductors and (b) as a 3D plot.

### 5.6.1 Scattering geometry

We want to study the influence of a phase difference between two superconducting point contacts on transport. An experimental realization of this could be a horseshoe-shaped superconductor connected to a normal metal at two points [see Fig. 5.32(a)]. Applying a magnetic field through the hole formed between normal- and superconductor creates a phase difference  $\Delta\phi$  between the two end points of the superconductor [see  $B$  in Fig. 5.32(a)].  $\Delta\phi$  is directly proportional to the magnetic flux  $\Phi$  through the hole,

$$\Delta\phi = 2\pi \frac{2e}{h} \Phi = 2\pi \frac{\Phi}{\Phi_0}. \quad (5.55)$$

As a consequence,  $\Delta\phi$  may easily be tuned in an experimental setup.

To model the above system, we consider an ideal metallic waveguide in contact with two superconducting regions with phase difference  $\Delta\phi$ . To simulate disorder, we include randomly distributed point impurities [see Fig. 5.32(b)]. We average over different realizations  $\xi$  of the position of the point scatterers to avoid non-generic effects related to a specific distribution of scatterers. The scatterer density was chosen such that the transmission in the non-superconducting case is  $N/2$ , where  $N = 14$  is the number of open modes in the waveguide.

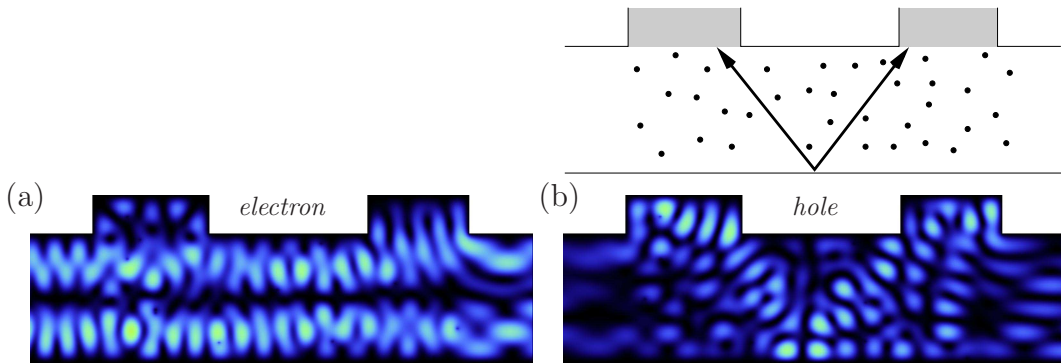


Figure 5.34: (a) Electron and (b) hole sheet of the scattering state of the geometry shown in Fig. 5.32, at energy  $\varepsilon = 0$ . The hole part of the corresponding periodic Andreev orbit is shown in the inset.

We find that the averaged conductance  $\langle G_0 \rangle_\xi$  of the scattering device features, indeed, a strong dependence on the phase difference  $\Delta\phi$ : The average conductance  $G_0 \approx N/2 = 7$  is suppressed for  $\Delta\phi = 0$  and enhanced near  $\Delta\phi = \pi$  (see Fig. 5.33). This effect is robust against changes in the density of point scatterers, the width of the waveguide and the distance  $L$  between

the two superconducting contacts. To understand this behavior, we consider the periodic orbits formed by Andreev reflection in the system [see e.g. the inset in Fig. 5.34(b)]. For a semiclassical model, consider a periodic Andreev orbit of length  $s$  connecting the two superconductors:

$$\frac{2s\varepsilon}{\hbar v_F} = \Delta\phi + 2\pi n - 2 \arccos\left(\frac{\varepsilon}{\Delta}\right) \quad (5.56)$$

If the excitation energy  $\varepsilon$  is close to zero, the phase term due to the two Andreev reflections is approximately  $\pi$ . If  $\Delta\phi = \pi$ , the above relation is fulfilled for  $n = 0$  and  $\varepsilon \rightarrow 0$ . There exists thus an Andreev bound orbit, where an electron goes from the right superconductor to the left one, and a hole travels back (see Fig. 5.34). This resonant level enhances the conductance near  $\Delta\phi = 0$ . Conversely, if  $\Delta\phi = 0$ , the above relation has no solution near  $\varepsilon = 0$ . No resonance is available, and conduction is suppressed.

### 5.6.2 The Wiedemann-Franz law

Electrons (and holes) in mesoscopic conductors not only mediate an electrical current  $I_e$ , but also a heat current  $I_h$ . In good conductors, e.g. metals, the bulk of the thermal current is carried by the conduction electrons. This follows from the experimental observation that metals conduct heat much better than insulators do. Consequently heat transfer by lattice vibrations (i.e. phonons, present in both insulators and metals) is weaker than thermal conduction from conduction electrons (present only in good conductors) [23].

The Wiedemann-Franz law states that the ratio,  $G_h/G$ , of the thermal to the electrical conductance (or, equivalently, the ratio  $\kappa/\sigma$  of the thermal to the electrical conductivity) of a great number of metals is directly proportional to the temperature. The proportionality factor is given by the Lorenz number

$$l = \frac{G_h}{GT} = \frac{\pi^2}{3} \left(\frac{k_B}{e}\right)^2. \quad (5.57)$$

This connection has been verified experimentally and is well fulfilled for those systems where inelastic scattering is not dominant, i.e. when the same particles are responsible for electric current and heat current [23]. The reason for this is simple: Each electron carries an electrical current  $ve$  and a thermal current  $(\varepsilon - \mu)v/T$ . As a consequence, electrical current can only change by changing the average drift velocity  $v$  of the electrons, i.e. by scattering events. In the case of (approximately conserved) energy of the electrons (i.e. if scattering is elastic, or the energy transfer is small compared to  $k_B T$ ), scattering events reduce thermal current in precisely the same manner as electrical current. Only if the energy of electrons is not conserved in a scattering event,

the thermal current is changed by two effects: the change of  $v$  and of  $(\varepsilon - \mu)$ . In this case, the correlation between thermal and electrical current breaks down.

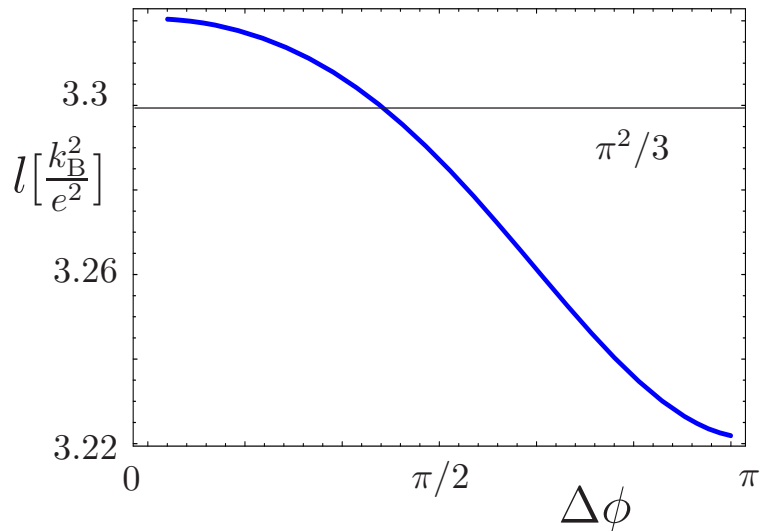


Figure 5.35: *Dependence of the Lorenz number  $l$  on the phase difference  $\Delta\phi$  between the two superconducting contacts in the scattering geometry of Fig. 5.32 at a temperature of 4K. The value  $l = \pi^2/3 \cdot k_B^2/e^2$  obtained at constant  $G(\varepsilon) = G_0$ , is plotted for comparison.*

In the case of constant  $G(\varepsilon)$ , relation (5.57) is exactly fulfilled (for a detailed derivation, see App. A.3). For finite  $T$ , mesoscopic fluctuations of  $G(\varepsilon)$  on the scale of  $k_B T$  may, however, lead to violation of the Wiedemann-Franz law. As an example, consider the scattering structure shown in Fig. 5.32(b). If we insert the averaged conductance  $\langle G(\varepsilon) \rangle_\xi$  for our scattering geometry [see Fig. 5.33] in the relation for the Lorenz number (5.57), we obtain, indeed, a dependence of  $l$  on the phase difference  $\Delta\phi$  between the two superconducting contacts, in contrast to predictions based on the Wiedemann-Franz law (see Fig. 5.35). This failure is not related to inelastic scattering, but is a direct consequence of the phase dependence of  $\langle G \rangle_\xi$ , i.e. of a quantum interference effect.

# Chapter 6

## Outlook

The numerical methods presented in this thesis offer a versatile tool set to investigate the dynamics of a wide range of phase-coherent nanostructures. Possible future directions include different device materials (e.g. silicon-based nanosensors) and device geometries (e.g. carbon nanotubes) and the inclusion of spin-based effects to describe spintronics (by the introduction of two sheets for the two spin-components). A further major point for future development is the inclusion of electron-electron interaction processes into our formalism, e.g. by a Keldysh-Green's function approach [3].

Time dependent dynamics of quantum wave packets represent another avenue for research. It is straightforward to use our modular discretization technique in conjunction with well-established time-propagation schemes, e.g. Lanczos time propagation [29]. We use this technique to study the time-evolution of wave packets in acoustic resonators. In the following, we give a brief outlook on one prototypical example, the time-evolution of Fano-resonances in acoustic resonators.

### 6.1 Fano resonances in Acoustic cavities

Asymmetric Beutler-Fano line shapes [157, 158] are an ubiquitous feature of resonance scattering when (at least) one resonant and one non-resonant pathway connect the entrance with the exit channel. Fano resonances can be observed in a variety of physical processes, ranging from photo-absorption in quantum well structures [11], transport through quantum dot structures [159], neutron scattering [160], atomic physics [161], to the microwave propagation through metallic cavities [162]. Details of the Fano lineshape reveal e.g., the amount of decoherence in a system. In the case of overlapping Fano resonances, this approach fails, however, as contributions of individual resonances

can no longer be easily distinguished. As a solution to this problem, the time-dependent evolution of Fano resonances has recently been proposed in the context of atomic physics [163]. The contribution of overlapping resonances become well-separated in the time dependent picture (due to the different lifetimes of the resonances in the resonator). However, the time-resolution needed to analyze the time dependent dynamics of atomic systems is of the order of a few femtoseconds, and thus requires e.g. femto-second laser technology [161]. We therefore propose to investigate the time-evolution of Fano resonances in classical resonators, that are much easier to handle.

The analogy between classical wave mechanics and quantum theory may be exploited to study “quantum interference effects” in macroscopic, classical wave systems. The advantage of these macroscopic wave-systems lies in their comparatively simple and robust experimental realization. Consider, for example, the Helmholtz equation from classical electrodynamics which is mathematically equivalent to the time-independent Schrödinger equation. Experiments performed on microwave cavities, with a typical length scale of half a meter, can be used to improve our understanding of the physics of nanoscale objects, that are much more difficult to realize experimentally [164]. To investigate time-dependent phenomena, these systems are not ideally suited, because of the short time-scales involved in the propagation of an electromagnetic pulse.

In contrast, acoustic cavities are perfectly suited for the experimental investigation of time-dependent resonance phenomena. The acoustic wavelength can be tuned from a few mm to several meters, easily allowing experimentalists to access different ratios of device geometry versus wavelength. This also allows for scattering structures to be manufactured as a table-top experiment, that can easily be handled without the need for expensive equipment. Indeed, the experiments described in this section were carried out on a cylindrical aluminum resonator using conventional microphones and loudspeakers. Acoustic wave packets travel at the speed of sound,  $v_S \approx 330m/s$ . The traversal time of a wave packet through a resonator of 35 cm length is thus about  $10ms$ , a time span easily accessible by moderately-priced laboratory equipment. As a remarkable consequence, the time-dependent evolution of Fano resonances, only accessible by e.g. femto-second laser technology [161], may be easily measured experimentally.

The acoustic resonator modeled in this thesis was built by Matzdorf et al. at the Universität Kassel [see Fig. 6.1 (a)]. To minimize friction at the cavity walls, a three-dimensional cylindrically shaped resonator was chosen (as opposed to a two-dimensional, rectangular shape which would lead to friction losses at the top and bottom wall). Two pipes of variable length  $L_i$ ,  $i = \{1, 2\}$  are connected to the resonator [see Fig.6.1(b)]. The dynamics

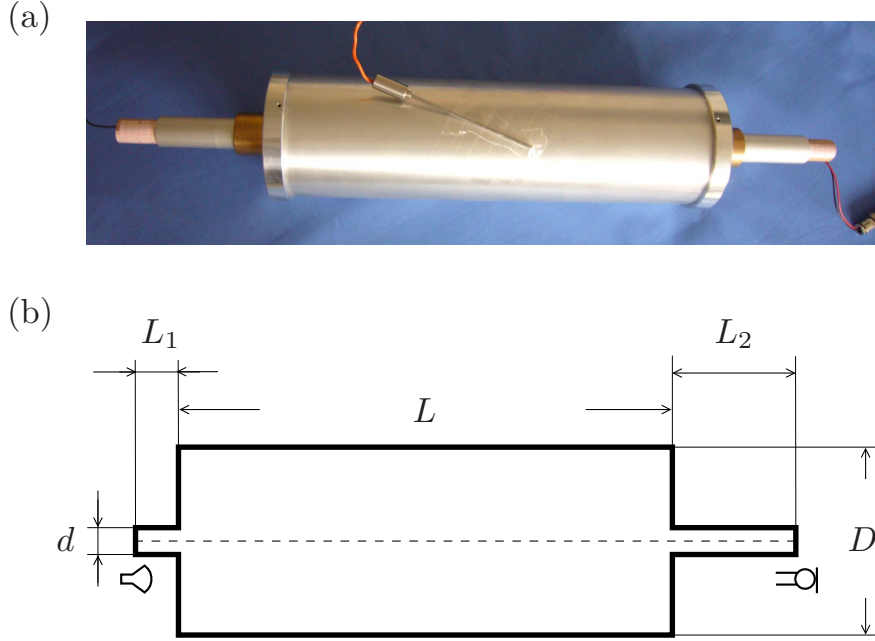


Figure 6.1: (a) Acoustic resonator built at the university of Kassel for the measurements we compare our results to. (b) Schematic drawing of the resonator geometry. The dimensions of the resonator are  $d = 20.7\text{mm}$ ,  $L = 349,6\text{mm}$  and  $D = 184.2\text{mm}$ . The geometry is rotationary symmetric about the central axis (dashed line) to obtain a cylinder. Two pipes connected to the main resonator house a loudspeaker (at distance  $L_1$  from the cavity) and microphone (at distance  $L_2$ ). These distances  $L_i$   $i = \{1, 2\}$  can be tuned in a range from 10 to 60mm by shifting the microphone/loudspeaker inside the tube. Damping batting was used to minimize backward reflection at the microphone.

of the acoustic signal is governed by the acoustic wave equation

$$\frac{\partial^2}{\partial t^2} p = \frac{1}{v_0^2} \Delta p(\mathbf{x}, t). \quad (6.1)$$

The numerical description of this resonator geometry is based entirely on the tool set developed in the first part of this thesis. The only difference to the description of graphene based nanostructures is the introduction of different matrices  $H_0$  and  $H_I$ . The tight binding parameters used for this structure are discussed in detail in Appendix A.4.

The resonator geometry we consider allows us to tune the position of resonances for the first and second transverse modes by changing the lengths



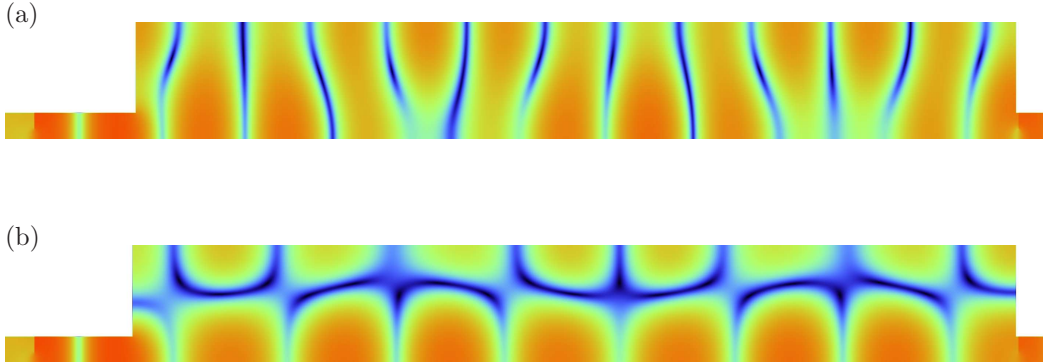


Figure 6.2: *Scattering states of the acoustic resonator featuring eigenstates of the (a) first and (b) second transverse modes.*

$L_1$ ,  $L_2$  [see Fig. 6.1(b)]: the resonance position of the second transverse cavity mode [see Fig. 6.1(b)] is determined by the distance between loudspeaker and microphone, i.e. by  $L_1 + L_2$ . In contrast, sharp Fano-lineshapes emerge from resonances of the first mode formed in the resonator [see Fig. 6.1(a)] making the resonance frequencies of the first cavity mode (to first order) independent of  $L_i$ .

We can exploit the different geometry dependence of the two resonances to investigate resonance crossing behavior: By changing  $L_1$  at fixed  $L_2$ , the position of the two types of resonances (i.e. resonances of the first and second transverse cavity mode) are shifted relative to each other [see Fig. 6.3(a)]. The MRGM predicts the resonance shifts observed in the experiment with high accuracy [compare Fig. 6.3(a,b)]. This allows us to investigate, in detail, the complicated interplay between the two different resonances. In particular, we are interested in parameter settings where the resonance positions overlap. In this case, avoided crossings emerge between the two resonances [see solid triangle in Fig. 6.3(b)].

The regime of overlapping resonances can be further investigated by considering the time-evolution of acoustic pulses. A Gaussian pulse of the form

$$p(r, z) = p_0 e^{-\left(\frac{x-x_0}{2\sigma}\right)^2} \cos(\nu_0 x) \quad (6.2)$$

was emitted by the speaker. The pulse width  $\sigma$  was chosen at  $2ms \approx 65cm$ . The microphone signal was then recorded as a function of time [see Fig. 6.1(a)]. Theoretically, we use a time-evolution of the initial wave packet (6.2) based on Lanczos diagonalization [29] to calculate the time-dependent amplitude at the microphone [see Fig. 6.1(b)]. We find pronounced beating

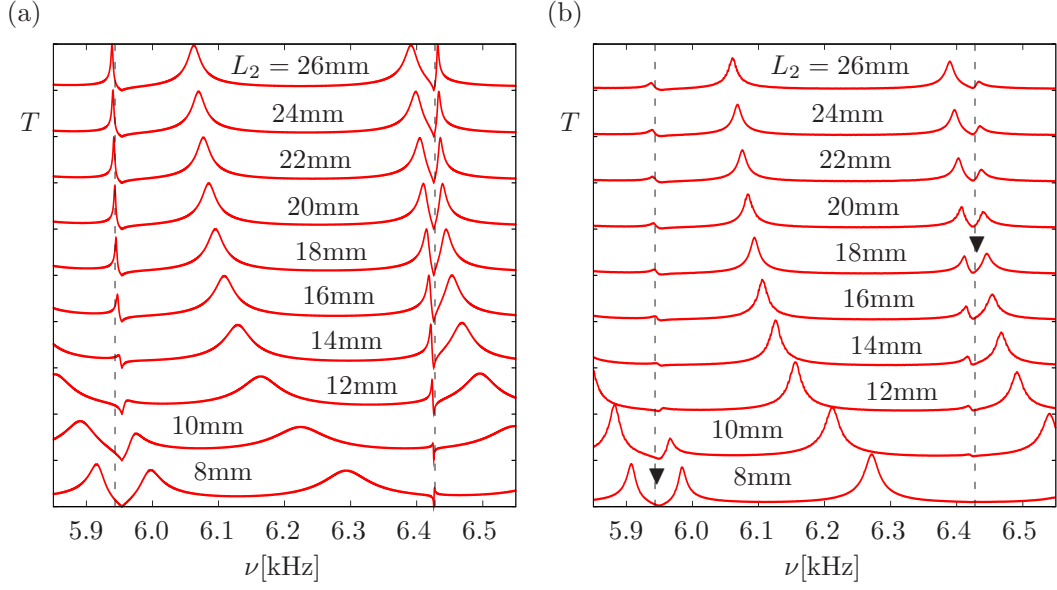


Figure 6.3: *Theoretical (a) and experimental (b) evolution of the resonance spectrum of the acoustic resonator for fixed length  $L_1 = 1.5\text{mm}$  and varying distance  $L_2$  between resonator and microphone. Dashed lines mark the position of resonances of the closed cylindrical cavity at 5945Hz and 6420Hz. Solid triangles mark the region of avoided crossings.*

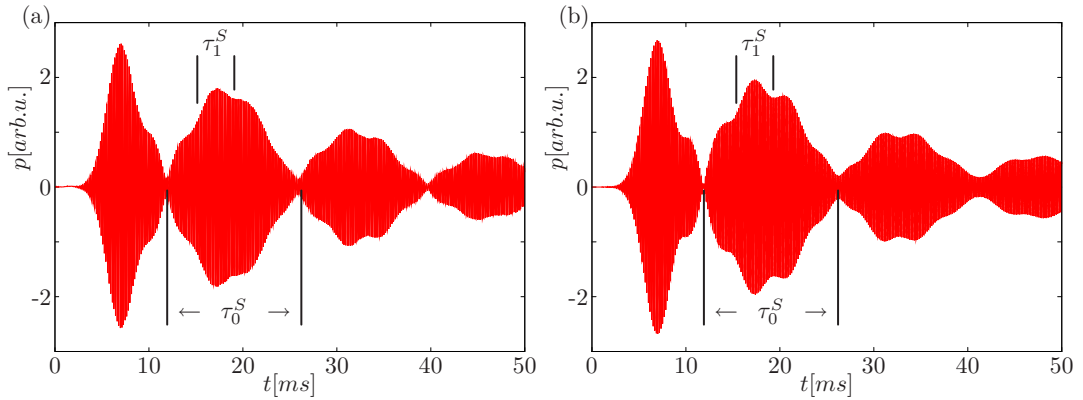


Figure 6.4: *Experimental (a) and theoretical (b) time evolution of an 2ms pulse at 5930Hz,  $L_l = 0$ ,  $L_r = 37\text{mm}$ . Two beating periods  $\tau_0^S$ ,  $\tau_1^S$  which emerge due to resonance interactions are marked (see text).*

patterns in the time-dependent signal featuring two different beating frequencies (see Fig. 6.1). The longer beating period  $\tau_0^S \approx 15\text{ms}$  is given by the frequency difference between the two adjacent resonances  $\delta\nu_0 = \tau_0^{-1} \approx 66\text{Hz}$ , while the shorter period  $\tau_1^S \approx 3.5\text{ms}$  is connected to the frequency interval to the next higher resonance  $\delta\nu_1 \approx 285\text{Hz}$ . Both of these estimates based solely on the time-dependent pulse measurements fit perfectly to the measured resonance spectra. In such a way, we can compare the merits and limitations of time-dependent and time-independent measurements for different resonance configurations as determined by the choice of geometry. We can investigate in detail the complex dynamics of overlapping Fano resonances, and the evolution of the Fano  $q$ -parameter during a resonance crossing. Inserting absorbing materials into the resonator additionally allows for the simulation of dissipative effects. The acoustic resonator geometry thus represents a perfect “playing ground” for the study of time-dependent interference phenomena.

# Chapter 7

## Summary

We investigated quantum effects in a variety of different phase-coherent systems. The physics of quantum interference plays a crucial role in a wide range of modern nanotechnology, including high-mobility nanoelectronics, quantum computation or high-precision interference-based metrology. However, the simulation of realistic quantum mechanical systems requires highly optimized numerical methods. For this purpose we developed a “toolbox” of numerical techniques to efficiently describe the density of states and individual eigenstates for closed systems, as well as transmission properties and individual scattering states for open (scattering) systems. The key approach we employed in our numerical investigations is the tight-binding method, which provides a matrix-based formulation of the Schrödinger, Bogoliubov-de Gennes and Dirac equations respectively. To determine the spectra of closed quantum dot structures, we applied the Lanczos diagonalization algorithm to calculate eigenenergies close to the Fermi energy. For open devices we presented a powerful Green’s function technique (based on a recursive coupling scheme) which allows for the efficient calculation of transmission probabilities as well as scattering states.

Our discretization-based approach turns out to be ideally suited for the investigation of graphene-based nanostructures. In these devices, effects due to the discreteness of the hexagonal graphene lattice play a key role, which is neglected in over-simplified models based on the Dirac equation. In particular, our simulations include the effects of edge roughness and impurity scattering in realistic graphene devices. Our calculations revealed unique features which differ from both Schrödinger or Dirac billiards of confined massive or massless free particles. The graphene bandstructure near the  $K$  point leaves clear imprints, including interference structures in the wave functions, enhanced confinement effects, and a delayed transition from Poisson to Wigner-Dyson nearest-neighbor distributions in the regular-to-chaotic

crossover. Furthermore, we found that the size and roughness of a graphene-based quantum dot can be inferred from its spectral properties. This result allows a characterization of the edge roughness and disorder concentration in experimental quantum dots based on the distribution of Coulomb blockade peaks. We investigated the eigenenergies of graphene-based quantum dots in a perpendicular magnetic field and give a simple counting argument to estimate the distribution of eigenstates in between Landau levels. Conversely, counting the number of Coulomb-blockade peaks in-between Landau levels allows an estimate of the amount of disorder in experiment.

We then applied our results on transport through graphene-based nanoribbons and assess the role of edge roughness and disorder scattering. We find that short-range impurities break pseudo-spin conservation, and thus lead to pronounced backscattering. For long ribbons, we find edge-disorder induced Anderson localization, including a stable exponential decay of the wave function over eight orders of magnitude. To elucidate in detail the role of scattering between (i) the two Dirac cones ( $K$ - $K'$  scattering) and (ii) the two lattice sites ( $AB$  scattering) in realistic graphene nanostructures, we calculate the Fourier transform of the scattering wavefunction. To disentangle the contributions of  $AB$  and  $K$ - $K'$  scattering, we consider two different types of lattice vacancies: we find that the visibility of size quantization plateaus in graphene is directly related to pseudo-spin conservation, and can thus motivate why quantization effects have not yet been observed in experiment. To ensure that our results are not related to a particular choice of lattice defects, we treat additional models of lattice defects in graphene, which result in the same properties as our simple lattice vacancies. For the transmission through a graphene-based point contact, we compare our results successfully to recent experimental data. We finally consider the potential impact of residual traces of a second graphene layer on the transport properties of monolayer graphene.

To investigate the correlation between quantum-mechanical description and semiclassical approximations (“quantum-classical correspondence”), we considered a special type of superconductor-normal conductor hybrid structures, so-called Andreev billiards. In these systems, a strong correlation between classical phase space structure and quantum mechanical density of states exists. We found that not only the general distribution of eigenvalues, but the superscar patterns of individual eigenstates can be understood by a simple Bohr-Sommerfeld quantization of periodic orbits. We systematically checked the predictions of this semiclassical approximation for different geometries and found systematic deviations. A thorough analysis of the Andreev reflection properties then allowed us to improve on the BS approximation for systems strongly coupled to the superconductor. In the limit

of weak coupling, we identified three distinct effects leading to the breakdown of the semiclassical description and provided quantitative criteria for the applicability of the semiclassical Bohr-Sommerfeld approximation. Our results are valid for a wide range of different geometries. We proceeded to the case of disordered Andreev billiards, where random diffractive scattering makes a semiclassical prediction impossible. In particular, we investigated the distribution of the lowest-lying eigenstates in these systems. In contrast to predictions based on random matrix theory, we found a decrease, rather than an increase, in the lowest eigenstate. We showed that this unexpected behavior can be understood by considering the distribution of the Wigner-Smith delay time values. In particular, their maximum value, instead of mean value, is the physically relevant quantity to describe the evolution of the excitation gap in Andreev billiards. By considering the Wigner-Smith delay time values, an understanding of the underlying dynamics of disordered Andreev billiards can thus be gained even for such systems for which a semiclassical description fails. We finally considered transport through open SN hybrid systems, and showed how quantum interference effects can be used to tune the device transmission on small energy scales. The resulting strong energy dependence of the transmission may lead to different behavior of the electrical and thermal conductance, deviating from the Wiedemann-Franz law.

For both graphene-based nanodevices as well as for SN hybrid structures, we found interference-based effects that lead to physical properties beyond those offered by simplified descriptions based on either the Dirac equation or the Bohr-Sommerfeld approximation. Both systems feature two “sheets”: The two sublattices of graphene and the electron and hole sheet of Andreev billiards. For both systems, widely used models predict that the dynamics in both sheets closely resemble each other. In contrast, we found that wave function patterns of the two sheets feature unexpected differences that are not contained in the simplified descriptions. In this spirit, I want to conclude this thesis with a quote:

*“Alles sollte so einfach wie möglich gemacht sein, aber nicht einfacher.”*  
*“Everything should be made as simple as possible, but not more simple.”*

Albert Einstein

# Appendix A

## Supplementary calculations

### A.1 The Arnoldi factorization

In this section, we briefly outline the Arnoldi-Lanczos factorization used in the calculation of eigenstates in this work. For a more thorough treatment, refer to [29, 30]. The idea behind the Arnoldi factorization is to find a suitably reduced projection  $a \in \mathbb{R}^{n \times n}$ ,  $n \ll N$ , of  $A \in \mathbb{R}^{N \times N}$  that can be diagonalized using standard numerical techniques. By proper choice of the projection method, the eigenvalues of  $a$  converge against selected eigenvalues of  $A$ . A possible choice is projection onto the Krylov-subspace

$$K_n(|q_0\rangle) := \{|q_0\rangle, A|q_0\rangle, A^2|q_0\rangle, \dots, A^n|q_0\rangle\} \quad (\text{A.1})$$

formed by iteratively applying a random vector  $|q_0\rangle$  on  $A$ . However, a naive calculation of  $K_n$  is numerically unstable. A better choice is the set

$$Q = \{|q_0\rangle, |q_1\rangle, \dots, |q_n\rangle\}, \quad |q_k\rangle = \alpha \left[ \mathbb{1} - \sum_{i=1}^{k-1} |q_i\rangle \langle q_i| \right] A |q_{k-1}\rangle. \quad (\text{A.2})$$

The term in square brackets ensures that all  $|q_i\rangle$  are orthogonal to each other while the constant  $\alpha$  is determined by normalization, i.e.  $\langle q_i | q_j \rangle = \delta_{ij}$ . The  $|q_i\rangle$  thus form an orthonormal basis set of  $K_n$ . The orthogonal projection of  $A$  onto  $K_n$ ,

$$a_{ij} := \langle q_i | A |q_j \rangle \quad (\text{A.3})$$

is diagonalized using standard techniques. One can show that the eigenvalues of  $a_{ij}$  converge to extreme eigenvalues of  $A$  (the largest and smallest ones) [29, 30]. The IRAL algorithm performs the above diagonalization of  $a$ , and then chooses a linear combination of those eigenvectors with the smallest absolute value as new  $|q_0\rangle$ . This is done iteratively until convergence is reached.





### A.3 Thermal currents

In the following, we will give a brief outline of diffusive thermal and electrical currents in metals in the presence of both a bias voltage and a temperature gradient. Our aim is to find linearized expressions for the heat conductance and electrical conductance in terms of the zero-temperature conductance  $G_0$ , that we can calculate using the *MRGM*. For a detailed introduction into the subject, see e.g. [165].

Consider two reservoirs connected by a perfect waveguide at finite temperature  $T$ . The presence of an electric voltage difference  $V$  between the reservoirs will generate an electrical current

$$I_e = GV, \quad (\text{A.8a})$$

where  $G$  denotes the electrical conductance. For finite  $T$ ,  $G$  can be expressed as

$$G(T) = \int G_0(\varepsilon) \frac{df}{d\varepsilon} d\varepsilon, \quad (\text{A.8b})$$

where  $G_0(\varepsilon)$  is the electrical conductance at zero temperature and  $f(\varepsilon)$  is the Fermi function that describes the distribution of electrons at finite temperature  $T$

$$f(\varepsilon - \mu) = \frac{1}{1 + e^{\beta(\varepsilon - \mu)}}, \quad \beta := \frac{1}{k_B T}. \quad (\text{A.8c})$$

The convolution with the derivative of  $f$  that appears in (A.8b) corresponds to an average over  $G(\varepsilon)$  around an energy interval  $k_B T$  [see Fig. 5.35].

The presence of a temperature gradient  $\delta T$  between the two reservoirs will generate a heat current

$$I_h = G_h \delta T, \quad (\text{A.8d})$$

where  $G_h$  denotes the thermal conductance [165]. More generally, if we combine both a finite  $V$  and  $\delta T$ , we obtain off-diagonal contributions [156]

$$I_e = GV + B\delta T, \quad (\text{A.9a})$$

$$I_h = \Gamma V + \Xi \delta T, \quad (\text{A.9b})$$

The coefficients  $B$ ,  $\Gamma$  and  $\Xi$  may be determined using statistical mechanics [165]. The coefficient  $\Xi$  can be expressed in terms of a convolution over  $G_0$  as [156]

$$\Xi = \int G_0(\varepsilon) \beta^2 (\varepsilon - \mu)^2 \frac{df}{d\varepsilon} d\varepsilon. \quad (\text{A.10})$$

In general,  $\Xi \neq G_h$ , because the existence of a thermal gradient will itself introduce a voltage drop  $V$  [165]. The heat conductance  $G_h$  is defined for vanishing electrical current, i.e.  $I_e = 0$ . Using (A.9), we can express  $G_h$  as

$$G_h = \frac{1}{\delta T}(\Gamma V + \Xi \delta T) \Big|_{I_e=0} = \Xi - \frac{\Gamma B}{G}. \quad (\text{A.11})$$

The off-diagonal coefficients  $B$  and  $\Gamma$  in (A.9) relate the heat current created by a voltage drop and the electrical current created by a temperature difference. They are related by Onsager's principle:  $B = -\Gamma$  [166]. The corresponding processes can be understood by considering reservoirs at different potentials, but constant temperature  $T$ , i.e.  $\delta T = 0$ . A current of both electrons as well as holes (in opposite directions) will flow to offset the voltage difference. The contribution to the heat current of an electron [hole] at energy  $\mu + \varepsilon$  [ $\mu - \varepsilon$ ] is thus  $(\varepsilon - \mu)G(\varepsilon)$  [ $(-\varepsilon + \mu)G(-\varepsilon)$ ]. Consequently, if the zero temperature conductance  $G(\varepsilon)$  is equal for electrons and holes, no net heat current flows. If there are, however, fluctuations of  $G(\varepsilon)$  on a scale below  $k_B T$ , then a net heat current of

$$V\Gamma = -V \int G(\varepsilon)(\varepsilon - \mu) \frac{\partial}{\partial \varepsilon} f(\varepsilon - \mu) d\varepsilon, \quad (\text{A.12})$$

is generated. As the term  $\varepsilon - \mu$  is odd in Eq. (A.12) the integral vanishes for constant  $G(\varepsilon)$ , as expected.

## A.4 The acoustic wave equation

To derive the acoustic wave equation, we consider a gas-filled cavity. The local displacement of the gas from its equilibrium position is noted by the vector field  $\xi(\mathbf{x}, t)$ . The scalar local pressure  $p(\mathbf{x}, t)$  creates a force on the displaced gas that tries to bring it back to equilibrium,

$$\rho_0 \frac{\partial^2 \xi}{\partial t^2} = -\nabla p(\mathbf{x}, t), \quad (\text{A.13})$$

according to Newton's law. According to the law of mass conservation, fluctuations in the equilibrium density  $\rho_0$  can be related to gas flow,

$$\nabla \cdot \xi(\mathbf{x}, t) = \frac{1}{\rho_0} \rho(\mathbf{x}, t), \quad (\text{A.14})$$

where the local density  $\rho(\mathbf{x}, t)$  can be expressed by the ideal gas equation as

$$pV = Nk_B T, \quad \rightarrow \quad \rho = \frac{Vm}{Nmk_B T} = \frac{m_0}{k_B T} p \quad (\text{A.15})$$

By applying the nabla operator to Eq. (A.13), one thus arrives at

$$\rho_0 \nabla \cdot \frac{\partial^2 \xi}{\partial t^2} = \frac{\partial^2}{\partial t^2} p = -\frac{m_0}{k_B T} \nabla \cdot \nabla p(\mathbf{x}, t) = \frac{1}{v_0^2} \Delta p(\mathbf{x}, t), \quad (\text{A.16})$$

with  $v_0 = k_B T / m_0$  is the speed of sound,  $v_0 \approx 330 \text{ m/s}$ . The above equation is a three-dimensional wave equation for the scalar local pressure  $p(\mathbf{x}, t)$ . Because we want to model a cylindrical resonator, we introduce cylindrical coordinates  $(\rho, \phi, z)$  in (A.16), yielding

$$\Delta p = \frac{1}{r} \partial_r (r \partial_r p) + \frac{1}{r^2} \partial_\phi^2 p + \partial_z^2 p = \frac{\omega^2}{v_0^2} p. \quad (\text{A.17})$$

Due to the rotational symmetry of the resonator,  $\partial_\phi p \equiv 0$ , resulting in an effectively two-dimensional, elliptic differential equation, which can well be solved using the MRGM. Note that we have assumed constant temperature  $T$  in the above derivation, which, unfortunately, is not valid for metallic resonators. Additionally, the effect of friction at the walls of the resonator have been neglected. Both effects lead to dissipation of energy by heating of the resonator walls.

The boundary conditions for the above wave equation are, in contrast to the Schrödinger equation, von Neumann conditions at the cavity walls, as the velocity of the gas is always parallel to its walls,

$$\mathbf{n}_\perp \cdot \xi \equiv 0 \rightarrow \mathbf{n}_\perp \cdot \nabla p = 0. \quad (\text{A.18})$$

To describe the continuous wave equation (6.1), we use a tight binding grid in the continuum limit (see 2.1.3). For a cylindrical region of diameter  $D = 2R$  and length  $L$  we discretize space in cylindrical coordinates according to

$$(r, z) \rightarrow (r_i, z_i) = ([j - \frac{1}{2}] \Delta r, i \Delta z), \quad \Delta r = \frac{1}{N_r + 1} R, \quad \Delta z = \frac{1}{N_z + 1} L. \quad (\text{A.19})$$

We choose the matrix elements of  $H_0$  and  $H_I$  in such a way that in the limit of  $N_j \rightarrow \infty$  the continuum equation is restored. In discretized form the wave equation (A.17) for  $p(z_i, r_j) =: p_{ij}$  reads

$$\frac{1}{r_j} \left[ \frac{p_{ij+1} r_{j+\frac{1}{2}} - 2p_{ij} r_j + p_{ij-1} r_{j-\frac{1}{2}}}{(2\Delta r)^2} \right] + \frac{p_{i+1j} - 2p_{ij} + p_{i-1j}}{(\Delta z)^2} = \frac{\omega^2}{v_0^2} p_{ij}. \quad (\text{A.20})$$

As single blocks, we choose all sites with the same  $z$ ,  $H_0$  thus mediates the interactions in  $r$ -direction. It can be implemented as a tri-diagonal matrix

with elements

$$\begin{aligned} (H_0)_{j,j} &= -2 \left( \frac{1}{\Delta z^2} + \frac{1}{2\Delta r^2} \right), \\ (H_0)_{j,j-1} &= -\frac{r_{j-\frac{1}{2}}}{4r_j\Delta r}, \quad (H_0)_{j,j+1} = -\frac{r_{j+\frac{1}{2}}}{4r_j\Delta r}, \end{aligned} \tag{A.21}$$

while  $H_I$ , mediating the interaction in  $z$ -direction, is diagonal,

$$H_I = -\frac{1}{\Delta z^2} \mathbb{1}. \tag{A.22}$$

To introduce the von Neumann boundary conditions (A.18) at  $r_N = R$ , we use the condition

$$\partial_r p|_{r=R} \iff p_{i,N_r+1} = p_{i,N_r} \tag{A.23}$$

to replace  $p_{i,N_r+1}$  in the equation for  $p_{i,N_r}$ . This changes the definition of the outmost matrix element of  $H_0$  to

$$(H_0)_{N_r,N_r} \rightarrow (H_0)_{N_r,N_r} + (H_0)_{N_r,N_r+1}. \tag{A.24}$$

# Appendix B

## A complete reference for the MRGM

### B.1 Green's function of the infinite waveguide

Starting from Eq. (3.11), we will now show that the Green's function of the infinite waveguide is given by Eq. (3.13). We expand the Green's function in Bloch states of the infinite waveguide (Eq. 3.10):

$$g_{x>x'}^+ = \sum_{j=1}^N |\chi_j\rangle e^{ik_j(x-x')} \langle a_j|, \quad g_{x<x'}^- = \sum_{\bar{j}=1}^N |\chi_{\bar{j}}\rangle e^{ik_{\bar{j}}(x-x')} \langle b_{\bar{j}}|. \quad (\text{B.1})$$

with yet undetermined  $\langle a|$  and  $\langle b|$ . We then use the continuity condition

$$\lim_{x \rightarrow x'} g^+ = \sum_{j=1}^N |\chi_j\rangle \langle a_j| = \lim_{x \rightarrow x'^-} g^- = \sum_{\bar{j}=1}^N |\chi_{\bar{j}}\rangle \langle b_{\bar{j}}|. \quad (\text{B.2})$$

The most general solution of this equation is an ansatz of the form

$$\langle a_j| = \langle \chi_j| V^{-1}, \quad \langle b_{\bar{j}}| = \langle \chi_{\bar{j}}| V^{-1}, \quad (\text{B.3})$$

with some yet undetermined matrix  $V$ . Here,  $\langle \chi_n|$  is defined by  $\langle \chi_i | \chi_j \rangle = \delta_{ij}$  (and likewise for  $\langle \chi_{\bar{j}}|$ ), resulting in the completeness relation  $\sum |\chi_j\rangle \langle \chi_j| = \mathbb{1}$ .

The matrix  $V$  can be determined using Eq. (3.11):

$$\begin{aligned}
(H - E)g_{x=x'} &= \left[ \sum_{j=1}^N \overbrace{(H_0 - E + H_I e^{ik_j \Delta x})}^{-H_I^\dagger e^{-ik_j \Delta x} |\chi_j\rangle} |\chi_j\rangle \langle \chi_j| + H_I^\dagger \overline{D}(-1) \right] V^{-1} \\
&= H_I^\dagger [\overline{D}(-\Delta x) - D(-\Delta x)] V^{-1} = \mathbb{1}, \\
V &= H_I^\dagger [D(-\Delta x) - \overline{D}(-\Delta x)]. \tag{B.4}
\end{aligned}$$

where we have used the shorthand-notation (3.12b).

## B.2 Green's function of a half-infinite waveguide

The interface Green's functions of the half-infinite waveguide were already derived in section 3.2.2,

$$g^L H_I = \overline{D}(\Delta x) \tag{B.5a}$$

$$g^R H_I^\dagger = D(\Delta x). \tag{B.5b}$$

If a point  $\xi$  lies within the waveguide, Dyson equation can be used to obtain

$$g_{1\xi}^R = [\mathbb{1} - D(\Delta x)\overline{D}(\Delta x)] g_{1\xi} \tag{B.6a}$$

$$g_{1\xi}^L = [\mathbb{1} - \overline{D}(\Delta x)D(\Delta x)] g_{1\xi} \tag{B.6b}$$

Last but not least, a Green's function of an infinite waveguide connecting to points in the bulk can be determined using

$$g_{\eta\xi} = g_{\eta\xi}^R + g_{\eta 1} H_I^\dagger g^L H_I g_{1\xi}^R, \tag{B.7}$$

resulting in

$$g_{\eta\xi}^R = g_{\eta\xi} - g_{\eta 1} H_I D(\Delta x) [\mathbb{1} - D(\Delta x)\overline{D}(\Delta x)] g_{1\xi} \tag{B.8a}$$

and likewise

$$g_{\eta\xi}^L = g_{\eta\xi} - g_{\eta 0} H_I^\dagger \overline{D}(\Delta x) [\mathbb{1} - \overline{D}(\Delta x)D(\Delta x)] g_{1\xi}. \tag{B.8b}$$

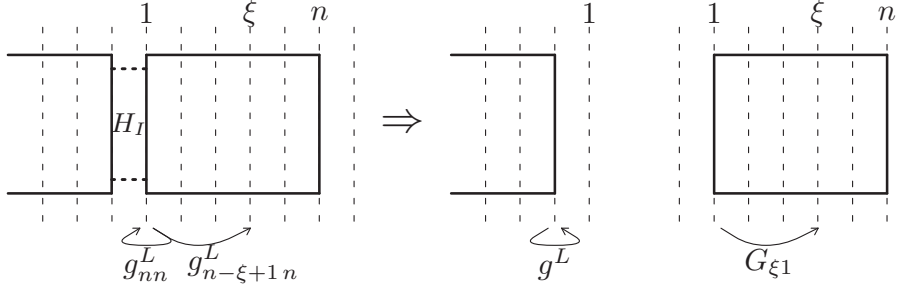


Figure B.1: *Cutting a rectangular module off a half-infinite waveguide extending to  $+\infty$  (a) [ $-\infty$  (b)] by use of a matrix Dyson equation. The  $x$  coordinates in reference to the rectangle are given. The Green's functions appearing in Eq. B.10 are marked.*

### B.3 Green's function of a rectangular module

An expression for the Green's function from an arbitrary point  $\xi$  inside a rectangle to its right side was derived in section 3.2.3

$$g_{\xi n}^R = G_{\xi n} + G_{\xi n} H_I g^R H_I^\dagger g_{nn}^R \Rightarrow G_{\xi n} = g_{\xi n}^R \frac{1}{\mathbb{1} + H_I g^R H_I^\dagger g_{nn}^R}. \quad (\text{B.9})$$

$G_{\xi 1}$  may be expressed using a waveguide extending to  $-\infty$  [see Fig. B.1]. Care must be taken in this case to avoid confusion with the indices labeling the  $x$  coordinate in lead and rectangle, respectively: The coordinate  $\xi \in [1, n]$  in the rectangle refers to position  $\zeta = n - \xi + 1$  of the left lead, counted from the rightmost stripe of the lead (see Fig. B.1):

$$g_{\zeta n}^L = G_{\xi 1} + G_{\xi 1} H_I^\dagger g^L H_I g_{nn}^L \Rightarrow G_{\xi 1} = g_{\zeta n}^L \frac{1}{\mathbb{1} + H_I^\dagger g^L H_I g_{nn}^L}. \quad (\text{B.10})$$

### B.4 Assembling the modules

To assemble the entire scattering structure, we start with the Green's function of the left lead,  $\mathcal{G}^{(0)}$ , and iteratively attach the rectangular modules. In step number  $k$ , we solve the Dyson equations for the four unknown Green's functions  $\mathcal{G}_{i,j}^{(k)}$  by first calculating the intermediate Green's functions (see Fig. B.2)

$$\mathcal{G}_{1^{(0)}n^{(k-1)}}^{(k)} = \mathcal{G}_{1^{(0)}n^{(k-1)}}^{(k-1)} \frac{1}{\mathbb{1} - H_I^{(k)} G_{11}^{(k)} H_I^{\dagger(k)} \mathcal{G}_{n^{(k-1)}n^{(k-1)}}^{(k-1)}} \quad (\text{B.11a})$$

$$\mathcal{G}_{n^{(k)}n^{(k-1)}}^{(k)} = G_{n1}^{(k)} \frac{1}{\mathbb{1} - H_I^{\dagger(k)} \mathcal{G}_{n^{(k-1)}n^{(k-1)}}^{(k-1)} H_I^{(k)} G_{11}^{(k)}}. \quad (\text{B.11b})$$

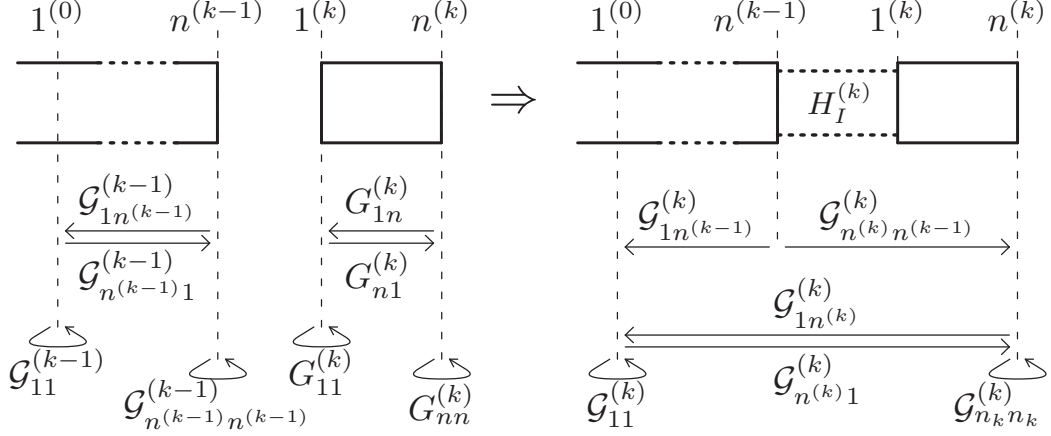


Figure B.2: Dyson equation to attach module  $k$  (described by the Green's functions  $G_{ij}^{(k)}$ ) to the Green's function  $\mathcal{G}^{(k-1)}$  already containing the left lead and  $k-1$  rectangles. The resulting Green's functions  $\mathcal{G}^{(k)}$  are given in Eq. (B.12).

The denominator introduces the change from  $\mathcal{G}^{(k-1)}$  to  $\mathcal{G}^{(k)}$  in all orders due to the interaction with the rectangle ( $k$ ). The updated  $G^{(k)}$  can now be written as (see Fig. B.2)

$$\mathcal{G}_{1^{(0)}1^{(0)}}^{(k)} = \mathcal{G}_{1^{(0)}1^{(0)}}^{(k-1)} + \mathcal{G}_{1^{(0)}n^{(k-1)}}^{(k)} H_I^{(k)} G_{11}^{(k)} H_I^{\dagger(k)} \mathcal{G}_{n^{(k-1)}1^{(0)}}^{(k-1)} \quad (\text{B.12a})$$

$$\mathcal{G}_{1^{(0)}n^{(k)}}^{(k)} = \mathcal{G}_{1^{(0)}n^{(k-1)}}^{(k)} H_I^{(k)} G_{1n}^{(k)} \quad (\text{B.12b})$$

$$\mathcal{G}_{n^{(k)}1^{(0)}}^{(k)} = \mathcal{G}_{n^{(k)}n^{(k-1)}}^{(k)} H_I^{\dagger(k)} \mathcal{G}_{n^{(k-1)}1}^{(k-1)}, \quad (\text{B.12c})$$

$$\mathcal{G}_{n^{(k)}n^{(k)}}^{(k)} = G_{n^{(k)}n^{(k)}}^{(k)} + \mathcal{G}_{n^{(k)}n^{(k-1)}}^{(k)} H_I^{\dagger(k)} \mathcal{G}_{n^{(k-1)}n^{(k-1)}}^{(k-1)} H_I^{(k)} G_{1n}^{(k)}. \quad (\text{B.12d})$$

The above procedure is performed iteratively for all rectangular modules and the left lead to obtain the total Green's function  $\mathcal{G}$  of the entire scattering geometry.

## B.5 Transmission coefficients

The transmission (reflection) amplitude of mode  $n$  incident from the left lead to be scattered into mode  $m$  on the right (left) lead is given by  $t_{mn}$  ( $r_{mn}$ ). Likewise, if mode  $n$  is incident from the right lead, the amplitudes  $t'_{mn}$  and  $r'_{mn}$  are used. We will consider here the general case where the left and right lead are different: The Bloch eigenstates of the right (left) lead will be labeled



$|\chi_n^R\rangle$  ( $|\chi_n^L\rangle$ ). The number of open modes in the left and right lead are  $N_L$  and  $N_R$  respectively. As shown in Sec. 3.2.6, the transmission and reflection amplitudes can be expressed in terms of the total green's function  $\mathcal{G}$  as

$$t_{mn} = \sqrt{\frac{v_m^R}{v_n^L}} \langle \chi_m^R | \mathcal{G}_{RL} V^L | \chi_n^L \rangle, \quad t \in \mathbb{C}^{N_R \times N_L}, \quad (\text{B.13a})$$

$$r_{mn} = \sqrt{\frac{-\bar{v}_m^L}{v_n^L}} \langle \chi_m^L | \mathcal{G}_{LL} V^L - \mathbb{1} | \chi_n^L \rangle, \quad r \in \mathbb{C}^{N_L \times N_L}, \quad (\text{B.13b})$$

$$t'_{mn} = \sqrt{\frac{v_m^L}{v_n^R}} \langle \chi_m^L | \mathcal{G}_{LR} V^R | \chi_n^R \rangle, \quad t' \in \mathbb{C}^{N_L \times N_R}, \quad (\text{B.13c})$$

$$r'_{mn} = \sqrt{\frac{v_m^R}{-v_n^R}} \langle \chi_m^R | \mathcal{G}_{RR} V^R - \mathbb{1} | \chi_n^R \rangle, \quad r' \in \mathbb{C}^{N_R \times N_R}. \quad (\text{B.13d})$$

Here, the indices  $L$  and  $R$  denote (the first stripe of) the left and right lead respectively. The scattering matrix  $S$  can now be assembled as

$$S = \begin{pmatrix} r & t' \\ t & r' \end{pmatrix}, \quad S \in \mathbb{C}^{(N_R+N_L) \times (N_R+N_L)}. \quad (\text{B.14})$$

The total transmission and reflection coefficients  $R$  and  $T$  (or  $R'$  and  $T'$  if the electron is incident from the right) are now obtained by summing over the amplitude

$$T = \sum_{m=1}^{N_R} \sum_{n=1}^{N_L} |t_{mn}|^2, \quad R = \sum_{m,n=1}^{N_L} |r_{mn}|^2, \quad (\text{B.15a})$$

$$T' = \sum_{m=1}^{N_L} \sum_{n=1}^{N_R} |t'_{mn}|^2, \quad R' = \sum_{m,n=1}^{N_R} |r'_{mn}|^2. \quad (\text{B.15b})$$

## B.6 Wave-function pictures

We will now give a derivation for the vectors  $|p^{(k)}\rangle$  and  $|q^{(k)}\rangle$  used in Eq. (3.36) to efficiently calculate the scattering state of a complicated scattering structure. The  $\xi$ -dependence of the Green's function of a rectangular module can be determined by inserting Eq. (B.8) into Eq. (3.23),

$$\begin{aligned} G_{\xi_1}^{(k)} &= \left[ g_{\xi_1} - g_{\xi_n} H_I g^R H_I^\dagger g_{n1}^L \right] \frac{1}{\mathbb{1} + H_I^\dagger g^L H_I g_{nn}^L}, \\ G_{\xi_n}^{(k)} &= \left[ g_{\xi_n} - g_{\xi_1} H_I^\dagger g^L H_I g_{1n}^R \right] \frac{1}{\mathbb{1} + H_I g^R H_I^\dagger g_{nn}^R}. \end{aligned} \quad (\text{B.16})$$

By using the projection operator  $P$  (see 3.33), we can reduce the  $\xi$ -independent contribution to one-dimensional vectors,

$$\left| \phi_1^{(k)} \right\rangle = \frac{1}{\mathbb{1} + H_I^\dagger g^L H_I g_{nn}^L} H_I^{\dagger(k)} \mathcal{G}_{n^{(k-1)}, 1^{(0)}} P, \quad (\text{B.17})$$

$$\left| \phi_n^{(k)} \right\rangle = \frac{1}{\mathbb{1} + H_I g^R H_I^\dagger g_{nn}^R} H_I^{(k)} \mathcal{G}_{1^{(k+1)}, 1^{(0)}} P. \quad (\text{B.18})$$

Together with (B.19), we obtain

$$\left| p^{(x)} \right\rangle := V^{-1} \left[ \left| \phi_a \right\rangle - H_I^\dagger g^L H_I g_{1n}^R \left| \phi_d^{(x)} \right\rangle \right], \quad (\text{B.19a})$$

$$\left| q^{(x)} \right\rangle := V^{-1} \left[ \left| \phi_d \right\rangle - H_I g^R H_I^\dagger g_{n1}^L \left| \phi_a^{(x)} \right\rangle \right]. \quad (\text{B.19b})$$

For reasons of numerical efficiency, the above equations should be evaluated from the right to the left, in order to replace matrix-matrix multiplication by much quicker matrix-vector multiplications. Using (B.19), the wave function inside rectangle ( $k$ ) can be written as

$$\psi^{(k)}(\mathbf{x}) = \overline{D}(1-x) \left| p^{(k)} \right\rangle + D(x-l) \left| q^{(k)} \right\rangle. \quad (\text{B.20})$$

# Bibliography

- [1] A. MacKinnon and B. Kramer. The scaling theory of electrons in disordered solids: Additional numerical results. *Z. Phys. B*, 53:1, 1983.
- [2] A. MacKinnon. The calculation of transport properties and density of states of disordered solids. *Z. Phys. B*, 59:385, 1985.
- [3] D. K. Ferry and S. M. Goodwick. *Transport in Nanostructures*. Cambridge University Press, 1999.
- [4] L. Schweitzer, B. Kramer, and A. MacKinnon. The conductivity of a two-dimensional electronic system of finite width in the presence of a strong perpendicular magnetic field and a random potential. *Z. Phys. B*, 59:379, 1985.
- [5] E. R. Mucciolo, A. H. Castro Neto, and C. H. Lewenkopf. Conductance quantization and transport gap in disordered graphene nanoribbons. arXiv:0806.3777, 2008.
- [6] Y. Nakamura, Yu. A. Pashkin, and J. S. Tsai. Coherent control of macroscopic quantum states in a single-cooper-pair box. *Nature*, 398:786, 1999.
- [7] B. Trauzettel, D. V. Bulaev, D. Loss, and G. Burkard. Spin qubits in graphene quantum dots. *Nature Physics*, 3:192, 2007.
- [8] M. P. Blencowe. Quantum-displacement detection: Squid's at the limit. *Nature Physics*, 4:753, 2008.
- [9] A. K. Geim and K. S. Novoselov. The rise of graphene. *Nature Materials*, 6:183, 2007.
- [10] C. Stampfer, J. Güttinger, F. Molitor, D. Graf, T. Ihn, and K. Ensslin. Tunable coulomb blockade in nanostructured graphene. *Appl. Phys. Lett.*, 92:012102, 2008.

- [11] J. Faist, F. Capasso, C. Sirtori, K. W. West, and L. N. Pfeiffer. Controlling the sign of quantum interference by tunnelling from quantum wells. *Nature*, 390:589, 1997.
- [12] K. S. Novoselov, A. K. Geim, V. Morozov S, D. Jiang, M. Y. Zhang, S. V. Dubonos, I. V. Grigorieva, and A. A . Firsov. Electric field effect in atomically thin carbon films. *Science*, 306:666, 2004.
- [13] K. S. Novoselov, Z. Jiang, Y. Zhang, S. V. Morozov, H. L. Stormer, U. Zeitler, J. C. Maan, G. S. Boebinger, P. Kim, and A. K. Geim. Room-temperature quantum Hall effect in graphene. *Science*, 315:1379, 2007.
- [14] J. Davies. *The physics of low-dimensional semiconductors*. Cambridge University press, 1998.
- [15] H.-J. Stöckmann. *Quantum Chaos*. Cambridge University press, 1999.
- [16] C. M. Marcus, A. J. Rimberg, R. M. Westervelt, P. F. Hopkins, and A. C. Gossard. Conductance fluctuations and chaotic scattering in ballistic microstructures. *Phys. Rev. Lett.*, 69:506, 1992.
- [17] I. V. Zozoulenko, R. Schuster, K. F. Berggren, and K. Ensslin. Ballistic electrons in an open square geometry: Selective probing of resonant-energy states. *Phys. Rev. B*, 55:10209, 1997.
- [18] O. Bohigas, M. Giannoni, and C. Schmit. Characterization of chaotic quantum spectra and universality of level fluctuation laws. *Phys. Rev. Lett.*, 52:1, 1984.
- [19] E. Heller. Bound-state eigenfunctions of classically chaotic Hamiltonian systems: Scars of periodic orbits. *Phys. Rev. Lett.*, 53:1515, 1984.
- [20] L. Kouwenhoven and C. M. Marcus. Quantum dots. *Physics World*, June, 1998.
- [21] P. De Gennes. *Superconductivity of Metals and Alloys*. Benjamin, New York, 1966.
- [22] F. Jensen. *Introduction to computational chemistry*. John Wiley and sons, 1999. Chapter 6.
- [23] N. W. Ashcroft and N. D. Mermin. *Solid state Physics*. Thomson Learning Inc., 1976.

- [24] L. D. Landau. On the theory of the Fermi liquid. *Sov. Phys. JETP*, 8:70, 1959.
- [25] S. Sanvito, C. J. Lambert, J. H. Jefferson, and A. M. Bratkovsky. General green's-function formalism for transport calculations with *spd* Hamiltonians and giant magnetoresistance in co- and ni-based magnetic multilayers. *Phys. Rev. B*, 59:11936, 1999.
- [26] S. Sanvito. *Giant magnetoresistance and quantum transport in magnetic hybrid nanostructures*. PhD thesis, School of Physics and Chemistry, Lancaster University, Lancaster, LA1 4 YB, 1999.
- [27] L. A. Ponomarenko, F. Schedin, M. I. Katsnelson, R. Yang, E. H. Hill, K. S. Novoselov, and A. K. Geim. Chaotic Dirac billiard in graphene quantum dots. *Science*, 320:356, 2008.
- [28] K. J. Maschhoff and D. C. Sorensen. *P\_ARPACK: An efficient portable large scale eigenvalue package for distributed memory parallel architectures*, volume 1184 (Applied Parallel Computing in Industrial Problems and Optimization) of *Lecture Notes in Computer Science*. Springer-Verlag, 1996. Editors: Jerzy Wasniewski, Jack Dongarra, Kaj Madsen, and Dorte Olesen.
- [29] C. Lanczos. An iteration method for the solution of the eigenvalue problem of linear differential and integral operators. *J. Research of the National Bureau of Standards*, 45:255, 1950.
- [30] W. E. Arnoldi. The principle of minimized iterations in the solution of the matrix eigenvalue problem. *Quart. J. Applied Mathematics*, 9:17, 1951.
- [31] E. Prange and S. M. Girvin. *The quantum Hall effect*. Springer, 1987.
- [32] Y. Aharonov and D. Bohm. Significance of electromagnetic potentials in the quantum theory. *Phys. Rev.*, 115:485, 1959.
- [33] R. E. Peierls. Zur Theorie des Diamagnetismus von Leitungselektronen. *Z.Phys.*, 80, 1933.
- [34] A. Messiah. *Quantum mechanics*. North Holland publishing company, 1968.
- [35] S. Rotter, B. Weingartner, N. Rohringer, and J. Burgdörfer. Ballistic quantum transport at high energies and high magnetic fields. *Phys. Rev. B*, 68:165302, 2003.

- [36] Stefan Rotter, Jian-Zhi Tang, Ludger Wirtz, Johannes Trost, and Joachim Burgdörfer. Modular recursive green's function method for ballistic quantum transport. *Phys. Rev. B*, 62:1950, Jul 2000.
- [37] R. Landauer. Spatial variation of currents and fields due to localized scatterers in metallic conduction. *IBM J. Res. Dev.*, 1:223, 1957.
- [38] J. Feist, A. Bäcker, R. Ketzmerick, S. Rotter, B. Huckestein, and J. Burgdörfer. Nano-wires with surface disorder: Giant localization length and quantum-to-classical crossover. *Phys. Rev. Lett.*, 97:116804, 2007.
- [39] K. S. Novoselov, A. K. Geim, S. V. Morozov, D. Jiang, M. I. Katsnelson, I. V. Grigorieva, S. V. Dubonos, and A. A. Firsov. Two-dimensional gas of massless Dirac fermions in graphene. *Nature*, 438:197, 2005.
- [40] Y. Zhang, Y.-W. Tan, H. Stormer, and P. Kim. Experimental observation of quantum Hall effect and Berry's phase in graphene. *Nature*, 438:201, 2005.
- [41] M. V. Berry and R. J. Mondragon. Neutrino billiards: time-reversal symmetry-breaking without magnetic fields. *Proc. R. Soc. Lond. A*, 412:53, 1987.
- [42] H. Min, J. E. Hill, N. A. Sinitsyn, B. R. Sahu, L. Kleinman, and A. H. MacDonald. Intrinsic and Rashba spin-orbit interactions in graphene sheets. *Phys. Rev. B*, 74:165310, 2006.
- [43] N. Tombros, C. Jozsa, M. Popinciuc, H. T. Jonkman, and B. J. van Wees. Electronic spin transport and spin precession in single graphene layers at room temperature. *Nature*, 448:571, 2007.
- [44] N. Dombay and A. Calogeracos. Seventy years of the Klein paradox. *Phys. Rep.*, 315:41, 1999.
- [45] M. I. Katsnelson, K. S. Novoselov, and A. K. Geim. Chiral tunneling and the Klein paradox in graphene. *Nature Physics*, 2:620, 2006.
- [46] N. Stander, B. Huard, and D. Goldhaber-Gordon. Observation of Klein tunneling in graphene  $p$ - $n$  junctions. arXiv:0806.2319, 2008.
- [47] Z. Chen, Y. Lin, M. Rooks, and P. Avouris. Graphene nanoribbon electronics. *Physica E*, 40:228, 2007.

- [48] M. Y. Han, B. Özyilmaz, Y. Zhang, and P. Kim. Energy band gap engineering of graphene nanoribbons. *Phys. Rev. Lett.*, 98:206805, 2007.
- [49] Y.-M. Lin, V. Perebeinos, Z. Chen, and P. Avouris. Conductance quantization in graphene nanoribbons. cond-mat/0805.0035, 2008.
- [50] F. Miao, S. Wijeratne, Y. Zhang, U. C. Coskun, W. Bao, and C. N. Lau. Phase coherent transport of charges in graphene quantum billiards. *Science*, 317:1530, 2007.
- [51] C. Stampfer, E. Schurtenberger, F. Molitor, J. Güttinger, T. Ihn, and K. Ensslin. Tunable graphene single electron transistor. *Nano Letters*, in press.
- [52] F. Guinea, B. Horovitz, and P. Le Doussal. Gauge field induced by ripples in graphene. *Phys. Rev. B*, 77:205421, 2008.
- [53] S. Reich, J. Maultzsch, and C. Thomsen. Tight-binding description of graphene. *PRB*, 66:035412, 2002.
- [54] A. H. Castro Neto, F. Guinea, N. M. R. Peres, K. S. Novoselov, and A. K. Geim. The electronic properties of graphene. arXiv:0709.1163, to be published in *Rev. Mod. Phys.*, 2008.
- [55] G. W. Semenoff. Condensed-matter simulation of a three-dimensional anomaly. *Phys. Rev. Lett.*, 53:2449, 1984.
- [56] M. Evaldsson, I. V. Zozoulenko, H. Xu, and T. Heinzel. Edge disorder induced Anderson localization and conduction gap in graphene nanoribbons. arXiv:0805.4326, 2008.
- [57] D. Gunlycke, D. A. Areshkin, and C. T. White. Semiconducting graphene nanostrips with edge disorder. *Appl. Phys. Lett.*, 90:142104, 2007.
- [58] O. Hod, V. Barone, J. E. Peralta, and G. E. Scuseria. Enhanced half-metallicity in edge-oxidized zigzag graphene. *Nano Lett.*, 7:2295, 2007.
- [59] Y. Zhang, Y.-W. Tan, H. L. Stormer, and P. Kim. Experimental observation of the quantum Hall effect and Berry's phase in graphene. *Nature*, 438:201, 2005.
- [60] Y.-W. Son, M. L. Cohen, and S. G. Louie. Energy gaps in graphene nanoribbons. *Phys. Rev. Lett.*, 97:216803, 2006.

- [61] J.-H. Chen, C. Jang, S. Adam, M. S. Fuhrer, E. D. Williams, and M. Ishigami. Tunable graphene single electron transistor. *Nature Physics*, 4:377, 2008.
- [62] N. M. R. Peres, A. H. C. Neto, and F. Guinea. Conductance quantization in mesoscopic graphene. *Phys. Rev. B*, 73:195411, 2006.
- [63] J. Fernandez-Rossier, J. J. Palacios, and L. Brey. Electronic structure of gated graphene and graphene ribbons. *Phys. Rev. B*, 75:205441, 2007.
- [64] T. A. Brody. A statistical measure for repulsion of energy levels. *Lett. Nuov. Cim.*, 7:482, 1973.
- [65] F. M. Izrailev. Quantum localization and statistics of quasienergy spectrum in a classically chaotic system. *Phys. Lett. A*, 134:13, 1988.
- [66] E. Caurier, G. Grammaticos, and A. Ramani. Level repulsion near integrability: A random matrix analogy. *J. Phys. A*, 23:4903, 1990.
- [67] G. Lenz and F. Haake. Reliability of small matrices for large spectra with nonuniversal fluctuations. *Phys. Rev. Lett.*, 67:1, 1991.
- [68] M. V. Berry and M. Robnik. Semiclassical level spacings when regular and chaotic orbits coexist. *J. Phys. A*, 17:2413, 1984.
- [69] H. J. Mikeska, H. Hasegawa and H. Frahm. Stochastic formulation of energy-level statistics. *Phys. Rev. A*, 38:395, 1988.
- [70] C. E. Porter and R. G. Thomas. Fluctuations of nuclear reaction widths. *Phys. Rev.*, 104:483, 1956.
- [71] K. S. Novoselov, E. McCann, V. Morozov, S. V. I. Fal'ko, M. I. Katsnelson, U. Zeitler, D. Jiang, F. Schedin, and A. K. Geim. Unconventional quantum Hall effect and Berry's phase of  $2\pi$  in bilayer graphene. *Nature Physics*, 2:177, 2005.
- [72] K. S. Novoselov, A. K. Geim, V. Morozov, S. D. Jiang, M. I. Katsnelson, I. V. Grigorieva, S. V. Dubonos, and A. A. Firsov. Two-dimensional gas of massless Dirac fermions in graphene. *Nature*, 438:197, 2005.
- [73] K. Wakabayashi, Y. Takane, M. Yamamoto, and M. Sgrist. Edge effect on electronic transport properties of graphene nanoribbons and presence of perfectly conducting channel. arXiv:0809.2648, 2008.



- [74] P. W. Anderson. Absence of diffusion in certain random lattices. *Phys. Rev.*, 109:1492, 1958.
- [75] A. Cortijo and M. A. H. Vozmediano. Electronic properties of curved graphene sheets. *Eur. Phys. Lett.*, 77:47002, 2007.
- [76] H. Min, S. Bhagawan, S. K. Banerjee, and A. H. MacDonald. Ab initio theory of gate induced gaps in graphene bilayers. *Phys. Rev. B*, 75:155115, 2008.
- [77] P. Wissgott. Transport through bilayer graphene. Project report, Institute for theoretical physics, 2008.
- [78] T. Ohta, A. Bostwick, T. Seyller, K. Horn, and E. Rotenberg. Controlling the electronic structure of bilayer graphene. *Science*, 18:951, 2006.
- [79] C. Stampfer, L. Wirtz, A. Jungen, D. Graf, F. Molitor, C. Hierold, and K. Ensslin. Raman imaging of doping domains in graphene on  $S_iO_2$ . *Appl. Phys. Lett.*, 91:241907, 2007.
- [80] W. L. McMillan. Tunneling model of the superconducting proximity effect. *Phys. Rev.*, 175:537, 1968.
- [81] S. Guéron, H. Pothier, N. O. Birge, D. Estève, and M. H. Devoret. Superconducting proximity effect probed on a mesoscopic length scale. *Phys. Rev. Lett.*, 77:3025, 1996.
- [82] M. G. Vavilov, P. W. Brouwer, V. Ambegaokar, and C. W. J. Beenakker. Universal gap fluctuations in the superconductor proximity effect. *Phys. Rev. Lett.*, 86:874, Jan 2001.
- [83] A. Andreev. The thermal conductivity of the intermediate state in superconductors. *Sov. Phys. JETP*, 19:1228, 1964.
- [84] J. E. Zimmerman and A. H. Silver. Macroscopic quantum interference effects through superconducting point contacts. *Phys. Rev.*, 141:367–375, Jan 1966.
- [85] B. D. Josephson. Possible new effects in superconductive tunneling. *Phys. Lett.*, 1:7, 1962.
- [86] T. A. Fulton, P. L. Gammel, D. J. Bishop, L. N. Dunkleberger, and G. J. Dolan. Observation of combined Josephson and charging effects in small tunnel junction circuits. *Phys. Rev. Lett.*, 63:1307, 1989.

- [87] J. E. Mooij, T. P. Orlando, L. Levitov, Lin Tian, C. H. van der Wal, and S. Lloyd. Josephson persistent-current qubit. *Science*, 285:1036, 1999.
- [88] M. Hämmäläinen, R. Haari, R. J. Ilmoniemi, J. Knuutila, and O. V. Lounasmaa. Magnetoencephalography—theory, instrumentation, and applications to noninvasive studies of the working human brain. *Rev. Mod. Phys.*, 65:413, Apr 1993.
- [89] G. Blonder, M. Tinkham, and T. Klapwijk. Transition from metallic to tunneling regimes in superconducting microconstrictions: Excess current, charge imbalance and supercurrent conversion. *Phys. Rev. B*, 45:15:7, 1982.
- [90] H. Weber and O. Hittmair. *Supraleitung*. Verlag Karl Thieme München, 1979.
- [91] J. Bardeen, L. Cooper, and J. Schrieffer. Theory of superconductivity. *Phys. Rev. Lett.*, 108:1175, 1957.
- [92] H. Fröhlich, H. Pelzer, and S. Zienau. Properties of slow electrons in polar materials. *Philos. Mag.*, 41:221, 1950.
- [93] C. W. J. Beenakker. Random-matrix theory of quantum transport. *Rev. Mod. Phys.*, 69:731, 1997.
- [94] R. Enderlein and N. Horing. *Fundamentals of Semiconductor Physics and Devices*. World Scientific, 1997.
- [95] A. A. Abrikosov. *Fundamentals of the theory of metals*. North-Holland, Amsterdam, 1988.
- [96] N. A. Mortensen, K. Flensberg, and A.-P. Jauho. Angle dependence of Andreev scattering at semiconductor-superconductor interfaces. *Phys. Rev. B*, 59:10176, 1999.
- [97] J. Cserti, A. Bondor, J. Koltai, and G. Vattay. Excitation spectra for Andreev billiards of box and disk geometries. *Phys. Rev. B*, 66:064528, 2002.
- [98] A. F. Morpurgo, S. Holl, B. J. van Wees, T. M. Klapwijk, and G. Borghs. Phase conjugated Andreev backscattering in two-dimensional ballistic cavities. *Phys. Rev. Lett.*, 78:2636, 1997.

- [99] H. Pothier, S. Guéron, D. Esteve, and M. H. Devoret. Flux-modulated Andreev current caused by electronic interference. *Phys. Rev. Lett.*, 73:2488, 1994.
- [100] P. Charlat, H. Courtois, Ph. Gandit, D. Mailly, A. F. Volkov, and B. Pannetier. Reentrance of the metallic conductance in a mesoscopic proximity superconductor. *Phys. Rev. Lett.*, 77:4950, 1996.
- [101] C. J. Lambert and R. Raimondi. Phase-coherent transport in superconducting nanostructures. *J. Phys. Condens. Matter*, 10:901, 1998.
- [102] P. F. Bagwell. Suppression of the Josephson current through a narrow, mesoscopic, semiconductor channel by a single impurity. *Phys. Rev. B*, 46:12573, 1992.
- [103] M. Stone. Spectral flow, magnus force, and mutual friction via the geometric optics limit of Andreev reflection. *Phys. Rev. B*, 54:13222, 1996.
- [104] I. Kosztin, D. Maslov, and P. Goldbart. Chaos in Andreev billiards. *Phys. Rev. Lett.*, 75:1735, 1995.
- [105] J. Wiersig. Pseudointegrable Andreev billiards. *Phys. Rev. E*, 65:036221, 2002.
- [106] K. P. Duncan and B. L. Györfy. Semiclassical theory of quasiparticles in the superconducting state. *Annals of Physics*, 298:273, 2002.
- [107] J. Cserti, G. Vattay, J. Koltai, F. Taddei, and C. J. Lambert. Negative length orbits in normal-superconductor billiard systems. *Phys. Rev. Lett.*, 85:3704, 2000.
- [108] C. W. J. Beenakker. Andreev billiards. *Lect. Notes Phys.*, 667:131, 2005. (see especially chapters 3 and 6.3).
- [109] J. A. Melsen, P. W. Brouwer, K. M. Frahm, and C. W. J. Beenakker. Induced superconductivity distinguishes chaotic from integrable billiards. *Europhys. Lett.*, 35:7, 1996.
- [110] A. Lodder and Y. Nazarov. Density of states and the energy gap in Andreev billiards. *Phys. Rev. B*, 58:5783, 1998.
- [111] A. Kormanyos, Z. Kaufmann, J. Cserti, and C. J. Lambert. A logarithmic contribution to the density of states of rectangular Andreev billiards. *Phys. Rev. B*, 67:172506, 2003.

- [112] I. Adagideli and P. M. Goldbart. Quantal Andreev billiards: Density of states oscillations and the spectrum-geometry relationship. *Phys. Rev. B*, 65:201306(R), 2002.
- [113] J. Cserti, P. Polinak, G. Palla, U. Züllicke, and C. J. Lambert. Ring-shaped Andreev billiards in quantizing magnetic fields. *Phys. Rev. B*, 69:134514, 2004.
- [114] F. Libisch, S. Rotter, J. Burgdörfer, A. Kormányos, and J. Cserti. Bound states in Andreev billiards with soft walls. *Phys. Rev. B*, 72:075304, 2005.
- [115] C. W. J. Beenakker. Andreev billiards. *Lect. Notes Phys.*, 667:131, 2005.
- [116] J. Cserti, B. Berit, P. Pollner, and Z. Kaufmann. Andreev bound states for cake shape superconducting-normal systems. *submitted to J. Phys. C*, 2004.
- [117] W. Ihra, M. Leadbeater, J. Vega, and K. Richter. Semiclassical theory of integrable and rough Andreev billiards. *Eur.Phys.J.B.*, 21:425, 2001.
- [118] L. Wirtz, J. Tang, and J. Burgdörfer. Gauge-invariant theory for semiclassical magnetotransport through ballistic microstructures. *Phys. Rev. B.*, 59:2956, 1999.
- [119] L. Wirtz, C. Stampfer, S. Rotter, and J. Burgdörfer. Semiclassical theory for transmission through open billiards: Convergence towards quantum transport. *Phys. Rev. E*, 67:016206, 2003.
- [120] J. Cserti, A. Kormanyos, Z. Kaufmann, and J. Koltai. Proximity-induced supgaps in Andreev billiards. *Phys. Rev. Lett.*, 89:057001, 2002.
- [121] S. Gnutzmann, B. Seif, F. von Oppen, and M. R. Zirnbauer. Universal spectral statistics of Andreev billiards: Semiclassical approach. *Phys. Rev. E*, 67:046225, 2003.
- [122] H. Schomerus and C. Beenakker. Excitation spectrum of Andreev billiards with a mixed phase space. *Phys. Rev. Lett.*, 82:2951, 1999.
- [123] A. Altland and M. Zirnbauer. Random matrix theory of a chaotic Andreev quantum dot. *Phys. Rev. Lett.*, 76:3420, 1996.
- [124] L. Wirtz. Semiclassical scattering in mesoscopic ballistic semiconductor devices. Master's thesis, University of Tennessee, 1997.

- [125] M. Brack and R. Bhaduri. *Semiclassical physics*. Addison Wesley Publishing Company, 1997.
- [126] L. Wirtz, J.-Z. Tang, and J. Burgdörfer. Geometry-dependent scattering through ballistic microstructures: Semiclassical theory beyond the stationary-phase approximation. *Phys. Rev. B*, 56:7589, 1997.
- [127] F. Libisch. Electron and hole wavefunctions in Andreev billiards. Master's project, Vienna University of Technology, Institute for Theoretical Physics, 2004.
- [128] K. Husimi. Some formal properties of the density matrix. *Proc. Phys. Math. Soc. Jpn.*, 22:264, 1940.
- [129] E. Bogomolny and C. Schmit. Structure of wave functions of pseudointegrable billiards. *Phys. Rev. Lett.*, 92:244102, 2002.
- [130] P. G. Silvestrov, M. C. Goorden, and C. W. J. Beenakker. Adiabatic quantization of Andreev levels. *Phys. Rev. Lett.*, 90:116801, 2003.
- [131] M. C. Goorden, Ph. Jacquod, and C. W. J. Beenakker. Quasiclassical fluctuations of the superconductor proximity gap in a chaotic system. *Phys. Rev. B*, 68:220501, 2003.
- [132] J. Cserti, A. Bodor, J. Koltai, and G. Vattay. Excitation spectra for Andreev billiards of box and disk geometries. *Phys. Rev. B*, 66:064528, Aug 2002.
- [133] D. Taras-Semchuk and A. Altland. Quantum interference and the formation of the proximity effect in chaotic normal-metal/superconducting structures. *Phys. Rev. B*, 64:014512, 2001.
- [134] I. Adagideli and C. W. J. Beenakker. Ehrenfest-time-dependent excitation gap in a chaotic Andreev billiard. *Phys. Rev. Lett.*, 89:237002, 2002.
- [135] M. G. Vavilov and A. I. Larkin. Quantum disorder and quantum chaos in Andreev billiards. *Phys. Rev. B*, 67:115335, 2003.
- [136] A. Lodder and Yu. V. Nazarov. Density of states and the energy gap in Andreev billiards. *Phys. Rev. B*, 58:5783, Sep 1998.
- [137] J. Wiersig. Spectral properties of quantized barrier billiards. *Phys. Rev. E*, 65:046217, 2002.

- [138] C. Stampfer, L. Wirtz, S. Rotter, and J. Burgdörfer. Pseudo-path semi-classical approximation to transport through open quantum billiards: Dyson equation for diffractive scattering. *Phys. Rev. E*, 72:036223, 2005.
- [139] F. Aigner, S. Rotter, and J. Burgdörfer. Shot noise in the chaotic-to-regular crossover regime. *Phys. Rev. Lett.*, 94:216801, 2005.
- [140] E. G. Altmann, A. E. Motter, and H. Kantz. Stickiness in mushroom billiards. *Chaos*, 15:033105, 2005.
- [141] A. A. Golubov and M. Yu. Kuprianov. Thermal investigation of Josephson tunnel junctions with spatially inhomogeneous superconducting electrodes. *J. Low Temp. Phys.*, 70:83, 1988.
- [142] W. Belzig, C. Bruder, and G. Schön. Local density of states in a dirty normal metal connected to a superconductor. *Phys. Rev. B*, 54:9443, 1996.
- [143] S. Pilgram, W. Belzig, and C. Bruder. Excitation spectrum of mesoscopic proximity structures. *Phys. Rev. B*, 62:12462, 2000.
- [144] D. Saint-James. Elementary excitations in the vicinity of a normal metal-superconducting metal contact. *J. Phys. (France)*, 25:899, 1964.
- [145] Ioan Kosztin, Dmitrii L. Maslov, and Paul M. Goldbart. Chaos in Andreev billiards. *Phys. Rev. Lett.*, 75:1735, Aug 1995.
- [146] A. Kormányos, Z. Kaufmann, J. Cserti, and C. J. Lambert. Logarithmic contribution to the density of states of rectangular Andreev billiards. *Phys. Rev. B*, 67:172506, 2003.
- [147] N. G. Fytas, F. K. Diabonos, P. Schmelcher, M. Scheid, A. Lassel, K. Richer, and G. Fagas. Order and chaos in semiconductor microstructures. *Phys. Rev. B*, 72:085336, 2005.
- [148] H. Schomerus and C. W. J. Beenakker. Excitation spectrum of Andreev billiards with a mixed phase space. *Phys. Rev. Lett.*, 82:2951, 1999.
- [149] Felix T. Smith. Lifetime matrix in collision theory. *Phys. Rev.*, 118:349, Apr 1960.
- [150] Eugene P. Wigner. Lower limit for the energy derivative of the scattering phase shift. *Phys. Rev.*, 98:145, Apr 1955.

- [151] V. L. Lyuboshitz. On collision duration in the presence of strong overlapping resonance levels. *Phys. Lett.*, 72B:41, 1977.
- [152] C. W. J. Beenakker. Universal limit of critical-current fluctuations in mesoscopic Josephson junctions. *Phys. Rev. Lett.*, 67:3836, 1991.
- [153] M. G. A. Crawford and P. W. Brouwer. Density of proper delay times in chaotic and integrable quantum billiards. *Phys. Rev. E*, 65:026221, Jan 2002.
- [154] W. A. Lin, J. B. Delos, and R. V. Jensen. Order and chaos in semiconductor microstructures. *Chaos*, 3:655, 1993.
- [155] P. W. Brouwer, K. M. Frahm, and C. W. J. Beenakker. Quantum mechanical time-delay matrix in chaotic scattering. *Phys. Rev. Lett.*, 78:4737, 1997.
- [156] M. G. Vavilov and A. D. Stone. Failure of the Wiedemann-Franz law in mesoscopic conductors. *Phys. Rev. B*, 72:205107, 2005.
- [157] H. Beutler. Über Absorptionsserien von Argon, Krypton und Xenon in Termen zwischen den beiden Ionisierungsgrenzen  $^2P_3^{2/0}$  und  $^2P_3^{2/0}$ . *Z. Phys.*, 93:177, 1935.
- [158] U. Fano. Effects of configuration interaction on intensities and phase shifts. *Phys. Rev.*, 124:1866, 1961.
- [159] A. Fuhrer, P. Brusheim, T. Ihn, M. Sigrist, K. Ensslin, W. Wegscheider, and M. Bichler. Fano effect in a quantum-ring quantum-dot system with tunable coupling. *Phys. Rev. B*, 73:205326, 2006.
- [160] R. K. Adair, C. K. Bockelman, and R. E. Peterson. Experimental corroboration of the theory of neutron resonance. *Phys. Rev.*, 76:308, 1949.
- [161] M. Drescher, M. Hentschel, R. Kienberger, M. Uiberacker, V. Yakovlev, A. Scrinzi, Th. Westerwalbesloh, U. Kleineberg, U. Heinzmann, and F. Krausz. Time-resolved atomic inner-shell spectroscopy. *Nature*, 419, 2002.
- [162] S. Rotter, F. Libisch, J. Burgdörfer, U. Kuhl, and H.-J. Stöckmann. Tunable Fano resonances in transport through microwave billiards. *Phys. Rev. E*, 69:046208, 2004.

- [163] M. Wickenhauser, J. Burgdörfer, F. Krausz, and M. Drescher. Time resolved Fano resonances. *Phys. Rev. Lett.*, 94:023002, 2005.
- [164] J. Stein, H.-J. Stöckmann, and U. Stoffregen. Microwave studies of billiard green functions in propagators. *Phys. Rev. Lett.*, 75:53, 1995.
- [165] W. Jones and N. H. March. *Theoretical solid state physics*. Dover Publications Inc., 1973. Volume 2, see esp. chapter 6.
- [166] L. Onsager. Reciprocal relations in irreversible processes. *Phys. Rev.*, 37:405, 1931.



# Acknowledgments

At this point, I would like to thank the people who made this work possible, and helped me on the way. I would not have completed this work without them.

- My advisor Prof. Joachim Burgdörfer for his guidance, ideas, and many fruitful discussions.
- My co-advisor Dr. Stefan Rotter for encouragement, suggestions and always finding time for every question.
- Prof. Klaus Ensslin, for his hospitality, interesting discussions and his willingness to referee my thesis as well as to serve as examiner at the defense of this thesis.
- Dr. Christoph Stampfer, for many interesting discussions, ideas, his hospitality and his delicious cooking.
- Dipl.-Ing. Johannes Feist, for interesting discussions, both on physics and computer science, and a perfect collaboration during the quantum theory exercises.
- Prof. Karl Svozil, for offering me my first teaching opportunity, and for a flawless collaboration during the statistical mechanics class.
- My project students Richard Korytar, Andreas Bärentaler, Jürgen Möller and Philipp Wissgott, for asking difficult questions.
- Dr. Christoph Lemell, for solving computer problems and showing me how to optimize my code.
- Prof. Renè Matzdorf, Dr. Ulle Kuhl, Prof. Hans-Jürgen Stöckmann and Prof. Maxim Vavilov for fruitful collaboration, suggestions and challenging discussions.

- Many thanks are also due to my colleagues and friends at the Institute for Theoretical Physics at the Technical University of Vienna.
- I would also like to acknowledge the support of Mr. Hochfellner, Mrs. Höller, Mrs. Mössmer, and Mrs. Uden, for keeping the administration at the institute running perfectly.

The numerical calculations were performed on computers of the Zentraler Informatikdienst der TU Wien. Many thanks to Dr. Haunschmid for quickly solving any upcoming problems.

Last but not least, I would like to thank both my parents and my friends for their support during my studies, as well as all those to whom I apologize for not having been able to mention them.